S-1 MPC

S-1A & S-1B Annual Performance Report for 2016

Reference:	MPC-0366
Nomenclature:	DI-MPC-APR
Issue:	1. 1
Date:	2017,Apr.04

CLS (siège)
8-10 rue Hermès
Parc technologique du Canal
31520 Ramonville Saint-Agne
FRANCE

Tél. : +33 (0)5 61 39 47 00
Fax : +33 (0)5 61 75 10 14
Mél. : info@cls.fr
Web : www.cls.fr

CLS Brest Le Ponant
Avenue La Pérouse
29280 Plouzané
FRANCE

Tél. : +33 (0)2 98 05 76 80
Fax : +33 (0)2 98 05 76 90

Chronology Issues:

Issue:	Date:	Reason for change:	Author
0.1	23.02.17	First Draft	ESLs
1.0	10.03.2017	Initial version	ESLs
1.1	24.04.2017	Update after global review by ESLs and Technical Officer. Remove footer on disclosure of the document. Updated S-1A EW DLR transponder plots and text. Revision to S-1A BAE corner reflector plot and text. Revision to S-1B co-registration (Table 37). Comment added for S-1A gain imbalance. Text on the S-1A Tile 11 anomaly updated. Added reference to S-1B azimuth ambiguities section. Updated description of S-1A burst synchronization seasonal trend (Section 3.6). Updated description of S-1A DC increasing trend (Section 4.1.4) Update FDBAQ monitoring sections (Sections 4.1.3 and 6.1.3) Added S-1A PSCAL trend characterization (Section 4.2.3.2)	ESLs

People involved in this issue:

Written by (*):	Peter Meadows	Date + Initials:(visa or ref)
Checked by (*):	G.Hajduch	Date + Initial:(visa ou ref) 03/05/2017
Approved by (*):	G.Hajduch	Date + Initial:(visa ou ref) 03/05/2017

**In the opposite box: Last and First name of the person + company if different from CLS*

Index Sheet:

Context:	Sentinel-1 Mission Performance Centre
Keywords:	Sentinel-1, Mission Performance Centre, Annual Report
Hyperlink:	

Distribution:

Company	Means of distribution	Names
CLS ESA	Notification	

List of tables and figures

List of tables:

Table 1 Noise power stability (3-sigma): period JAN 2016 – DEC 2016 11
Table 2 Average bitrate for each acquisition mode. 14
Table 3 SM Azimuth and Slant Range Spatial Resolutions 17
Table 4 IW Azimuth and Slant Range Spatial Resolutions 17
Table 5 EW Azimuth and Slant Range Spatial Resolutions 18
Table 6 SM & IW Sidelobe Ratios 18
Table 7: SLC Relative Radar Cross-Section for the DLR transponders (dB) 20
Table 8: SM SLC Relative Radar Cross-Section for the DLR transponders (dB) 20
Table 9: IW & EW SLC Relative Radar Cross-Section for the DLR transponders (dB) 21
Table 10: IW SLC Relative Radar Cross-Section for the DLR transponders (dB) 22
Table 11: EW SLC Relative Radar Cross-Section for the DLR transponders (dB) 22
Table 12: IW SLC Relative Radar Cross-Section for the Australian Corner Reflectors (dB) 23
Table 13: Gain Imbalance using the DLR transponders 25
Table 14: Gain Imbalance using the DLR transponders 26
Table 15: Phase Imbalance using the DLR transponders 27
Table 16 Polarimetric Calibration Measurements 27
Table 17 S-1A/Radarsat-2 Mutual Interference during 2016 32
Table 18 Radar Data Base Changes History. 52
Table 19 Noise power stability (3-sigma): period JUN 2016 – DEC 2016 56
Table 20 Average bitrate for each acquisition mode. 58
Table 21: Pointing results on Elevation Notch products 58
Table 22: Pointing results on Elevation Notch products 59
Table 23 SM Azimuth and Slant Range Spatial Resolutions 62
Table 24 IW Azimuth and Slant Range Spatial Resolutions 62
Table 25 EW Azimuth and Slant Range Spatial Resolutions 63
Table 26 SM & IW Sidelobe Ratios 63
Table 27: Azimuth Ambiguity Ratios 65
Table 28: SLC Relative Radar Cross-Section for the DLR transponders (dB) 68
Table 29: SM SLC Relative Radar Cross-Section for the DLR transponders (dB) 68
Table 30: IW & EW SLC Relative Radar Cross-Section for the DLR transponders (dB) 69
Table 31: IW SLC Relative Radar Cross-Section for the DLR transponders (dB) 69
Table 32: EW SLC Relative Radar Cross-Section for the DLR transponders (dB) 70
Table 33: IW SLC Relative Radar Cross-Section for the Australian Corner Reflectors (dB) 70
Table 34: Gain Imbalance using the DLR transponders 74
Table 35: Gain Imbalance using the DLR transponders 75
Table 36: Phase Imbalance using the DLR transponders 76
Table 37: SLC Polarimetric Co-registration 77

Table 38: SLC Cross-talk 79

List of figures:

Figure 1: H (top) and V (bottom) polarisation error matrixes computed the 15-06-2016, before tile 11 issue happened. 3

Figure 2: H (top) and V (bottom) polarisation error matrixes computed the 27-06-2016, after SAR operation successful recovery. 4

Figure 3 Gain (*top)* and phase (*bottom)* stability of the SAR antenna tiles (average of the RFC coefficients in TX H over rows). The Tile#11 event on June can be recognized. 5

Figure 4 Gain (top) and phase (bottom) stability of the SAR antenna tiles (average of the RFC coefficients in TX V over rows). The Tile#11 event on June can be recognized. 5

Figure 5 Gain (top) and phase (bottom) stability of the SAR antenna tiles (average of the RFC coefficients in RX H over rows). 6

Figure 6 Gain (top) and phase (bottom) stability of the SAR antenna tiles (average of the RFC coefficients in RX V over rows). 6

Figure 7 S-1A Burst synchronization monitoring. 8

Figure 8 Internal calibration parameters over time. The colour represents the sub-swath. 9

Figure 9 Internal calibration parameters over time. The colour represents the polarisation. ... 9

Figure 10 EW HH (left) and HV (right) PG gain divided by sub-swath. 10

Figure 11 IW VV (left) and VH (right) PG gain divided by sub-swath. 10

Figure 12 Noise power versus time. The colour represents the different beams. 11

Figure 13 (Left) Noise power histogram for IW1 VV data. (Right) Geographical noise power distribution. 12

Figure 14 I/Q channel imbalance. 13

Figure 15 Doppler Centroid versus time. Average on a data-take basis (dots) and daily average (red line). The star-trackers reconfigurations events are marked by the vertical black lines. The STT calibration campaign is marked by the vertical green lines. 15

Figure 16 SM Azimuth and Slant Range Spatial Resolutions 16

Figure 17 IW Azimuth and Slant Range Spatial Resolutions 17

Figure 18 EW Azimuth and Slant Range Spatial Resolutions 17

Figure 19 Improvement in IW Azimuth Spatial Resolution with IPF v2.70 18

Figure 20: IW SLC DLR Transponder IRF and Azimuth Ambiguity 19

Figure 21: SM SLC Relative Radar Cross-Section for the DLR transponders 20

Figure 22: IW SLC Relative Radar Cross-Section for the DLR transponders 21

Figure 23: EW SLC Relative Radar Cross-Section for the DLR transponders 21

Figure 24: IW SLC Relative Radar Cross-Section for the BAE Corner Reflector 22

Figure 25 Permanent Scatter Calibration time series for TopSAR IW V/V (left) and V/H (right) over Paris. 23

Figure 26 Permanent Scatter Calibration trends after tile 11 issue for TopSAR IW V/V (left) and V/H (right) over Paris. 23

Figure 27: ALE estimates for S-1A StripMap and IW SLC product time series acquired over the Swiss test sites using precise state vectors (AUX_POEORB). Product date ranges are given in brackets (N.B. no S-1A SM acquisitions were made over Switzerland during the 2016 campaign). Point colours represent beam/subswath. The S-1A SWST (range) bias (output of the commissioning and calibration phase) was applied in both cases. 25

Figure 28: IW Gain Imbalance using the DLR transponders. 26

Figure 29: Phase Imbalance using the DLR transponders. 27

Figure 30: NESZ measures for IW. Blue is the measured NESZ and the red lines are the predicted NESZ at minimum orbital altitude. 28

Figure 31: NESZ measures for EW. Blue is the measured NESZ and the red lines are the predicted NESZ at minimum orbital altitudes. 28

Figure 32: S-1A solar panel before and after debris collision on 23 August 2016 (red arrow indicates panel damage). 29

Figure 33: S-1A solar panel before and after debris collision on 23 August 2016 (detail). 30

Figure 34: An example of Radio Frequency Interference over Japan 31

Figure 35: S-1A/Satellite Interference 8th December 2016 over Florida, USA 33

Figure 36: SAR Wind speed compared with reference wind speed for IW mode VV polarisation. 34

Figure 37: SAR-derived wind estimation provided in the Level-2 OWI products showing the coastal margin introduced by the ice mask update. 35

Figure 38: Sea surface roughness of a Sentinel-1 product acquired over Greenland on 2016/04/29 (left) and the associated ice masked OWI product with background ice concentration (right). 36

Figure 39 Ocean surface wind monthly performances for WV1 (a) and WV2 (b) and number of acquisitions co-located to reference data for validation for WV1 (bottom-left) and WV2 (bottom- right). For top panels, colored thick solid lines stand for the mean difference between Sentinel-1 and ECMWF model wind speeds. Colored thin solid lines are for standard deviation. 38

Figure 40 scatter plot of wind speed from S-1A WV1 versus ECMWF Dec 2016 (left WV1 and right WV2). 39

Figure 41 S-1A WV1 and WV2 Ocean Swell monthly performances as function of time. 40

Figure 42 scatter plot of effective significant wave height from S-1A WV1 versus WW3 significant wave height Dec 2016. The model outputs are considered as reference here. This is only valid from a statistical point of view 41

Figure 43 Geophysical Doppler as included in the Level 2 products as a function of radial wind speed (wind speed projected in the line of sight of the radar) for WV1 and WV2. The colour code indicates the latitude. 42

Figure 44 WV1 Doppler bias as a function of latitude estimated over ocean (blue) and land (red). 43

Figure 45: a) Doppler anomaly and b) radial velocity field from Sentinel 1A IW RVL product acquired over Agulhas in ascending mode. Here land areas are used to calibrate the Doppler anomaly before computing the radial velocity. C) Scatterplot of radial surface current component derived from S-1A data and surface drifters acquired over Agulhas. 44

Figure 46: S-1A EM DC offset computed from antenna model (full line) with error matrix corresponding to the day of acquisition, and estimated from rain forest data using the Level 2 processor (***). A) EW mode in HH-polarisation, B) EW mode in VV-polarisation, C) IW mode in HH-polarisation, D) IW mode in VV-polarisation 45

Figure 47 Sentinel-A geophysical calibration constant given by CMOD-IFRv2 for WV1 VV polarisation between 50° and -50° latitude. Panel 1 shows the mean bias between ECMWF and Sentinel-1A. Panel 2 shows the bias standard deviation. Panel 3 shows the number of SAFE used to perform the analysis. 46

Figure 48 Sentinel-A geophysical calibration constant given by CMOD-IFRv2 for WV2 VV polarisation between 50° and -50° latitude. Panel 1 shows the mean bias between ECMWF and Sentinel-1A. Panel 2 shows the bias standard deviation. Panel 3 shows the number of SAFE used to perform the analysis. 47

Figure 49 S-1B antenna status on 31/12/2016. The top charts refer to RX elements and the bottom charts refer to TX elements 49

Figure 50 Gain (*top)* and phase (*bottom)* stability of the SAR antenna tiles (average of the RFC coefficients in TX H over rows). 50

Figure 51 Gain (top) and phase (bottom) stability of the SAR antenna tiles (average of the RFC coefficients in TX V over rows). 50

Figure 52 Gain (top) and phase (bottom) stability of the SAR antenna tiles (average of the RFC coefficients in RX H over rows). 51

Figure 53 Gain (top) and phase (bottom) stability of the SAR antenna tiles (average of the RFC coefficients in RX V over rows). 51

Figure 54 S-1B burst synchronization since the end of the Commissioning Phase. 53

Figure 55 Burst synchronization statistics for IW (left) and EW (right). 53

Figure 56 Internal calibration parameters over time. The colour represents the sub-swath. 54

Figure 57 Internal calibration parameters over time. The colour represents the polarisation. 54

Figure 58 EW HH (left) and HV (right) PG gain divided by sub-swath. 55

Figure 59 IW VV (left) and VH (right) PG gain divided by sub-swath. 55

Figure 60 Noise power versus time. The colour represents the different beams. 56

Figure 61 I/Q channel imbalance. 57

Figure 62 Doppler Centroid versus time. Average on a data-take basis (dots) and daily average (red line). The star-trackers reconfigurations events are marked by the vertical black lines. 60

Figure 63 SM Azimuth and Slant Range Spatial Resolutions 62

Figure 64 IW Azimuth and Slant Range Spatial Resolutions 62

Figure 65 EW Azimuth and Slant Range Spatial Resolutions 63

Figure 66: SM SLC Early Azimuth Ambiguity, DLR Transponder IRF and Late Ambiguity 64

Figure 67: IW Early Azimuth Ambiguity, DLR Transponder IRF and Late Ambiguity 64

Figure 68: IW Early Azimuth Ambiguity, ESTEC Transponder IRF and Late Ambiguity 65

Figure 69: S-1B IW Image of SE England and N France with the location of range ambiguities indicated (acquisition 5th August 2016, 17:40:17 UT). 66

Figure 70: Extract of ambiguity region showing various range ambiguities plus other point targets. 67

Figure 71: Detail of ambiguity region (left) and the source of the ambiguity in Rotterdam (right). 67

Figure 72: SM SLC Relative Radar Cross-Section for the DLR transponders 68

Figure 73: IW SLC Relative Radar Cross-Section for the DLR transponders 69

Figure 74: EW SLC Relative Radar Cross-Section for the DLR transponders 69

Figure 75: IW SLC Relative Radar Cross-Section for the BAE Corner Reflector 70

Figure 76: ALE estimates for S-1B StripMap, IW and EW SLC product time series acquired over the Swiss test sites using precise state vectors (AUX_POEORB). Product date ranges are given in brackets. Point colours represent beam/subswath. The SWST (range) bias (output of the commissioning and calibration phase) was applied in all cases. 73

Figure 77: Gain Imbalance using the DLR transponders. 75

Figure 78: Phase Imbalance using the DLR transponders. 75

Figure 79: SLC Co-registration Examples 77

Figure 80: SLC Cross-talk Examples 79

Figure 81: NESZ measures for SM. Blue is the measured NESZ and the red lines are the predicted NESZ at minimum and maximum orbital altitudes. 83

Figure 82: NESZ measures for IW. Blue is the measured NESZ and the red lines are the predicted NESZ at the minimum orbital altitude. 84

Figure 83: NESZ measures for EW. Blue is the measured NESZ and the red lines are the predicted NESZ at the minimum orbital altitude. 85

Figure 84: NESZ measures for WV . Blue is e measured NESZ and the red lines are the predicted NESZ at minimum and maximum orbital altitudes. 86

Figure 85: An example of Radio Frequency Interference 87

Figure 86: An example of Radarsat-2/Sentinel1-A Interference (2nd July 2016) 87

Figure 87: SAR Wind speed compared with reference wind speed for IW mode VV polarisation. 89

Figure 88 S-1B WV1 and WV2 wind speed performances as function of time. Ocean surface wind monthly performances for WV1 (top-left) and WV2 (top-right) and number of acquisitions co-located to reference data for validation for WV1 (bottom-left) and WV2 (bottom- right). For top panels, colored thick solid lines stand for the mean difference between Sentinel-1 and ECMWF model wind speeds. Colored thin solid lines are for standard deviation. 90

Figure 89: Scatter plot of wind speed from S-1B WV1 versus ECMWF Dec 2016. The model outputs are considered as reference here. This is only valid from a statistical point of view. 91

Figure 90 S-1B WV1 Ocean Swell monthly performances as function of time. For top panels, colored thick solid lines stand for the mean difference between effective significant wave height from Sentinel-1 and from WW3 model. Colored thin solid lines are for standard deviation. 91

Figure 91: Significant wave height for the long waves performances for December 2016 in Wave Mode 1. The model outputs from WW3 are considered as reference here. This is only valid from a statistical point of view. 92

Figure 92 Geophysical Doppler as included in the Level 2 products as a function of radial wind speed (wind speed projected in the line of sight of the radar) for WV1 and WV2 December 2016. The color code indicates the latitude. Only Descending orbits are taken into account. 93

Figure 93 Doppler WV1 and WV2 bias as a function of latitude estimated over ocean (blue) and land (red). 93

Figure 94: Scatter plot of total DC model versus measured DC from the period of 26-31 October 2016 from S-1B acquired in WV1. The green dots are data acquired over land areas. 94

Figure 95: Upper: Geometric Doppler computed from data (red) and from restituted attitude data (pink) for 28 October 2016 for Sentinel 1b WV1. Lower: Location of tracks. The green points are data acquired over land areas. 94

Figure 96: Doppler anomaly field from Sentinel 1B IW OCN RVL product acquired over Agulhas in ascending mode. Here land areas are used to calibrate the Doppler. A clear signature of the Agulhas current is observed. 96

Figure 97: S-1B IW OCN RVL mean DC bias as function of azimuth pixel. Data acquired over ocean areas. 96

Figure 98: S-1B EM DC offset computed from antenna model (full line) with error matrix corresponding to the day of acquisition, and estimated from rain forest data using the Level 2 processor (***). A) EW mode in HH-polarisation, B) EW mode in VV-polarisation, C) IW mode in HH-polarisation, D) IW mode in VV-polarisation 97

Figure 99 Sentinel-1B geophysical calibration constant given by CMOD-IFRv2 for WV1 VV polarisation between 50° and -50° latitude. Panel 1 shows the mean bias between ECMWF and Sentinel-1B. Panel 2 shows the bias standard deviation. Panel 3 shows the number of SAF SAFE used to perform the analysis. 99

Figure 100 Sentinel-1B geophysical calibration constant given by CMOD-IFRv2 for WV2 VV polarisation between 50° and -50° latitude. Panel 1 shows the mean bias between

ECMWF and Sentinel-1B. Panel 2 shows the bias standard deviation. Panel 3 shows the number of SAFE used. 100

Figure 101 PSCAL time series for IW DV acquisitions over Paris. The colour represents the sensor. 101

Figure 102 S-1B vs. S-1A burst synchronization since the end of the Commissioning Phase. 102

Figure 103 S-1B vs. S-1A burst synchronization statistics for IW (left) and EW (right)..... 102

Figure 104: S-1A and S-1B IW SLC Relative Radar Cross-Section for the BAE Corner Reflector..... 103

Applicable documents

[AD-01] Sentinel-1 Product Specification, S1 RS-MDA-52-7441, Issue 3/3, October 2016

[AD-02] Sentinel-1 Product Definition, S1-RS-MDA-57-7440, Issue 2/7, March 2016

[AD-03] Sentinel-1 IPF Detailed Algorithm Definition, S1-TN-MDA-52-7445, Issue 2/1, January 2017

[AD-04] Sentinel-1 IPF Auxiliary Product Specification, S1-RS-MDA-52-7443, Issue 3/2, October 2016

Reference documents

[S1-RD-01] S-1A Performance Report for 2015, DI-MPC-CPR MPC-0139, Issue 1.0, March 2016.

[S1-RD-02] S-1B MPC Commissioning Phase Report DI-MPC-CPR MPC-0326, Issue 1.1, January 2017.

[S1-RD-03] Sentinel-1A Performance Status and Sentinel-1B Preliminary Performance Results, Nuno Miranda, Peter Meadows, Alan Pilgrim, Guillaume Hajduch, Romain Husson, Pauline Vincent, Riccardo Piantanida, Davide Giudici, Andrea Recchia, David Small, Alexis Mouche, Harald Johnsen, Proceedings of the ESA Living Planet Symposium, 9-13 May 2016, Prague, Czech Republic.

[S1-RD-04] Results for calibration of Sentinel-1A using the Australian corner reflector array, Medhavy Thankappan, Matthew Garthwaite , Peter Meadows, Nuno Miranda, Adrian Schubert, David Small, Proceedings of the ESA Living Planet Symposium, 9-13 May 2016, Prague, Czech Republic.

[S1-RD-05] The Copernicus Sentinel-1 Constellation Product Quality and Preliminary Calibration Results, Nuno Miranda, Peter Meadows, Alan Pilgrim, Guillaume Hajduch, Riccardo Piantanida, Davide Giudici, Andrea Recchia, David Small, Adrian Schubert, Alexis Mouche (CLS, France) & Harad Johnsen, European Conference on Synthetic Aperture Radar (EUSAR), 6-9 June 2016, Hamburg, Germany.

[S1-RD-06] Calibration of Sentinel-1 using the Australian Geophysical Observing System Corner Reflector Array, Medhavy Thankappan, Matthew Garthwaite, Peter Meadows, Nuno Miranda, Adrian Schubert & David Small, Proceedings of the CEOS SAR Workshop, 7-9 September 2016, Tokyo, Japan.

[S1-RD-07] Sentinel-1B Preliminary Results Obtained During the Orbit Acquisition Phase, Nuno Miranda, Peter J. Meadows, Alan Pilgrim, Riccardo Piantanida, Andrea Recchia, Davide Giudici, David Small and Adrian Schubert, SARWatch: Advances in the Science and Applications of SAR Interferometry, 5-7 October 2016, Porto, Portugal.

[S1-RD-08] Sentinel-1A Tile #11 Failure, OI-MPC-OTH-0324, Issue 1.2, October 2016

[S1-RD-09] Sentinel-1A Debris Collision, DI-MPC-ACR-0352, Issue 1.0, October 2016

[S1-RD-10] Pietro Guccione, Michele Belotti, Davide Giudici, Andrea Monti Guarnieri, Ignacio Navas-TraverSentinel-1A: Analysis of FDBAQ Performance on Real Data, IEEE TRANSACTIONS ON GEOSCIENCE AND REMOTE SENSING, 2015.

[S1-RD-11] Schubert, A., D. Small, N. Miranda, D. Geudtner, E. Meier. Sentinel-1A Product Geolocation Accuracy: Commissioning Phase Results. Remote Sens. 2015, 7, 9431–9449. doi: 10.3390/rs70709431.

[S1-RD-12] Schubert, A., D. Small, N. Miranda, D. Geudtner, E. Meier. Sentinel-1A Product Geolocation Accuracy: Beyond the Calibration Phase. Presented at CEOS SAR Calibration & Validation Workshop; Noordwijk, The Netherlands, 2015.

[S1-RD-13] Small, D., A. Schubert. Guide to ASAR Geocoding, UZH technical note for ESA-ESRIN, Contract No. 20907/07/I-EC, RSL-ASAR-GC-AD, Iss. 1.01; University of Zurich: Zurich, Switzerland, 2008, 36p.

[S1-RD-14] GMES Sentinel-1 Team. GMES Sentinel-1 System Requirements Document, Ref. S1-RS-ESA-SY-0001, Iss. 3, Rev. 3, 2010.

[S1-RD-15] S-1A MPC Commissioning Phase Report DI-MPC-CPR MPC-0184, Issue 1.3, March 2015

List of Contents

1. Introduction 1
1.1. Purpose of the document 1
1.2. Structure of the document 1
2. Executive Summary 2
3. S-1A Instrument Status 3
3.1. S-1A Antenna Status 3
3.2. S-1A Instrument Unavailability 7
3.3. S-1A Auxiliary Date File Updates 7
3.4. S-1A Radar Data Base Updates 7
3.5. S-1A Orbit Manoeuvres 7
3.6. S-1A Burst synchronization 7
3.7. S-1A Internal Calibration 8
3.7.1. PG monitoring 8
3.7.2. Noise power monitoring 10
4. S-1A Products Status 13
4.1. S-1A Level 0 Products 13
4.1.1. Timeline and missing lines 13
4.1.2. I/Q statistics 13
4.1.3. FDBAQ 13
4.1.4. Instrument Pointing 14
4.2. S-1A Level 1 Products 15
4.2.1. Level 1 Processor Updates 15
4.2.2. Image Quality 16
4.2.2.1. Spatial Resolution 16
4.2.2.2. Sidelobe Ratios 18
4.2.2.3. ENL and Radiometric Resolution 18
4.2.2.4. Ambiguity Analysis 18
4.2.2.4.1. Azimuth Ambiguities 18
4.2.2.4.2. Range Ambiguities 19
4.2.3. Radiometric Calibration 19
4.2.3.1. Absolute Radiometric Calibration 20
4.2.3.2. Permanent Scatter Calibration 23
4.2.4. Geometric Validation 24
4.2.5. Polarimetric Calibration 25
4.2.5.1. Gain Imbalance 25
4.2.5.2. Phase Imbalance 26
4.2.5.3. Coregistration 27

4.2.5.4. Cross-talk 27
4.2.6. Elevation Antenna Patterns 28
4.2.7. Azimuth Antenna Patterns 28
4.2.8. Noise Equivalent Radar Cross-section 28
4.2.9. S-1A Tile 11 Failure 29
4.2.10. S-1A Debris Collision 29
4.2.11. Summary of Anomalies 30
4.2.11.1. Radio Frequency Interference 30
4.2.11.2. Radarsat-2/Sentinel1-A Mutual Interference 31
4.2.11.3. Other S-1A/Satellite Interference 32
4.2.12. Quality Disclaimers 33
4.3. S-1A Level 2 products 33
4.3.1. Wind measurement 33
4.3.1.1. Image Mode (SM-IW-EW) 33
4.3.1.2. Wave Mode 37
4.3.2. Swell Measurement 39
4.3.2.1. Wave Mode 39
4.3.3. Radial Velocity Measurement 42
4.3.3.1. Wave Mode 42
4.3.3.2. TOPS Mode 43
4.3.4. Geophysical Calibration 46
4.3.4.1. Wave Mode 46
5. S-1B Instrument Status 49
5.1. S-1B Antenna Status 49
5.2. S-1B Instrument Unavailability 51
5.3. S-1B Auxiliary Date File Updates 52
5.4. S-1B Radar Data Base Updates 52
5.5. S-1B Orbit Manoeuvres 52
5.6. S-1B Burst synchronization 52
5.7. S-1B Internal Calibration 53
5.7.1. PG monitoring 53
5.7.2. Noise power monitoring 55
6. S-1B Products Status 57
6.1. S-1B Level 0 Products 57
6.1.1. Timeline and missing lines 57
6.1.2. I/Q statistics 57
6.1.3. FDBAQ 57
6.1.4. Instrument Pointing 58
6.2. S-1B Level 1 Products 60
6.2.1. Level 1 Processor Updates 60

6.2.2. Image Quality 61
6.2.2.1. Spatial Resolution 61
6.2.2.2. Sidelobe Ratios 63
6.2.2.3. ENL and Radiometric Resolution 63
6.2.2.4. Ambiguity Analysis 64
6.2.2.4.1. Azimuth Ambiguities 64
6.2.2.4.2. Range Ambiguities 65
6.2.3. Radiometric Calibration 68
6.2.3.1. Absolute Radiometric Calibration 68
6.2.3.2. Permanent Scatter Calibration 71
6.2.4. Geometric Calibration 71
6.2.5. Polarimetric Calibration 74
6.2.5.1. Gain Imbalance 74
6.2.5.2. Phase Imbalance 75
6.2.5.3. Coregistration 76
6.2.5.4. Cross-talk 78
6.2.6. Elevation Antenna Patterns 79
6.2.7. Azimuth Antenna Patterns 79
6.2.8. Noise Equivalent Radar Cross-section 79
6.2.9. Summary of Anomalies 86
6.2.9.1. Radio Frequency Interference 86
6.2.9.2. Radarsat-2/Sentinel1-A Mutual Interference 87
6.2.10. Quality Disclaimers 88
6.3. S-1B Level 2 products 88
6.3.1. Wind measurement 88
6.3.1.1. Image Mode (SM-IW-EW) 88
6.3.1.2. Wave Mode 89
6.3.2. Swell Measurement 91
6.3.2.1. Wave Mode 91
6.3.3. Radial Velocity Measurement 92
6.3.3.1. Wave Mode 92
6.3.3.2. TOPS Mode 95
6.3.4. Geophysical Calibration 98
6.3.4.1. Wave Mode 98
7. S-1A and S-1B Cross-comparison 101
7.1. Cross-platform Permanent Scatter Calibration 101
7.2. Cross-interferometry burst synchronization 101
7.3. Absolute Calibration 102
Appendix A - List of Acronyms 104
Appendix B - ESA S-1A & S-1B Technical Reports 105

Appendix C - S-1A Orbit Cycles 106
Appendix D - S-1A Transmit Receive Module Failures 107
Appendix E - S-1A Instrument Unavailability 108
Appendix F - S-1A Auxiliary Data Files 109
Appendix G - S-1A Orbit Manoeuvres 111
Appendix H - S-1A Quality Disclaimers 114
Appendix I - S-1A Antenna Pointing 115
Appendix J - S-1B Orbit Cycles 122
Appendix K - S-1B Transmit Receive Module Failures 123
Appendix L - S-1B Instrument Unavailability 124
Appendix M - S-1B Auxiliary Data Files 125
Appendix N - S-1B Orbit Manoeuvres 126
Appendix O - S-1B Quality Disclaimers 127
Appendix P - S-1B Antenna Pointing 128

1. Introduction

1.1. Purpose of the document

The purpose of this document is to provide the status on the S-1A instrument and product performance during 2016 and the S-1B instrument and product performance since the start of the routine phase in September 2016.

1.2. Structure of the document

The outline of this report is given below:

- Chapter 1 : this introduction
- Chapter 2 : Executive Summary
- Chapter 3 : S-1A Instrument Status
- Chapter 4 : S-1A Products Status
- Chapter 5 : S-1B Instrument Status
- Chapter 6 : S-1B Products Status
- Chapter 7 : S-1A and S-1B Cross-comparison

The following appendices are also provided:

- Appendix A : List of Acronyms
- Appendix B : ESA S-1A & S-1B Technical Reports
- Appendix C : S-1A Orbit Cycles
- Appendix D : S-1A Transmit Receive Module Failures
- Appendix E : S-1A Instrument Unavailability
- Appendix F : S-1A Auxiliary Data Files
- Appendix G : S-1A Orbit Manoeuvres
- Appendix H : S-1A Quality Disclaimers
- Appendix I : S-1A Antenna Pointing
- Appendix J : S-1B Orbit Cycles
- Appendix K : S-1B Transmit Receive Module Failures
- Appendix L : S-1B Instrument Unavailability
- Appendix M : S-1B Auxiliary Data Files
- Appendix N : S-1B Orbit Manœuvres
- Appendix O : S-1B Quality Disclaimers
- Appendix P : S-1B Antenna Pointing

2. Executive Summary

This report gives the status of the S-1A instrument and product performance during 2016 and the S-1B instrument and product performance since the start of the routine phase in September 2016.

As will be seen in Chapters 3 & 4 (S-1A), Chapters 5 & 6 (S-1B) and Chapter 7 (S-1A and S-1B Cross-Calibration) many aspects of the instrument and products are considered with the aim of ensuring users receive high quality products.

3. S-1A Instrument Status

3.1. S-1A Antenna Status

The Antenna status is routinely monitored using the dedicated RFC calibration mode. The RFC products are processed in order to generate the Antenna Error Matrix from which it is possible to retrieve the failure and drift of each TRM.

Figure 1 shows the antenna Transmit/Receive Module (TRM) status at June 2016. Ten (10) failures are counted in total among TX-RX and H-V. A full list of all TRM failures so far is given in Appendix D -. Since mid-2015, after switch to redundancy for tile 5, no antenna events were recorded.

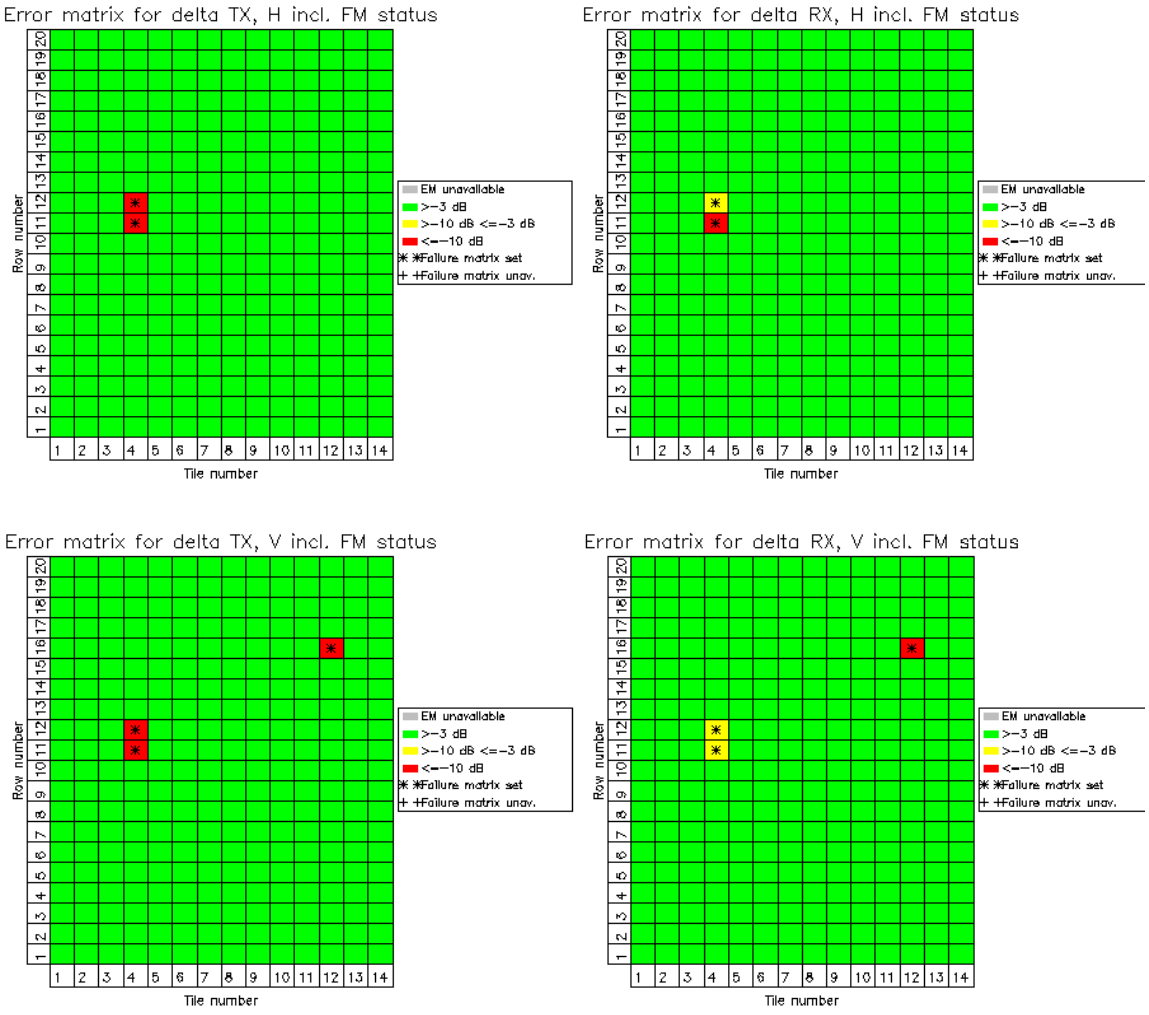

Figure 1: H (top) and V (bottom) polarisation error matrixes computed the 15-06-2016, before tile 11 issue happened.

On the 16-06-2016 SAR went to pause refuse mode for the first time due to a current/voltage anomaly on TPSU-1 within tile 11. After several attempts to recover SAR operations, the SAR was definitely available again since the 27-06-2016 June. In order to ensure SAR operation a reduction of the Tx power for half tile 11 was necessary. This can be clearly noticed in the figure below, reporting the error matrixes computed on the 27-06-2016 June. The figure represents the status of the S-1A antenna at the end of 2016.

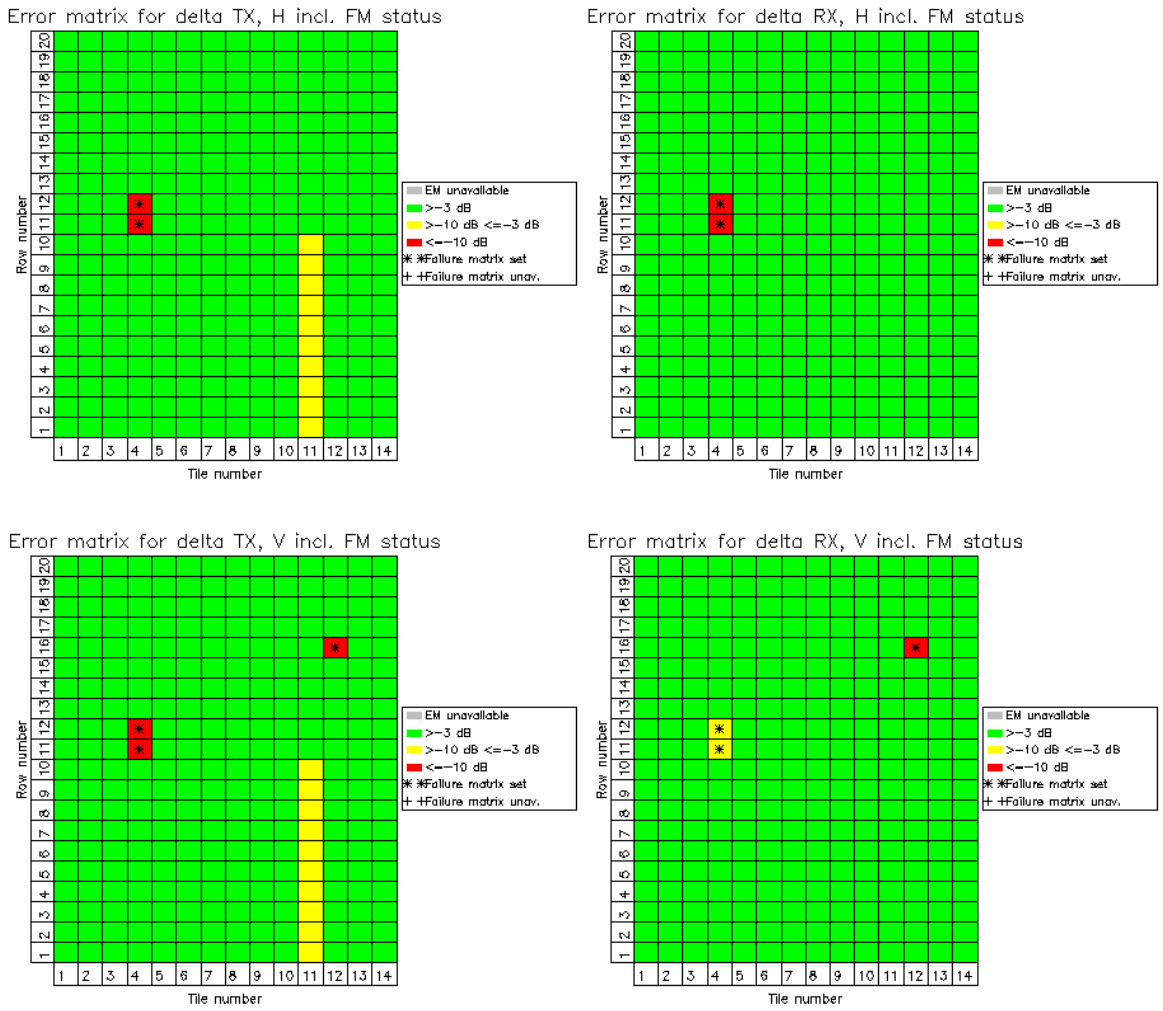

Figure 2: H (top) and V (bottom) polarisation error matrixes computed the 27-06-2016, after SAR operation successful recovery.

A further effect of the instrument configuration change was a drop of the phase of all the TRMs of tile 11 (not only the ones with reduced TX power). This can be clearly noticed in the following plots, showing the TX excitation coefficients (averaged per tile) obtained processing RFC products of 2016. Tile 11 shows an average gain reduction of about 4 dB and an average phase drop of about 30 deg. Please note that other tiles show a small increase of the gain due to the fact that, during RFC processing, the coefficients are normalized. The plots showing the RX excitation coefficients have also been reported. Tile 11 coefficients show an average gain increase of about 1 dB. For more details on the anomaly please refer to [S1-RD-08].

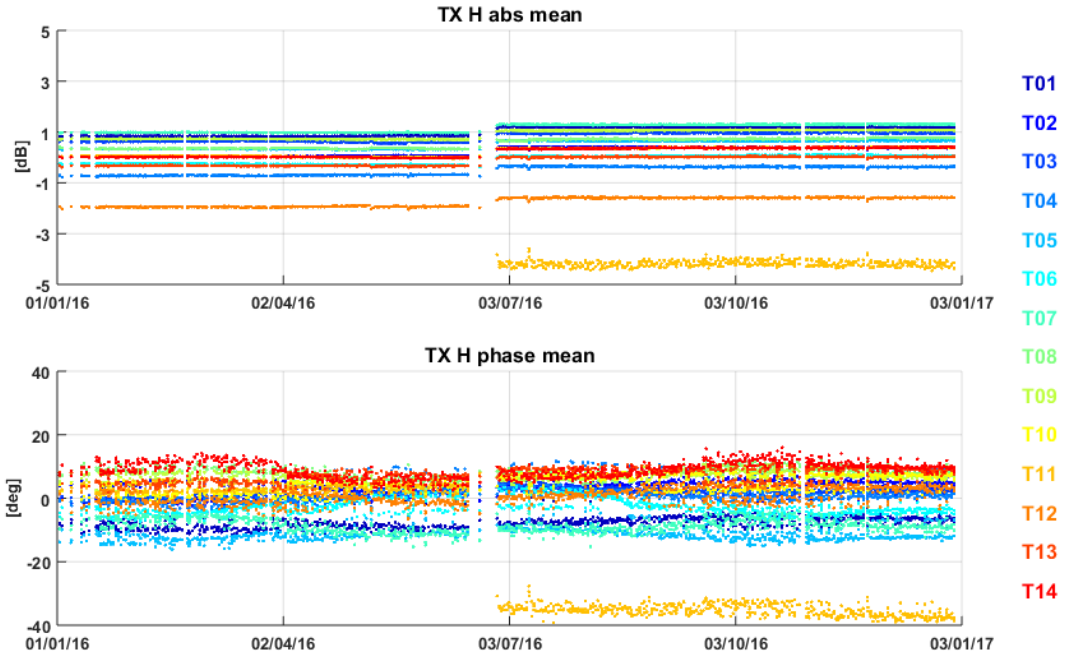

Figure 3 Gain (*top)* and phase (*bottom)* stability of the SAR antenna tiles (average of the RFC coefficients in TX H over rows). The Tile#11 event on June can be recognized.

Figure 4 Gain (top) and phase (bottom) stability of the SAR antenna tiles (average of the RFC coefficients in TX V over rows). The Tile#11 event on June can be recognized.

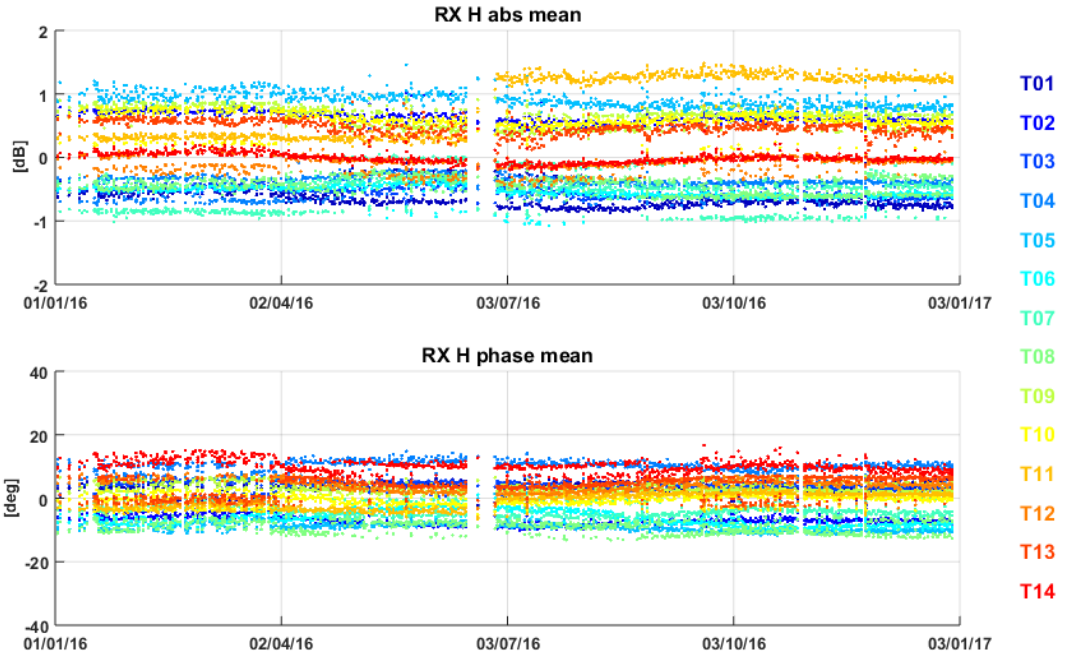

Figure 5 Gain (top) and phase (bottom) stability of the SAR antenna tiles (average of the RFC coefficients in RX H over rows).

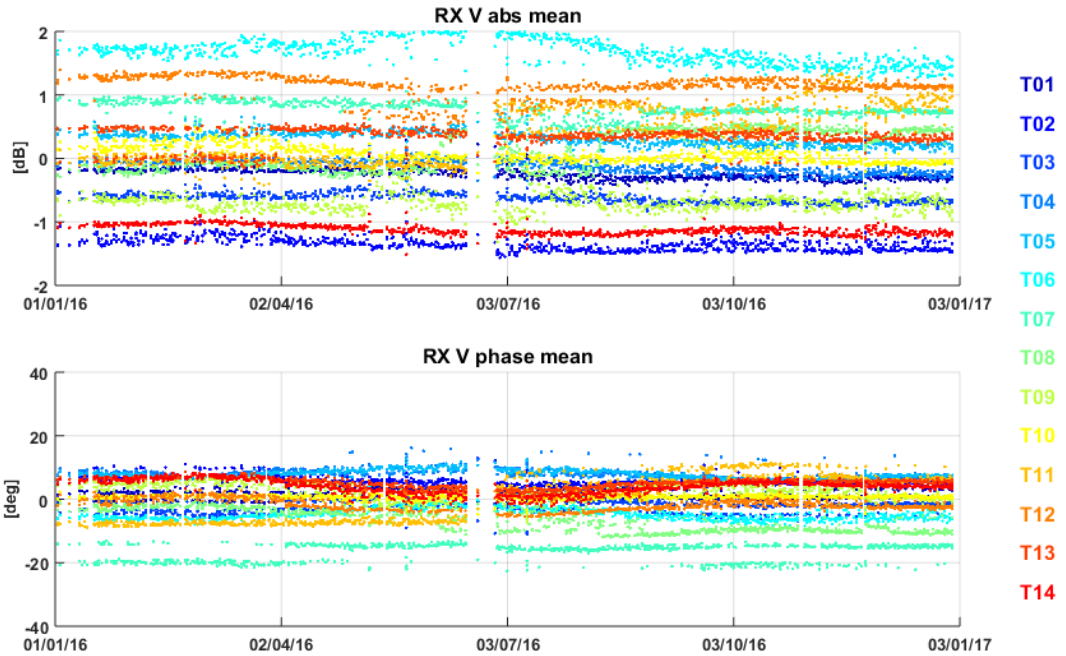

Figure 6 Gain (top) and phase (bottom) stability of the SAR antenna tiles (average of the RFC coefficients in RX V over rows).

Excluding the tile 11 issue, the antenna shows overall a stable behaviour: 0.4 dB of average temporal stability for the gain and 5° for the phase have been computed.

3.2. S-1A Instrument Unavailability

A list of S-1A instrument unavailabilities during 2016 is given in Appendix E -.

3.3. S-1A Auxiliary Date File Updates

A list of S-1A Auxiliary Data Files (ADFs) updates during 2016 is given in Appendix F -.

3.4. S-1A Radar Data Base Updates

No RDB updates occurred during 2016. The current RDB version is #5 endorsed on 22 July 2015

3.5. S-1A Orbit Manoeuvres

A list of all S-1A orbit manoeuvres during 2016 is given in Appendix G -.

3.6. S-1A Burst synchronization

The burst synchronization between repeat pass interferometric acquisitions is relevant for the TOPSAR modes (IW and EW) to provide an indication of the quality of the interferometric phase that can be expected. The SAR acquisition start time is planned over a discrete set of points round orbit with precision down to milliseconds. The performance of the synchronization is monitored by the PDGS OBS tool.

Figure 7 shows the burst synchronization over time for IW and EW mode. Each dot represents a repeat pass acquisition, considering as reference cycle number 60 (30 September - 12 October 2015). It can be noticed that the synchronization is always very high, above 98% for most of the time. Only few EW acquisitions show lower synchronization values (always better than 95% in any case).

It is interesting to note a small seasonal trend in the burst synchronization, with lower values between November and February. This small periodicity should be further investigated and could be originated by some long term orbit perturbation.

A similar trend can be observed also for S-1B burst synchronization (see Figure 54), even if the available data do not cover yet a full year. A better comparison of the two trends will be performed as soon as a full year of S-1B OBS products will be available (after June 2017).

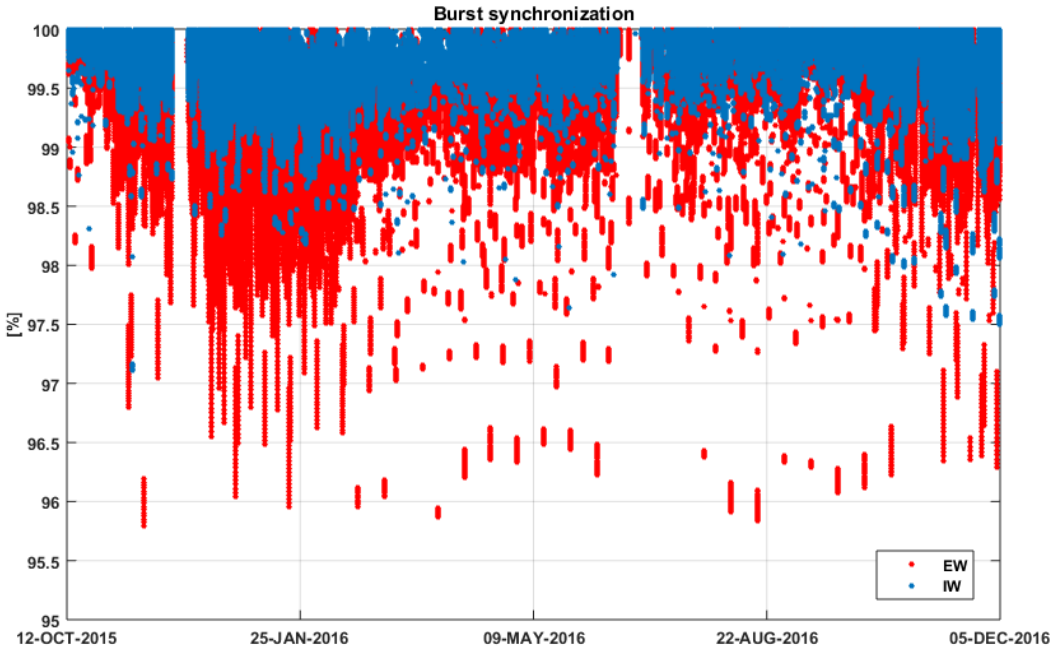

Figure 7 S-1A Burst synchronization monitoring.

3.7. S-1A Internal Calibration

3.7.1. PG monitoring

The instrument stability over time is monitored through the internal calibration signals. The following plots show the main parameters monitored: PG gain and phase, instrument delay and Rx gain offset. In Figure 8 the colour represents the sub-swath whereas in Figure 9 the colour represents the polarisation.

All the monitored parameters are stable in the reporting period except for the PG gain which, after the tile 11 Tx power reduction on June 2016 to prevent instrument switch off (see section 4.2.9), decreased of 0.4 dB. This is an expected behaviour allowing to radiometrically compensate the reduced TX gain of half tile 11. Figure 10 and Figure 11 show a more detailed picture of the PG trend during the reporting period for EW DH and IW DV acquisitions. No particular trends can be identified during the reporting period even if some long slow fluctuations can be observed in particular for RX H beams (EW HH and IW VH). Such fluctuations are in any case quite small with a peak to peak variation around 0.1 dB.

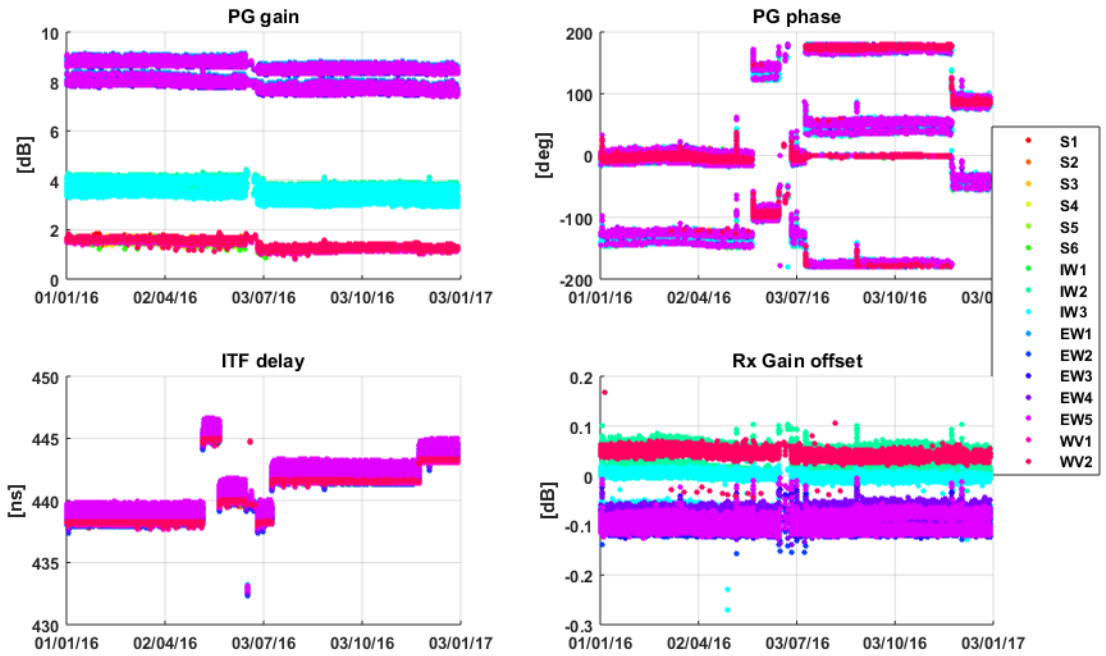

Figure 8 Internal calibration parameters over time. The colour represents the sub-swath.

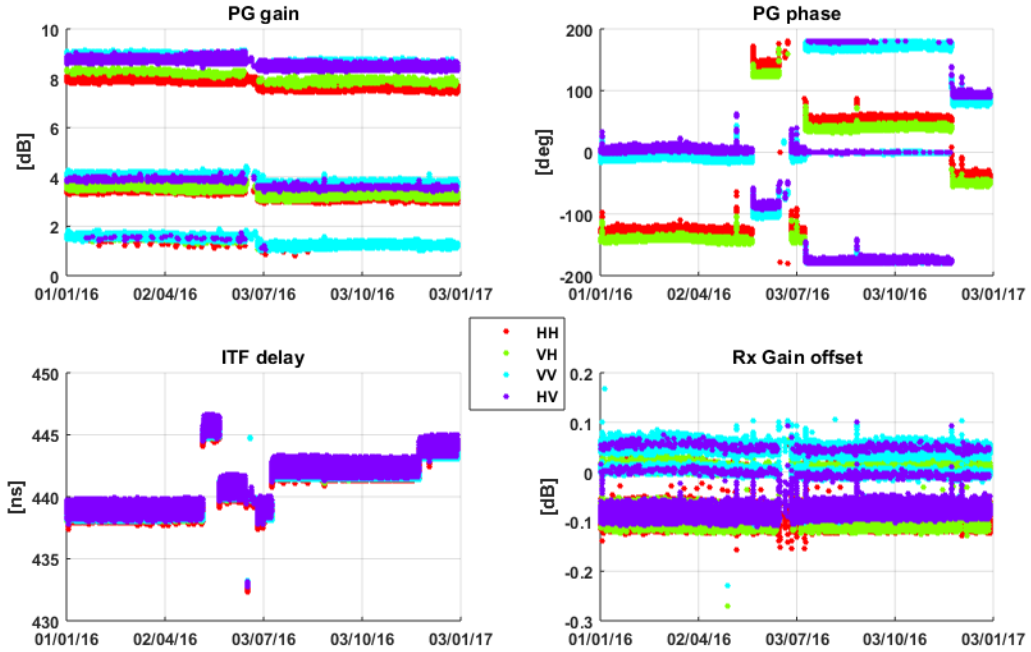

Figure 9 Internal calibration parameters over time. The colour represents the polarisation.

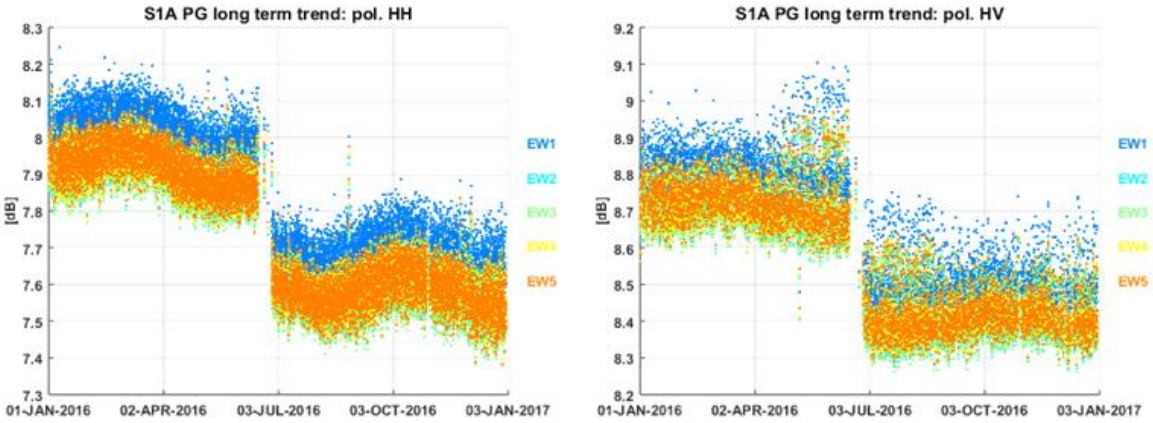

Figure 10 EW HH (left) and HV (right) PG gain divided by sub-swath.

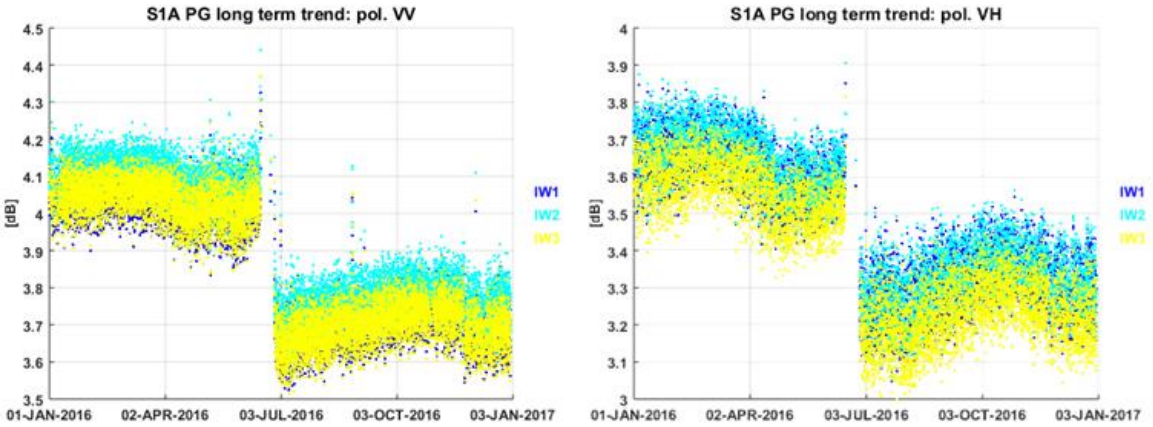

Figure 11 IW VV (left) and VH (right) PG gain divided by sub-swath.

3.7.2. Noise power monitoring

The noise power is monitored through the dedicated internal calibration pulses processing embedded at the start/stop of each data-take. Figure below shows the noise power versus time in the period January-December 2016. The noise power is stable in the reporting period. The table below reports the noise power stability (3σ) averaged over the full reporting period. The number in the parenthesis is the number of products considered.

Acquisition mode	Noise power stability [dB]
SM	HH: 5.5±0.9 (114) VV: 4.7±0.9 (530) HV: 5.6±0.9 (114) VH: 4.9±1.1 (244)
IW	HH: 6.6±1.1 (10413) VV: 7.4±1.4 (84006) HV: 7.3±1.0 (3138) VH: 6.7±1.5 (48930)
EW	HH: 5.2±1.0 (109760) VV: 6.0±1.0 (6080)

	HV: 6.3±0.9 (58934) VH: 4.9±1.1 (4675)
WV	HH: 6.0±1.1 (1344) VV: 6.2±0.9 (42410)

Table 1 Noise power stability (3-sigma): period JAN 2016 – DEC 2016

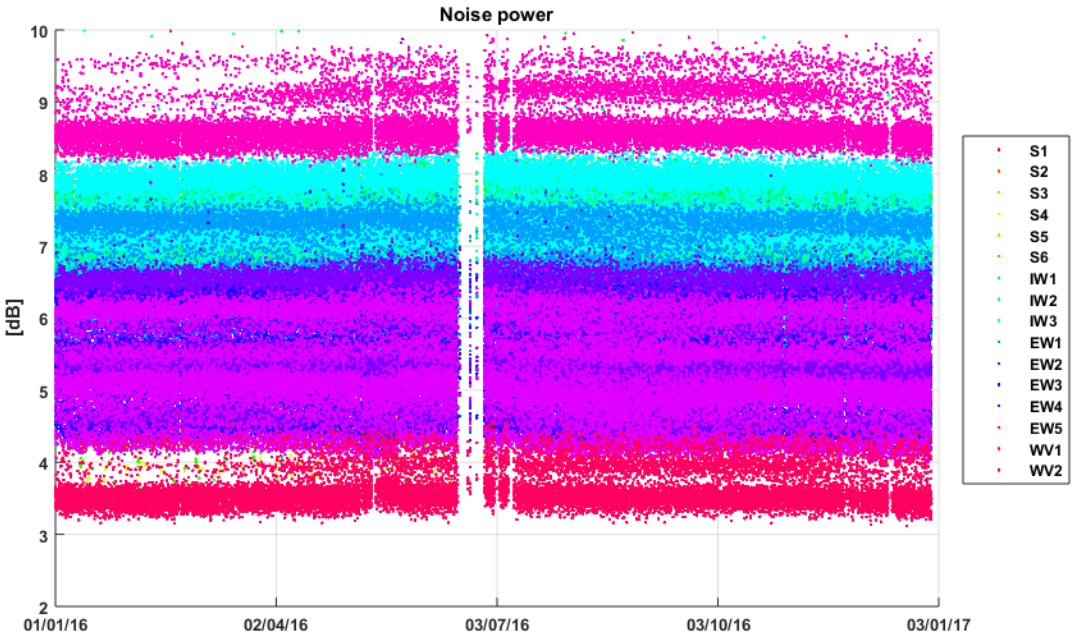

Figure 12 Noise power versus time. The colour represents the different beams.

Further analyses on noise power have shown that the noise power distribution is bi-modal for all beams and polarisations, as reported in the following figure on the left. This noise behaviour is observed for both S-1A and S-1B. It is originated by the scene underlying the sensor at the moment of the noise acquisition. Indeed Earth emissivity is different between land and sea. The S-1A and S-1B instruments are good enough to capture the different emissivity of the Earth as clearly shown in the following figure on the right, where noise power samples are plotted according to the location where they have been acquired. Blue dots (low noise power) are mostly located over the sea whereas yellow dots (high noise power) are mostly located over land (Sahara desert is particularly bright).

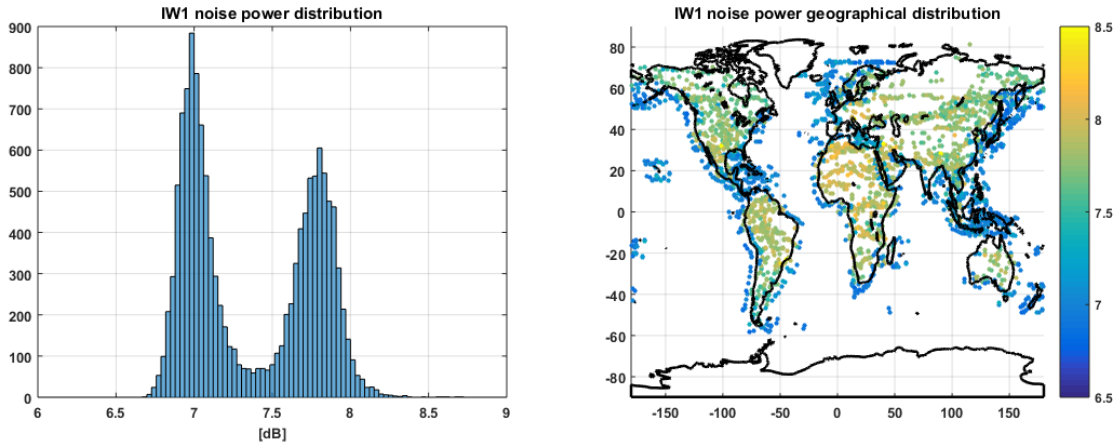

Figure 13 (Left) Noise power histogram for IW1 VV data. (Right) Geographical noise power distribution.

4. S-1A Products Status

4.1. S-1A Level 0 Products

4.1.1. Timeline and missing lines

The L0 quality monitoring is carried out as a routine task within the QCSS. The checks on the timeline and missing lines have not detected significant problems.

4.1.2. I/Q statistics

The analysis of I/Q bias and standard deviation allow to state that the L0 data quality is nominal. Figure 14 shows the channel imbalance analysis for IW, showing the standard deviation that the two channels are very well aligned along the bisector of the I/Q plane.

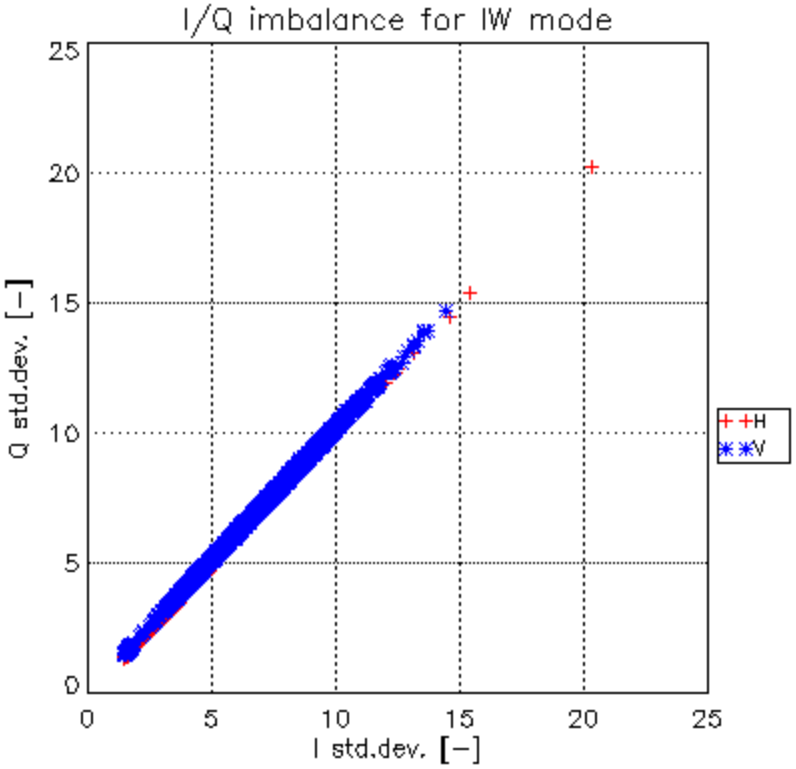

Figure 14 I/Q channel imbalance.

4.1.3. FDBAQ

The FDBAQ quantization scheme performs nominally. A detailed analysis of the FDBAQ behaviour for the first year can be found in [S1-RD-10].

The long-term statistics over the acquired data is shown by the average Mbit/s as reported in the following table. Note that the average bitrate for all acquisition modes is well below the downlink limit of 260Mbit/sec. Only S1 acquisitions (about 0.3% of S-1A total acquisitions during 2016) average data rate is close to the downlink limit. This is expected since S1 beam is the most demanding in

terms of azimuth and range data sampling. The S-1A bitrate is in line with the S-1B bitrate, reported in Table 20.

Acquisition mode/swath	Average bitrate [Mbit/s]
S1	254.9
S2	199.6
S3	210.6
S4	176.0
S5	N/A
S6	170.8
IW	192.3
EW	59. 1
WV	18.7

Table 2 Average bitrate for each acquisition mode.

4.1.4. Instrument Pointing

The instrument pointing in elevation has been calibrated during the commissioning phase exploiting the availability of the elevation notch acquisitions over the Amazonian rain forest. The pointing was verified with further Elevation Notch acquisitions in 2015 and no relevant deviations were observed. No Elevation Notch acquisitions were performed in 2016.

Plots of the spacecraft attitude (yaw, pitch and roll) are shown in Appendix I -.

The stability of the pointing in azimuth can be monitored through the Doppler Centroid, estimated directly from SAR data. Figure 15 shows the average Doppler Centroid on a data-take basis (dots) and on a daily basis (red line) versus time. The bias varies along time in correspondence of the different configurations of the star trackers (marked by the vertical black lines). Activities are on-going in order to reduce the DC dependency w.r.t. the STT configuration. A dedicated STT calibration campaign was performed on November (marked by the vertical green lines). Note that, in the second half of the year, under STT 1+2 configuration, an increase of the daily average DC values up to 40 Hz can be observed. This can give a loss of about 10% of coherence in S-1A/S-1B cross-interferometry for IW acquisitions.

The origin of this DC increase is currently under investigation and should be fixed with the final STT calibration. In any case, as reported in Figure 62, the S-1B average DC is stable during the same period, meaning that the observed trend is probably sensor rather than orbit related.

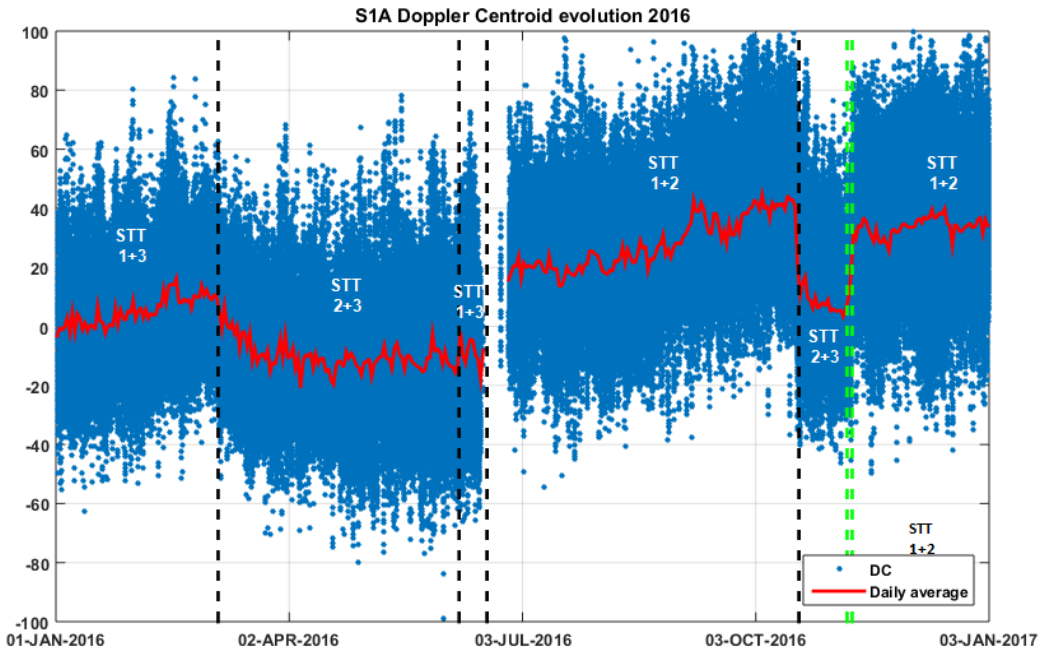

Figure 15 Doppler Centroid versus time. Average on a data-take basis (dots) and daily average (red line). The star-trackers reconfigurations events are marked by the vertical black lines. The STT calibration campaign is marked by the vertical green lines.

4.2. S-1A Level 1 Products

A general summary of status of S-1A Level 1 products was presented at several conferences and workshops (see [S1-RD-03], [S1-RD-04], [S1-RD-05], [S1-RD-06] and [S1-RD-07]).

4.2.1. Level 1 Processor Updates

The main improvements introduced in the Level-1 Processor and impacting data quality are here below described, classified according to the release in which they have been included.

IPF v2.7.0 (31/03/2016) + v2.7.1 (21/04/2016)

- Update of Topsar processing parameters in order to improve data quality (spectra shape, ambiguities level, …)
- Improvement of WV SLC products annotations (attitude, replicas, Doppler Centroid estimations quality, …)
- Solved blocking issue in the generation of WV L2 products (no manifest file)
- Improvement of orbit propagation algorithm through integration of updated EO CFI libraries
- Improvement of denoising vectors annotation through proper management of noise measurements

IPF v2.7.2 (29/07/2016)

- Solved issue on holes between Topsar consecutive slices (missing bursts)
- Solved issue on Stripmap SLC products data sampling grid (wrong azimuth start time w.r.t. internal SLC products)

- Solved issue on presence of black stripes in Stripmap data (present e.g. in first S-1B images with not null Doppler Centroid)

IPF v2.8.0 (15/11/2016)

- Introduced full review of processor normalization approach for Topsar data
- Solved issue in the management of Doppler Centroid estimations causing the presence of radiometric artefacts in Topsar data (darker bursts)
- Review and correction of terrain height different annotations in L1 products

In addition to the described L1 Processor upgrades, a summary of S-1A Auxiliary Data Files (ADFs) updates during the reporting period is provided, together with an explanation of the updates, in Appendix F. The main ones are here below summarized:

AUX_INS

- Updated PG model and default noise values

AUX_PP1

- Update of IPF internal configuration parameters
- Update of processing gains to improve WV calibration (VV polarisation)

AUX_SCS

- Introduction of AUX_SCS

4.2.2. Image Quality

The DLR Transponders & Corner Reflectors, the BAE Corner Reflector and the Australian Corner Reflector array have been used to assess various impulse response function parameters as described below. The products analysed were acquired in 2016 and processed with the Sentinel-1 IPF v2.60, v2.62, v2.70, v2.71 and v2.72.

4.2.2.1. Spatial Resolution

The Figures and Tables below give the azimuth and range spatial resolutions derived from SM, IW and EW SLC data. The numbers in brackets indicate the number of measurements.

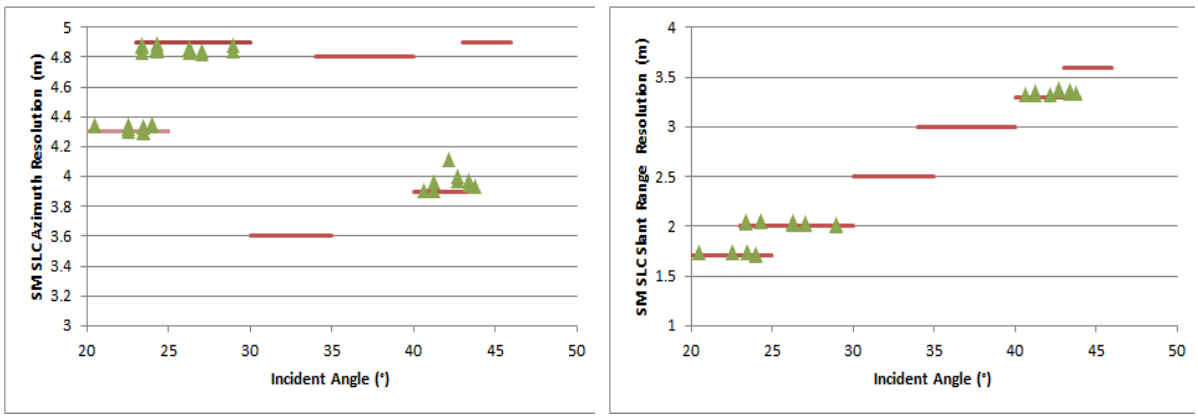

Figure 16 SM Azimuth and Slant Range Spatial Resolutions

Mode/Swath	Azimuth Spatial Resolution (m)	Slant Range Spatial Resolution (m)
S1	4.33±0.02 (12)	1.73±0.01 (12)
S2	4.86±0.02 (16)	2.03±0.01 (16)
S5	3.97±0.06 (9)	3.35±0.02 (9)

Table 3 SM Azimuth and Slant Range Spatial Resolutions

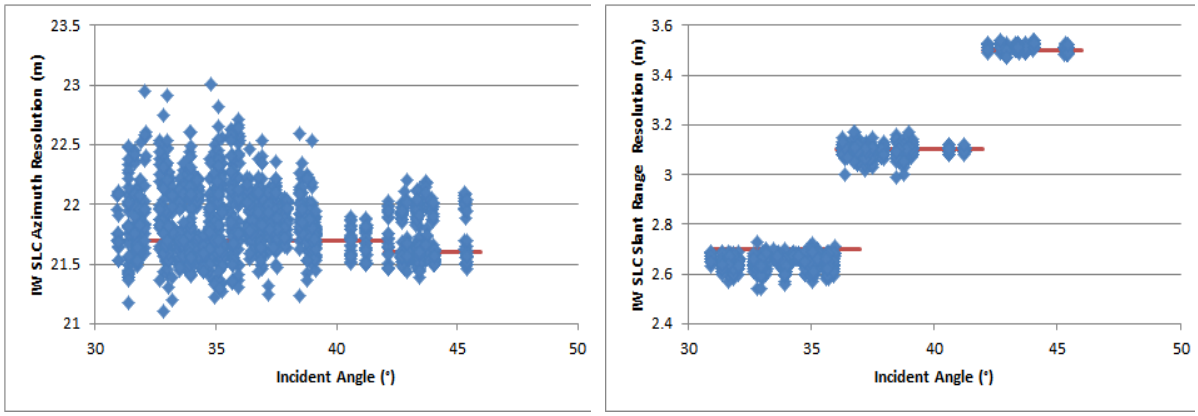

Figure 17 IW Azimuth and Slant Range Spatial Resolutions

Mode/Swath	Azimuth Spatial Resolution (m)	Slant Range Spatial Resolution (m)
IW1	21.87±0.33 (729)	2.65±0.03 (729)
IW2	21.84±0.21 (457)	3.10±0.02 (457)
IW3	21.72±0.21 (291)	3.51±0.01 (291)

Table 4 IW Azimuth and Slant Range Spatial Resolutions

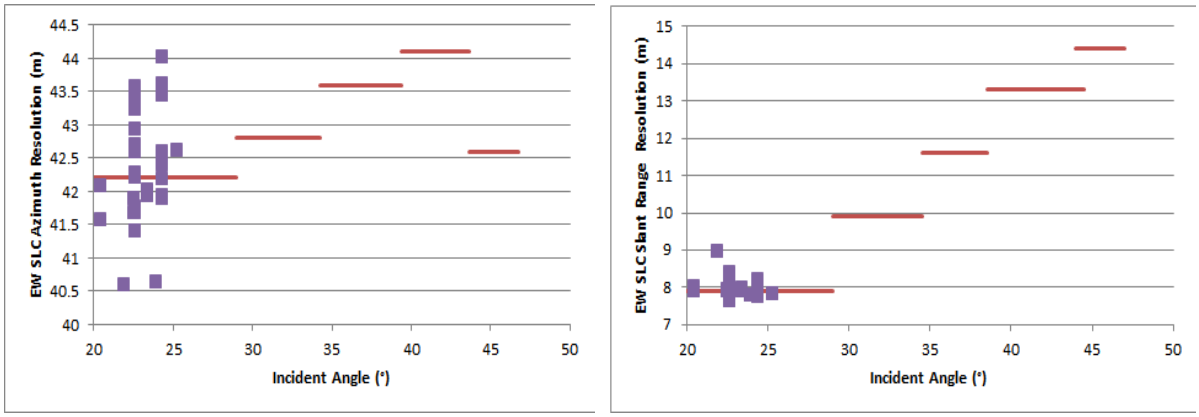

Figure 18 EW Azimuth and Slant Range Spatial Resolutions

Mode/Swath	Azimuth Spatial Resolution (m)	Slant Range Spatial Resolution (m)
EW1	42.40±0.85 (31)	7.95±0.24 (31)

Table 5 EW Azimuth and Slant Range Spatial Resolutions

The issue with the azimuth filter length being too short resulting in higher than expected IW & EW spatial resolutions was fixed with an IPF update during 2016 (v2.70 in April 2016). Lengthening the azimuth filter resulted in the IW & EW azimuth spatial resolution being closer to theoretical values as shown in Figure 19 for IW mode. Otherwise the measured spatial resolutions match the predicted resolutions as indicated by the red horizontal lines.

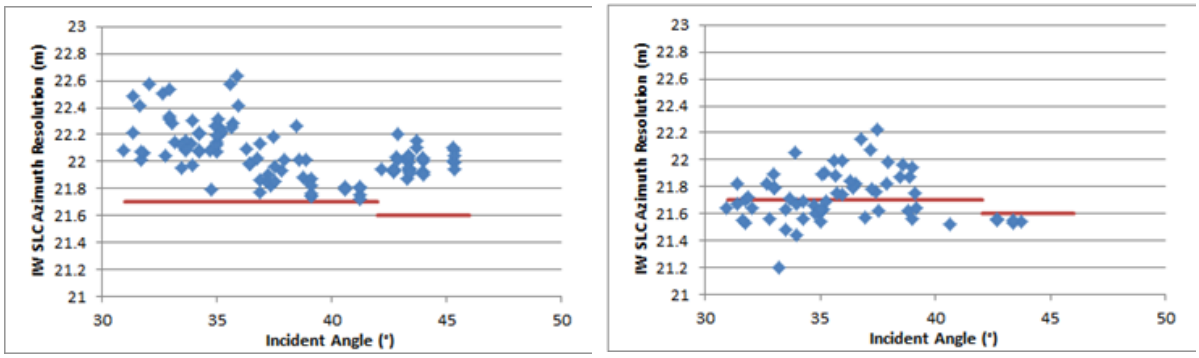

IPF v2.62 IPF v2.70

Figure 19 Improvement in IW Azimuth Spatial Resolution with IPF v2.70

4.2.2.2. Sidelobe Ratios

The table below gives the measured impulse response function sidelobe ratios derived from SM, IW and EW SLC data – these indicate acceptable values.

Mode/Swath	Integrated Sidelobe Ratio (dB)	Peak Sidelobe Ratio (dB)	Spurious Sidelobe Ratio (dB)
SM	-13.27±0.44	-20.63±0.44	-27.69±0.84
IW	-12.16±4.82	-19.74±1.27	-23.43±3.57
EW	-8.85±4.56	-20.74±4.54	-18.05±4.73

Table 6 SM & IW Sidelobe Ratios

4.2.2.3. ENL and Radiometric Resolution

No specific Equivalent Number of Look (ENL) and Radiometric Resolution measurements were performed during 2016.

4.2.2.4. Ambiguity Analysis

4.2.2.4.1. Azimuth Ambiguities

Another improvement with the lengthening of the azimuth filter in IPF v2.70 in April 2016 was the removal on unexpected azimuth ambiguities [S1-RC-01]. This is shown in Figure 20 where the unexpected ambiguities shown next to the red arrow are removed in IPF v2.70. There is no change

in the expected ambiguity shown next to the green arrow. No other specific azimuth ambiguity measurements were performed during 2016.

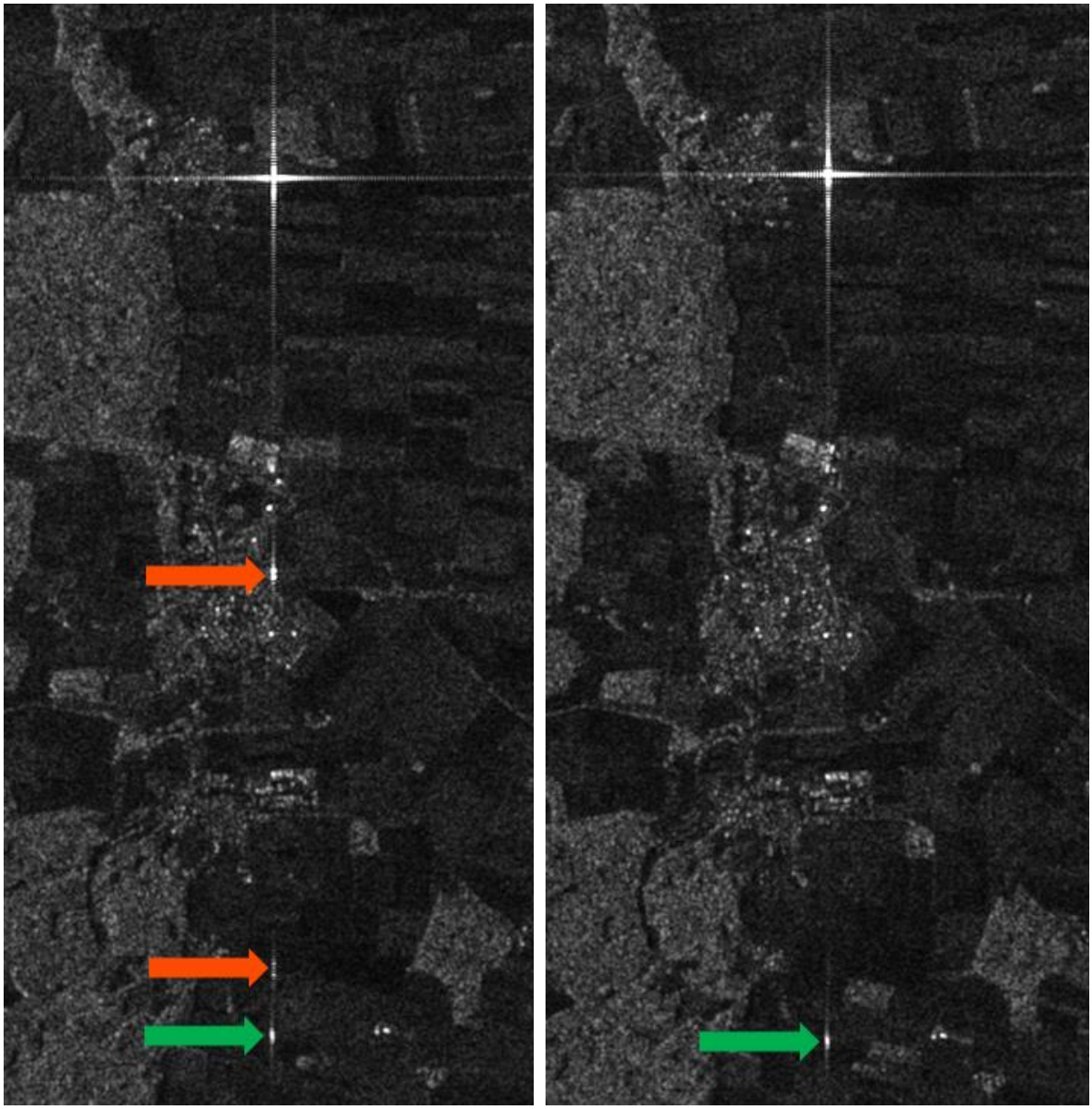

IPF v2.62 IPF v2.70

Figure 20: IW SLC DLR Transponder IRF and Azimuth Ambiguity

4.2.2.4.2. Range Ambiguities

No specific range ambiguity measurements were performed during 2016.

4.2.3. Radiometric Calibration

The DLR Transponders & Corner Reflectors, the BAE Corner Reflector and the Australian Corner Reflector array have been used to measure their radar cross-section as described below. The products analysed were acquired in 2016 and processed with the Sentinel-1 IPF v2.60, v2.62, v2.70, v2.71 and v2.72.

4.2.3.1. Absolute Radiometric Calibration

DLR Transponders have been used to calculate the relative radar cross-section for SM, IW and EW modes during 2016. The results per mode are shown in Table 7 where mean (radiometric accuracy) and standard deviation (radiometric stability) of the relative radar cross-section in dB are given. The number of measurements is given in brackets. The majority of the transponder measurements are for IW mode which reflects the acquisition planning strategy for S-1A during 2016. Note that the IW radiometric accuracy is close to zero while the radiometric stability is better 0.5dB. For SM and EW modes, the radiometric accuracy is also close to zero but the stability is higher due to the small number of measurements.

SM	IW	EW
0.00±0.65 (28)	-0.04±0.31 (477)	-0.07±0.46 (6)

Table 7: SLC Relative Radar Cross-Section for the DLR transponders (dB)

The following results are also for the DLR transponders but are separated by polarisation. Figure 21 and Table 8 give the results for SM mode – the relative radar cross-sections indicate a reasonable radiometric calibration, especially given the small number of SM measurements.

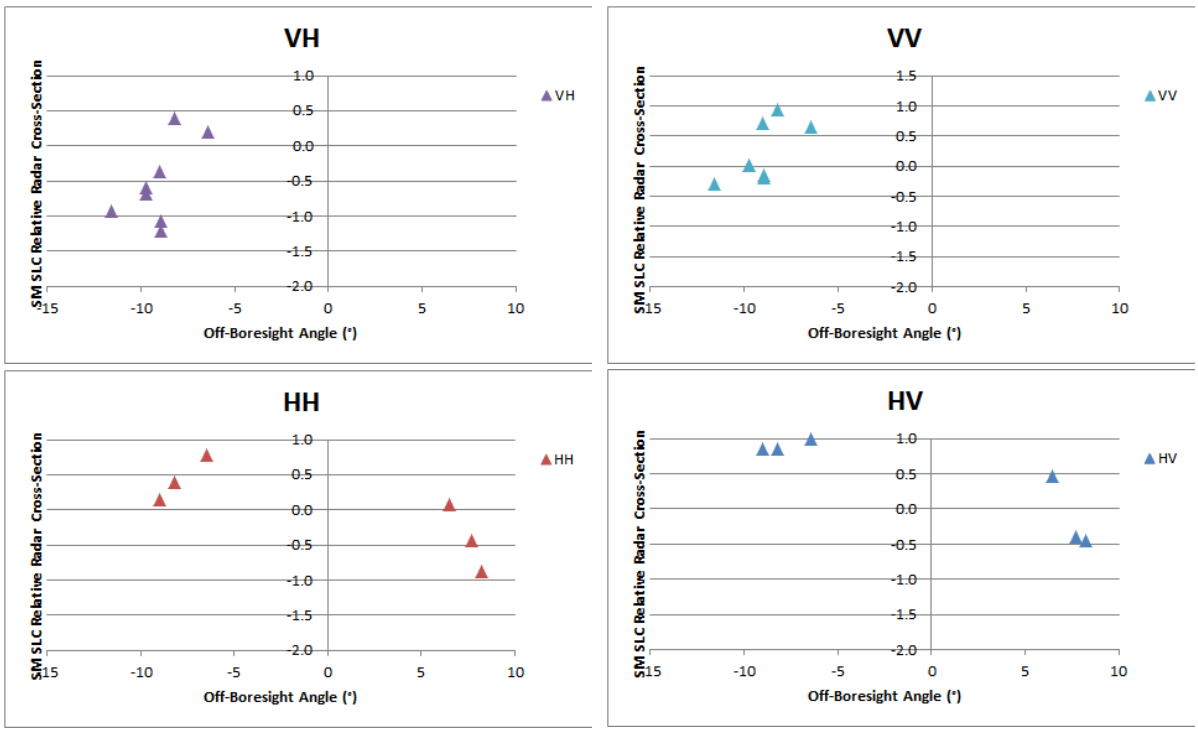

Figure 21: SM SLC Relative Radar Cross-Section for the DLR transponders

	VH	VV	HH	HV
S1	-0.90±0.25 (5)	-0.12±0.13 (5)		
S2	0.08±0.39 (3)	0.77±0.15 (3)	0.44±0.32 (3)	0.90±0.08 (3)
S5			-0.41±0.48 (3)	0.90±0.08 (3)

Table 8: SM SLC Relative Radar Cross-Section for the DLR transponders (dB)

The IW results below indicate a good radiometric calibration with many mean relative radar cross-section values close to zero (the radiometric accuracy) and a standard deviation of typically 0.3dB (the radiometric stability). Differences between polarisations are also small (see also Section 4.2.5.1). For EW only one acquisition over the DLR transponders occurred during 2016 and consequently only three measurements are available.

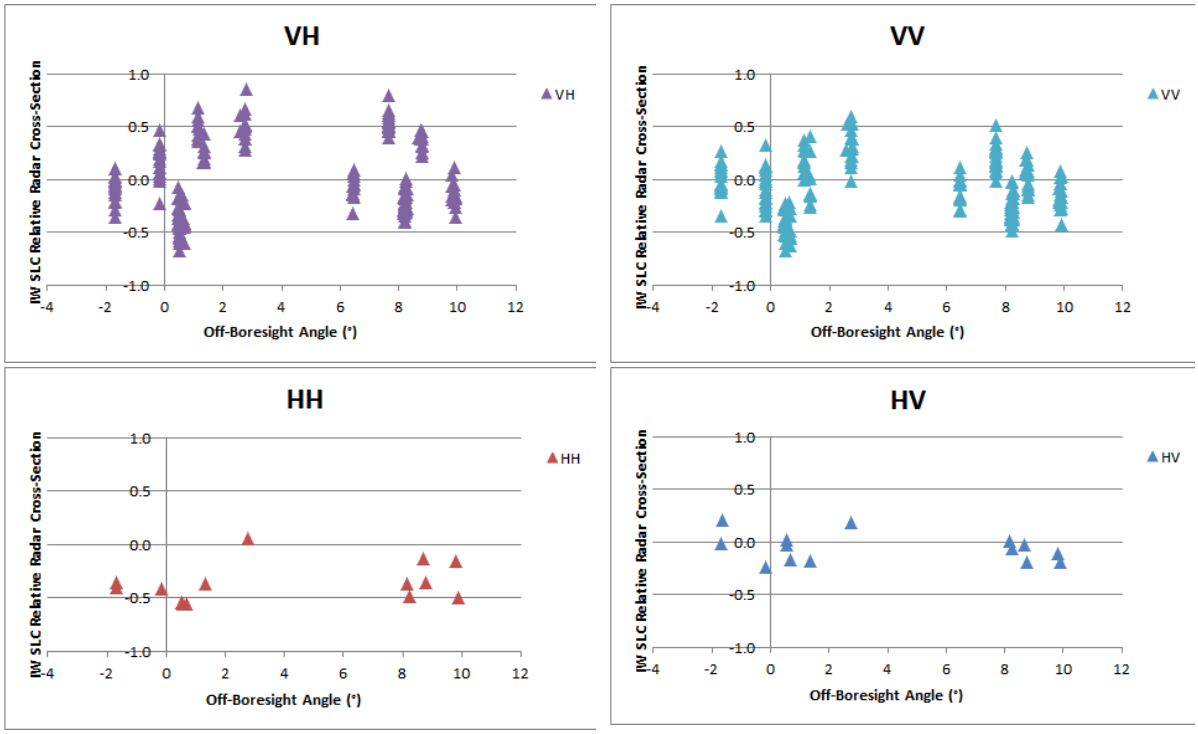

Figure 22: IW SLC Relative Radar Cross-Section for the DLR transponders

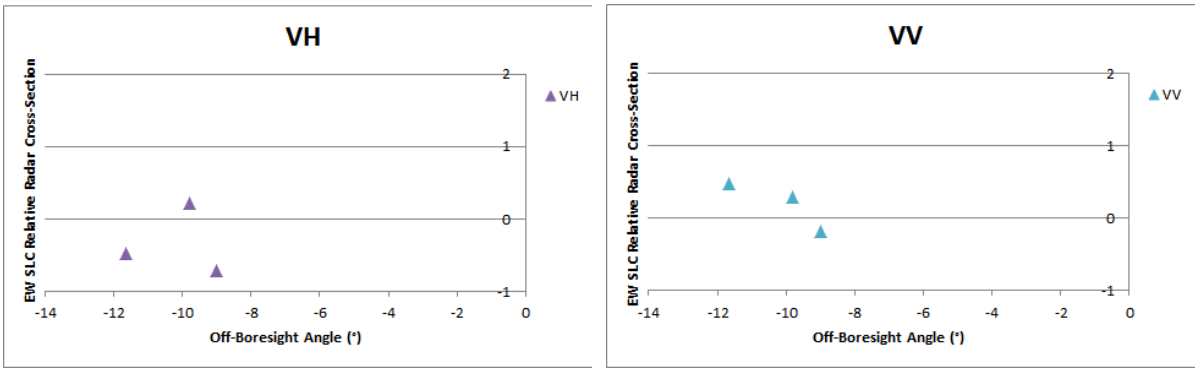

Figure 23: EW SLC Relative Radar Cross-Section for the DLR transponders

	VH	VV	HH	HV
IW	0.03±0.35 (224)	-0.09±0.26 (225)	-0.37±0.18 (14)	-0.06±0.14 (14)
EW	-0.32±0.48 (3)	0.19±0.33 (3)	Not measured	Not measured

Table 9: IW & EW SLC Relative Radar Cross-Section for the DLR transponders (dB)

	IW1	IW2	IW3
VH	-0.06±0.34 (97)	0.23±0.31 (31)	0.05±0.34 (96)

VV	-0.15±0.26 (98)	0.12±0.25 (31)	-0.10±0.23 (96)
HH	-0.46±0.09 (7)	0.06 (1)	-0.33±0.16 (6)
HV	-0.06±0.15 (7)	0.18 (1)	-0.10±0.08 (6)

Table 10: IW SLC Relative Radar Cross-Section for the DLR transponders (dB)

	EW1	EW2	EW3	EW4	EW5
VH	-0.32±0.48 (3)				
VV	-0.19±0.33 (3)				
HH					
HV					

Table 11: EW SLC Relative Radar Cross-Section for the DLR transponders (dB)

The radiometric calibration results using the BAE Corner Reflector and IW SLC products are shown in Figure 24 from imagery acquired during 2016 (VV polarisation only). The derived relative radar cross-section for all data acquired during 2016 is -0.16±0.23dB. The blue vertical line is the date of the Tile 11 Anomaly in June 2016 (see Section 4.2.9). Relative radar cross-section measurements after the anomaly show a small gradual decrease in relative radar cross-section. This is under investigation.

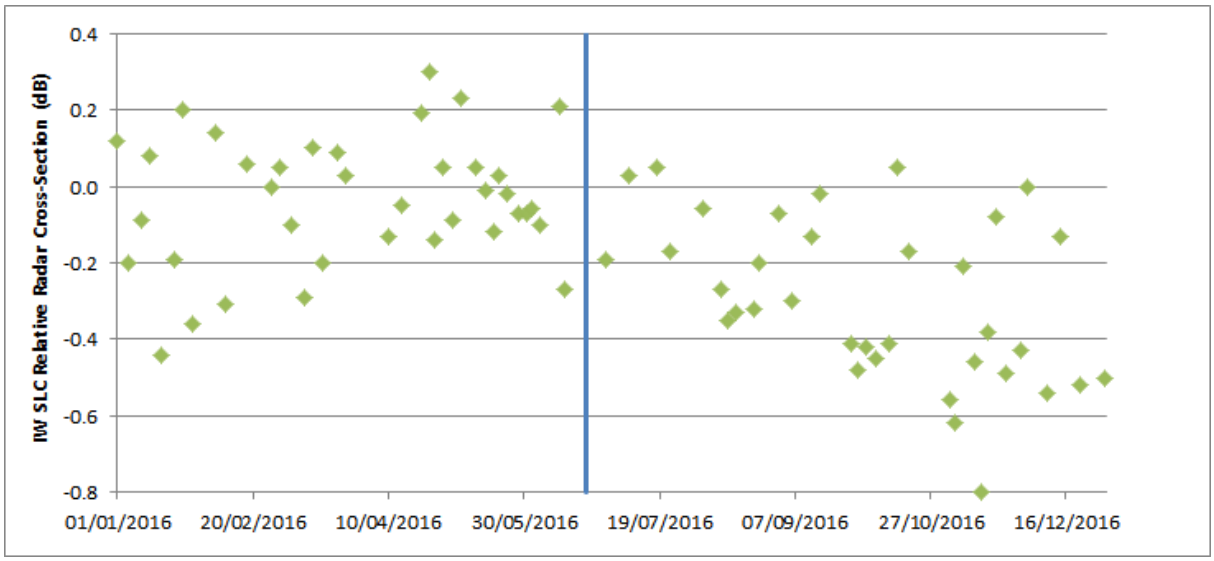

Figure 24: IW SLC Relative Radar Cross-Section for the BAE Corner Reflector

An array of 40 corner reflectors has been deployed near Brisbane, Australia as a component of the Australian Geophysical Observing System (AGOS) – see [S1-RD-04], [S1-RD-06] for further details. The CRs are size 1.5m (34), 2.0m (3) and 2.5m (3) with fixed orientations. Given that these corner reflectors have a fixed elevation and azimuth orientation they will not be pointing directly at S-1A. However, for IW acquisitions the reduction in radar cross-section compared to the case of a perfect orientation is small at less than 0.05dB. Table 12 gives the radiometric accuracy and stability for all corner reflector measurements during 2016 together with results for IW1 and IW2 sub-swaths and for VV and HH polarisations. The numbers in brackets refer to the number of measurements. The results indicate an accuracy close to zero while the stability is less than 0.5dB but larger than derived from the DLR transponders above.

All	IW1	IW2	IW1 VV	IW1 HH	IW2 VV	IW2 HH
-0.13±0.48 (721)	-0.12±0.49 (425)	-0.13±0.48 (296)	-0.19±0.37 (73)	-0.11±0.51 (352)	-0.14±0.44 (53)	-0.13±0.49 (243)

Table 12: IW SLC Relative Radar Cross-Section for the Australian Corner Reflectors (dB)

4.2.3.2. Permanent Scatter Calibration

Figure 25 shows a recent IW VV Permanent Scatter Calibration series over Paris. The series covers the whole 2016 and includes the tile 11 issue (June 2016). after the issue only a small reduction of the calibration constant can be observed (about 0.1 dB), meaning that the TX power reduction for half tile 11 is well captured by the internal calibration PG product.

Note that after tile 11 issue a radiometric trend can be observed in the PSCAL results as reported in Figure 26. The measured trend is -0.27 dB/year for co-pol and -0.13 dB/year for cross-pol. The same trend is observed from transponder acquisitions as well. It shall be further investigated since it is not captured by RFC and internal calibration measurements.

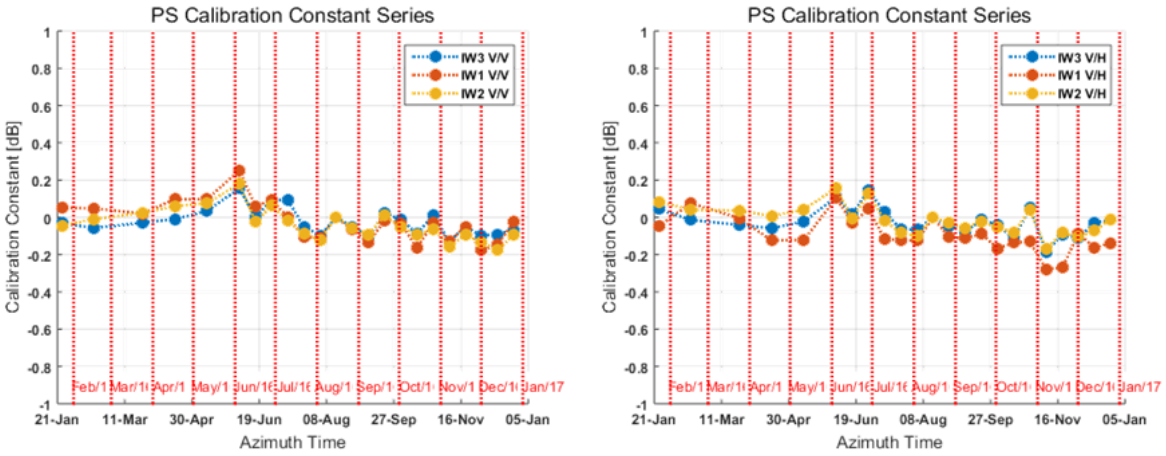

Figure 25 Permanent Scatter Calibration time series for TopSAR IW V/V (left) and V/H (right) over Paris.

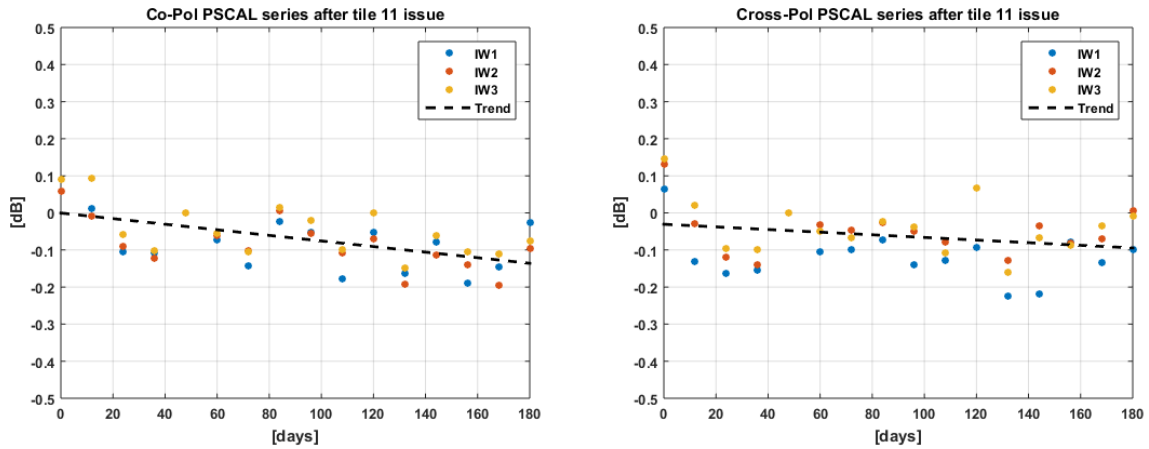

Figure 26 Permanent Scatter Calibration trends after tile 11 issue for TopSAR IW V/V (left) and V/H (right) over Paris.

4.2.4. Geometric Validation

In 2016, S-1A geolocation quality was monitored during the S-1B commissioning and calibration phase. Trihedral corner reflectors (CRs) whose positions were surveyed with cm-level accuracy were used as reference targets. StripMap (SM) products have the best resolution and represent the native sensor characteristics more closely than other product types, which is why they are also used for sensor calibration. Geolocation accuracy was estimated for IW SLC products as well, also acquired over the same two test sites in 2016.

For a particular CR visible in an S-1A image product, its predicted azimuth and slant range image pixel position was calculated as follows:

- The surveyed CR position was adjusted for acquisition-time "epoch" plate **tectonic drift** and **solid Earth tide** (SET), as described in [S1-RD-11].
- The relevant timing annotations were extracted from the product annotations; these included the azimuth zero-Doppler time stamps, the orbital state vectors, the near-range fast time, and the range and azimuth sample spacings.
- Range-Doppler geolocation was performed for the CR coordinate as described e.g. in [S1-RD-13], giving range and azimuth times as the output.
- The slant range prediction was corrected by adding the modelled **atmospheric path delay**, and the azimuth time was corrected by subtracting the **bistatic** residual. These effects and their associated corrections are described in more detail in [S1-RD-11].

The above steps resulted in a range-azimuth *predicted* position for each target that could be compared to the position of the peak intensity in the image raster itself, i.e., the *measured* CR position. The differences between predicted and measured positions were then plotted, with the results shown for the SM and IW SLC product time series in Figure 27, with product date ranges indicated. Please refer to [S1-RD-11] and [S1-RD-12] for details on the evolution of the standard IPF processing and the geolocation methodology.

The ALE estimates were originally made using SM data acquired and processed during the S-1A commissioning phase. The initial geolocation results based on SM SLC products served as a basis for an update to the Sampling Window Start Time (SWST) bias annotation in the instrument auxiliary files ingested by the S1 processor. The plots shown in Figure 27 show the ALE estimates as they appear *after* accounting for the respective SWST biases (either in the S1 processor itself, or during post-processing). Note that no analogous azimuth timing correction has yet been incorporated into the processor.

Figure 27(a) shows the SM SLC ALE plot for S-1A. Although the mean range offset is small (~3.8 cm), it is not exactly zero even though the official SWST bias was applied during geolocation estimation. This is due to improvements made to the atmospheric path delay model *after* the original SWST bias estimate had been incorporated into the IPF. As a result, the slant range estimates for the targets in Figure 27(a) products changed, corresponding to an updated range ALE.

The S-1A IW SLC plot is shown in Figure 27(b). The clear grouping of the points by subswath is a known issue under continued investigation. Some indication of a similar beam-specific grouping can be seen in the SM SLC plot as well (Figure 27(a)).

The ALE plots in Figure 27 indicate that given bias compensations, the localisation performance was well within the original requirements (according to sections 5.5.2.1 and 5.5.2.2 in [S1-RD-14]). The observed beam/subswath-dependent azimuth ALE remains under investigation. A method for integrating azimuth bias compensation annotations in the IPF is under study.

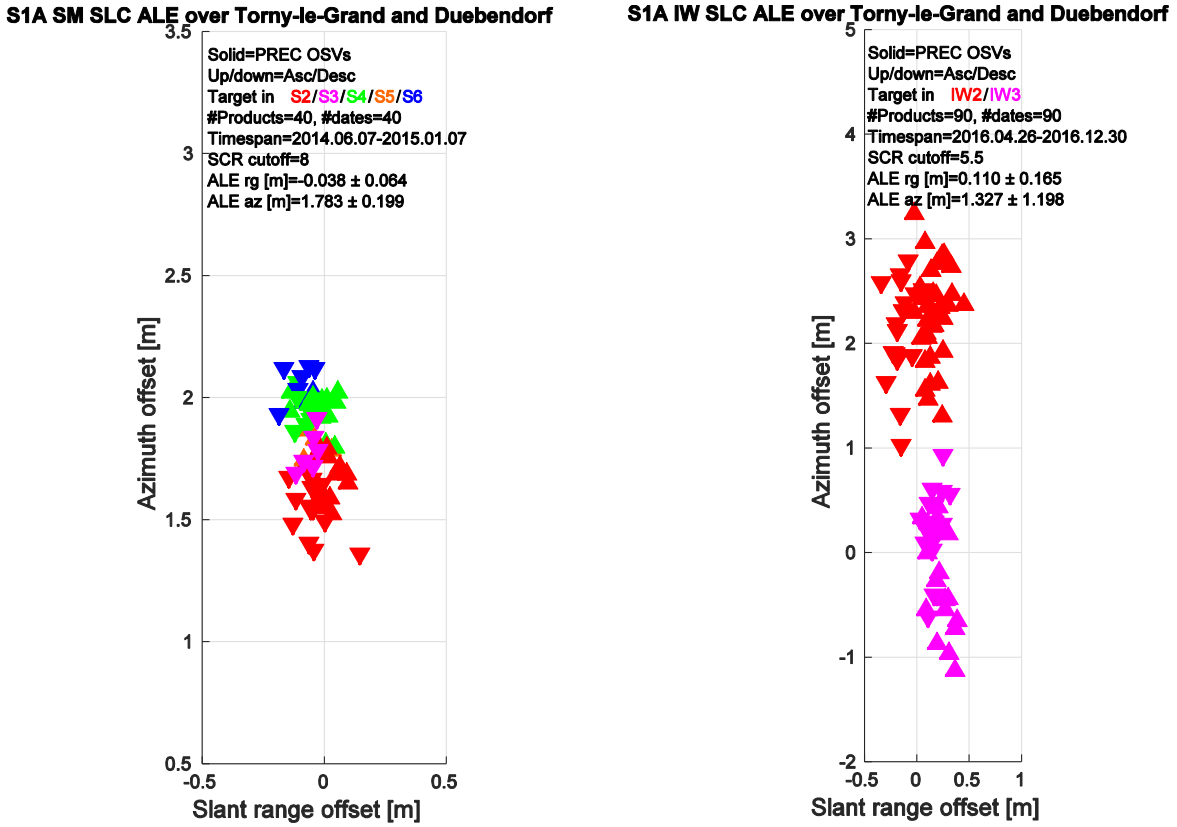

(a) S-1A SM SLC (2014.06.07 – 2015.01.07) (b) S-1A IW SLC (2016.04.26 – 2016.12.30)

Figure 27: ALE estimates for S-1A StripMap and IW SLC product time series acquired over the Swiss test sites using precise state vectors (AUX_POEORB). Product date ranges are given in brackets (N.B. no S-1A SM acquisitions were made over Switzerland during the 2016 campaign). Point colours represent beam/subswath. The S-1A SWST (range) bias (output of the commissioning and calibration phase) was applied in both cases.

4.2.5. Polarimetric Calibration

4.2.5.1. Gain Imbalance

The DLR transponders have also been used to calculate the gain imbalance (the difference in radar cross-section between the two polarisations of dual polarisation products). Table 13 gives a summary of the gain imbalance for the SM, IW and EW modes. The majority of the measurements are for IW mode for which the mean gain imbalance is close to zero. For SM and EW modes, further measurements are required to determine if the gain imbalance needs to be corrected.

	Gain Imbalance (dB)
SM	-0.59±0.30 (14)
IW	-0.10±0.20 (238)
EW	-0.51±0.44 (3)

Table 13: Gain Imbalance using the DLR transponders

The following results show the gain imbalance split between the two possible polarisation of VH/VV and HH/HV. Table 14 give the gain imbalance for SM, IW and EW for acquisitions during 2016 while Figure 28 shows the gain imbalance for IW.

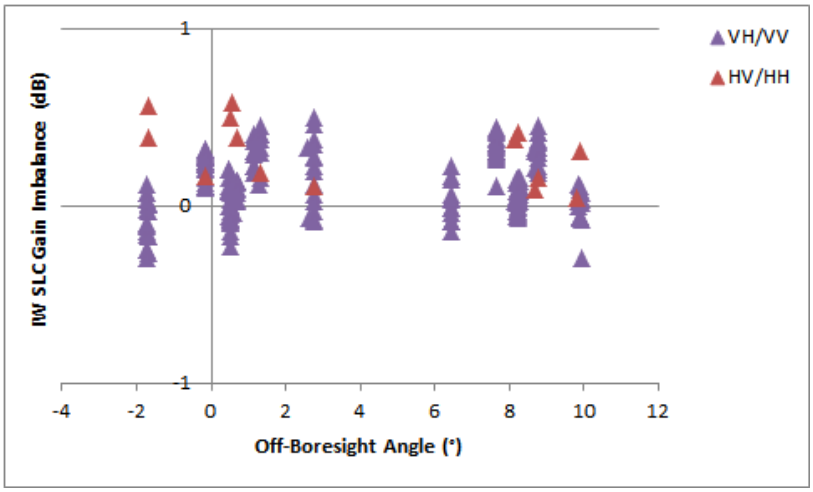

Figure 28: IW Gain Imbalance using the DLR transponders.

	VH/VV	HV/HH
SM	-0.75±0.23 (8)	-0.37±0.23 (6)
IW	0.12±0.17 (224)	0.31±0.18 (14)
EW	-0.51±0.44 (3)	

Table 14: Gain Imbalance using the DLR transponders

4.2.5.2. Phase Imbalance

The DLR transponders have been used to calculate the phase imbalance (the difference in peak phase between the two polarisations of dual polarisation products). Figure 29 and Table 15 give the gain imbalance for SM, IW and EW for acquisitions during 2016. As expected the phase difference is close to zero.

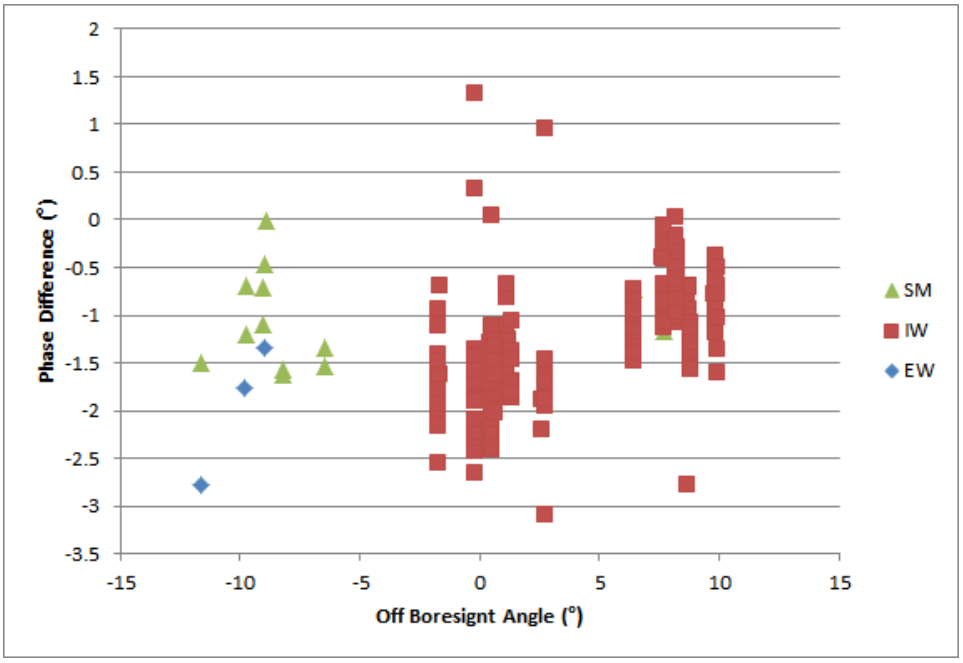

Figure 29: Phase Imbalance using the DLR transponders.

	Phase Difference (°)
SM	-1.02±0.49 (14)
IW	-1.20±0.65 (238)
EW	-1.96±0.74 (3)

Table 15: Phase Imbalance using the DLR transponders

4.2.5.3. Coregistration

The DLR transponders both provide an impulse response in both polarisations of dual polarisation imagery which enables coregistration to be performed between the two polarisation images. Table 16 below shows that the average measured polarimetic co-registration derived from SLC products acquired during 2016 is very small (the IRF peak position is measured to a 1/8 of a pixel).

Mode/Swath	Range Co-registration Accuracy (m)	Azimuth Co-registration Accuracy (m)	Number of Measurements
SM	0.04±0.11	0.00±0.00	28
IW	0.02±0.07	0.07±0.35	477
EW	0.00±0.00	0.00±0.00	6

Table 16 Polarimetric Calibration Measurements

4.2.5.4. Cross-talk

No specific cross-talk measurements were performed during 2016.

4.2.6. Elevation Antenna Patterns

There were no updates to the S-1A elevation antenna patterns during 2016.

4.2.7. Azimuth Antenna Patterns

There were no updates to the S-1A azimuth antenna patterns during 2016.

4.2.8. Noise Equivalent Radar Cross-section

S-1A imagery with low ocean backscatter can be used to estimate the Noise Equivalent Radar Cross-Section (NESZ). In Figure 30 and Figure 31 show NESZ measurements for IW and EW mode derived from data acquired in 2016. The requirement that the NESZ should be below -22 dB is met at all sub-swaths. For IW the measurements are slightly better than the prediction (red curves) while for EW the measurements are slightly worse than the prediction.

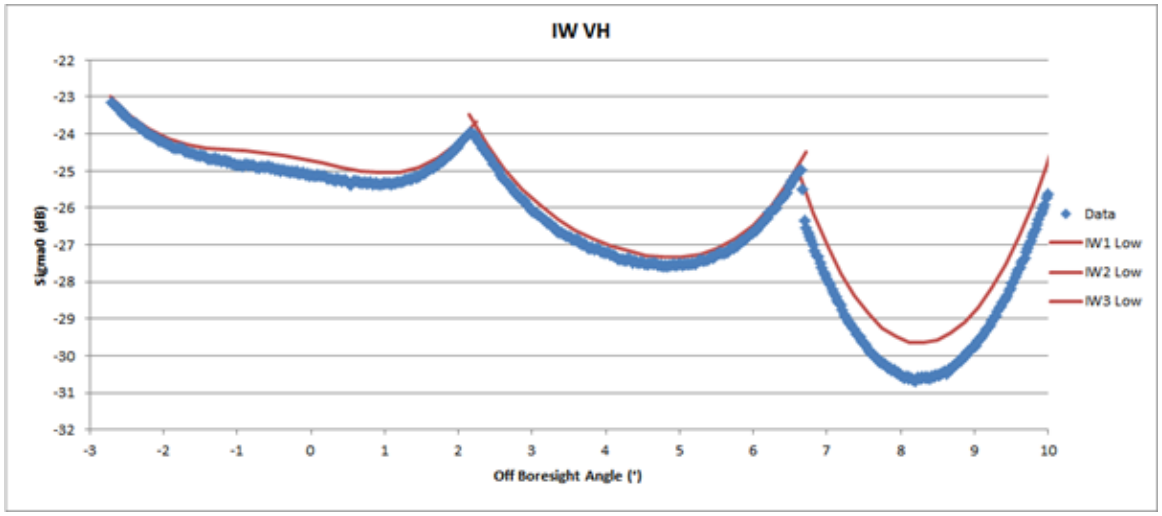

S1A_IW_GRDH_1SDV_20160126T054425_20160126T054450_009661_00E15D_9DC9.SAFE

Figure 30: NESZ measures for IW. Blue is the measured NESZ and the red lines are the predicted NESZ at minimum orbital altitude.

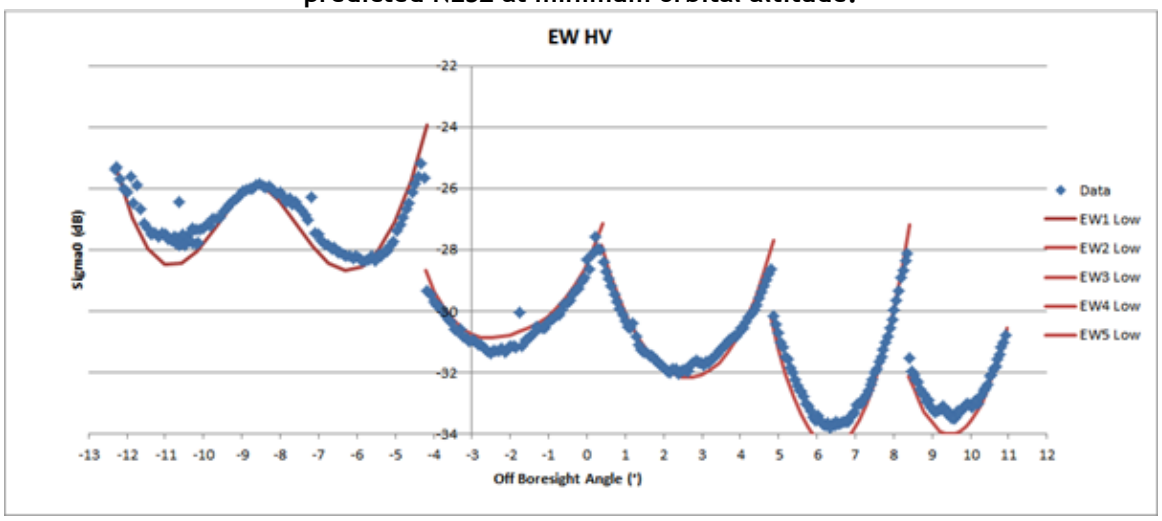

S1A_EW_GRDH_1SDH_20160124T055528_20160124T055632_009632_00E084_2194.SAFE

Figure 31: NESZ measures for EW. Blue is the measured NESZ and the red lines are the predicted NESZ at minimum orbital altitudes.

4.2.9. S-1A Tile 11 Failure

As described in Section 3.1, a problem with the transmit power supply on tile 11 occurred on 16th June 2016 led to reduced power for rows 1 to 10 in Tx H and Tx V. The resumption of operations occurred on 27th June 2016. An assessment on the impact on Level 1 products were performed [S1-RD-08]. Analysis was performed using the Amazon Rainforest (for changes on elevation antenna pattern) and calibration point targets (for changes on absolute calibration). This showed either no or a small (~0.1dB) reduction in radiometry. This indicates that the internal calibration is correctly compensating for the reduction in transmit power caused by the Tile 11 issue. Results from various point targets (the Australian CR array, the DLR transponders and corner reflectors and the BAE corner reflector) do not show any systematic reduction in relative RCS. As described in Section 4.2.3.1, the BAE Corner Reflector indicates a radiometric calibration drift since the S-1A tile 11 failure.

4.2.10. S-1A Debris Collision

The Sentinel-1A solar panel was hit by a small piece of space debris or micrometeoroid on 23rd August 2016 at 17:07 UT. As shown in Figure 32 and Figure 33 the location and size of the debris image is clearly visible from an on-board camera. The size of the affected area is about 40cm in diameter caused by a particle just a few mm in diameter. No unusual behaviour in either the spacecraft attitude or Doppler was found and no implications were found for processed Level 1 products. Further information can be found in [S1-RD-09].

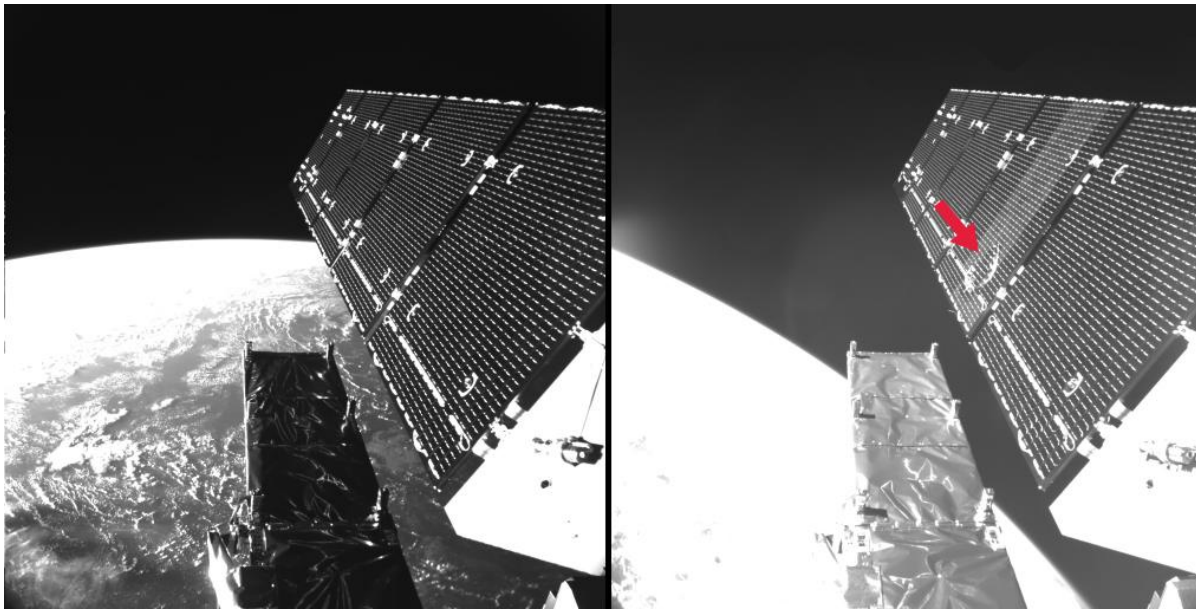

Figure 32: S-1A solar panel before and after debris collision on 23 August 2016 (red arrow indicates panel damage).

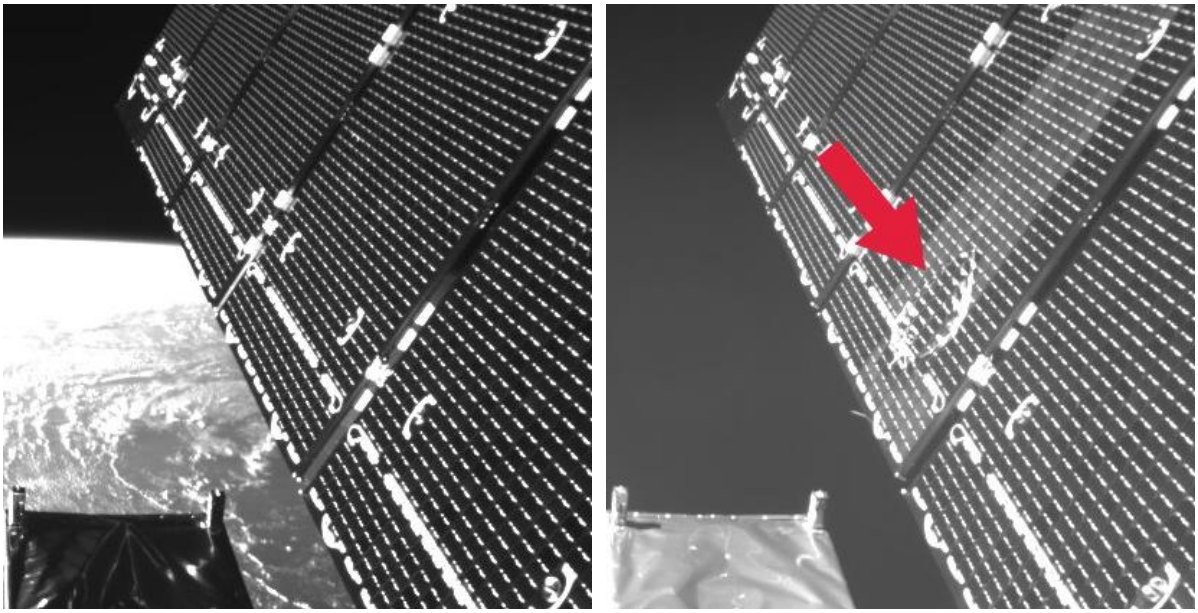

Figure 33: S-1A solar panel before and after debris collision on 23 August 2016 (detail).

4.2.11. Summary of Anomalies

4.2.11.1. Radio Frequency Interference

As small percentage of Sentinel-1A imagery is affected by the presence of Radio Frequency Interference from the ground. An example from 2016 is shown below over Japan. Usually RFI only affects a few range lines of raw data.

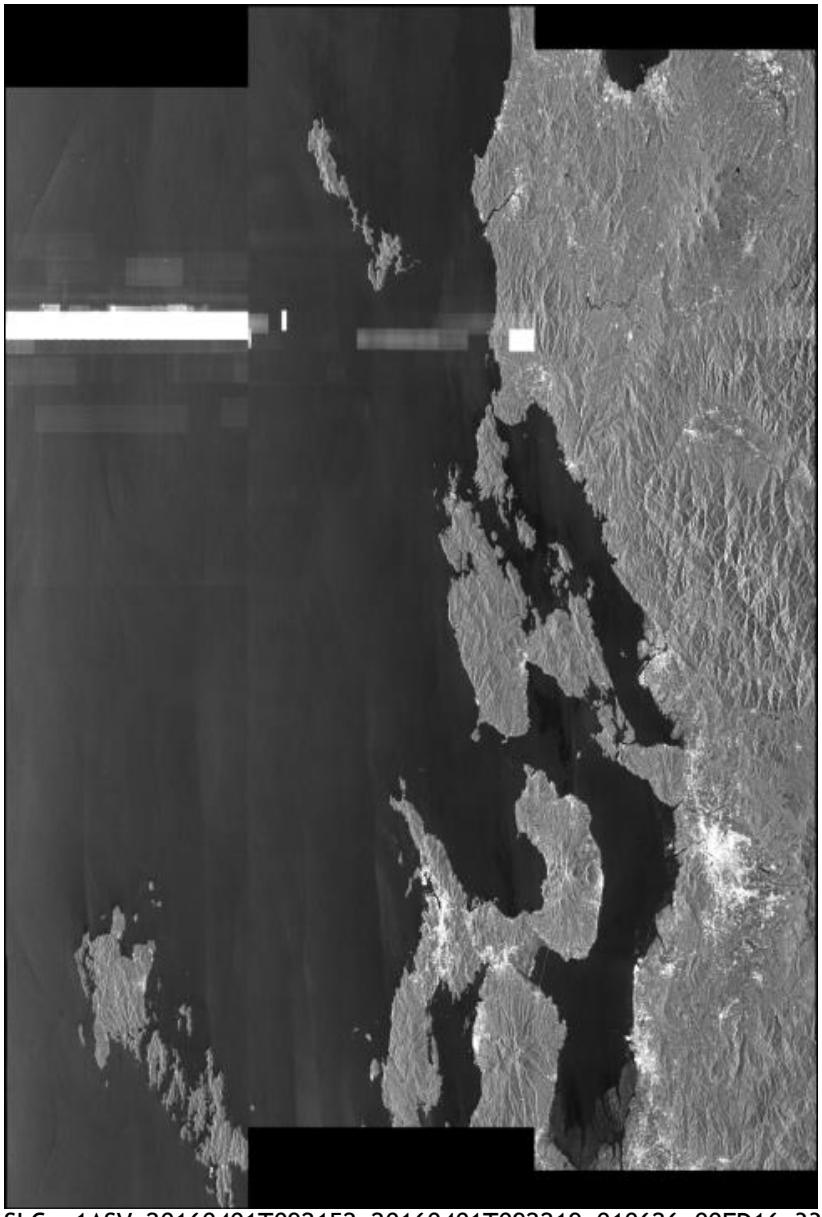

S1A_IW_SLC__1ASV_20160401T092152_20160401T092219_010626_00FD16_3336.SAFE

Figure 34: An example of Radio Frequency Interference over Japan

4.2.11.2. Radarsat-2/Sentinel1-A Mutual Interference

Although the orbit altitude of Radarsat-2 and Sentinel1-A are quite different (789 km and 693 km respectively) their repeat periods are a multiple of each other (24 days and 12 days respectively) and their equatorial crossing times are almost the same (~18:00 hrs at the ascending node). Another similarity is that both SARs operate at the same frequency.

The repeat period and crossing times mean that every 24 days, Radarsat-2 will be directly above Sentinel-1 and hence both may be imaging the region of the Earth's surface at the same time. If this occurs then mutual interference is detected. Further examples of such mutual interference occurred during 2016 as indicated in Table 17.

Satellite	Orbit	Relative Orbit	Acquisition Date	Start Time (UT)	End Time (UT)	Approx. Latitude	Approx. Location
S-1A	9391	44	7th January 2016	16:56	17:04	62° N	Sweden
S-1A	9741	44	31st January 2016	16:58	17:04	62° N	Sweden
S-1A	10091	44	24th February 2016	17:03	17:04	63° N	Norway
S-1A	12441	119*	3rd August 2016	20:40	20:41	73° N	NE Russia
S-1A	12741	69*	24th August 2016	10:24	10:24	70° N	Greenland
S-1A	13091	69*	17th September 2016	10:22	10:24	74° N	Greenland
S-1A	13223	35*	27th September 2016	04:10	04:11	53° N	Belarus/Russia
S-1A	13441	69*	11th October 2016	10:22	10:26	74° N	Greenland

*Descending pass

Table 17 S-1A/Radarsat-2 Mutual Interference during 2016

4.2.11.3. Other S-1A/Satellite Interference

Another type of interference between S-1A and another satellite was seen on 8th December 2016 over Florida, USA as shown in Figure 35. The interference is approximately 1200 km in azimuth extent and it has a visual appearance that is quite different from the S-1A/Radarsat-2 interference [S1-RD-01]. It occurred between 23:27:09 and 23:30:22 UT. No other occurrences of this type of interference have been observed and the source of the interference has not been identified.

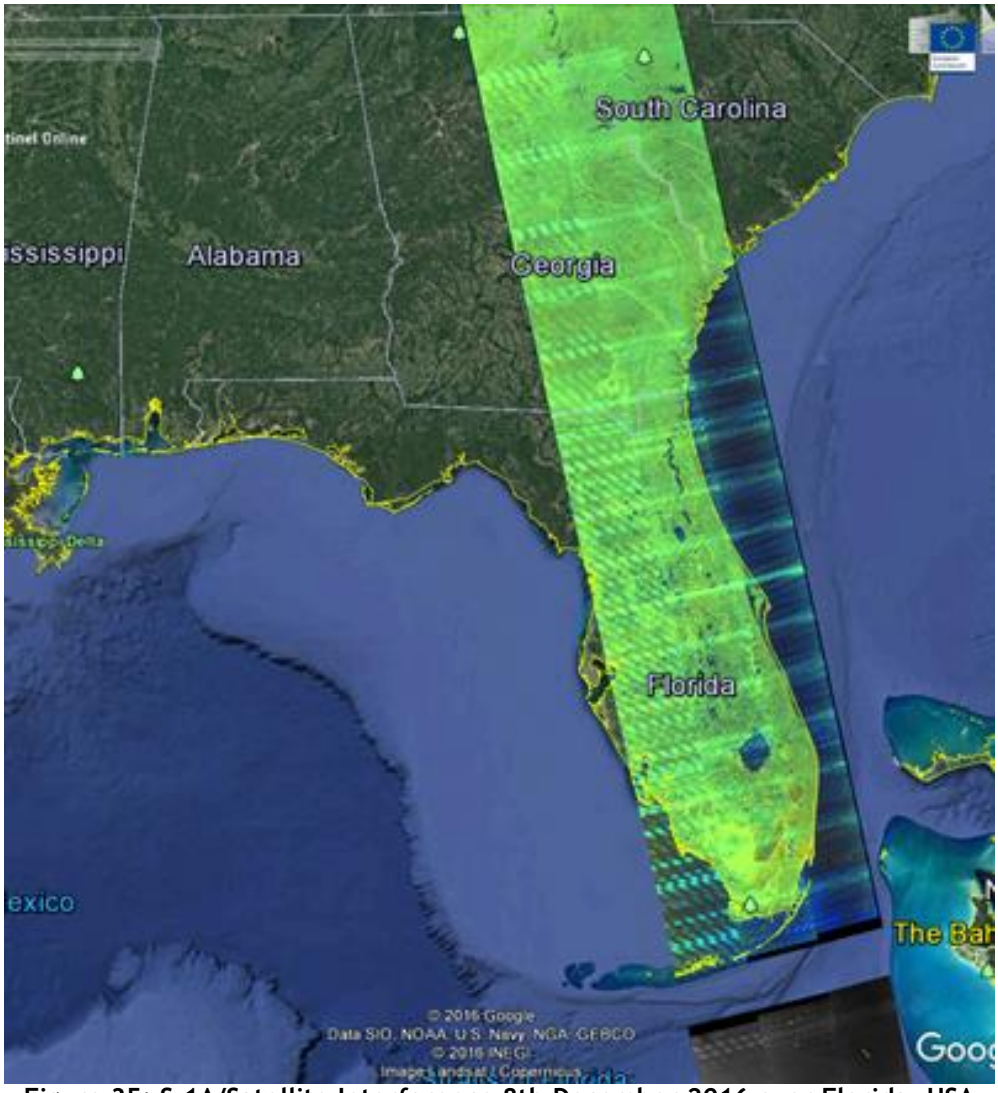

Figure 35: S-1A/Satellite Interference 8th December 2016 over Florida, USA

4.2.12. Quality Disclaimers

S-1A Quality disclaimers issued during 2016 are given in Appendix H -.

4.3. S-1A Level 2 products

4.3.1. Wind measurement

4.3.1.1. Image Mode (SM-IW-EW)

The SAR wind measurement is strongly dependant of the product calibration accuracy. It takes benefit from the efforts made on the SAR Level1 products to improve the calibration constant and align the gamma profile as the function of the elevation angle over Rain Forest. These improvements impact the wind measurements, making it appearing more consistent all along the subswath and also subswath by subswath.

Statement of the wind measurements accuracy:

The strategy to assess the accuracy of the wind retrieval is to compare it with an auxiliary wind source which is used as a reference. This source could be in-situ data from buoy, other satellite data (ex: scatterometer) or atmospherical model outputs. It is important to outline the importance to multiple the types and the number of the data used as reference, due to their coverage, resolution or possible bias. In this scope, Ifremer has performed systematic collocations with such data (model: ECMWF (global), Arome, Arpege (European), hundreds of buoys, Metop scatterometers ASCAT- A/B etc.) with L2 products generated by the ESA-IPF by PDGS.

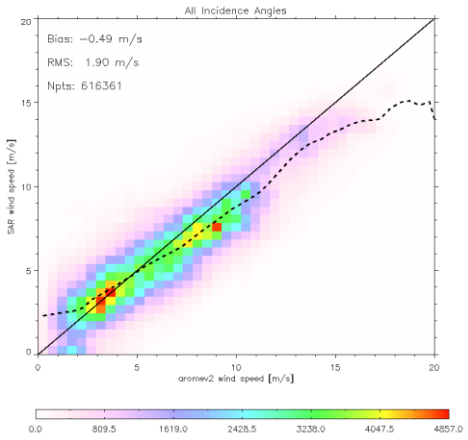

a) Arome

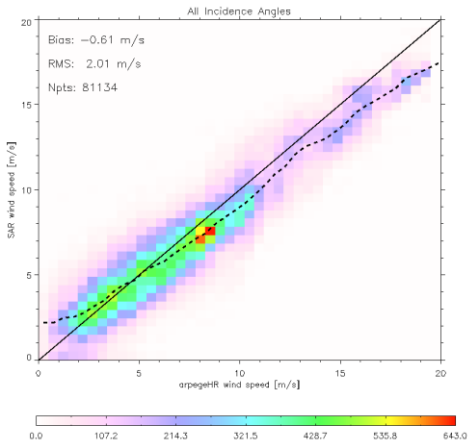

b) Arpege HR

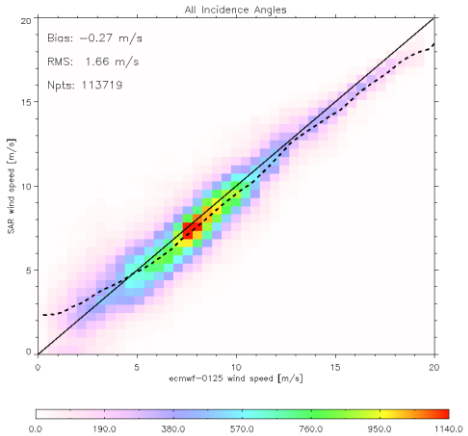

c) ECMWF

	bias	Rms
Arome	-0.49 m/s	1.90 m/s
Arpege	-0.61 m/s	2.01 m/s
ECMWF	-0.27m/s	1.66 m/s

Figure 36: SAR Wind speed compared with reference wind speed for IW mode VV polarisation.

Figure 36 presents the performances achieved on the three last months of 2016 for IW mode in VV polarisation of the retrieved wind compared to model references (Arome, Arpege and ECMWF). It can be noticed the strong correlation of the SAR-derived wind speeds with the wind references. The bias and the RMS are less important for ECMWF re-analysis since the wind inversion is based on the ECMWF forecast as an a priori wind input. As expected, at low wind speeds, the NESZ impacts the SAR wind measurement (over-estimation). At high wind speeds, the SAR tends to under-estimate the wind speed; however the number of samples is low, and may not be sufficient to conclude. A typical RMS of 1.5m/s to 2m/s is observed. The quality of the wind product derived for this mode is fairly good. Same kind of performances (bias nearly equal to zero and RMS of about 2m/s) is achieved on EW HH mode. Other modes such as SM, IW in HH and EW in VV are rarely acquired or processed up to Level 2 products.

Improvement performed during 2016:

Some improvements have been conducted during 2016.

1. Correction of the wind direction:

A minor issue on the look angle (relative angle between the input wind direction compared to the SAR geometry) used in the OWI process had been found at the end of 2015. This has been solved with IPF 2.70 version.

2. Attempt to improve the IceMask

   In the IPF 270 (IDL), as the initial implementation in the LOP of the ice mask estimation was not performing well, a correction for taking into account the ice border instead of the ice concentration mask was introduced.

   Whenever located in OSISAF ice region, the ice border is well taken into account and the filtering in the wind inversion behaves well.

   On the opposite, when no ice is present, a side effect is produced and the ice border interpolation on the wind field grid introduces a large margin to the coast, of sometimes 5 to 10 km which is especially an issue in island vicinity. This is illustrated in **Figure 37**. To correct for this effect, a patch will be proposed has part of next IPF python release.

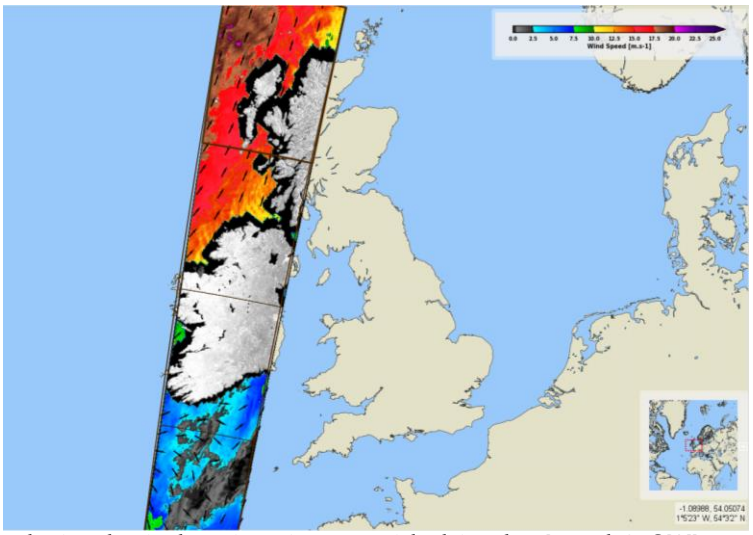

Figure 37: SAR-derived wind estimation provided in the Level-2 OWI products showing the coastal margin introduced by the ice mask update.
This margin is a side effect of the raw coastal polygon used in the ice border information provided in the ancillary ice information.

3. Preparation for the noise removal:

All the elements have been put in place in order to allow the activation of this functionality: the use of the annotated noise vectors in order to 'denoise' the measured NRCS before computing the wind measurement. This functionality is available since IPF2.70. It would allow reducing the impact of the NESZ on the wind measurements, in particular for low to moderate wind speeds (over-estimation + impact of the antenna lobes with respect to the elevation angle). The OWI detailed algorithm document and ADF format specification has been updated accordingly. A new field in the AUX_PP2 has been introduced in order to trigger the activation. However, the current noise annotations have been considered not accurate enough for the systematic activation of the denoising for 2016.

4. Adding of Noise information

As part of the preparation of the denoising, the new variable OwiNesz is computed (interpolation of the annotated noise vector on the OWI grid) and extracted in the L2 product, from IPF 2.7 and later versions. This is a new-information variable which was not present in the previous products.

The elevation angle has also been added in the L2 OWI product.

5. Development of a python version of the L2 processor

During 2015/2016, a new version of the LOP has been developed and consolidated using python rather than IDL. This new version is not currently on-production; it has no impact on the current wind retrieval performances.

Coming Improvements for 2017:

Some improvements of the SAR retrieved wind measurement remains in the scope of 2017.

1. Python version of the LOP

During 2015/2016, a new version of the LOP has been developed and consolidated using python rather than IDL. The start of the production using this version is planned for 2017. The impact on the wind measurement quality should be negligible. However the number of products processed to OCN level could increase.

2. Issue with Ice mask

The issue identified in the ice mask estimation mentioned in the previous paragraphs has been identified and a correction was developed in order to better take into account the presence/absence of ice indicated in the ancillary ice files. This correction is not yet implemented in the current operational IPF version.
The new correction takes into account the sea ice border information, whose information is not originally given in coastal regions (about 10km), but can be extended to the coast when judged relevant using image processing methods, as illustrated in Figure 38. The coastal margin shown in Figure 38 is removed from this processing when no ice is detected.

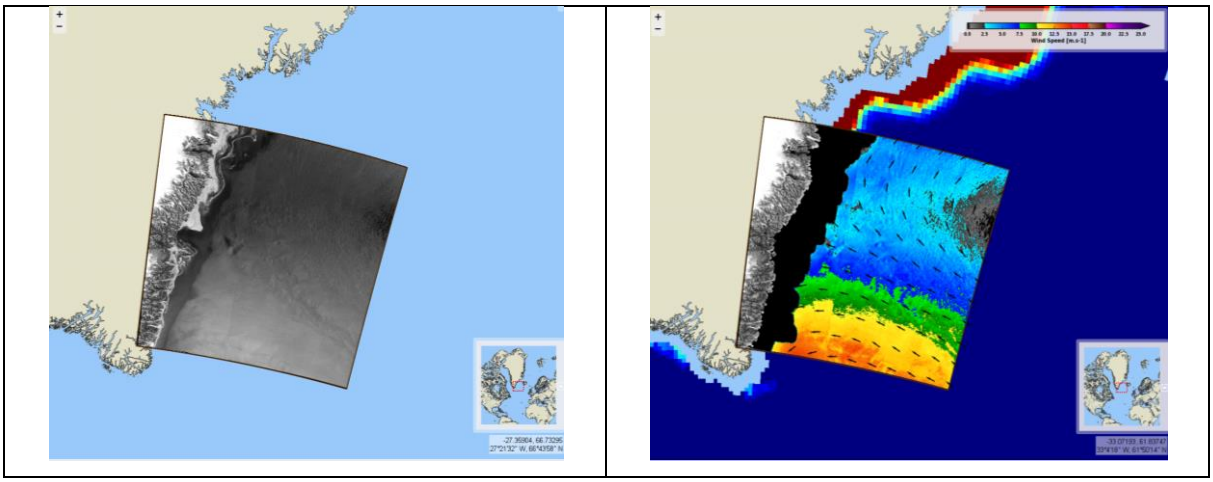

Figure 38: Sea surface roughness of a Sentinel-1 product acquired over Greenland on 2016/04/29 (left) and the associated ice masked OWI product with background ice concentration (right).

3. Issue with the Bright Target

The aim of the Pbright algorithm is to remove bright targets (such as the ships, oil rigs, offshore wind farms for example) from the averaging of the scattering level (normalized radar cross section) on the cell where the wind retrieval is performed to avoid their contribution. First quantitative inspection indicates that the results of the Pbright algorithm are not optimal and tend to over-estimate the number of bright targets in the wind cell. It means that it reduces the number of points for the averaging, and then could result in a less-confident and underestimated SAR-retrieved wind speed. Since the processing parameters used in the Pbright algorithm have not been re-adujsted after

Sentinel-1 launch, a quantitative estimation of the algorithm performances will be performed for the different acquisition modes and processing levels and adjustments will be proposed if necessary.

4. Activation of the noise removal

The activation of the noise removal will allow to reduce the impact of the NESZ on the wind measurements especially for low-to-moderate wind speed and for wind measurements performed at high incidence angle, resulting on an over-estimation of the SAR derived wind speed and possible modulation of the measured wind speed profiles by the antenna lobe. The noise vectors of the L1 product will be updated during 2017, to be more accurate. Once this activity and after performance assessment, it could be decided to activate the noise removal for wind retrieval production.

5. GMF change

GMF is the theoretical function from which a wind situation and observation configuration gives the measured sea-surface-backscattered level. SAR wind monitoring has outlined some deficiencies in the current GMF (Cmod-Ifr2). An activity on the assessment of the performances of several candidate GMFs of the Cmod5 family will be conducted during 2017. Then if benefit of using another GMF is demonstrated, the action will be taken to update this GMF.

4.3.1.2. Wave Mode

2016 is the first complete year with a nominal use of the wave mode for Sentinel-1 A. Following the acquisition plan, wave mode has always been activated at global scale over the oceans (excepted for June), producing a comprehensive and constant number (~25000 for WV1 and ~25000 for WV2 each month) acquisitions every cycle. This enables to investigate the stability of the Level-2 products performances with respect to time (e.g. seasonal variations) for the first time. In 2016, only acquisitions in VV polarisation have been done. Results are strictly based on VV in this report.

For wind parameters of the level-2 products as measured by Sentinel-1 A, the major change is:

- Update of the processing gains coefficients. This mostly impacts performances on ocean surface wind speed (oswWindSpeed)

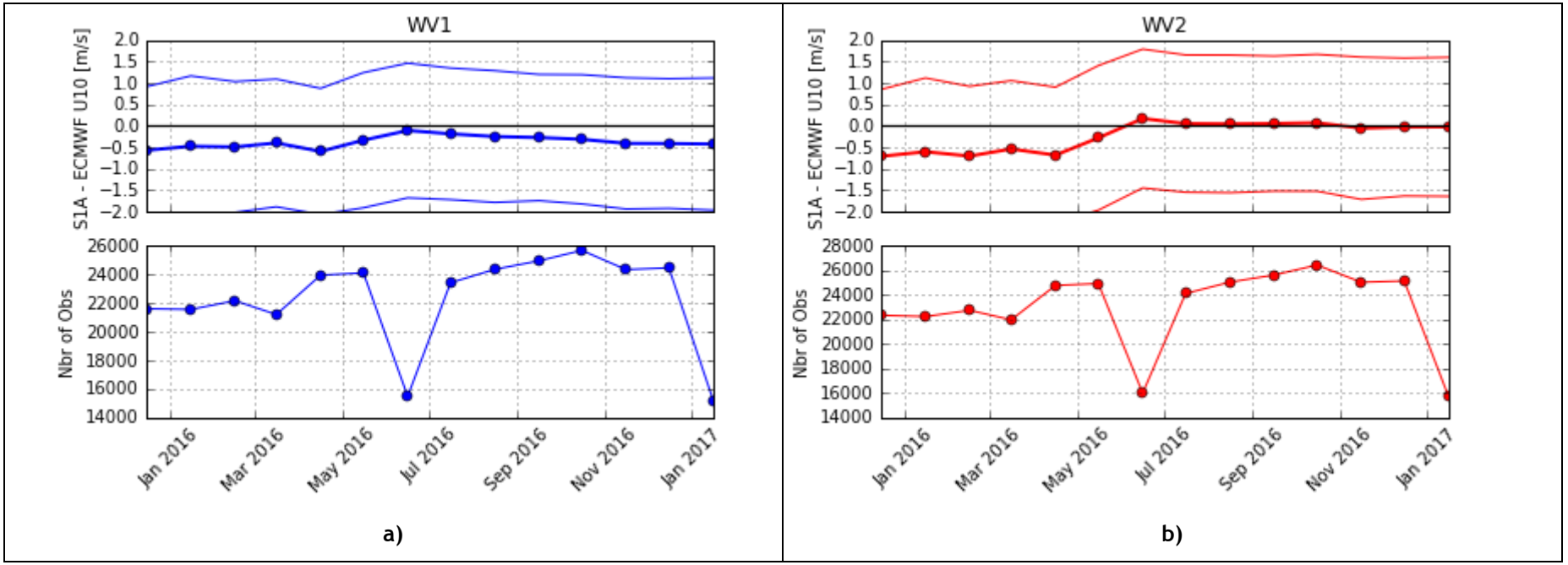

Figure 39 Ocean surface wind monthly performances for WV1 (a) and WV2 (b) and number of acquisitions co-located to reference data for validation for WV1 (bottom-left) and WV2 (bottom- right). For top panels, colored thick solid lines stand for the mean difference between Sentinel-1 and ECMWF model wind speeds. Colored thin solid lines are for standard deviation.

Figure 39 shows the monthly performances with respect to time in 2016 for WV1 resp. WV2. Top panel presents the bias and the standard deviation for the wind speed. Bottom panel presents the number of acquisitions and bottom panel the mean and median wind speed from ECMWF model. The bias is computed by comparing the wind speed from Sentinel-1 and the wind speed from ECMWF analysis (3 hours and 0.125 degrees). An example for December 2016 is shown on Figure 40

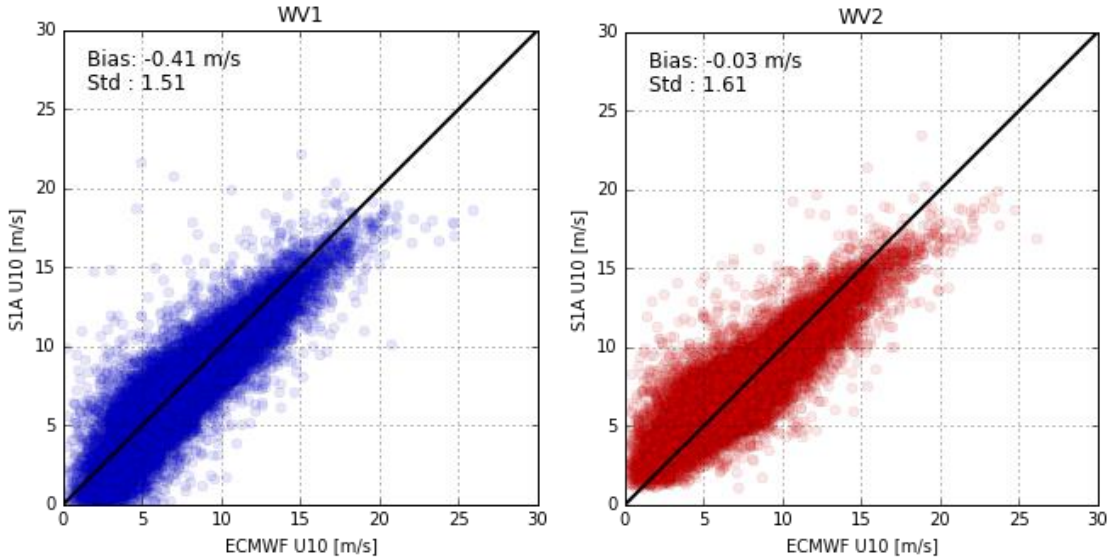

Figure 40 scatter plot of wind speed from S-1A WV1 versus ECMWF Dec 2016 (left WV1 and right WV2).

The model outputs are considered as reference here. This is only valid from a statistical point of view. Figure 39 shows a significant change in the wind speed bias after May 2016. This corresponds to a change in the processing gain coefficients. We observe that after May 2016 bias remain lower than -0.5 m/s and 0.1 m/s, respectively for WV1 and WV2. Standard deviation values are lower than 1.6 m/s and 1.7 m/s, respectively for WV1 and WV2. These results are within the specifications. The standard deviation of wind speed remains constant whereas a slight trend is observed for the bias decreasing from -0.1m/s in June to 0.41 m/s in December 2016 for WV1.

Coming improvements for 2017:

- The observed trend in the bias will be further monitored to check if this is a drift in the performances due to L1 quality issue or a seasonal variation. An explanation will be proposed.

- Massive acquisitions are foreseen in HH polarisation to assess the wind product component performances in this configuration.

4.3.2. Swell Measurement

4.3.2.1. Wave Mode

2016 is the first complete year with a nominal use of the wave mode for Sentinel-1 A. Following the acquisition plan, wave mode has always been activated at global scale over the oceans (excepted for June), producing a comprehensive and constant number (~25000 for WV1 and ~25000 for WV2 each month) acquisitions every cycle. This enables to investigate the stability of the Level-2 products

performances with respect to time (e.g. seasonal variations) for the first time. In 2016, only acquisitions in VV polarisation have been done. Results are strictly based on VV in this report.

For wave parameters of the level-2 products as measured by Sentinel-1 A, the major changes are:

- Stabilization of processing parameters for cross- and co-spectra computation. This mostly impacts performances on swell energy of the ocean swell spectrum (oswPolSpec) and the significant wave height for each partition (oswHs).

- Update of the processing gains coefficients. This mostly impacts performances on ocean surface wind speed (oswWindSpeed) but also the estimate of the non-linear part of the cross-spectrum. As shown on Figure 41.

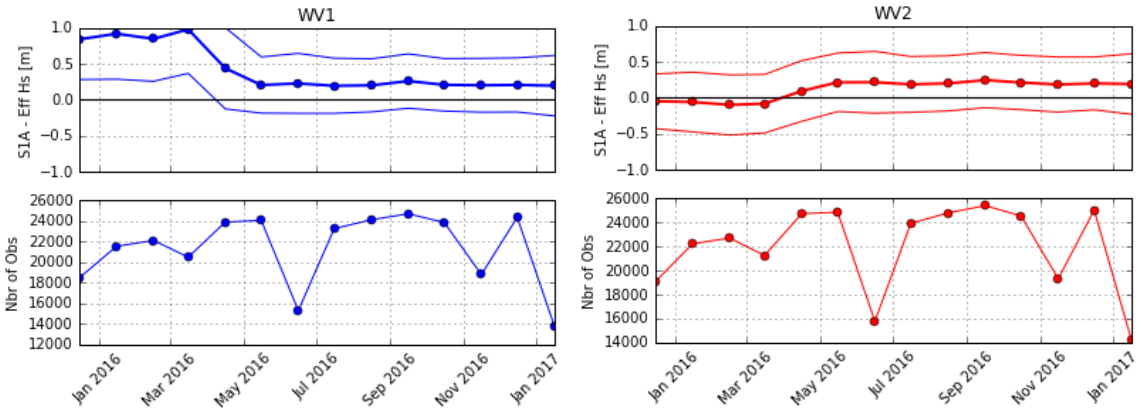

Figure 41 S-1A WV1 and WV2 Ocean Swell monthly performances as function of time.

For top panels, colored thick solid lines stand for the mean difference between effective significant wave height from Sentinel-1 and from WW3 model. Colored thin solid lines are for standard deviation.

Figure 41, the number of acquisitions is significantly lower in June comparing to other months. Indeed, in June Sentinel-1A suffered from a severe issue with the transmit power supplier on antenna tile 11. Operations were stopped between the 16th and the 27th of June 2016.

The waves performances are estimated by comparison between the significant wave height of the long waves as measured by Sentinel-1 and produced by Wave Watch 3 model (WW3). WW3 is used to produce a 2D ocean wave spectra for each Sentinel-1 acquisition. On a statistical basis and over open ocean, WW3 is used as the reference. For both S-1A and WW3, the significant wave height of the long waves is estimated by integration of the 2D ocean wave spectra up to the cut-off values (above this value, the inversion is not expected to work). Figure 42 shows an example of comparison between Sentinel-1 A and WW3, respectively for WV1 and WV2.

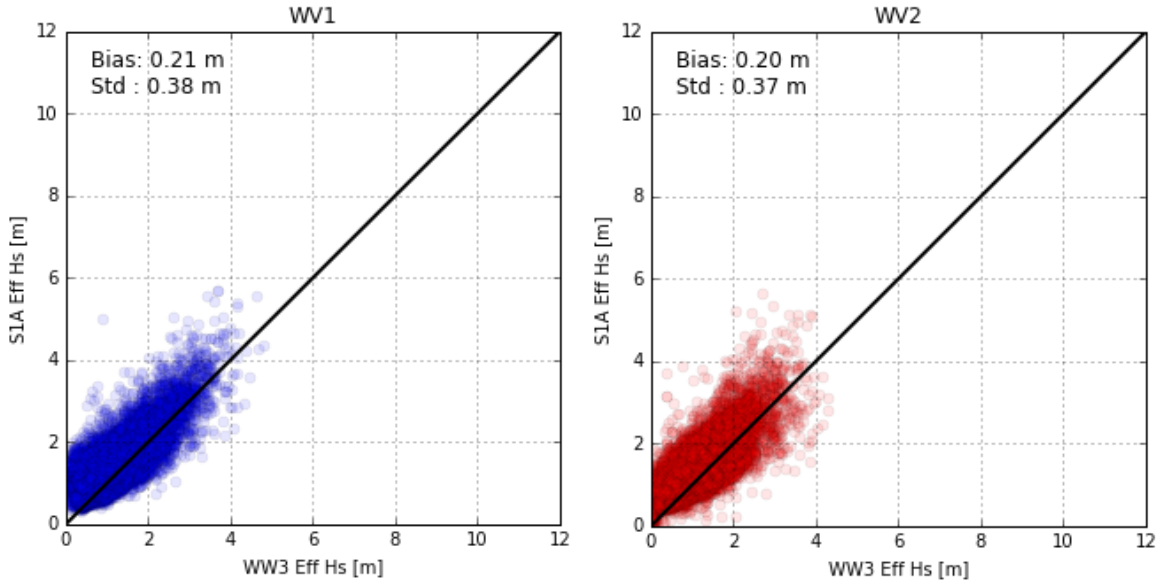

Figure 42 scatter plot of effective significant wave height from S-1A WV1 versus WW3 significant wave height Dec 2016. The model outputs are considered as reference here. This is only valid from a statistical point of view

Figure 41 shows a significant change in the effective significant wave height bias after May 2016. This corresponds to the stabilization of processing parameters for cross- and co-spectra computation. We observe that after May 2016 bias remains lower than 0.25 m for WV1 both WV2. Standard deviation values are lower than 0.5 m for both WV1 and WV2. These results are within the specifications. The standard deviation of the effective significant wave height remains constant whereas a slight change is observed for the bias in September 2016.

Coming improvements for 2017:

- The observed changes in September 2016 will be further investigated.
- Massive acquisitions are foreseen in HH polarisation to assess the wave product component performances in this configuration.
- In some cases the quality of the ocean swell spectrum is degraded. In particular
    - Azimuth cut-off is a key parameter for the wave inversion. The quality of its estimate will be investigated.
    - Heterogeneity in the SAR scene may impact the swell retrieval.
- We will propose a quality flag combining both heterogeneity and azimuth cut-off parameters (other may be added) to filter out cases where ocean swell measurement is not optimal.

4.3.3. Radial Velocity Measurement

4.3.3.1. Wave Mode

The radial velocity measurement is derived from the Geophysical Doppler anomaly. In the S-1 IPF, this geophysical Doppler is estimated by:

$$F_{dc_{RVL}} = F_{dc_{SAR}} - F_{dc_{attitude}} - F_{dc_{antenna}}$$

where:

- FdcSAR is estimated from the SAR data
- FdcOcean is the component related to the ocean radial velocities.
- FdcAttitude is estimated from the geometry knowledge (quaternion based)
- Fdcantenna is the antenna contribution related to TRM drifts, failures, misalignements, etc

At global scale, the expected relationship between the geophysical Doppler and the sea state (or ocean surface wind vector) is well known since Envisat/ASAR. The performances of the geophysical Doppler are assessed by estimating the bias between the expected Doppler given the sea state conditions (provided by ECMWF) and the geophysical Doppler as included in the Level 2 products.

Statement of the ocean surface radial velocities measurements accuracy:

Figure 43 show the geophysical Doppler as included in the Level 2 products as a function of radial wind speed (wind speed projected in the line of sight of the radar). The colour code indicates the latitude. As observed, the Doppler and the radial wind speed are strongly correlated for both WV1 and WV2. However, the colour code indicates a clear and non-geophysical dependence to the latitude. In addition, Doppler is not 0 Hz (as it should be) when radial wind speed is 0 m/s for WV1 and WV2. This shows that the geophysical Doppler shift deduced from the Level-2 products using the different Doppler components included in the Level-2 products is not only related to ocean surface radial velocities. This prevents us for getting any quantitative geophysical signature such as ocean surface currents in the product. It also illustrates the issue regarding the low precision on the attitude of the platform along its orbit and its consequence on the scattered relationship between Geophysical Doppler Centroid versus Radial wind-speed. There is no particular difference between WV1 and WV2.

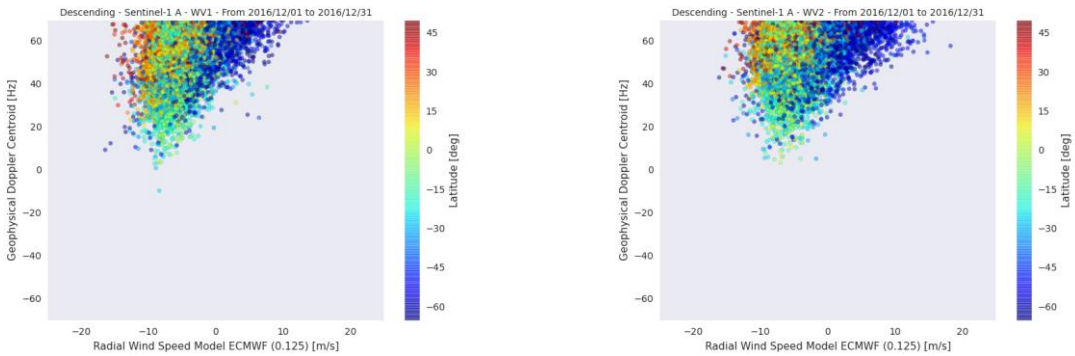

(WV1) (WV2)

Figure 43 Geophysical Doppler as included in the Level 2 products as a function of radial wind speed (wind speed projected in the line of sight of the radar) for WV1 and WV2. The colour code indicates the latitude.

Improvement performed during 2016: None

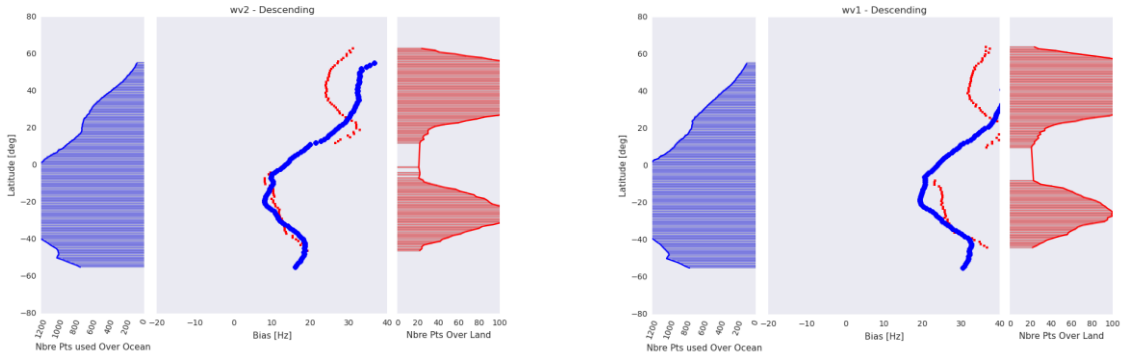

(WV1) (WV2)

Figure 44 WV1 Doppler bias as a function of latitude estimated over ocean (blue) and land (red).

The differences (around 10Hz) observed in the land Doppler between wv1 and wv2 can be well predicted by the recent antenna model as shown in Figure 44.

Coming improvement for 2017:

We recommend that the method implemented by ESTEC (and Norut) regarding the correction of low attitude sensitivity for RVL processing to be used in production to improve the quality of the products.

4.3.3.2. TOPS Mode

Statement of the ocean surface radial velocities measurements accuracy:

As for Wave Mode, the contamination of the geophysical Doppler by the geometry knowledge (quaternion based) and the antenna contribution prevents us for getting any quantitative geophysical signature such as ocean surface currents in the product. Nevertheless, in cases where land areas are present in the image an ad-hoc calibration has been performed, and the results shown are promising (see Figure 45). A limited number of S-1A IW and EW data from Agulhas were recalibrated using this approach followed by converting the radial velocity to surface current using CDOP, and validated against surface drifters. Results are shown in Figure 45 c.

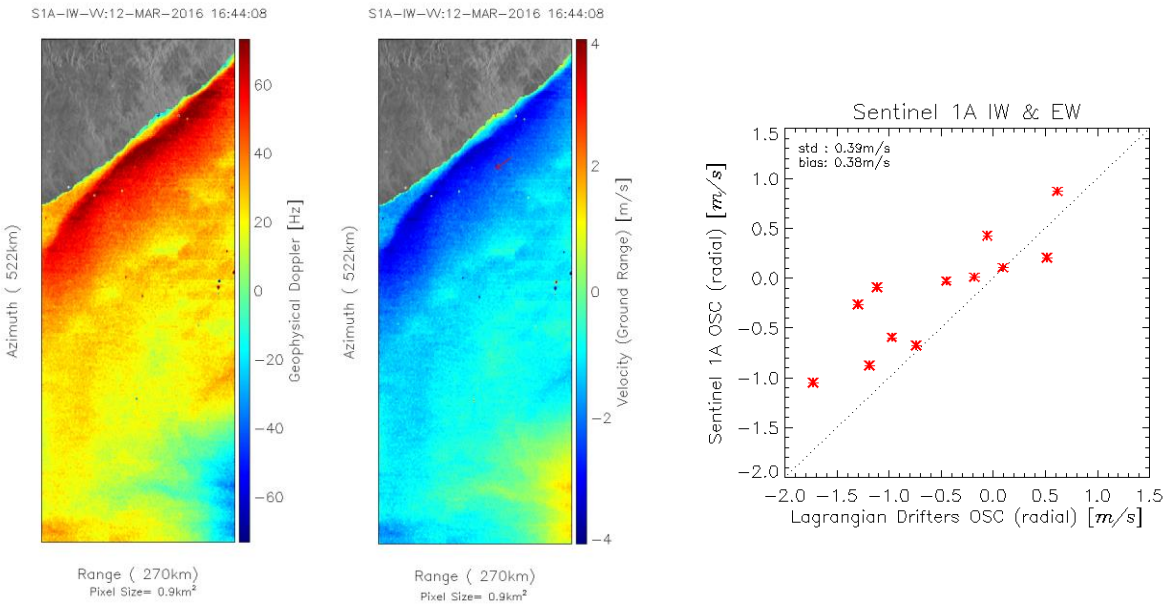

a) b) c)

Figure 45: a) Doppler anomaly and b) radial velocity field from Sentinel 1A IW RVL product acquired over Agulhas in ascending mode. Here land areas are used to calibrate the Doppler anomaly before computing the radial velocity. C) Scatterplot of radial surface current component derived from S-1A data and surface drifters acquired over Agulhas.

Improvement performed during 2016:

Efforts are undertaken to better predict and compensate the measured Doppler for the electromagnetic (EM) Doppler bias introduced by the skewness of the antenna elevation pattern. A new version of the antenna model parameters has been ingested into the Level 2 processor and the EM Doppler bias over IW and EW swaths are compared with the data driven Doppler estimated over rain forest areas (see Figure 46).

Although the relative trends over swaths are predicted well, a significant Doppler bias is observed between the model and data. Compared to previous results, the model and data are better aligned and the jumps between swaths are better predicted. Still we see that VV-polarisation performance better than HH – polarisation.

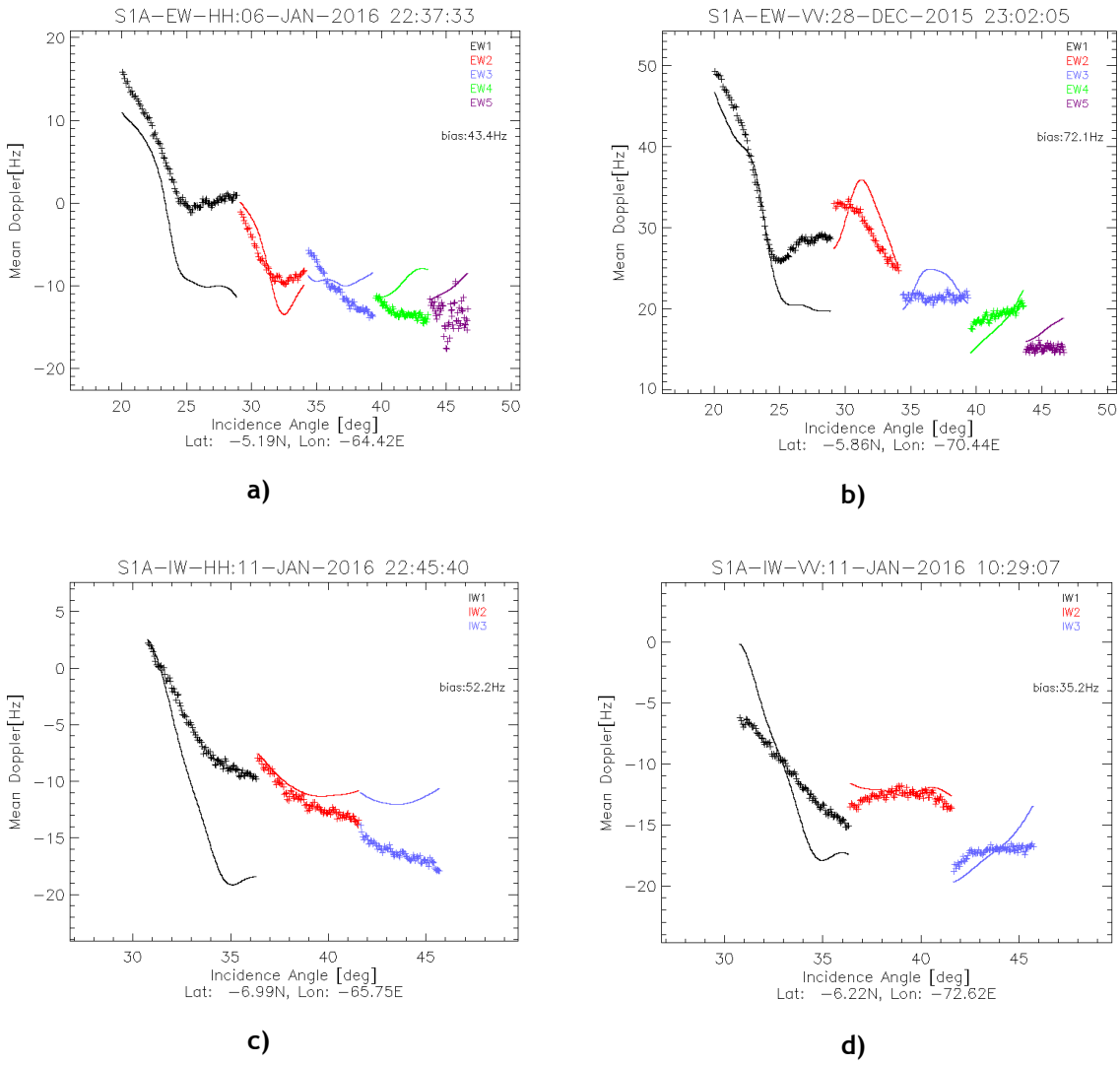

Figure 46: S-1A EM DC offset computed from antenna model (full line) with error matrix corresponding to the day of acquisition, and estimated from rain forest data using the Level 2 processor (***). A) EW mode in HH-polarisation, B) EW mode in VV-polarisation, C) IW mode in HH-polarisation, D) IW mode in VV-polarisation

Coming Improvements for 2017:

A further refinement of the de-scalloping will be investigated without increasing the processing time.

4.3.4. Geophysical Calibration

4.3.4.1. Wave Mode

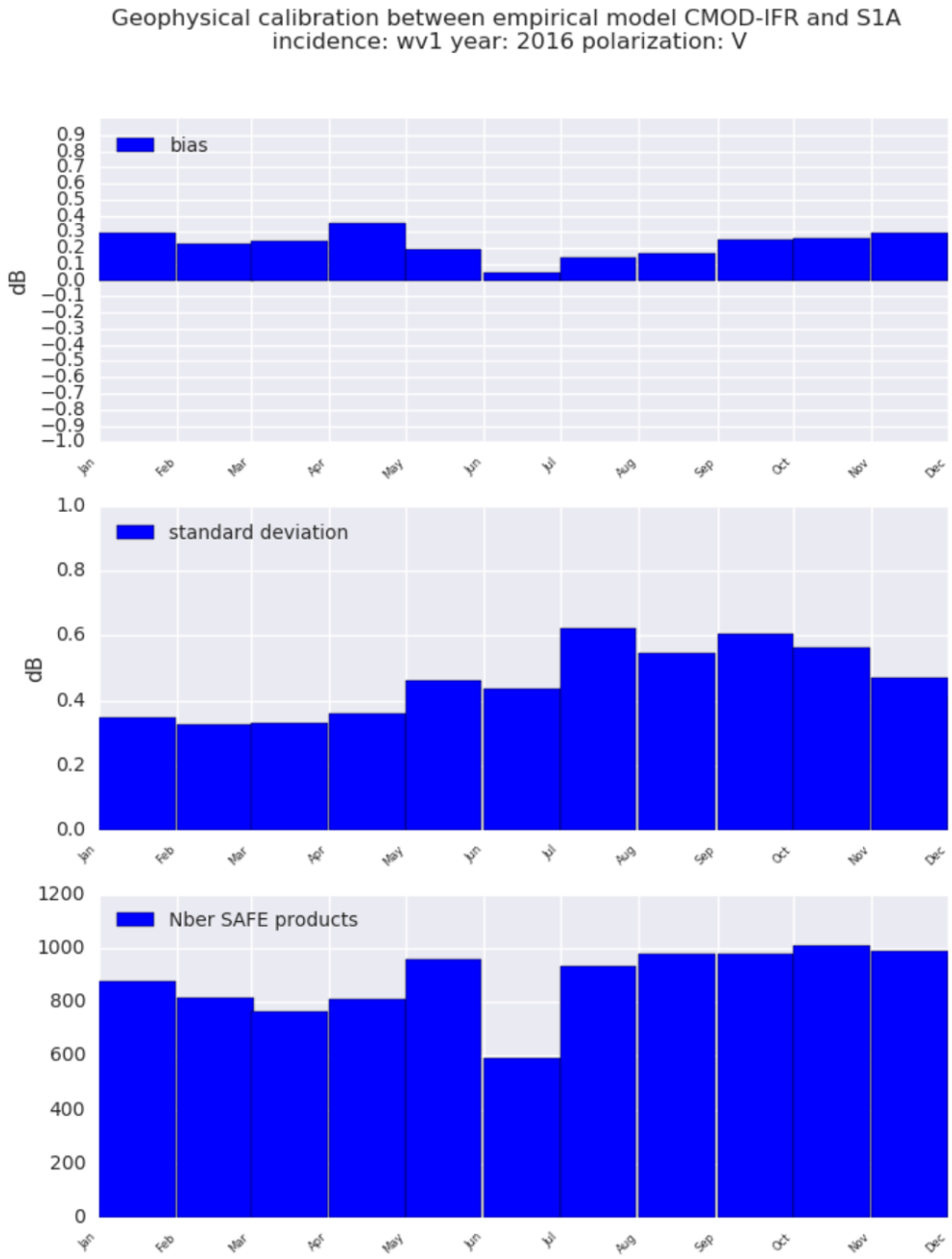

Figure 47 Sentinel-A geophysical calibration constant given by CMOD-IFRv2 for WV1 VV polarisation between 50° and -50° latitude. Panel 1 shows the mean bias between ECMWF and

Sentinel-1A. Panel 2 shows the bias standard deviation. Panel 3 shows the number of SAFE used to perform the analysis.

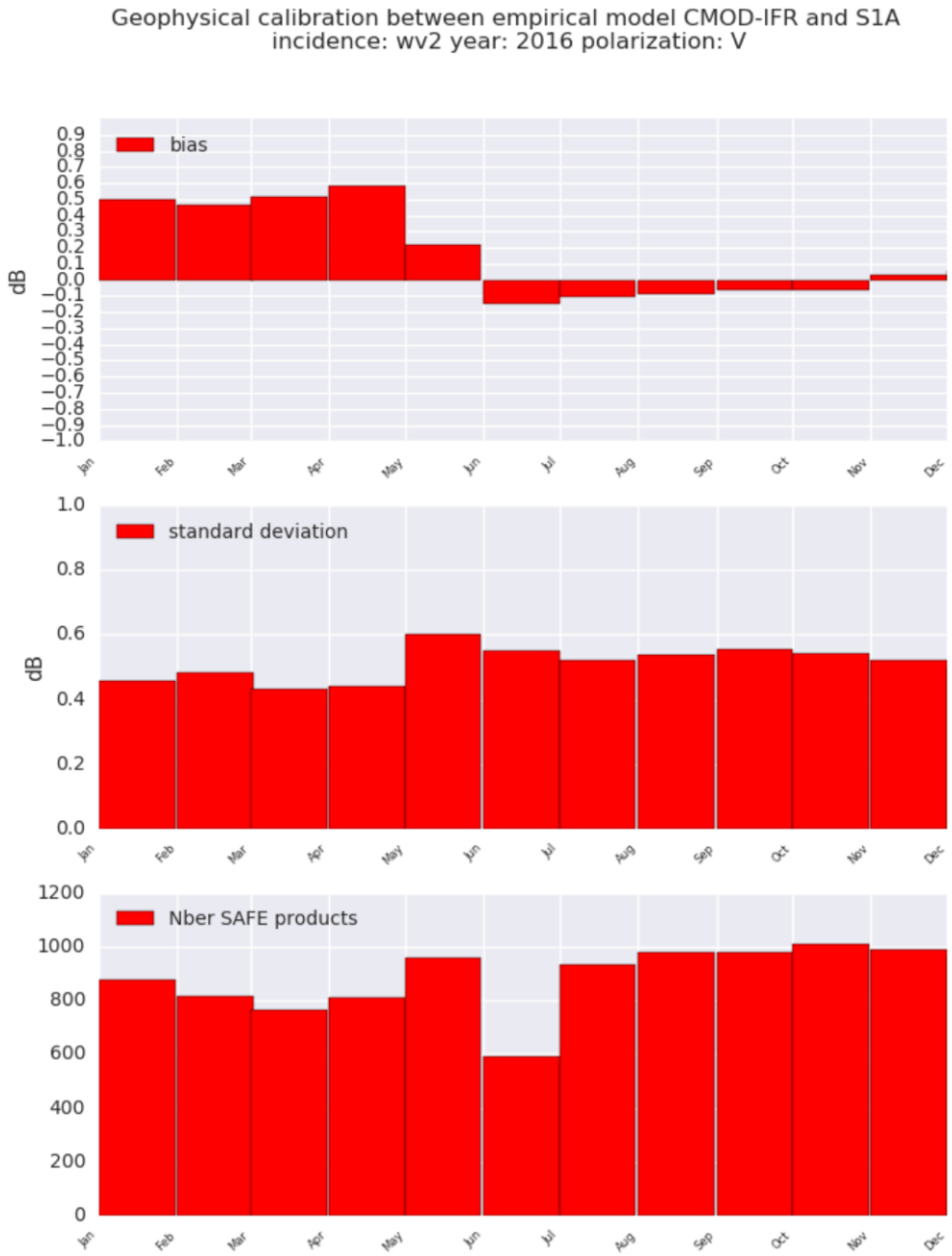

Figure 48 Sentinel-A geophysical calibration constant given by CMOD-IFRv2 for WV2 VV polarisation between 50° and -50° latitude. Panel 1 shows the mean bias between ECMWF and Sentinel-1A. Panel 2 shows the bias standard deviation. Panel 3 shows the number of SAFE used to perform the analysis.

As shown in Figure 47 and Figure 48 after the processing configuration change occurred in May, the Sentinel-1A geophysical calibration for WV1 seems to drift about 0.05dB/month on the last 6 months of 2016. On the other hand WV2 does not show any drift (bias near 0dB after May). The standard deviation increases of about 0.2 dB for WV1 and 0.1dB for WV2 during July-August-October-November.

This increase is not explained (hypothesis of ice contamination discard with sub-setting dataset between -50° and +50° latitude) and will be addressed in 2017.

5. S-1B Instrument Status

Here the status of the S-1B instrument since the start of the routine phase in September 2016:

5.1. S-1B Antenna Status

The Antenna status is routinely monitored using the dedicated RFC calibration mode. The RFC products are processed in order to generate the Antenna Error Matrix from which it is possible to retrieve the failure and drift of each TRM.

The Figure below shows the antenna Transmit/Receive Module (TRM) status at the end of 2016. Six (6) failures are counted in total among TX-RX and H-V. All the failed TRMs are connected to a single EFE, which probably failed during the S-1B launch. A full list of all TRM failures during 2016 is given in Appendix K -.

The impact of the failures on the antenna patterns shape is modelled by the antenna model and the data products are compensated accordingly within the level-1 processor.

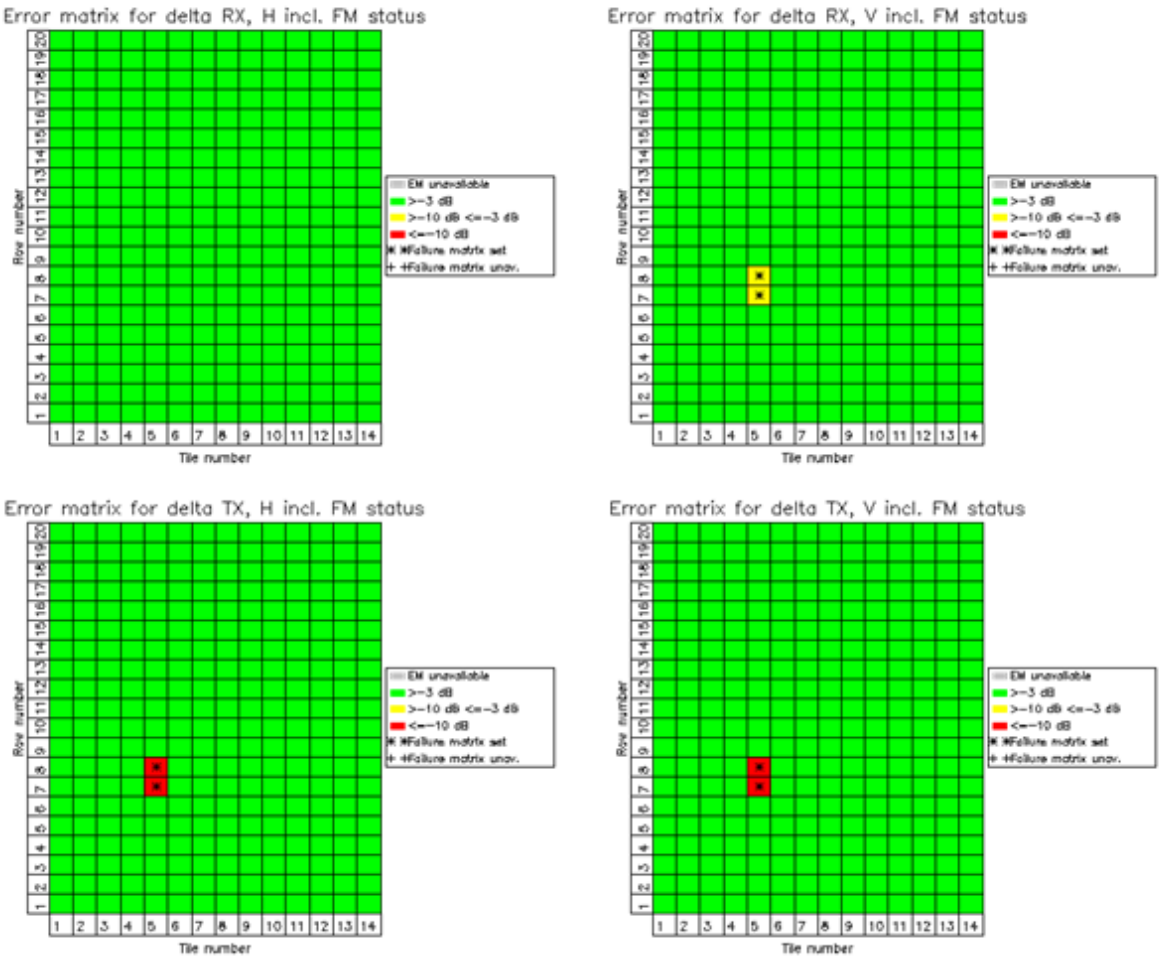

Figure 49 S-1B antenna status on 31/12/2016. The top charts refer to RX elements and the bottom charts refer to TX elements

The following figures show the TX and RX excitation coefficients (averaged per tile) stability since the beginning of the S-1B Commissioning Phase (CP) on 14th June 2016. Note that, during the CP, many RFC products per day were available to assess instrument stability. The overall antenna behaviour is very stable.

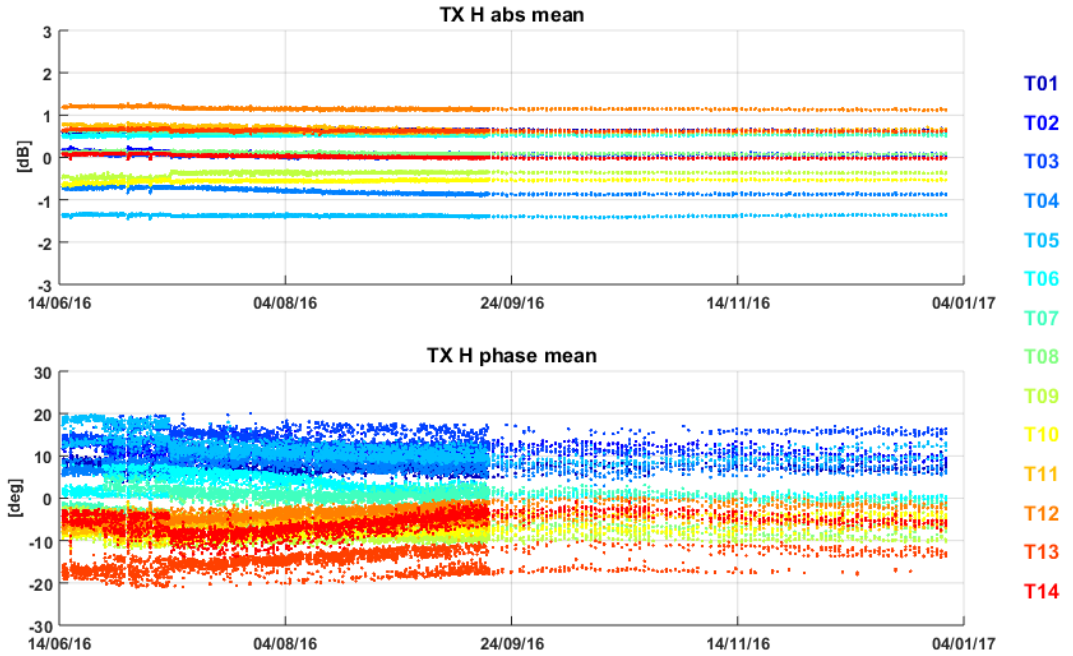

Figure 50 Gain (*top)* and phase (*bottom)* stability of the SAR antenna tiles (average of the RFC coefficients in TX H over rows).

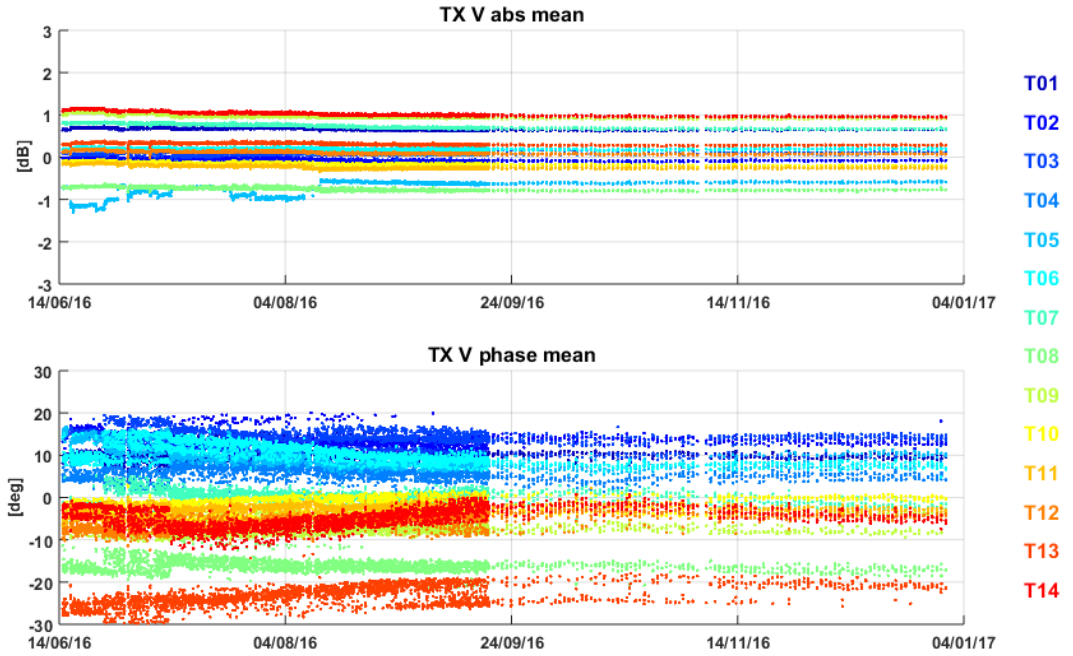

Figure 51 Gain (top) and phase (bottom) stability of the SAR antenna tiles (average of the RFC coefficients in TX V over rows).

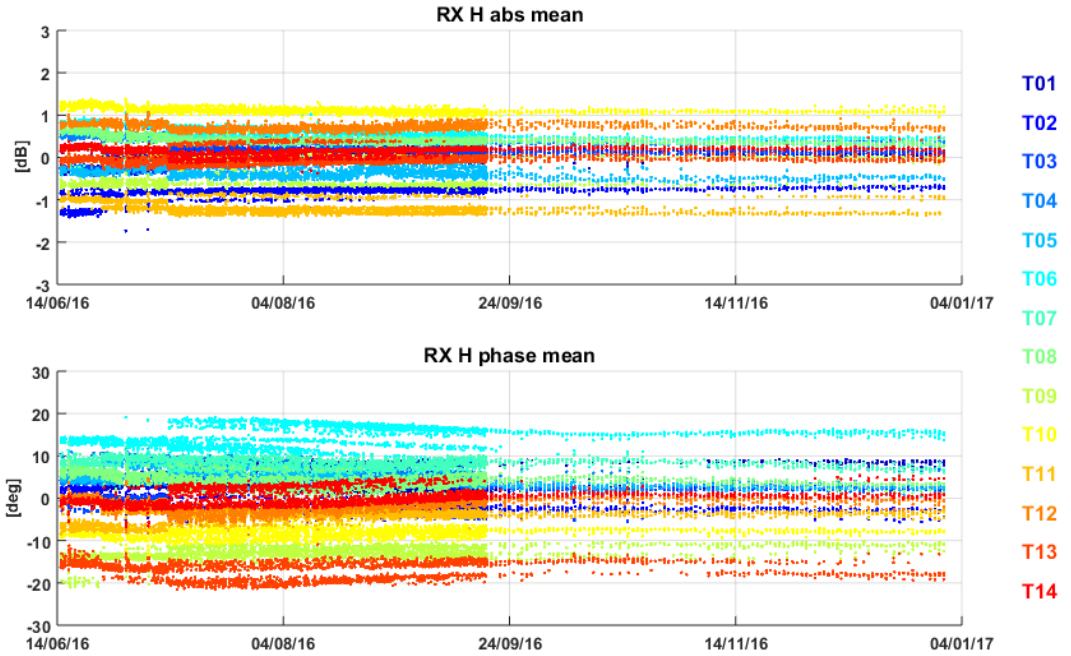

Figure 52 Gain (top) and phase (bottom) stability of the SAR antenna tiles (average of the RFC coefficients in RX H over rows).

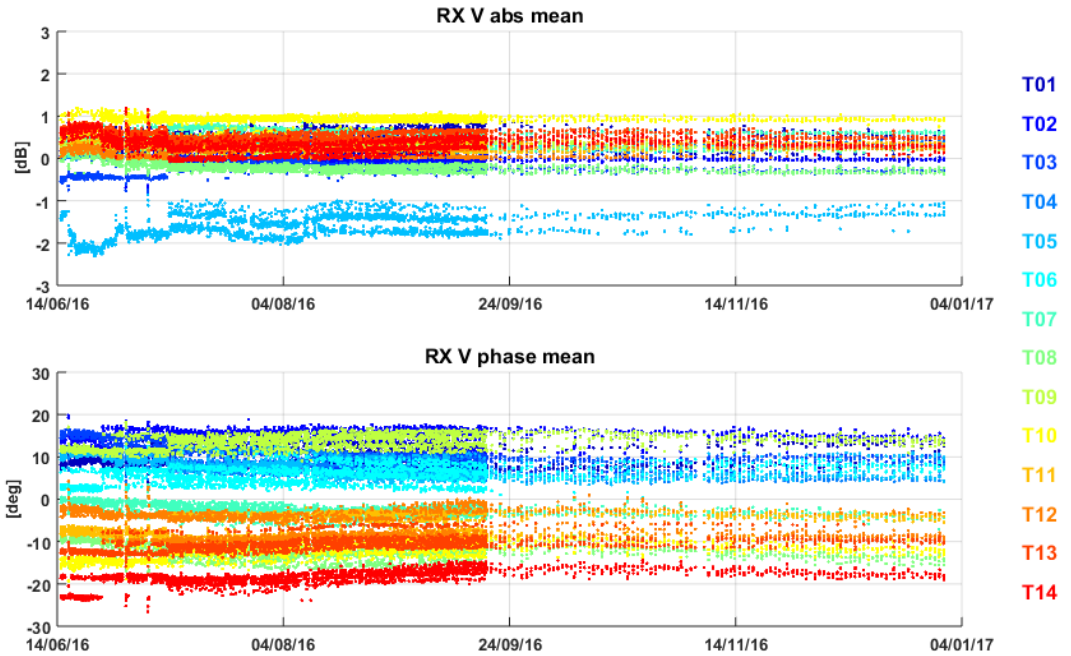

Figure 53 Gain (top) and phase (bottom) stability of the SAR antenna tiles (average of the RFC coefficients in RX V over rows).

5.2. S-1B Instrument Unavailability

A list of S-1B instrument unavailabilities since the start of the routine phase in September 2016 is given in Appendix L -.

5.3. S-1B Auxiliary Date File Updates

A list of S-1B Auxiliary Data Files (ADFs) updates since the start of the routine phase in September 2016 is given in Appendix M -.

5.4. S-1B Radar Data Base Updates

A summary of S-1B Radar Data Base (RDB) updates is provided in the following Table.

RDB ID	Date of endorsement	Update reason
RDB #1		Launch version

Table 18 Radar Data Base Changes History.

5.5. S-1B Orbit Manoeuvres

A list of all S-1B orbit manoeuvres since the start of the routine phase in September 2016 is given in Appendix N -.

5.6. S-1B Burst synchronization

The burst synchronization between repeat pass interferometric acquisitions is relevant for the TOPSAR modes (IW and EW) to provide an indication of the quality of the interferometric phase that can be expected. The SAR acquisition start time is planned over a discrete set of points round orbit with precision down to milliseconds. The performance of the synchronization is monitored by the PDGS OBS tool.

Figure 54 shows the burst synchronization over time for IW and EW mode. Each dot represents a repeat pass acquisition, considering as reference the first cycle after the end of the CP (number 19, 18-30 September 2016). Note that, as for S-1A, there seems to be a small burst synchronization reduction during November and December, probably due to some slow orbital aberration.

Figure 55 shows the burst synchronization distribution for IW and EW separately. It can be noticed that the synchronization is above 99% for most of the acquisitions.

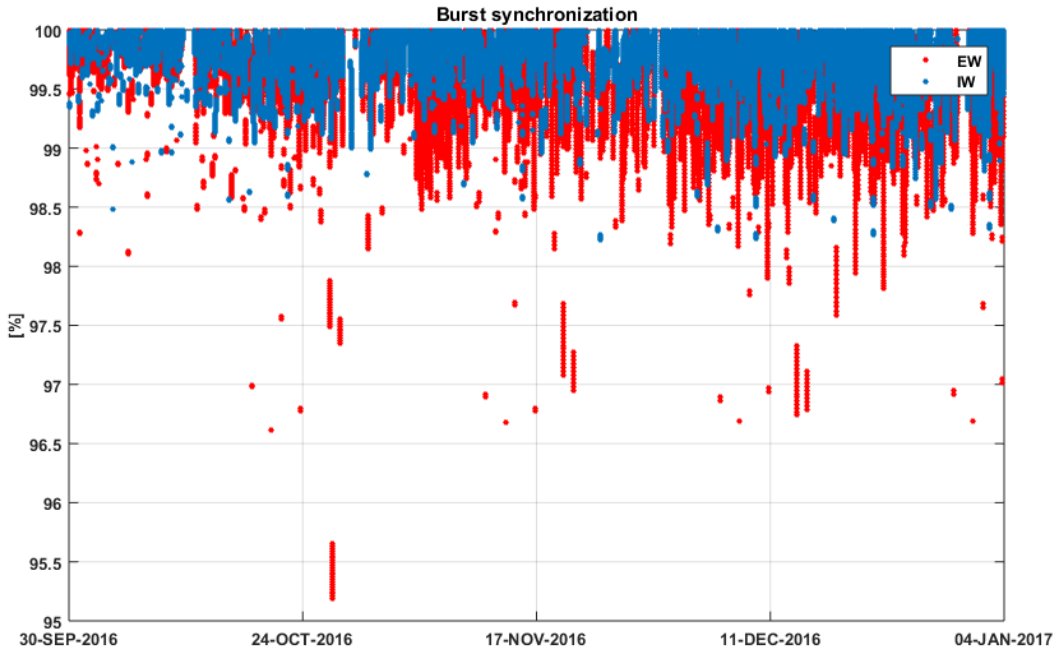

Figure 54 S-1B burst synchronization since the end of the Commissioning Phase.

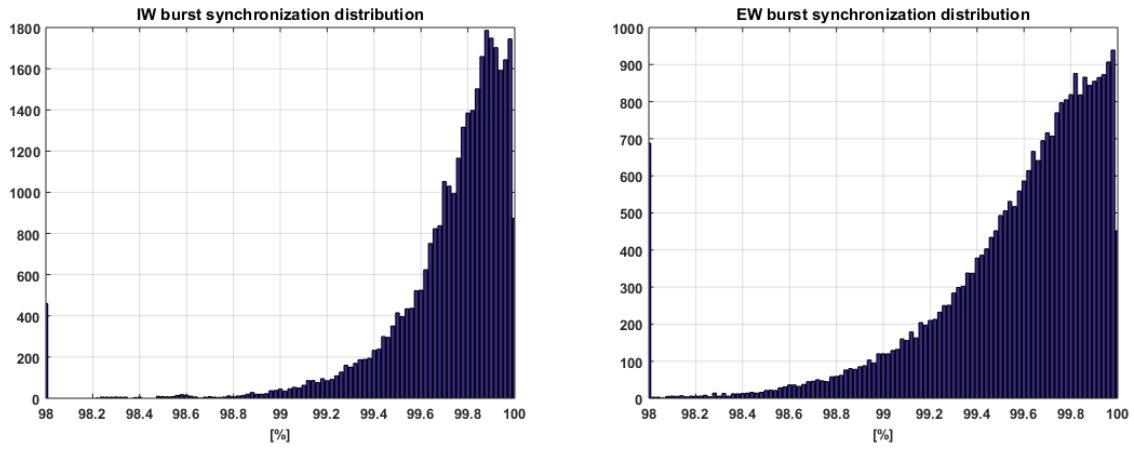

Figure 55 Burst synchronization statistics for IW (left) and EW (right).

5.7. S-1B Internal Calibration

5.7.1. PG monitoring

The instrument stability over time is monitored through the internal calibration signals. The following plots show the main parameters monitored: PG gain and phase, instrument delay and Rx gain offset. In Figure 56 the colour represents the sub-swath whereas in Figure 57 the colour represents the polarisation.

All the monitored parameters are quite stable in the reporting period. Figure 58 and Figure 59 show in detail the PG gain evolution for EW DH and IW DV acquisitions. No particular trends can be identified during the reporting period even if some long slow fluctuations can be observed in particular for RX H beams (EW HH and IW VH). Such fluctuations are in any case quite small with a peak to peak variation around 0.1 dB.

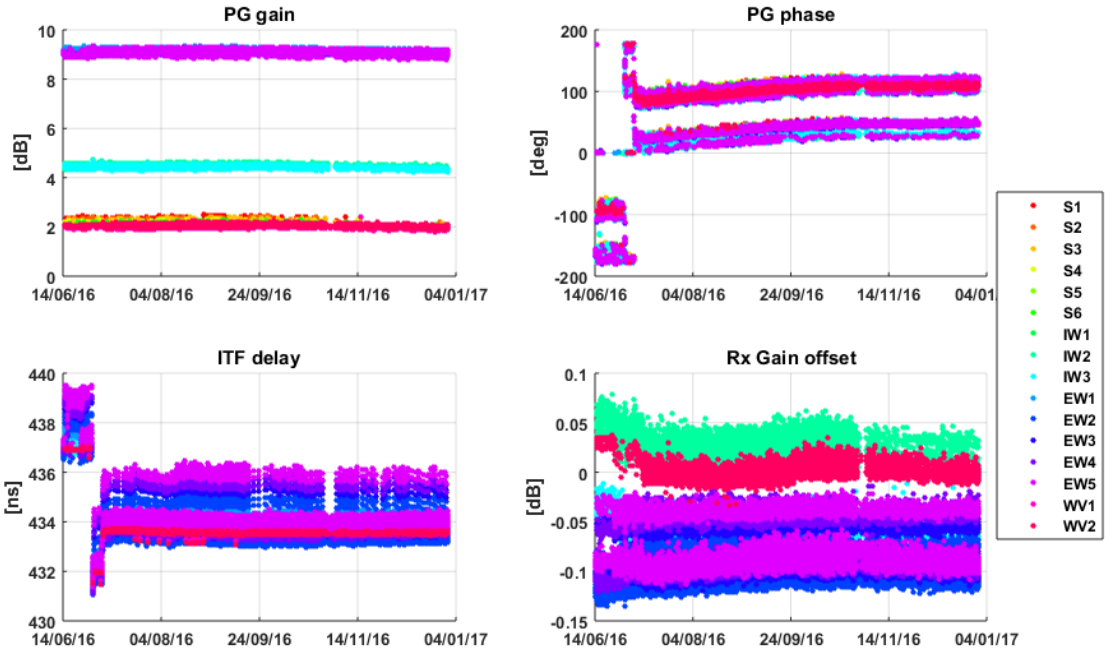

Figure 56 Internal calibration parameters over time. The colour represents the sub-swath.

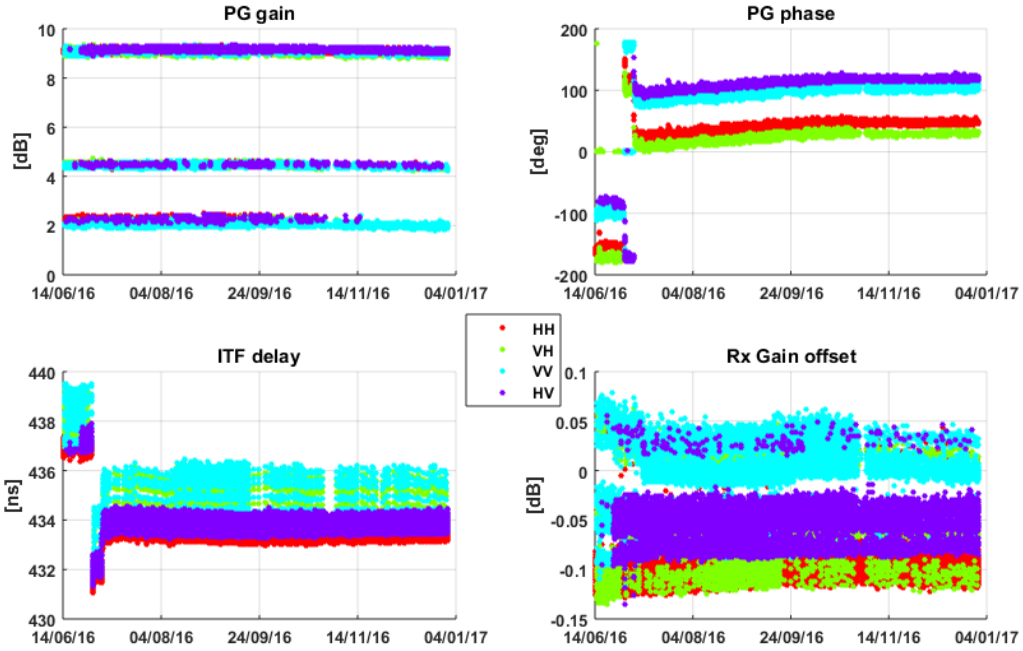

Figure 57 Internal calibration parameters over time. The colour represents the polarisation.

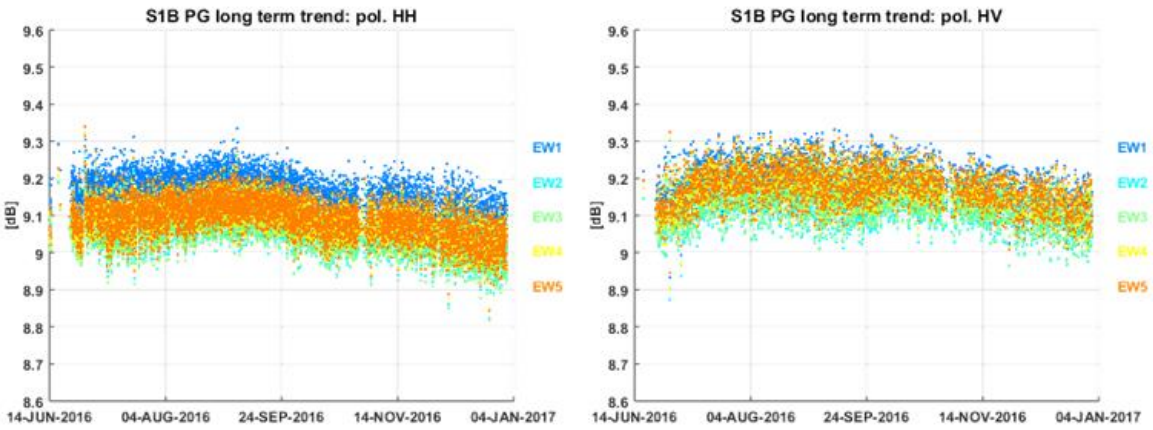

Figure 58 EW HH (left) and HV (right) PG gain divided by sub-swath.

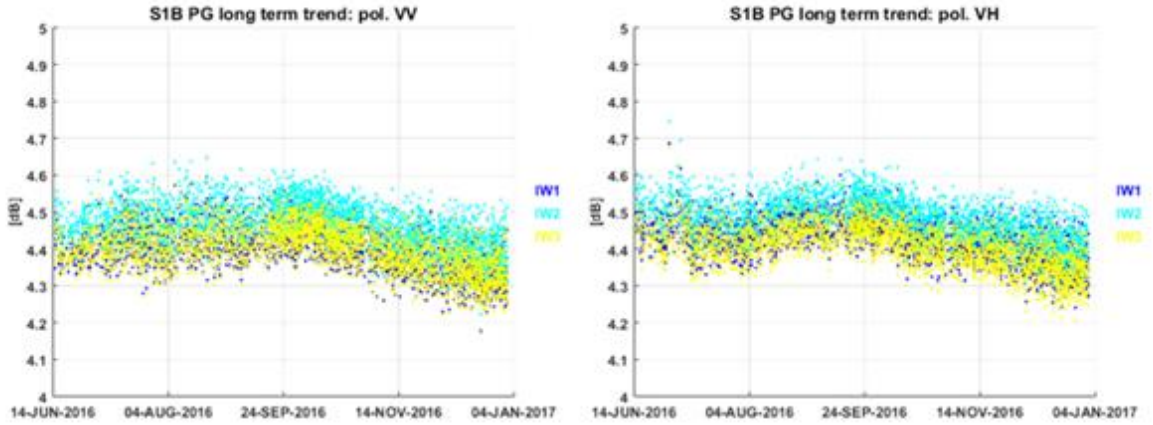

Figure 59 IW VV (left) and VH (right) PG gain divided by sub-swath.

5.7.2. Noise power monitoring

The noise power is monitored through the dedicated internal calibration pulses processing embedded at the start/stop of each data-take. Figure below shows the noise power versus time since the beginning of the Commissioning Phase. Overall, the noise power has a good stability, with a standard deviation of approximately 1 dB in the short term. Table below reports the noise power stability (3σ) averaged over the full reporting period. The number in the parenthesis represents the number of products considered. Note that the considerations on the noise bi-modality, reported in Section 3.7.2, are applicable for S-1B as well.

Acquisition mode	Noise power stability [dB]
SM	HH: 6.2±1.2 (1011) VV: 6.0±1.0 (1105) HV: 6.2±1.0 (684) VH: 6.0±1.3 (763)
IW	HH: 7.7±1.3 (3363) VV: 8.0±1.3 (24207)

	HV: 7.8±1.2 (1263) VH: 7.9±1.6 (20643)
EW	HH: 6.4±1.1 (64892) VV: 6.4±1.1 (5950) HV: 6.5±1.0 (30645) VH: 6.4±1.4 (5030)
WV	HH: 7.3±1.4 (72) VV: 7.0±0.7 (25670)

Table 19 Noise power stability (3-sigma): period JUN 2016 – DEC 2016

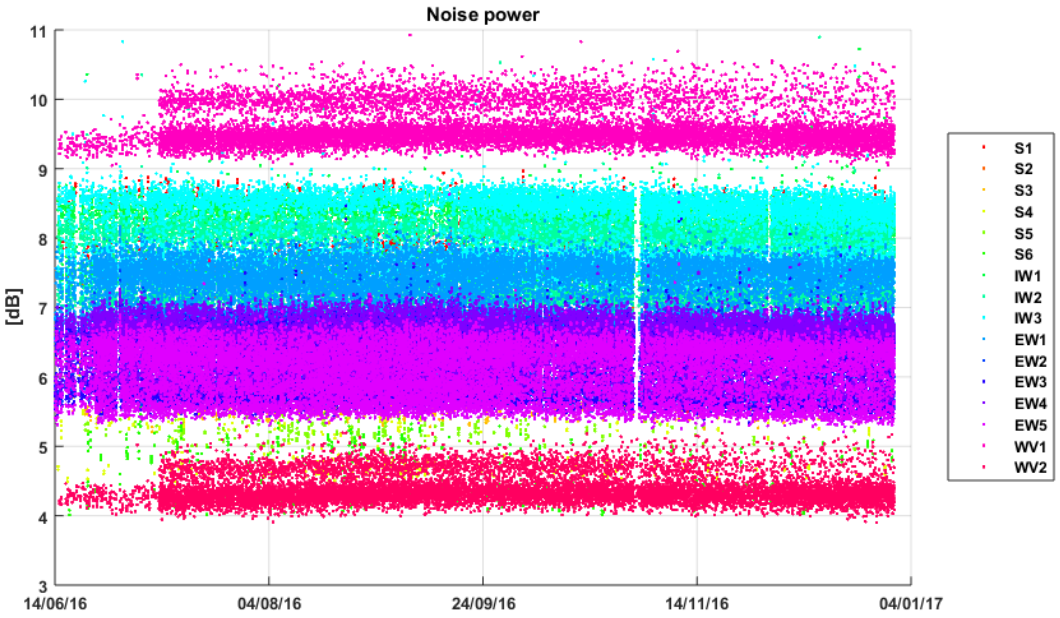

Figure 60 Noise power versus time. The colour represents the different beams.

6. S-1B Products Status

6.1. S-1B Level 0 Products

6.1.1. Timeline and missing lines

The L0 quality monitoring is carried out as a routine task within the QCSS. The checks on the timeline and missing lines have not detected significant problems.

6.1.2. I/Q statistics

The analysis of I/Q bias and standard deviation allow to state that the L0 data quality is nominal. Figure 61 shows the channel imbalance analysis for IW, showing the standard deviation that the two channels are very well aligned along the bisector of the I/Q plane.

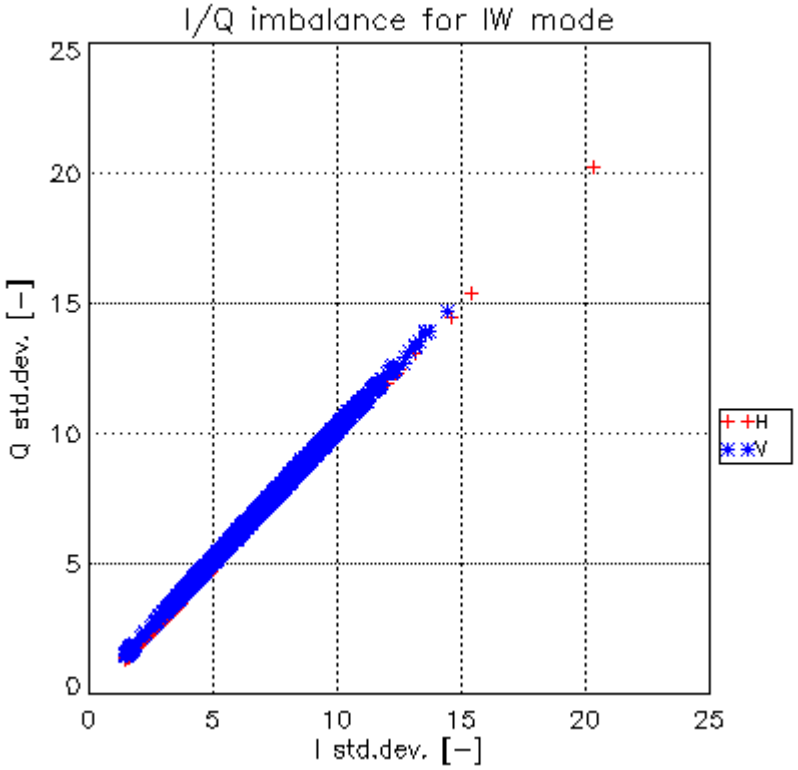

Figure 61 I/Q channel imbalance.

6.1.3. FDBAQ

The FDBAQ quantization scheme performs nominally. A detailed analysis of the FDBAQ behaviour for the first year can be found in [S1-RD-10].

The long-term statistics over the acquired data is shown by the average Mbit/s as reported in the following table. The values cover the period from the 1st September 2016 to the end of the year. Note that the average bitrate for all acquisition modes is well below the downlink limit of 260Mbit/sec. Only S1 acquisitions (about 0.6% of S-1B total acquisitions in the monitored period) average data rate is higher than the downlink limit. This is expected since S1 beam is the most demanding in terms of azimuth and range data sampling. The S-1B bitrate is in line with the S-1A bitrate, reported in Table 2.

Acquisition mode/swath	Average bitrate [Mbit/s]
S1	290.3
S2	207.3
S3	222.5
S4	177.9
S5	N/A
S6	171.1
IW	196.7
EW	60.6
WV1	19.0

Table 20 Average bitrate for each acquisition mode.

6.1.4. Instrument Pointing

The instrument pointing in elevation has been calibrated during the commissioning phase exploiting the availability of the elevation notch acquisitions over the Amazonian rain forest. The results of estimated roll mis-pointing are reported in the following table, referring only to the EN acquired before STT alignment on 28th July.

DT ID	Date	Duration [s]	Pol.	Ref. orbit	Slice	Sensor Altitude [km]	Average topography [m]	Roll ann. [deg]	Roll ANX [deg]	Roll alt. [deg]	Co-pol [mdeg]	Cross-pol [mdeg]
39B	14th June	120	DH	N	1	701.24	214.3	30.0587	30.0581	30.0420	μ: -28.7 σ: 45.5	μ: -10.7 σ: 27.1
					2	700.79	202.0	30.0844	30.0836	30.0675	**μ: -33.9 σ: 9.1**	**μ: -27.7 σ: 7.9**
					3	700.36	172.9	30.1086	30.1078	30.0918	**μ: -28.9 σ: 7.7**	**μ: -25.8 σ: 7.1**
42B	16th June	45	DH	Y	1	700.05	80.6	30.1202	30.1199	30.1092	μ: -26.7 σ: 24.5	μ: -20.1 σ: 18.6
53F	19th June	120	DH	Y	1	701.13	294.5	30.0590	30.0583	30.0482	μ: -24.5 σ: 12.0	μ: -17.2 σ: 13.5
					3	700.25	203.3	30.1082	30.1075	30.0976	**μ: -29.5 σ: 8.9**	**μ: -30.4 σ: 6.9**
5D5	21th June	120	DV	Y	1	701.15	172.6	30.0579	30.0577	30.0469	μ: -18.0 σ: 28.1	μ: -35.3 σ: 26.5
					2	700.71	150.8	30.0838	30.0827	30.0719	**μ: -20.0 σ: 9.3**	**μ: -23.1 σ: 7.4**
					3	700.28	130.7	30.1075	30.1070	30.0962	**μ: -25.7 σ: 6.5**	**μ: -27.1 σ: 8.3**

Table 21: Pointing results on Elevation Notch products

The analysis was repeated after STT alignment over a new set of Elevation Notch products. The obtained results are reported in the following table.

The processing of the available EN notches resulted in the following considerations:

- Before STT alignment the (weighted) average roll mispointing was around -26 mdeg. After including in the computation the expected tree height for the Rain Forest (30 m) a value around -22 mdeg is obtained.

- After STT alignment the (weighted) average roll mispointing (including tree height) is around -10 mdeg. The value was obtained considering only the available ascending acquisitions (DT 2380 discarded).
- The STT alignment led to an improvement of the roll mispointing of about 10 mdeg.
- The only available descending acquisition shows an average roll mispointing around 0 mdeg. This is compatible with the fact that the aberration correction is not performed on board. This results in an orbit oscillation with a maximum roll deviation around the Equator (EN case).

DT ID	Date	Duration [s]	Pol.	Pass	Slice	Sensor Altitude [km]	Average topography [m]	Roll ann. [deg]	Roll ANX [deg]	Roll alt. [deg]	Co-pol [mdeg]	Cross-pol [mdeg]
2283	13th August	120	DH	A	1	701.17	215.3	30.0567	30.0564	30.0459	μ: -6.7 σ: 62.3	μ: -4.6 σ: 54.2
					2	700.71	202.1	30.0828	30.0823	30.0719	μ: -4.4 σ: 17.4	μ: -22.0 σ: 19.7
					3	700.28	173.5	30.1076	30.1066	30.0963	μ: -7.8 σ: 8.5	μ: -17.1 σ: 8.9
					4	699.88	154.9	30.1292	30.1290	30.1188	μ: -11.4 σ: 12.6	μ: -17.6 σ: 12.2
2380	15th August	90	DV	D	1	699.72	148.6	30.1214	30.1255	30.1281	μ: 13.5 σ: 39.1	μ: -1.6 σ: 39.1
					2	700.11	184.8	30.0992	30.1033	30.1058	μ: 1.5 σ: 15.0	μ: -13.0 σ: 12.9
					3	700.54	235.8	30.0748	30.0794	30.0817	μ: 10.0 σ: 23.2	μ: -3.2 σ: 21.0
25D2	18th August	120	DH	A	1	701.17	302.9	30.0564	30.0556	30.458	μ: -10.4 σ: 17.5	μ: -21.3 σ: 20.1
					2	700.72	245.5	30.0819	30.0814	30.0717	μ: -5.8 σ: 19.4	μ: -23.5 σ: 19.4
					3	700.28	206.4	30.1064	30.1057	30.0961	μ: -8.6 σ: 10.4	μ: -25.3 σ: 9.3
					4	699.89	149.4	30.1284	30.1282	30.1186	μ: -12.8 σ: 10.4	μ: -19.7 σ: 9.5
26FC	20th August	120	DV	A	1	701.16	171.8	30.0576	30.0569	30.0465	μ: -29.6 σ: 35.7	μ: -32.9 σ: 40.9
					2	700.71	151.9	30.0837	30.0825	30.0721	μ: -9.4 σ: 16.1	μ: -16.3 σ: 17.4
					3	700.28	130.4	30.1070	30.1068	30.0964	μ: -17.3 σ: 25.2	μ: -30.9 σ: 23.4
					4	699.88	111.2	30.1299	30.1292	30.1189	μ: -4.3 σ: 16.8	μ: -20.8 σ: 16.9

Table 22: Pointing results on Elevation Notch products

Given the previous considerations and, the accuracy of the roll estimation method (around 10 mdeg) and the requirement on roll pointing (±10 mdeg) it was decided to not perform any roll calibration after the Commissioning Phase. The roll pointing verification will be repeated after the on board implementation of the relativistic aberration correction, with a dedicated set of EN acquisitions.

Plots of the spacecraft attitude (yaw, pitch and roll) are shown in Appendix I -.

The stability of the pointing in azimuth can be monitored through the Doppler Centroid, estimated directly from SAR data. The following figure shows the average Doppler Centroid on a data-take basis (dots) and on a daily basis (red line) versus time since the end of S-1B Commissioning Phase. The reported values are in line with expected S-1B pointing performances. The dashed vertical line represent the only star tracker configuration change occurred in the reporting period. Note that the DC jump corresponding to the star tracker configuration change is much smaller than those observed for S-1A, thanks to the star tracker calibration activities performed during S-1B Commissioning Phase.

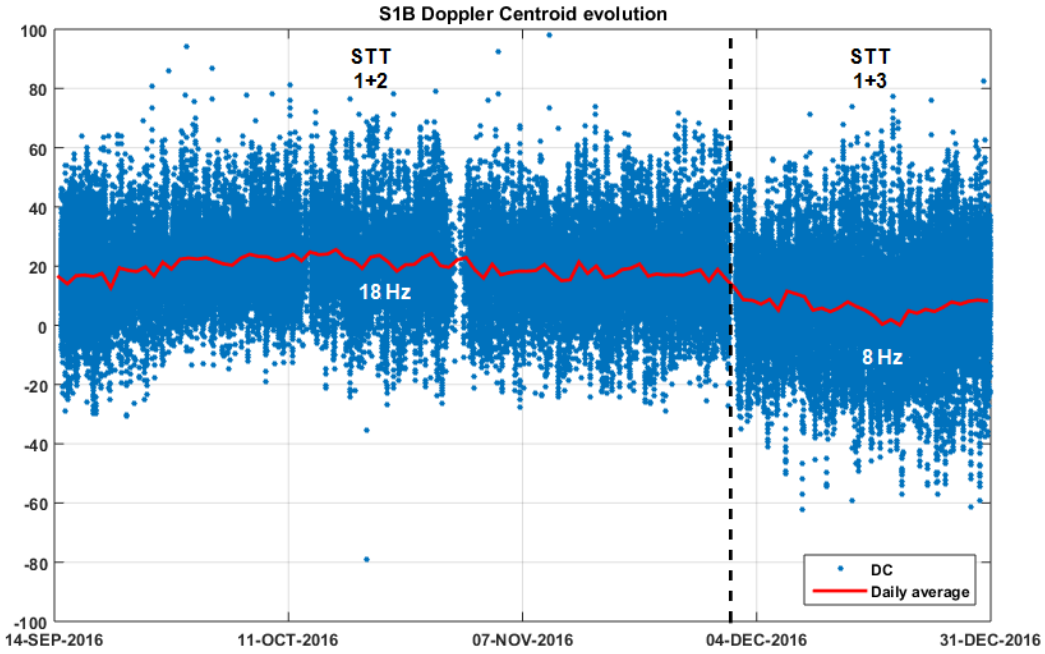

Figure 62 Doppler Centroid versus time. Average on a data-take basis (dots) and daily average (red line). The star-trackers reconfigurations events are marked by the vertical black lines.

6.2. S-1B Level 1 Products

A general summary of status of S-1B Level 1 products was presented at several conferences and workshops (see [S1-RD-03], [S1-RD-05] and [S1-RD-07]).

6.2.1. Level 1 Processor Updates

The main improvements introduced in the Level-1 Processor and impacting data quality are here below described, classified according to the release in which they have been included.

IPF v2.7.0 (31/03/2016) + v2.7.1 (21/04/2016)

- Update of Topsar processing parameters in order to improve data quality (spectra shape, ambiguities level, …)
- Improvement of WV SLC products annotations (attitude, replicas, Doppler Centroid estimations quality, …)
- Solved blocking issue in the generation of WV L2 products (no manifest file)
- Improvement of orbit propagation algorithm through integration of updated EO CFI libraries
- Improvement of denoising vectors annotation through proper management of noise measurements

IPF v2.7.2 (29/07/2016)

- Solved issue on holes between Topsar consecutive slices (missing bursts)
- Solved issue on Stripmap SLC products data sampling grid (wrong azimuth start time w.r.t. internal SLC products)
- Solved issue on presence of black stripes in Stripmap data (present e.g. in first S-1B images with not null Doppler Centroid)

IPF v2.8.0 (15/11/2016)

- Introduced full review of processor normalization approach for Topsar data
- Solved issue in the management of Doppler Centroid estimations causing the presence of radiometric artefacts in Topsar data (darker bursts)
- Review and correction of terrain height different annotations in L1 products

In addition to the described L1 Processor upgrades, a summary of S-1B Auxiliary Data Files (ADFs) updates since the start of the routine phase in September 2016 is provided, together with an explanation of the updates, in Appendix M. The main ones are here below summarized:

AUX_INS

- First applicable auxiliary file for user released products

AUX_CAL

- First applicable auxiliary file for user released products

AUX_PP1

- First applicable auxiliary file for user released products

AUX_PP2

- First applicable auxiliary file for user released products

AUX_SCS

- First applicable auxiliary file for user released products

6.2.2. Image Quality

The DLR Transponders & Corner Reflectors, the BAE Corner Reflector and the Australian Corner Reflector array have been used to assess various impulse response function parameters as described below. The products analysed were acquired during the commissioning phase and/or acquired since the start of the routine phase in September 2016 and processed with the Sentinel-1 IPF v2.71 and v2.72.

6.2.2.1. Spatial Resolution

The Figures and Tables below give the azimuth and range spatial resolutions derived from SM, IW and EW SLC data. The numbers in brackets indicate the number of measurements.

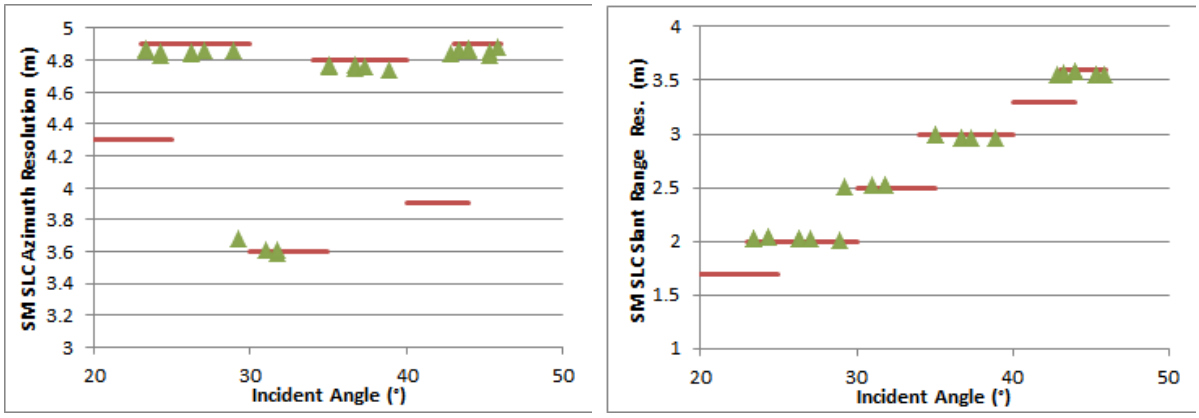

Figure 63 SM Azimuth and Slant Range Spatial Resolutions

Mode/Swath	Azimuth Spatial Resolution (m)	Slant Range Spatial Resolution (m)
S2	4.85±0.01 (8)	2.03±0.01 (8)
S3	3.62±0.04 (4)	2.52±0.01 (4)
S4	4.76±0.01 (6)	2.96±0.02 (6)
S6	4.86±0.02 (8)	3.57±0.01 (8)

Table 23 SM Azimuth and Slant Range Spatial Resolutions

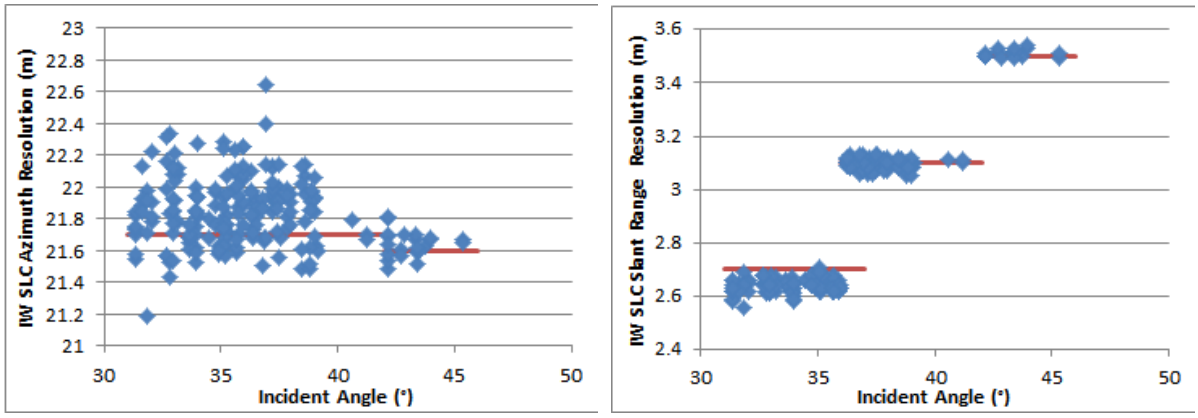

Figure 64 IW Azimuth and Slant Range Spatial Resolutions

Mode/Swath	Azimuth Spatial Resolution (m)	Slant Range Spatial Resolution (m)
IW1	21.84±0.22 (113)	2.64±0.03 (113)
IW2	21.87±0.20 (74)	3.10±0.02 (74)
IW3	21.64±0.08 (22)	3.51±0.01 (22)

Table 24 IW Azimuth and Slant Range Spatial Resolutions

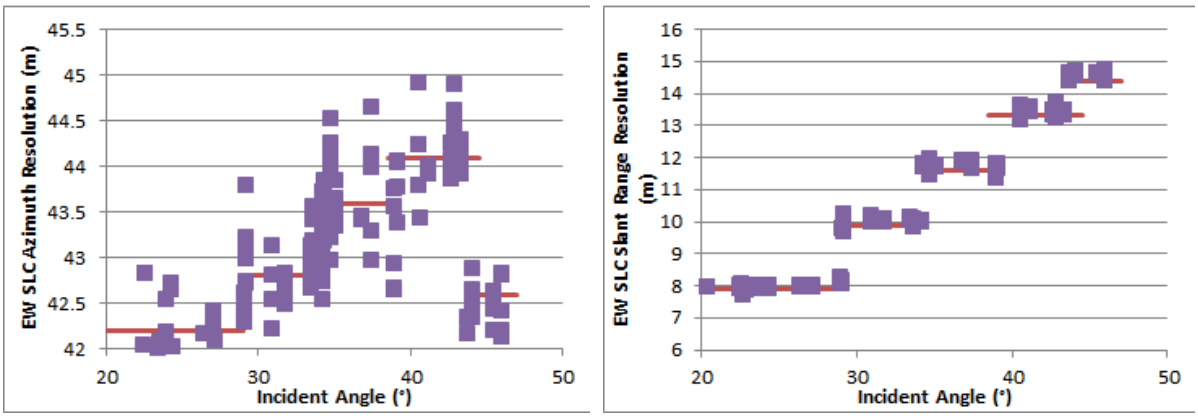

Figure 65 EW Azimuth and Slant Range Spatial Resolutions

Mode/Swath	Azimuth Spatial Resolution (m)	Slant Range Spatial Resolution (m)
EW1	41.94±0.33 (59)	7.96±0.07 (59)
EW2	42.87±0.34 (40)	10.01±0.11 (40)
EW3	43.58±0.38 (60)	11.73±0.11 (60)
EW4	44.09±0.26 (42)	13.43±0.10 (42)
EW5	42.43±0.43 (23)	14.57±0.10 (23)

Table 25 EW Azimuth and Slant Range Spatial Resolutions

The measured spatial resolutions match the predicted resolutions as indicated by the red horizontal lines.

6.2.2.2. Sidelobe Ratios

The table below gives the measured impulse response function sidelobe ratios derived from SM, IW and EW SLC data – these indicate acceptable values.

Mode/Swath	Integrated Sidelobe Ratio (dB)	Peak Sidelobe Ratio (dB)	Spurious Sidelobe Ratio (dB)
SM	-12.86±0.32	-20.64±0.54	-26.93±0.68
IW	-11.67±3.57	-19.64±0.99	-21.81±2.90
EW	-13.81±2.90	-20.80±3.57	-23.74±5.28

Table 26 SM & IW Sidelobe Ratios

6.2.2.3. ENL and Radiometric Resolution

No specific Equivalent Number of Look (ENL) and Radiometric Resolution measurements were performed on S-1B products. However, given that no changes have been made to the processing parameters that impact the ENL/RR since the commissioning phase of S-1A, the ENL/RR measurement for S-1B will be similar to those for S-1A [S1-RD-15].

6.2.2.4. Ambiguity Analysis

No specific ambiguity measurements were performed since the start of the S-1B routine phase in September 2016. Measurements below are re-produced from the S-1B MPC Commissioning Phase Report [S1-RD-02].

6.2.2.4.1. Azimuth Ambiguities

Azimuth ambiguities fall into two types: azimuth and range. Example azimuth ambiguities are shown in Figure 66 to Figure 68 for SM, IW and EW modes for the ESA ESTEC transponder, which in these examples is located over dark ocean backscatter. During the commissioning of S-1A, additional azimuth ambiguities like features were observed on IW and EW modes on both side of mainlobe. The source of features was identified after the S-1A commissioning phase and is related to a processing artifact of the TOPS products. This was solved by increasing the length of the UFR (Unfolding and Resampling filter) while deploying IPF 2.7x (see Section 4.2.2.4.1 for further details). Those features are not observed since then and are not observed on S-1B products.

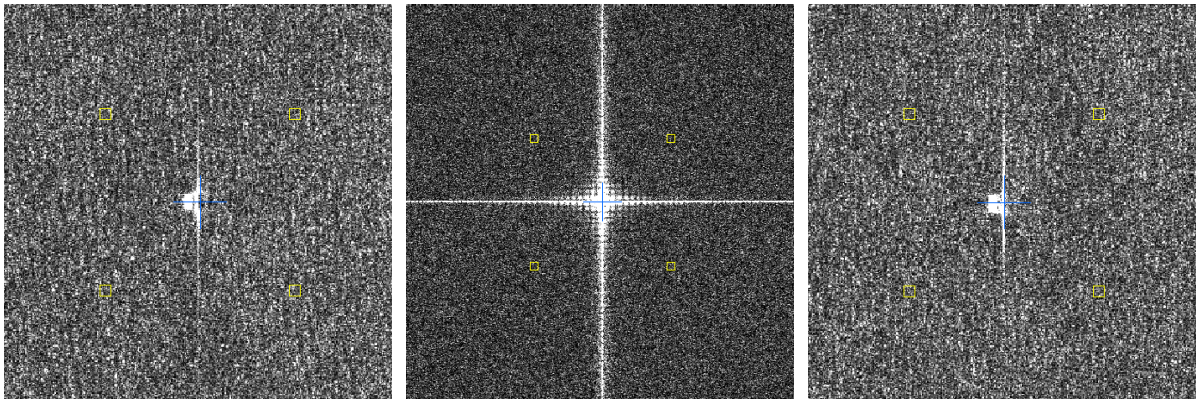

Early Ambiguity IRF Late Ambiguity

Figure 66: SM SLC Early Azimuth Ambiguity, DLR Transponder IRF and Late Ambiguity

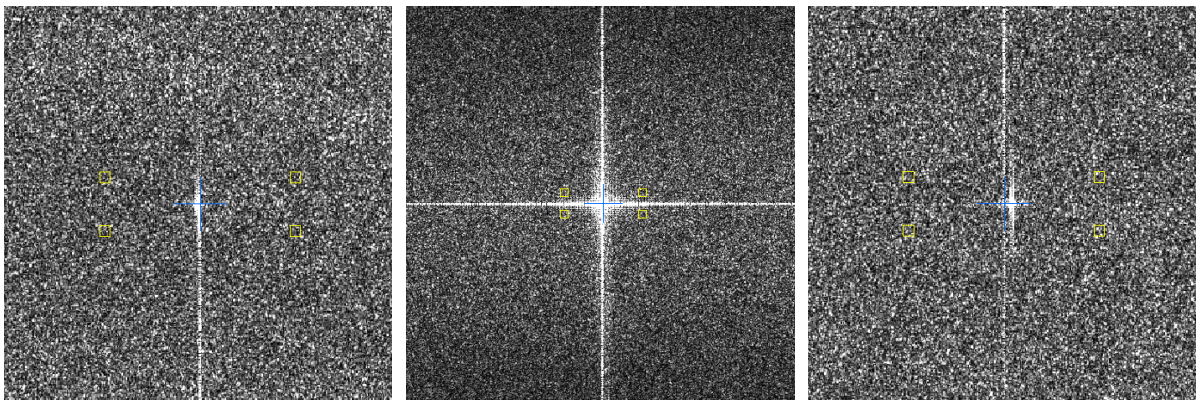

Early Ambiguity IRF Late Ambiguity

Figure 67: IW Early Azimuth Ambiguity, DLR Transponder IRF and Late Ambiguity

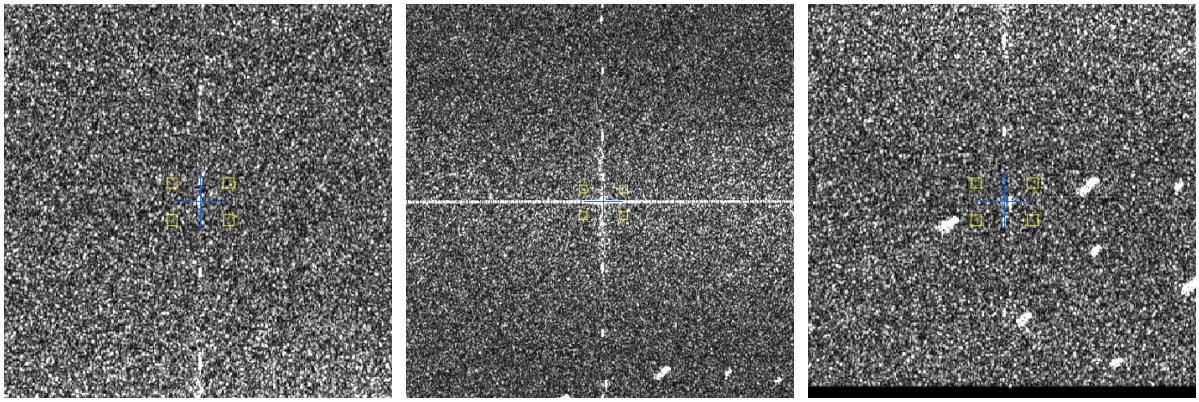

Early Ambiguity IRF Late Ambiguity

Figure 68: IW Early Azimuth Ambiguity, ESTEC Transponder IRF and Late Ambiguity

The table below gives mean azimuth ambiguity ratios for DLR transponder targets for SM, IW and EW modes. Note that for EW it can be hard to detect the azimuth ambiguities and so the values given should be considered as upper limits to the ambiguity ratio.

	SM	IW	EW
Early Azimuth Ambiguity Ratio (dB)	-29.16±5.80	-29.49±3.65	-30.58±1.58
Late Azimuth Ambiguity Ratio (dB)	-28.98±3.12	-28.60±3.88	-30.11±4.41

Table 27: Azimuth Ambiguity Ratios

6.2.2.4.2. Range Ambiguities

Range ambiguities have been identified in one IW scene to date and that being IW acquisitions over the BAE corner reflector that includes the North Sea (relative orbit 59). This scene from 5th August 2016 is shown in Figure 69 together with the region where range ambiguities are present (purple box). Figure 70 shows the ambiguity box where an extensive region of range ambiguities are seen together with non-ambiguous point targets including a wind farm. The western part of the range ambiguity is shown in Figure 71 together with the source of the range ambiguities located in the city of Rotterdam, The Netherlands, some 150km away to the east (taken from a S-1A image). The source of these range ambiguities is at higher slant ranges than the ambiguities (the first far range ambiguity).

Figure 69: S-1B IW Image of SE England and N France with the location of range ambiguities indicated (acquisition 5th August 2016, 17:40:17 UT).

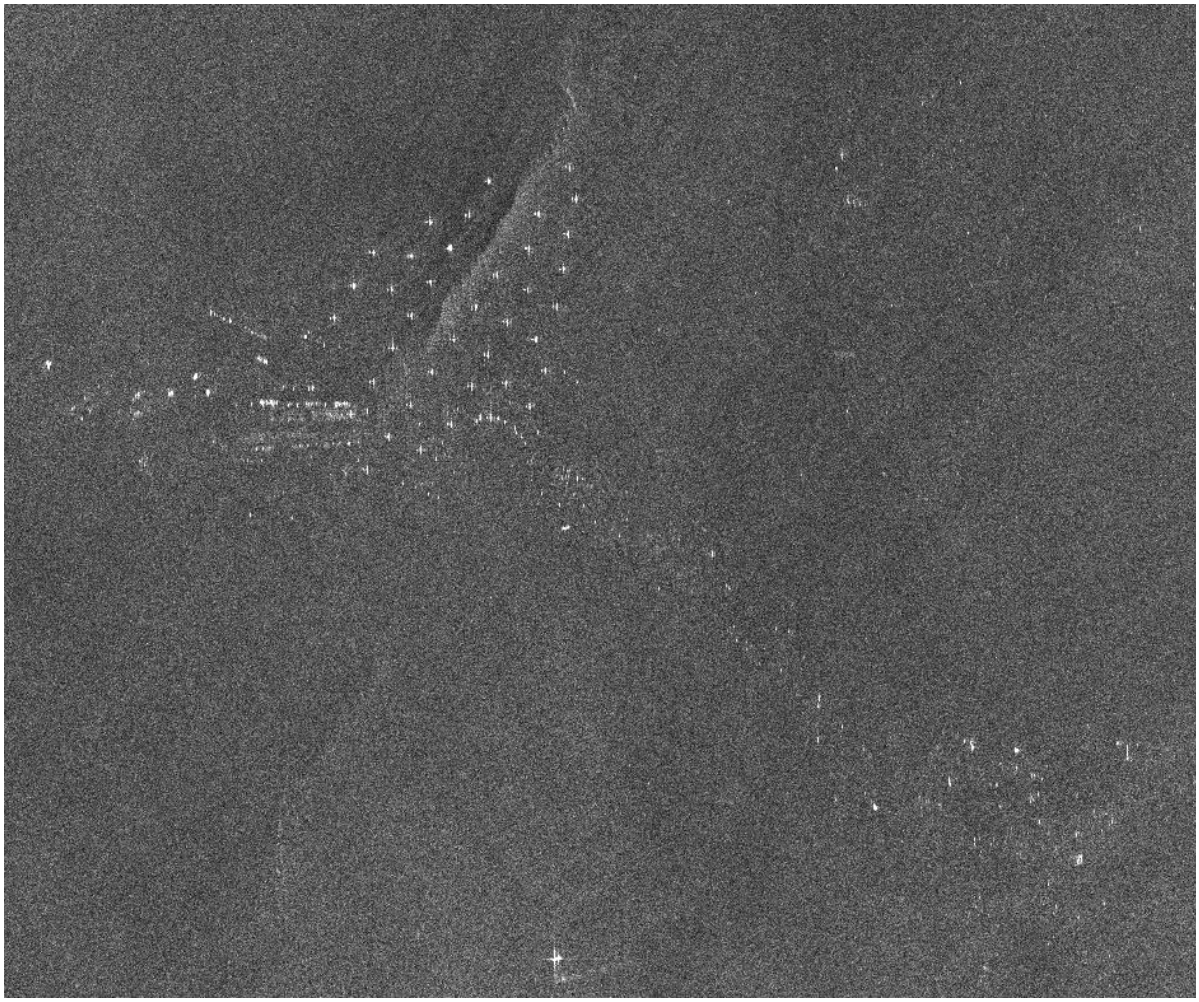

Figure 70: Extract of ambiguity region showing various range ambiguities plus other point targets.

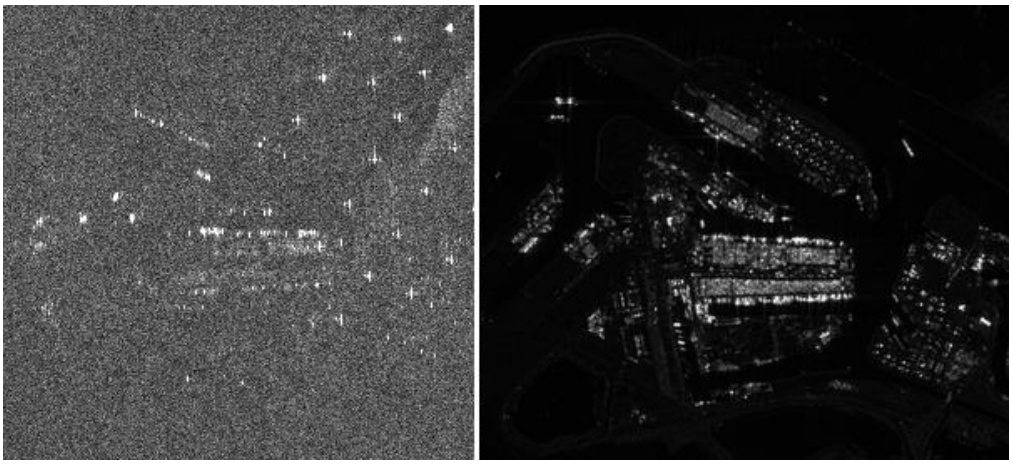

Figure 71: Detail of ambiguity region (left) and the source of the ambiguity in Rotterdam (right).

6.2.3. Radiometric Calibration

The DLR Transponders & Corner Reflectors, the BAE Corner Reflector and the Australian Corner Reflector array have been used to measure their radar cross-section as described below. The products analysed were acquired since the start of the routine phase in September 2016 and processed with the Sentinel-1 IPF v2.71 and v2.72.

6.2.3.1. Absolute Radiometric Calibration

DLR Transponders have been used to calculate the relative radar cross-section for SM, IW and EW modes since the start of the routine phase in September 2016. The results per mode are shown in Table 28 where mean (radiometric accuracy) and standard deviation (radiometric stability) of the relative radar cross-section in dB are given. The number of measurements is given in brackets. The majority of the transponder measurements are for EW mode which was used extensively after the commissioning phase. Note that the EW radiometric accuracy is close to zero while the radiometric stability is better 0.5dB. For SM and IW modes, the radiometric accuracy is also close to zero and good stabilities.

SM	IW	EW
-0.19±0.41 (18)	-0.09±0.21 (18)	-0.03±0.33 (146)

Table 28: SLC Relative Radar Cross-Section for the DLR transponders (dB)

The following results are also for the DLR transponders but are separated by polarisation. Figure 66 and Table 29 give the results for SM mode – the relative radar cross-sections indicate a reasonable radiometric calibration, especially given the small number of SM measurements.

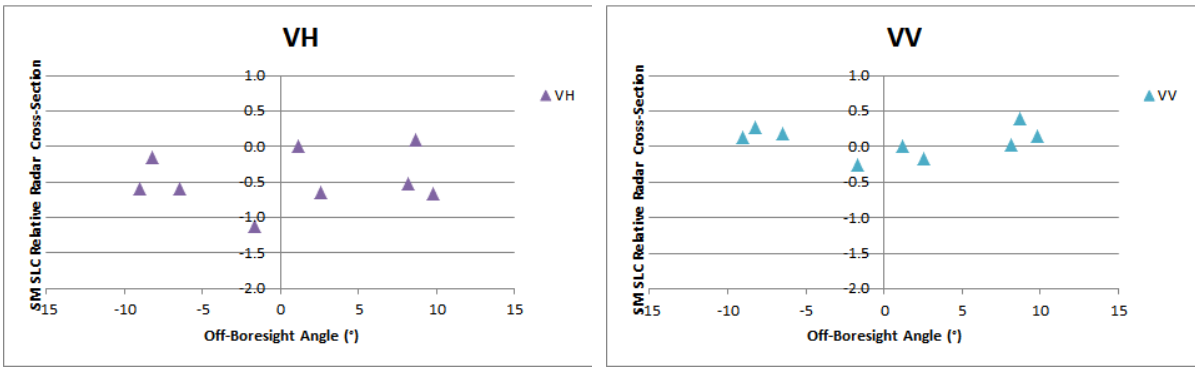

Figure 72: SM SLC Relative Radar Cross-Section for the DLR transponders

	VH	VV	HH	HV
S2	-0.45±0.25 (3)	0.20±0.08 (3)		
S3	-1.13 (1)	-0.26 (1)		
S4	-0.33±0.46 (2)	-0.08±0.13 (2)		
S6	-0.36±0.41 (3)	0.19±0.19 (3)		

Table 29: SM SLC Relative Radar Cross-Section for the DLR transponders (dB)

The IW and EW results below indicate a good radiometric calibration with many mean relative radar cross-section values close to zero (the radiometric accuracy) and a standard deviation of typically

0.3dB (the radiometric stability). Differences between polarisations are also small (see also Section 6.2.5.1).

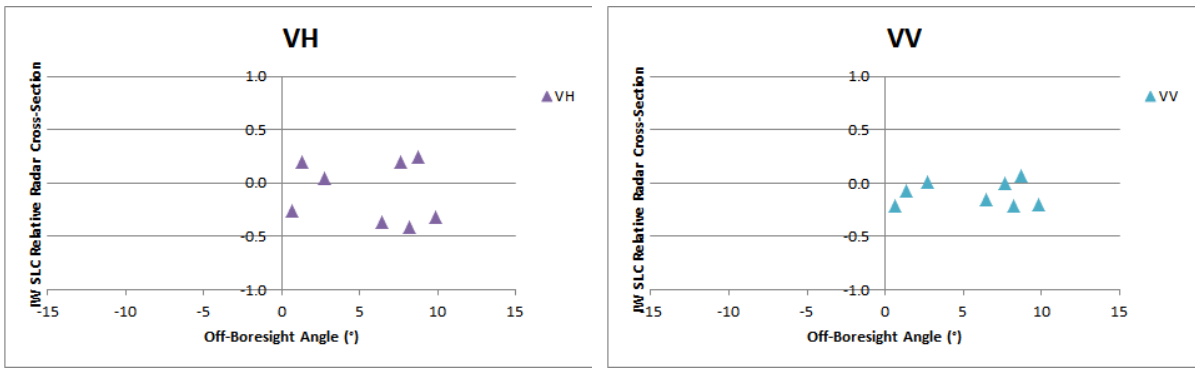

Figure 73: IW SLC Relative Radar Cross-Section for the DLR transponders

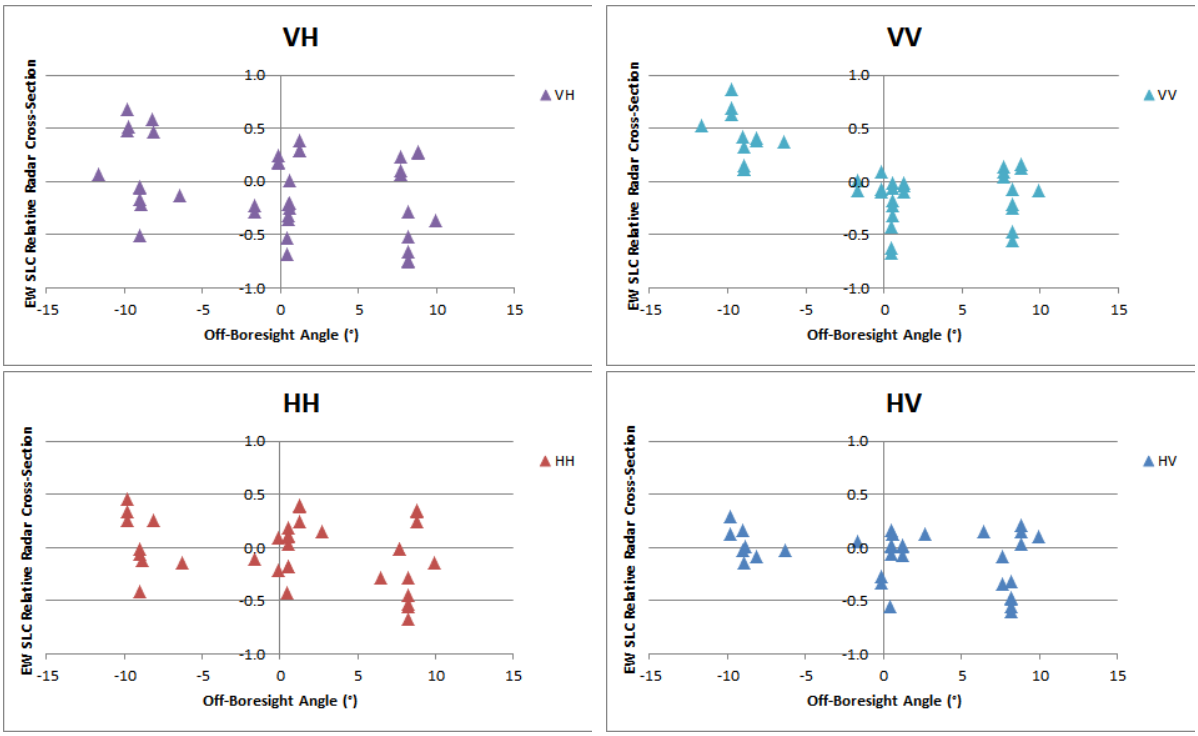

Figure 74: EW SLC Relative Radar Cross-Section for the DLR transponders

	VH	VV	HH	HV
IW	-0.09±0.28 (8)	-0.10±0.11 (8)		
EW	-0.06±0.39 (39)	0.03±0.35 (39)	-0.04±0.30 (34)	-0.08±0.25 (34)

Table 30: IW & EW SLC Relative Radar Cross-Section for the DLR transponders (dB)

	IW1	IW2	IW3
VH	-0.03±0.33 (2)	-0.17±0.29 (2)	-0.07±0.34 (4)
VV	-0.14±0.10 (2)	-0.08±0.12 (2)	-0.09±0.14 (4)

Table 31: IW SLC Relative Radar Cross-Section for the DLR transponders (dB)

	EW1	EW2	EW3	EW4	EW5
VH	0.14±0.39 (12)	-0.16±0.37 (7)	-0.04±0.29 (9)	-0.32±0.41 (8)	0.06±0.37 (3)
VV	0.42±0.24 (12)	-0.21±0.31 (7)	-0.15±0.15 (9)	-0.16±0.26 (8)	0.07±0.14 (3)
HH	0.01±0.25 (8)	-0.17±0.22 (4)	0.03±0.20 (10)	-0.35±0.25 (8)	0.20±0.23 (4)
HV	0.04±0.14 (8)	-0.28±0.25 (4)	0.05±0.08 (10)	-0.34±0.26 (8)	0.12±0.08 (4)

Table 32: EW SLC Relative Radar Cross-Section for the DLR transponders (dB)

The radiometric calibration results using the BAE Corner Reflector and IW SLC products are shown in Figure 75 from imagery acquired the start of the routine phase in September 2016 (VV polarisation only). The derived relative radar cross-section is -0.17±0.20dB.

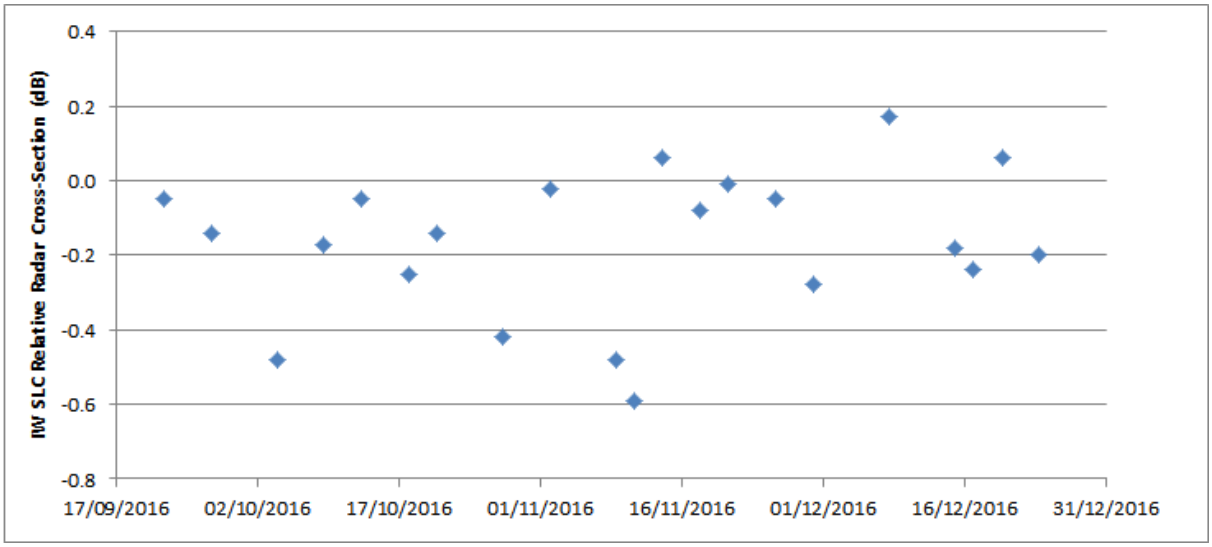

Figure 75: IW SLC Relative Radar Cross-Section for the BAE Corner Reflector

An array of 40 corner reflectors has been deployed near Brisbane, Australia as a component of the Australian Geophysical Observing System (AGOS) – see [S1-RD-04], [S1-RD-06] for further details. The CRs are size 1.5m (34), 2.0m (3) and 2.5m (3) with fixed orientations. Given that these corner reflectors have a fixed elevation and azimuth orientation they will not be pointing directly at S-1B. However, for IW acquisitions the reduction in radar cross-section compared to the case of a perfect orientation is small at less than 0.05dB. Table 33 gives the radiometric accuracy and stability for all corner reflector measurements during 2016 together with results for IW1 and IW2 sub-swaths and for VV and HH polarisations. The numbers in brackets refer to the number of measurements. The results indicate an accuracy close to zero while the stability is less than 0.5dB.

All	IW1	IW2	IW1 VV	IW1 HH	IW2 VV	IW2 HH
0.14±0.43 (164)	0.23±0.40 (98)	0.01±0.45 (66)		0.23±0.40 (98)		0.01±0.45 (66)

Table 33: IW SLC Relative Radar Cross-Section for the Australian Corner Reflectors (dB)

6.2.3.2. Permanent Scatter Calibration

No Permanent Scatter Calibration series have been generated yet due to the limit number of S-1B acquisitions so far.

6.2.4. Geometric Calibration

Geometric calibration of S-1B was performed by the University of Zurich (UZH) on the basis of a time series of products acquired between June and September 2016 over two test sites in Switzerland: *Torny-le-Grand* and *Dübendorf*. Trihedral corner reflectors (CRs) whose positions were surveyed with cm-level accuracy were used as reference targets. For calibration purposes, we initially focussed on StripMap (SM) products, as these have the best resolution and represent the native sensor characteristics more closely than other product types. Geolocation accuracy was estimated for IW and EW SLC products as well, also acquired over the same two test sites in 2016. For comparison, S-1A product geolocation estimates were made as well, during the S-1B commissioning. The S-1A results are shown and discussed in 4.2.4.

For a particular CR visible in an S-1B image product, its predicted azimuth and slant range image pixel position was calculated as follows:

- The surveyed CR position was adjusted for acquisition-time "epoch" plate **tectonic drift** and **solid Earth tide** (SET), as described in [S1-RD-11].
- The relevant timing annotations were extracted from the product annotations; these included the azimuth zero-Doppler time stamps, the orbital state vectors, the near-range fast time, and the range and azimuth sample spacings.
- Range-Doppler geolocation was performed for the CR coordinate as described e.g. in [S1-RD-13], giving range and azimuth times as the output.
- The slant range prediction was corrected by adding the modelled **atmospheric path delay**, and the azimuth time was corrected by subtracting the **bistatic** residual. These effects and their associated corrections are described in more detail in [S1-RD-11].

The above steps resulted in a range-azimuth *predicted* position for each target that could be compared to the position of the peak intensity in the image raster itself, i.e., the *measured* CR position. The differences between predicted and measured positions were then plotted, with the results shown for the SM, IW and EW SLC product time series in Figure 76, with product date ranges indicated. Please refer to [S1-RD-11] and [S1-RD-12] for details on the evolution of the standard IPF processing and the geolocation methodology.

The ALE estimates were originally made using StripMap data acquired and processed during the S-1B commissioning phase. The initial geolocation result based on SM SLC products served as a basis for an update to the Sampling Window Start Time (SWST) bias annotation in the instrument auxiliary files ingested by the S1 processor. All S-1B products processed after September 21, 2016 used the updated SWST bias. The plots shown in Figure 76 show the ALE estimates as they appear *after* accounting for the respective SWST biases (either in the S1 processor itself, or during post-processing). Note that no analogous azimuth timing correction has yet been incorporated into the processor.

Figure 76 (a) shows the SM SLC ALE plots for S-1B. Although the mean range offset is very small, is not exactly zero even though the official SWST bias was applied during geolocation estimation. This is because six products were acquired *after* the original SWST bias estimation, and contributed to the ~6 mm range offset in Figure 76 (a).

The SM SLC azimuth offset is ~1.9 m. Two apparent outliers in the S-1B plot in Figure 76 (a) can be seen with larger azimuth offsets than expected. No convincing explanation for the offset positions of these two points – from July 2016 products just two days apart – could be found.

The S-1B IW SLC plot is shown in Figure 76 (b). The clear grouping of the points by subswath is a known issue under continued investigation. Some indication of a similar beam-specific grouping can be seen in the SM SLC plots as well (Figure 76 (a)).

Figure 76 (c) shows the EW SLC ALE scatter. In spite of the higher spread caused by the coarser sample spacing, a similar pattern emerges to the IW case: subswath-specific azimuth offsets, and relatively consistent range geolocation.

The ALE plots in Figure 76 indicate that given bias compensations, the localisation performance was well within the original requirements (according to sections 5.5.2.1 and 5.5.2.2 in [S1-RD-14]). The observed beam/subswath-dependent azimuth ALE remains under investigation. A method for integrating azimuth bias compensation annotations in the IPF is under study.

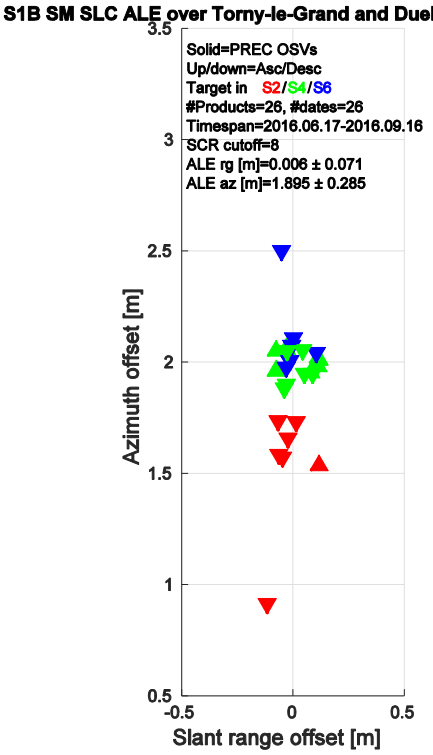

(a) S-1B SM SLC (2016.06.17 – 2016.09.16)

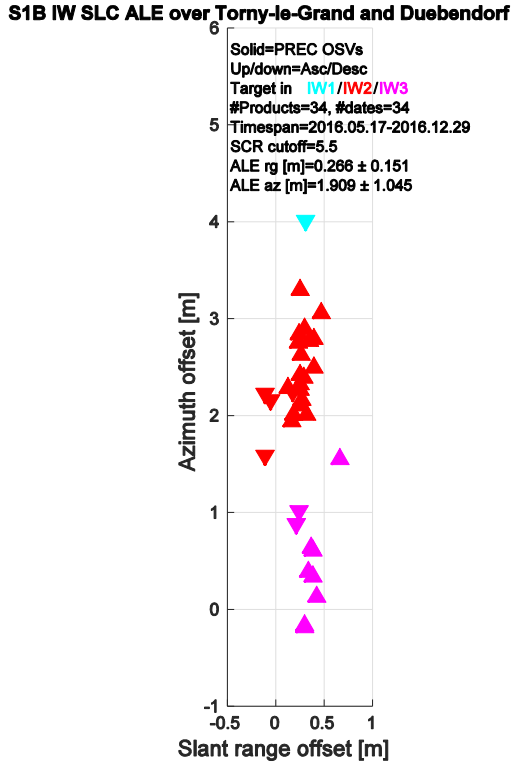

(b) S-1B IW SLC (2016.05.17 – 2016.12.29)

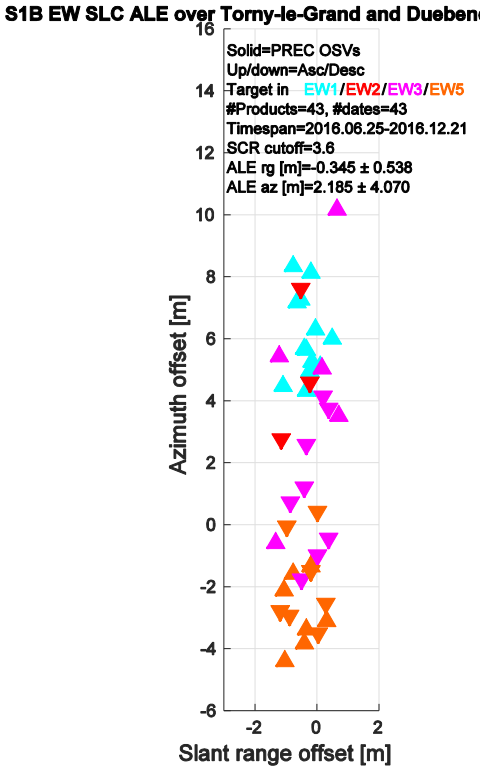

(c) S-1B EW SLC (2016.06.25 – 2016.12.21)

Figure 76: ALE estimates for S-1B StripMap, IW and EW SLC product time series acquired over the Swiss test sites using precise state vectors (AUX_POEORB). Product date ranges are given in brackets. Point colours represent beam/subswath. The SWST (range) bias (output of the commissioning and calibration phase) was applied in all cases.

6.2.5. Polarimetric Calibration

6.2.5.1. Gain Imbalance

The DLR transponders and acquisitions since the start of the routine phase in September 2016 have been used to calculate the gain imbalance (the difference in radar cross-section between the two polarisations of dual polarisation products). Table 34 give a summary of the gain imbalance for the SM, IW and EW modes.

	Gain Imbalance (dB)
SM	-0.55±0.28 (9)
IW	0.01±0.18 (8)
EW	-0.03±0.25 (74)

Table 34: Gain Imbalance using the DLR transponders

The following results show the gain imbalance split between the two possible polarisation of VH/VV and HH/HV. Figure 71 and Table 35 give the gain imbalance for IW and EW modes.

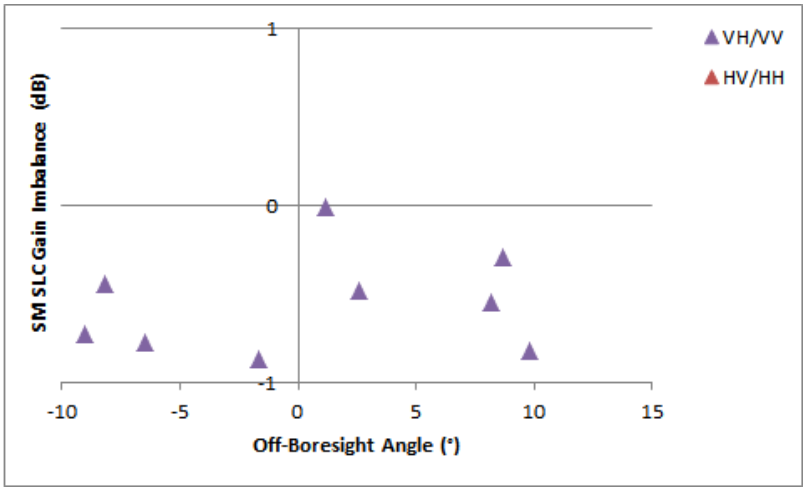

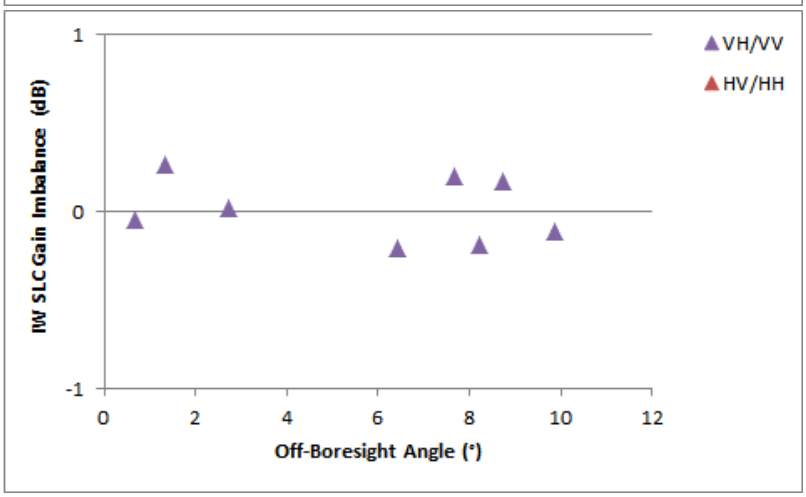

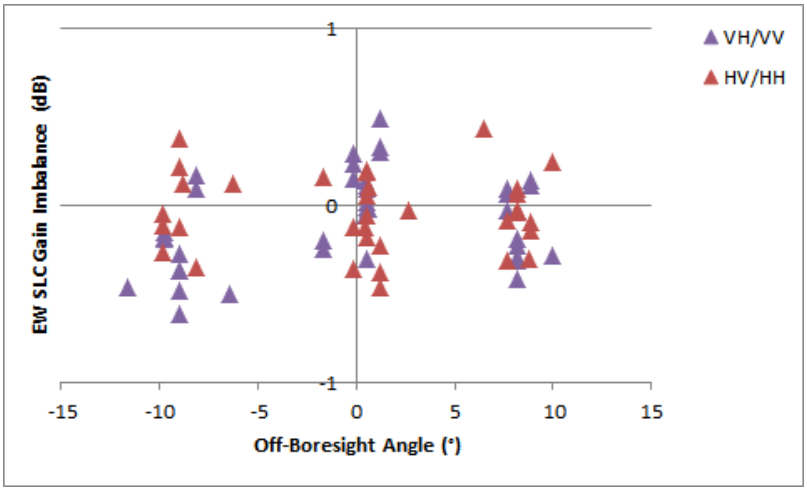

Figure 77: Gain Imbalance using the DLR transponders.

	VH/VV	HV/HH
SM	-0.55±0.28 (9)	
IW	0.01±0.18 (8)	
EW	-0.08±0.27 (39)	-0.04±0.22 (35)

Table 35: Gain Imbalance using the DLR transponders

6.2.5.2. Phase Imbalance

The DLR transponders have been used to calculate the phase imbalance (the difference in peak phase between the two polarisations of dual polarisation products). Figure 78 and Table 36 give the gain imbalance for SM, IW and EW for acquisitions start of the routine phase in September 2016. As expected the phase difference is close to zero.

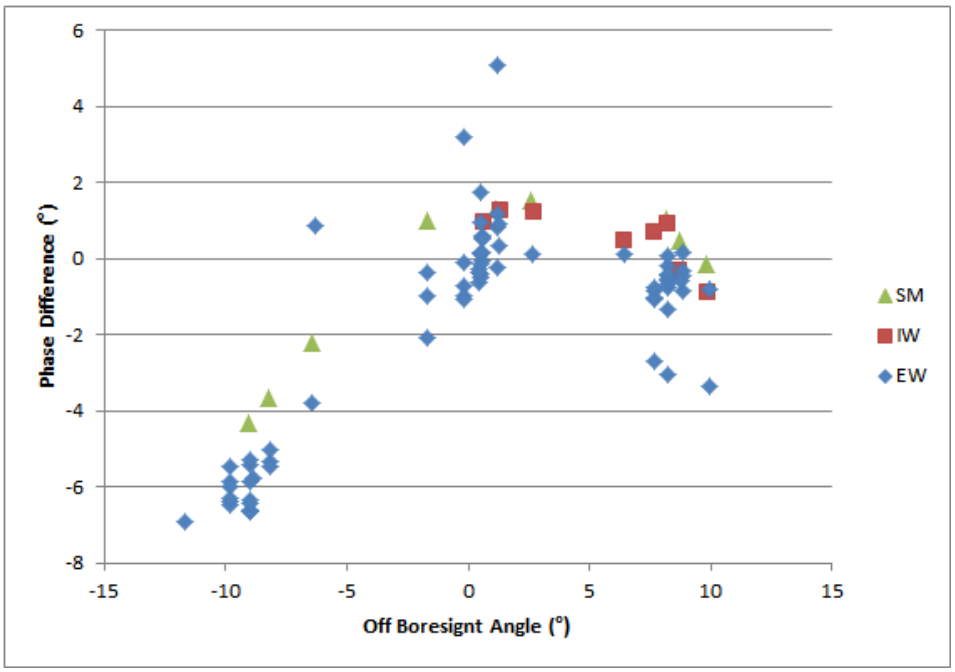

Figure 78: Phase Imbalance using the DLR transponders.

	Phase Difference (°)
SM	-1.11±2.26 (7)
IW	0.54±0.77 (8)
EW	-1.76±2.80 (74)

Table 36: Phase Imbalance using the DLR transponders

6.2.5.3. Coregistration

Coregistration measurements were performed during the S-1B commissioning phase and since the start of the S-1B routine phase in September 2016.

The point targets used for the coregistration analysis are either the ESA or DLR transponder as they both provide an impulse response in both polarisations of dual polarisation imagery. Figure 79 shows examples of SM, IW & EW co-registration for ESA and DLR transponders (for the ESA transponder, the shown images are at full resolution while for the DLR transponders, oversampled images are shown). In all three examples the co-registration was zero in both range and azimuth. Table 37 below shows that the average measured polarimetic co-registration derived from SLC products is very small.

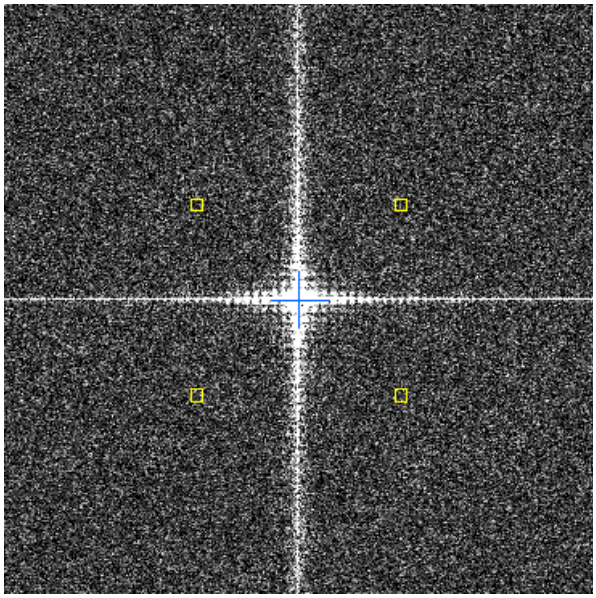

ESA T1 (S2 SLC VH)

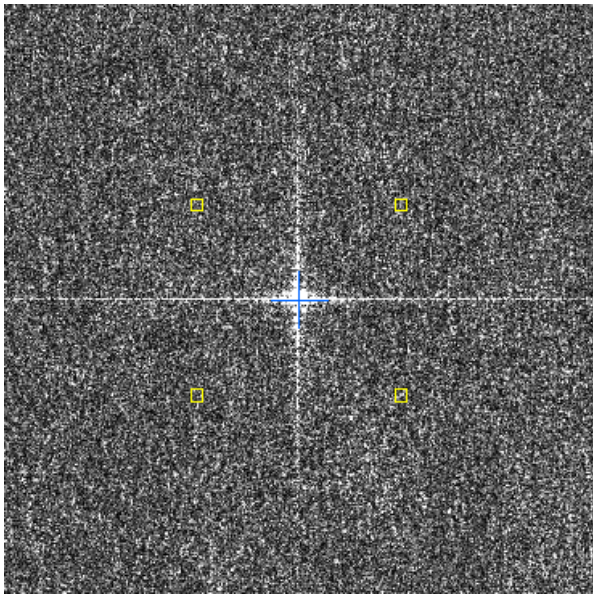

ESA NLR (S2 SLC VV)

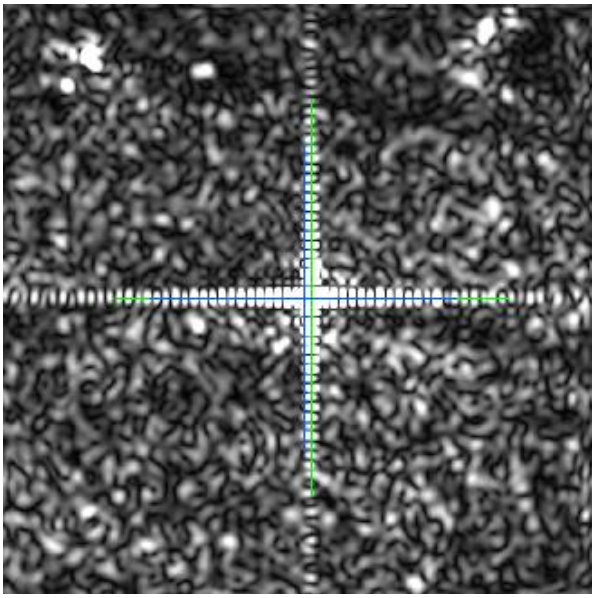

DLR D39 (IW SLC HH)

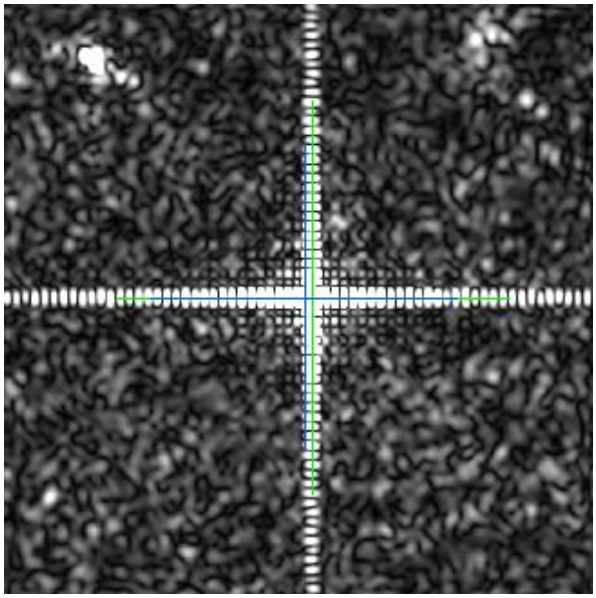

DLR D39 (IW SLC HV)

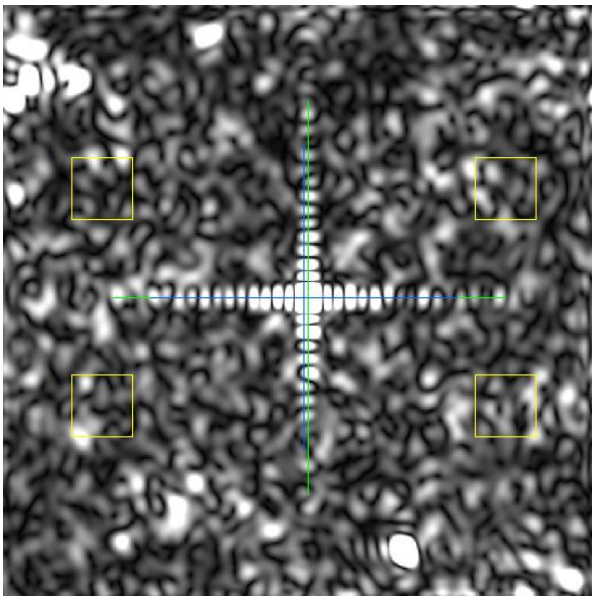

DLR D39 (EW SLC HH)

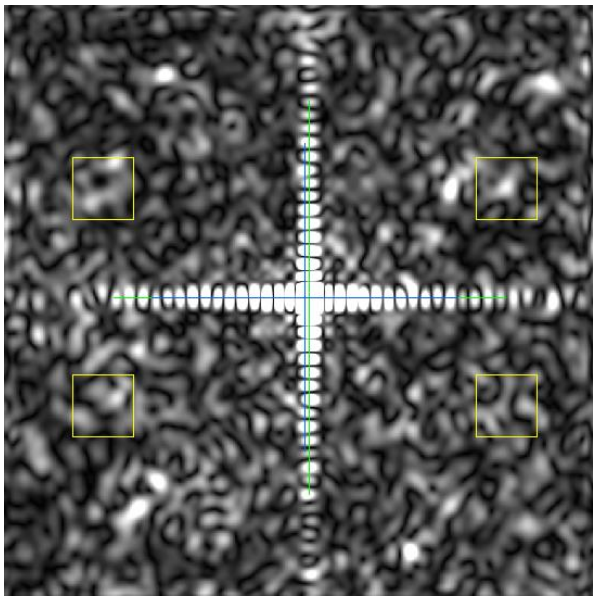

DLR D39 (EW SLC HV)

Figure 79: SLC Co-registration Examples

Mode/Swath	Range Co-registration Accuracy (m)	Azimuth Co-registration Accuracy (m)	Number of Measurements
SM	0.02±0.08	0.05±0.15	114
IW	0.01±0.05	0.21±0.57	134
EW	0.04±0.16	0.32±0.90	213

Table 37: SLC Polarimetric Co-registration

6.2.5.4. Cross-talk

No specific coregistration measurements were performed since the start of the S-1B routine phase in September 2016. Measurements below are re-produced from the S-1B MPC Commissioning Phase Report [S1-RD-02].

The point targets used for the cross-talk analysis are either the DLR or BAE trihedral corners reflector as they both provide an impulse response in only one polarisation (HH or VV) of dual polarisation imagery. Figure 80 shows examples of SM, IW & EW cross-talk for DLR corner reflector (the images shown are oversampled): the measured cross-talk for SM is -41.3dB, for IW is -34.14dB while for EW no cross-talk IRF could be identified. As shown in Table 38 below, the average measured cross-talk is very low.

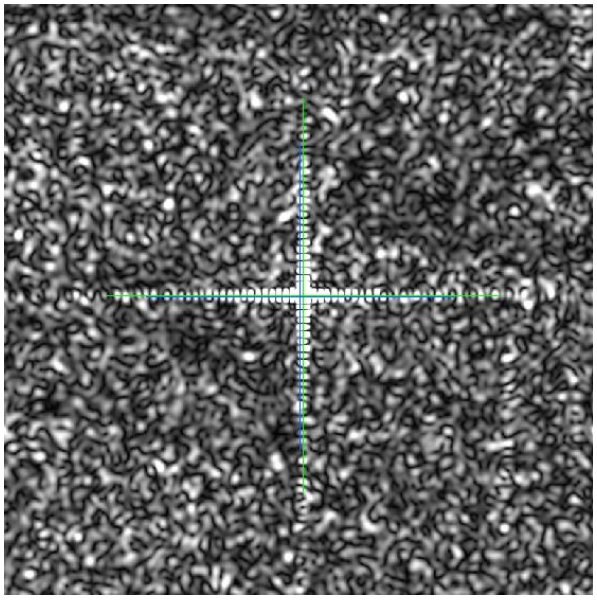

DLR CR D38 (S5 SLC HH)

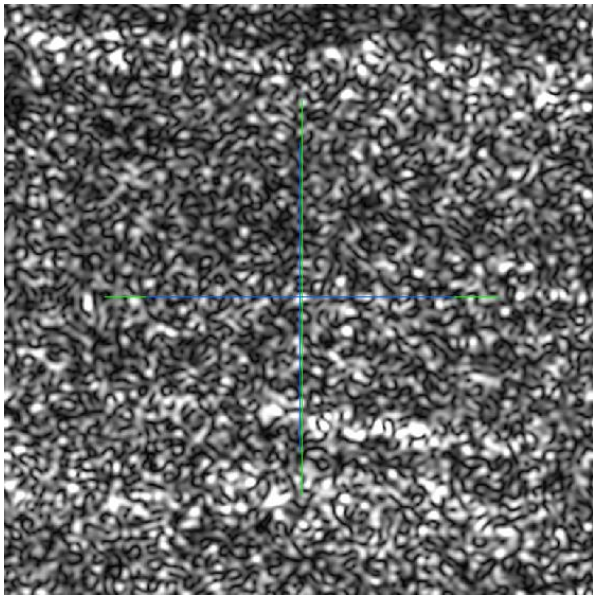

DLR CR D38 (S5 SLC HV)

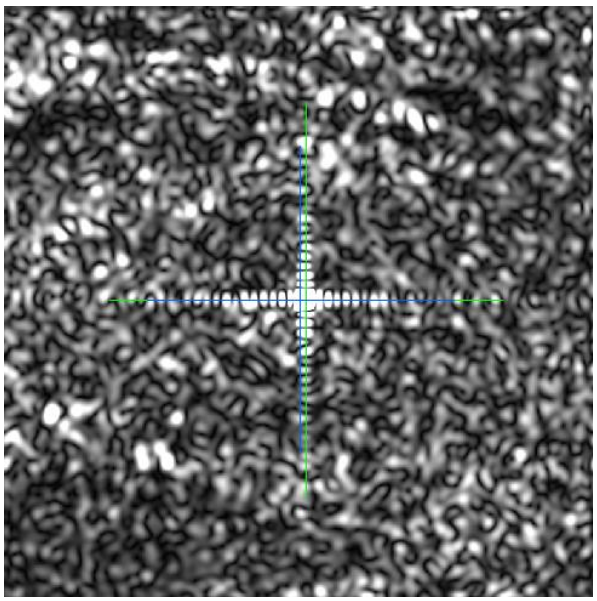

DLR CR D38 (IW SLC HH)

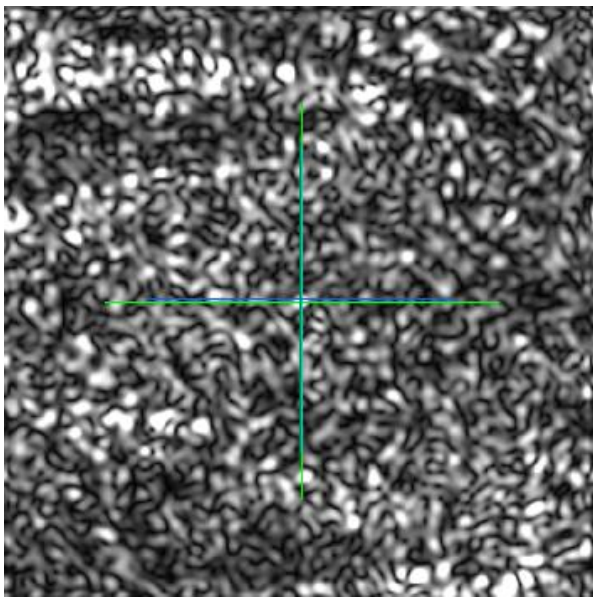

DLR CR D38 (IW SLC HV)

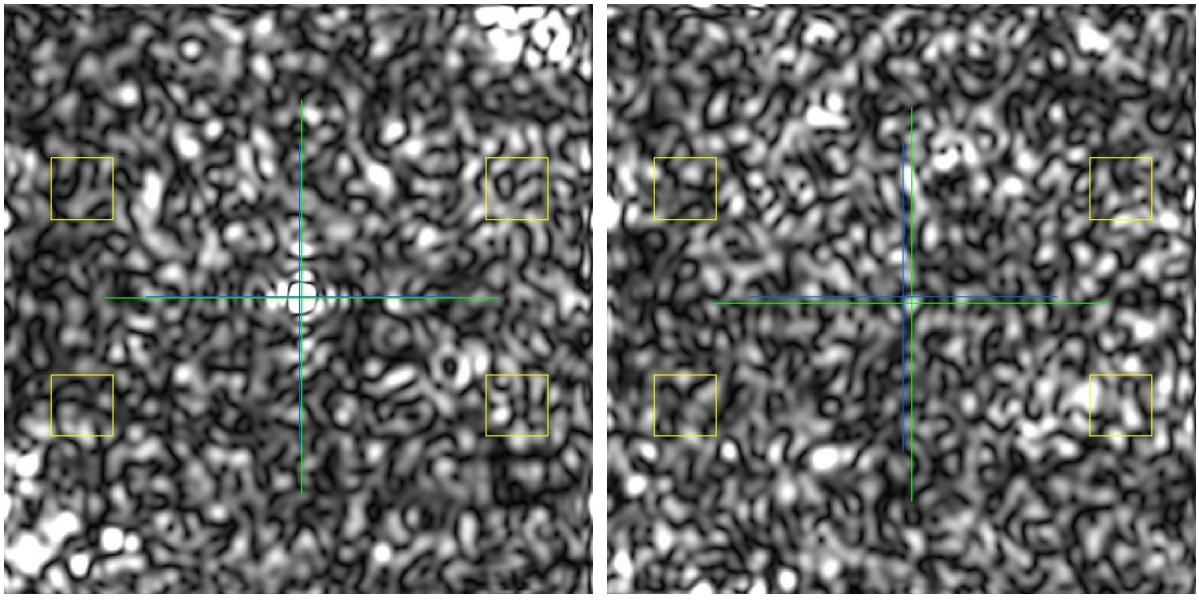

DLR CR D42 (EW SLC HH) DLR CR D42 (EW SLC HV)

Figure 80: SLC Cross-talk Examples

Corner Reflector Cross-talk (dB)	Number of Measurements
-37.4±4.7	11

Table 38: SLC Cross-talk

6.2.6. Elevation Antenna Patterns

No new elevation antenna patterns were derived since the start of the S-1B routine phase in September 2016.

6.2.7. Azimuth Antenna Patterns

No new azimuth antenna patterns were derived since the start of the S-1B routine phase in September 2016.

6.2.8. Noise Equivalent Radar Cross-section

No specific Noise Equivalent Radar Cross-Section (NESZ) measurements were performed since the start of the S-1B routine phase in September 2016. Measurements below are re-produced from the S-1B MPC Commissioning Phase Report [S1-RD-02].

Examples of S-1B imagery with low ocean backscatter have been used to estimate the NESZ for most modes and swaths. These are shown in Figure 81 to Figure 84 for SM, IW, EW and WV modes respectively. For all but WV mode, the majority of the NESZ estimates have been performed in cross-polarisation (HV or VH) as the ocean backscatter is much lower compared to co-polarisation. For WV mode where the imagettes are only acquired in co-polarisation, suitable data has been selected by the extraction of the I and Q channel standard deviation parameter from the product annotation (a low standard deviation indicates a low radar cross-section). In addition to the measured NESZ, all the plots show the predicted NESZ (at low and high orbital altitudes).

In Figure 81 for SM, the measured NESZ are close to the predicted NESZ. In addition, for many SM swaths the measured NESZ exceeds the NESZ requirements of -22 dB. The main exception is S3 where the measured NESZ is -20dB at mid-swath. For some of the other swaths, the requirement is not met at the edges of the swath.

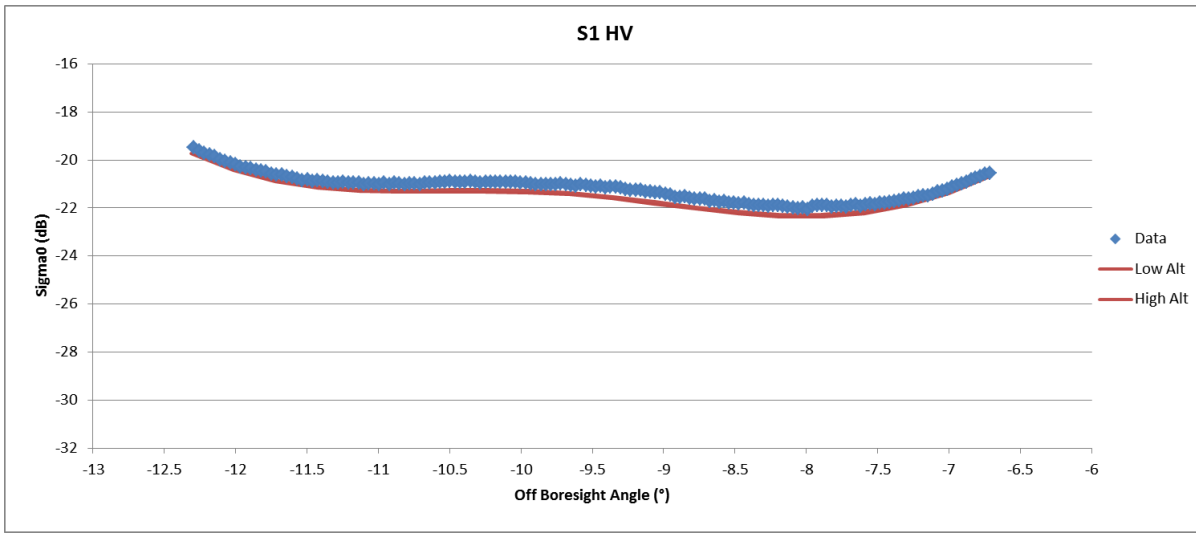

S1B_S1_GRDH_1SDH_20160826T220944_20160826T221015_001794_002AE1_451F.SAFE

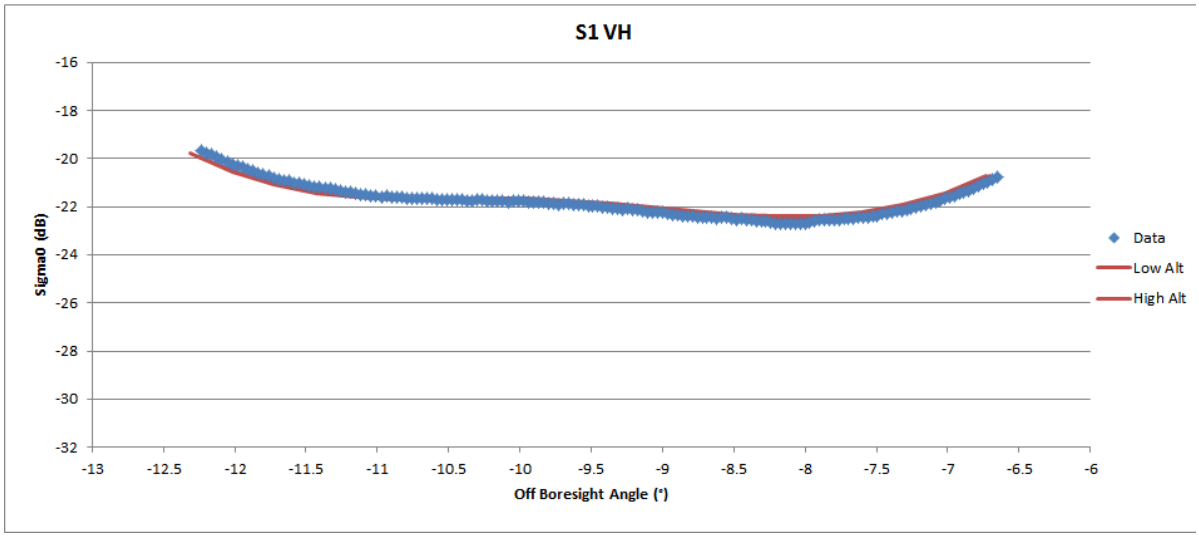

S1B_S1_GRDH_1SDV_20160826T142337_20160826T142402_001789_002A9E_DA91.SAFE

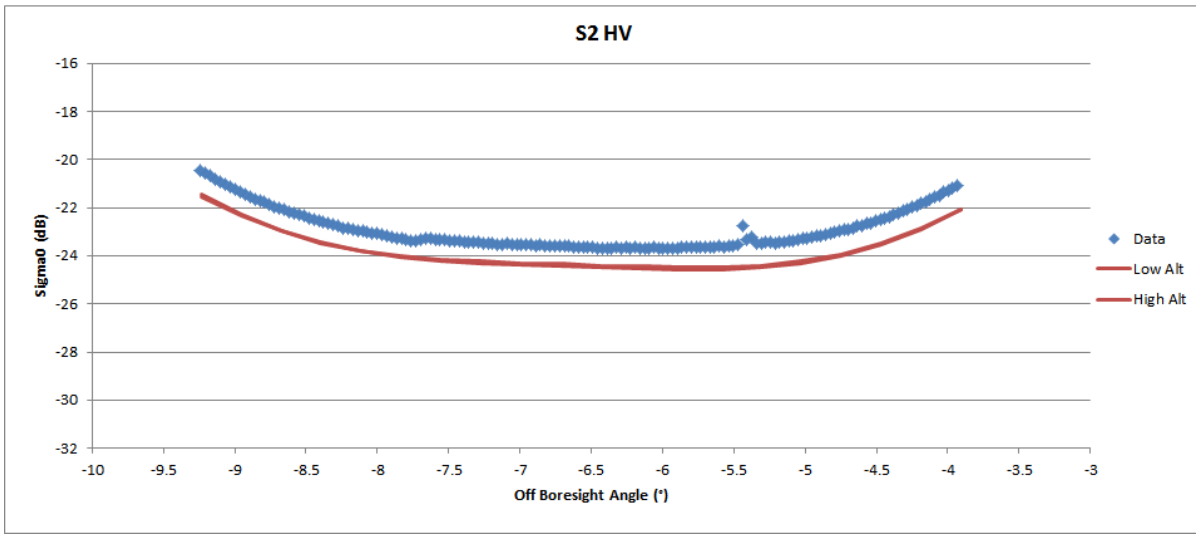

S1B_S2_GRDH_1SDH_20160905T062039_20160905T062054_001930_00309F_BAAD.SAFE

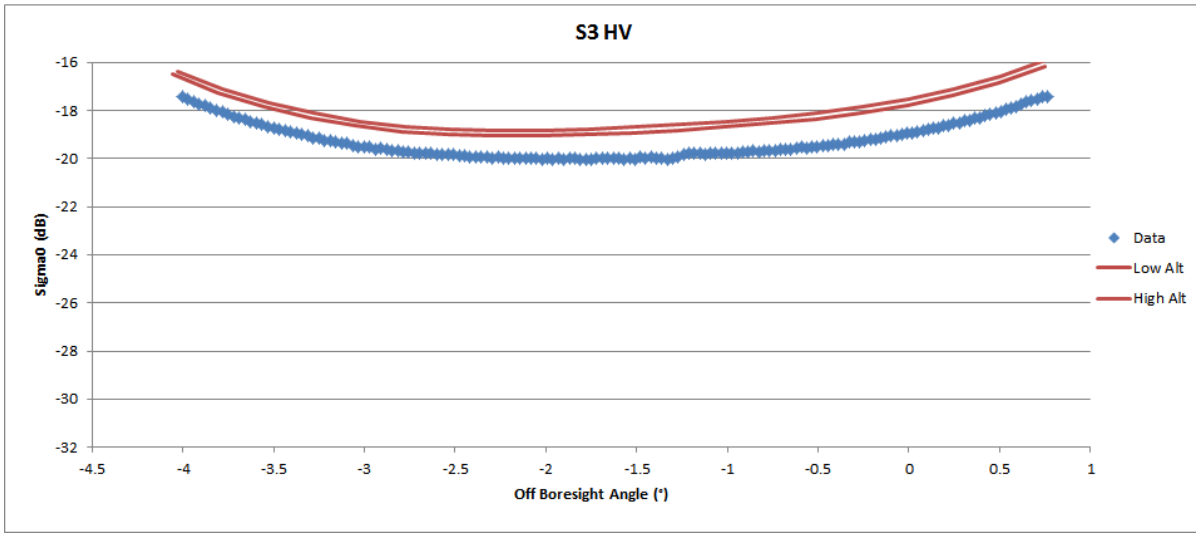

S1B_S3_GRDH_1SDH_20160827T164708_20160827T164732_001805_002B57_CD0D.SAFE

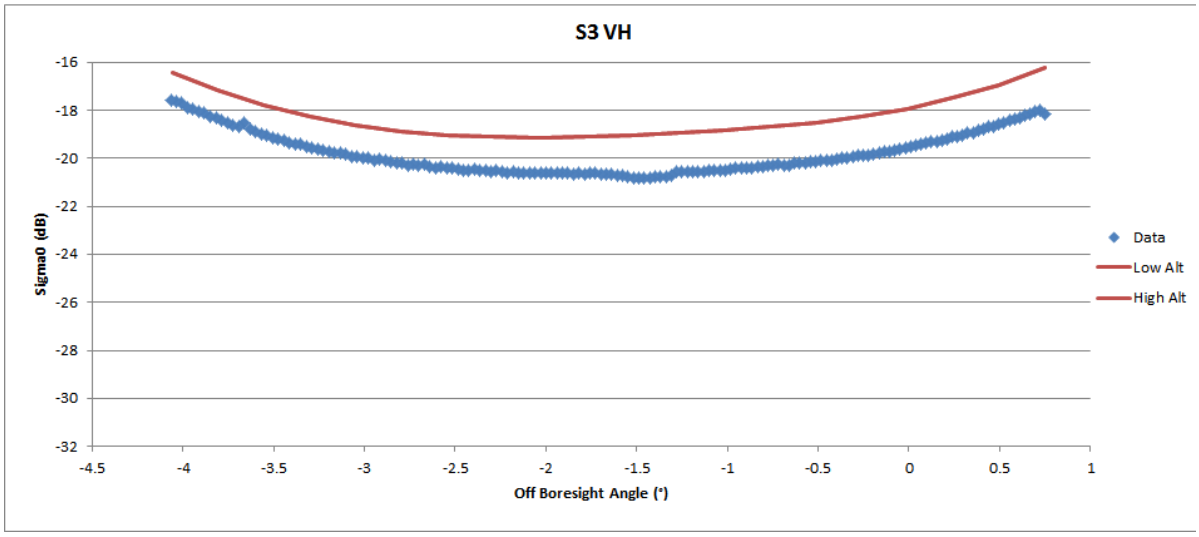

S1B_S3_GRDH_1SDV_20160831T061321_20160831T061330_001857_002DA2_23C0.SAFE

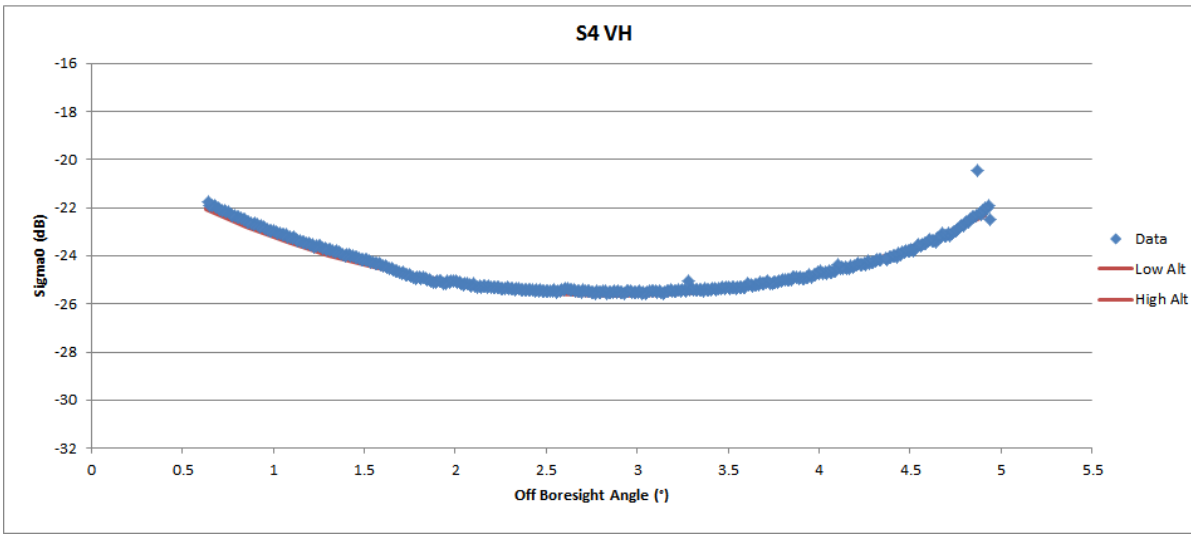

S1B_S4_GRDF_1SDV_20160831T061339_20160831T061413_001857_002DA3_720C.SAFE

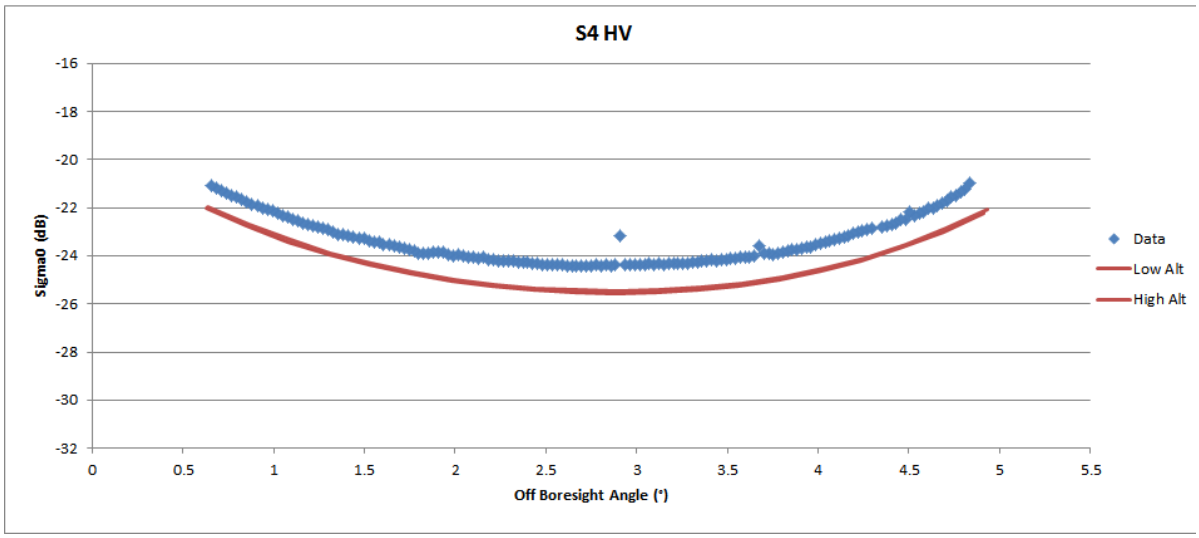

S1B_S4_GRDH_1SDH_20160726T061338_20160726T061412_001332_0017C3_30FD.SAFE

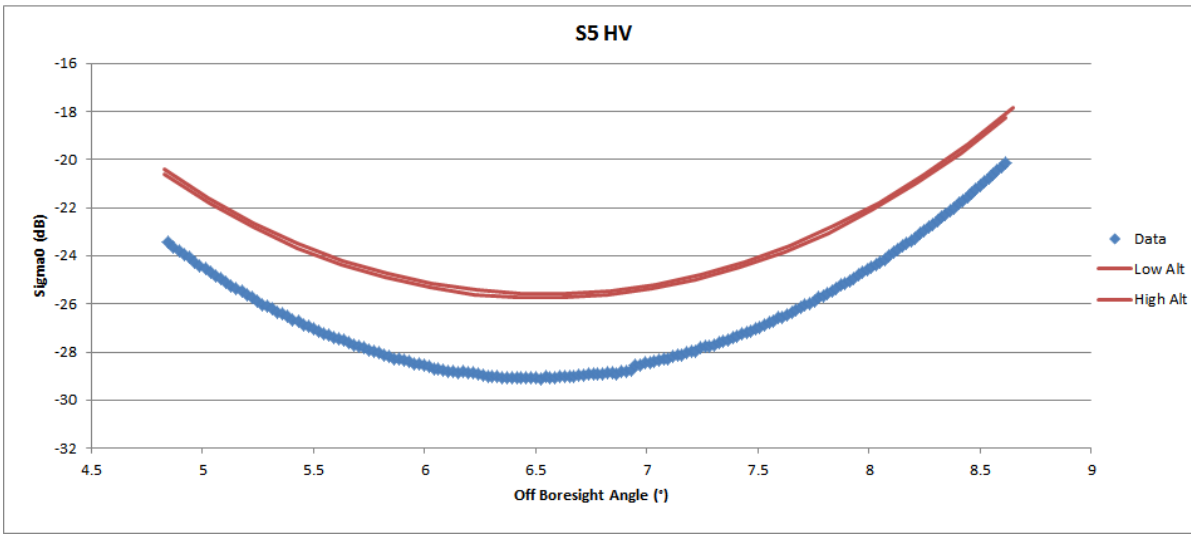

S1B_S5_SLC__1SDH_20160717T174817_20160717T174851_001208_0012BC_C648.SAFE

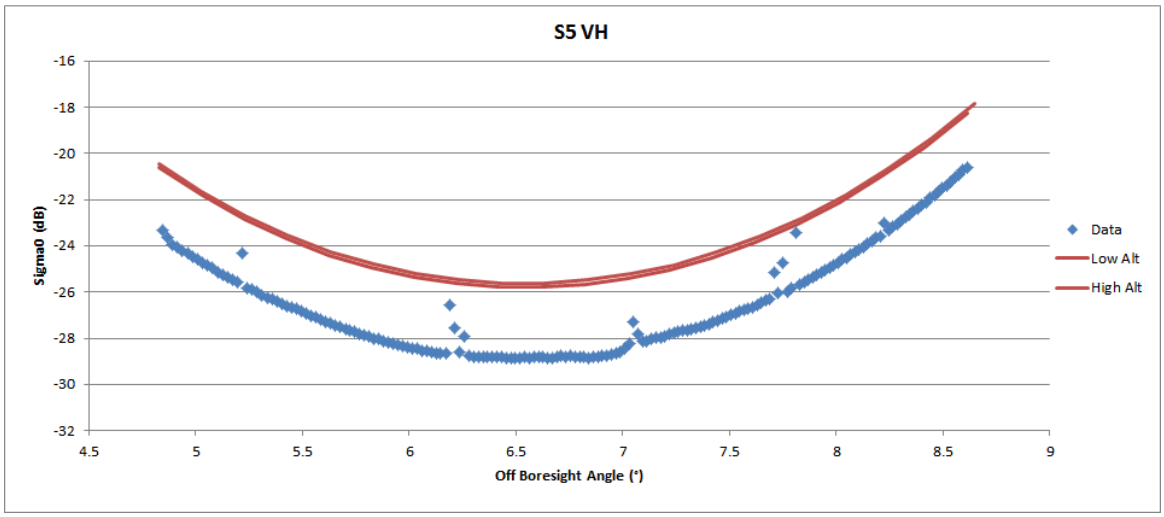

S1B_S5_SLC__1SDV_20160729T174816_20160729T174850_001383_001976_8672.SAFE

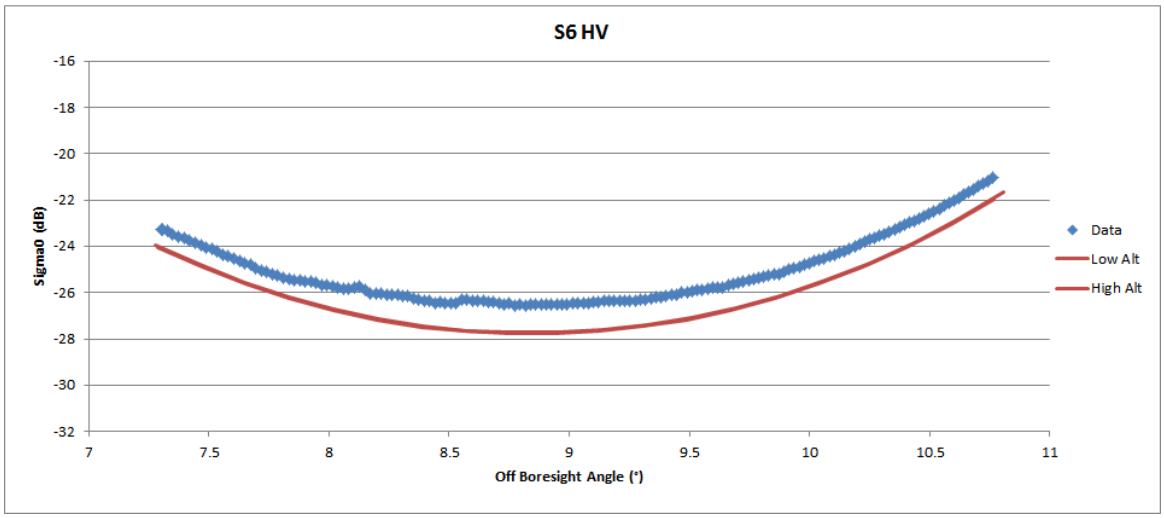

S1B_S6_GRDH_1SDH_20160822T145218_20160822T145246_001731_0027F0_E9CE.SAFE

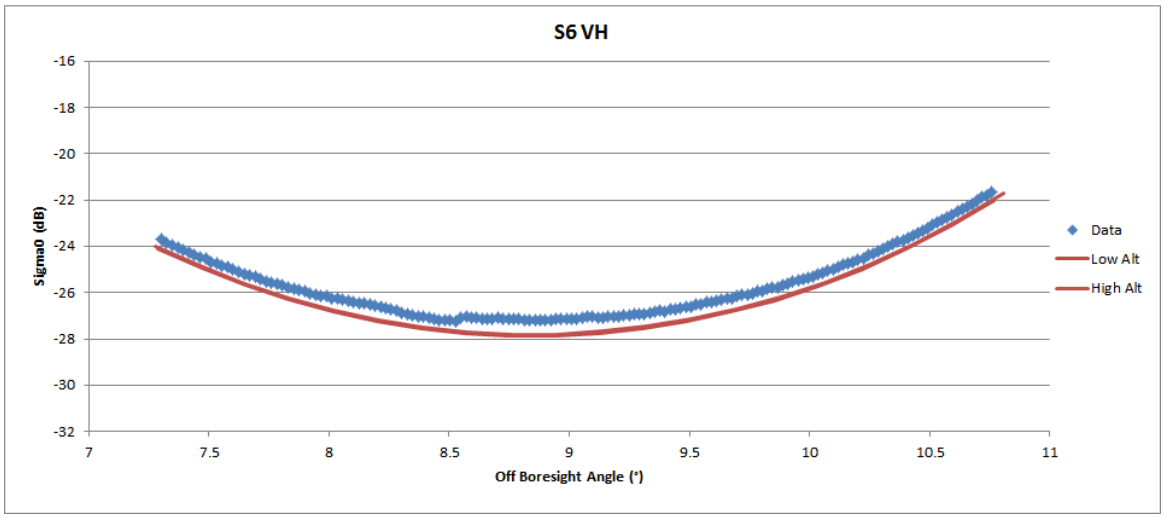

S1B_S6_GRDH_1SDV_20160823T140012_20160823T140037_001745_002899_FB6D.SAFE

Figure 81: NESZ measures for SM. Blue is the measured NESZ and the red lines are the predicted NESZ at minimum and maximum orbital altitudes.

In **Figure 30** for IW and **Figure 31** for EW, the -22 dB requirement is met at all sub-swaths and all off-boresight angles. For some sub-swaths the measured NESZ is slightly worse than the prediction while for other it is close to the prediction.

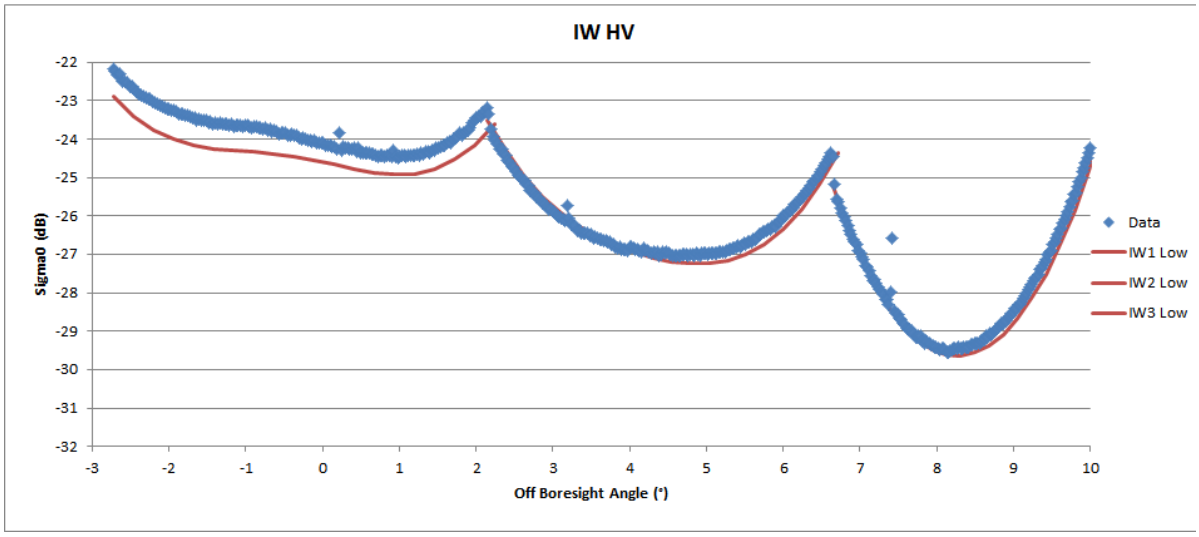

S1B_IW_GRDH_1SDH_20160824T173245_20160824T173305_001762_002961_F24D.SAFE

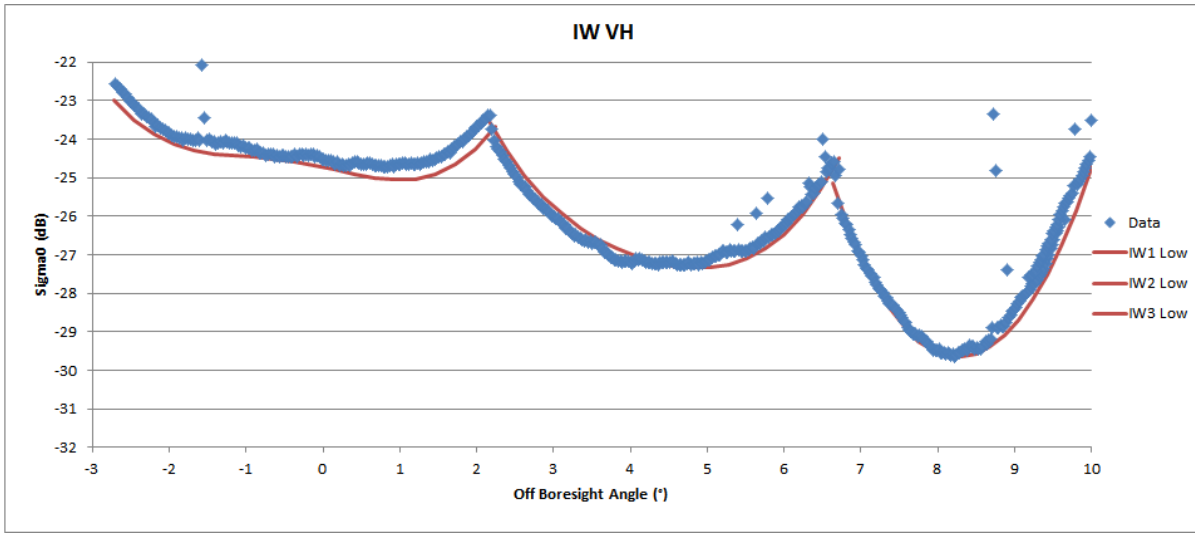

S1B_IW_GRDH_1SDV_20160822T174824_20160822T174849_001733_002804_6DD1

Figure 82: NESZ measures for IW. Blue is the measured NESZ and the red lines are the predicted NESZ at the minimum orbital altitude.

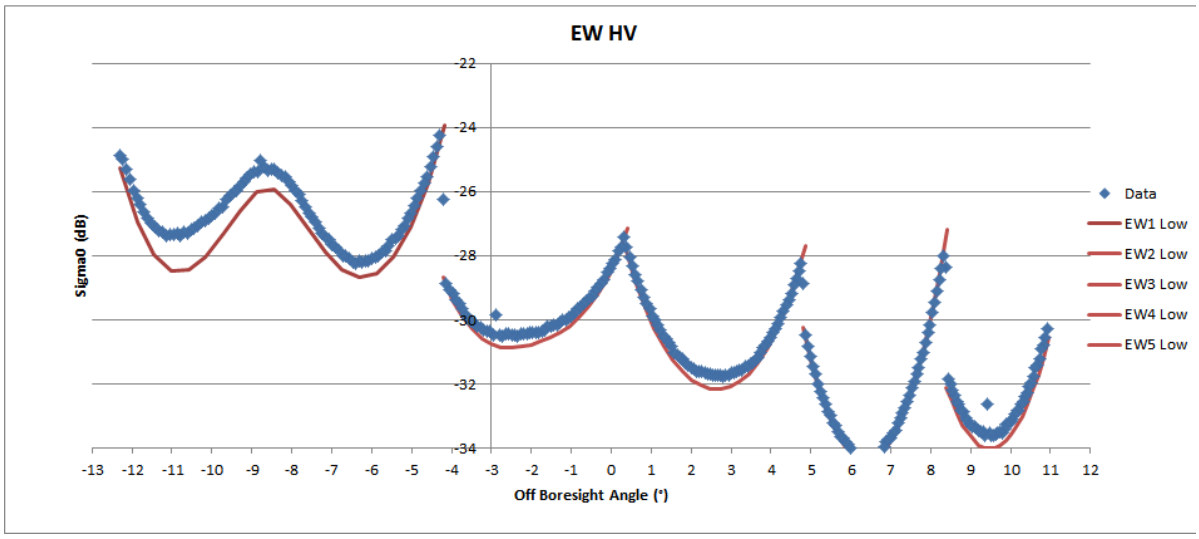

S1B_EW_GRDH_1SDH_20160904T054412_20160904T054512_001915_002FF1_35D0.SAFE

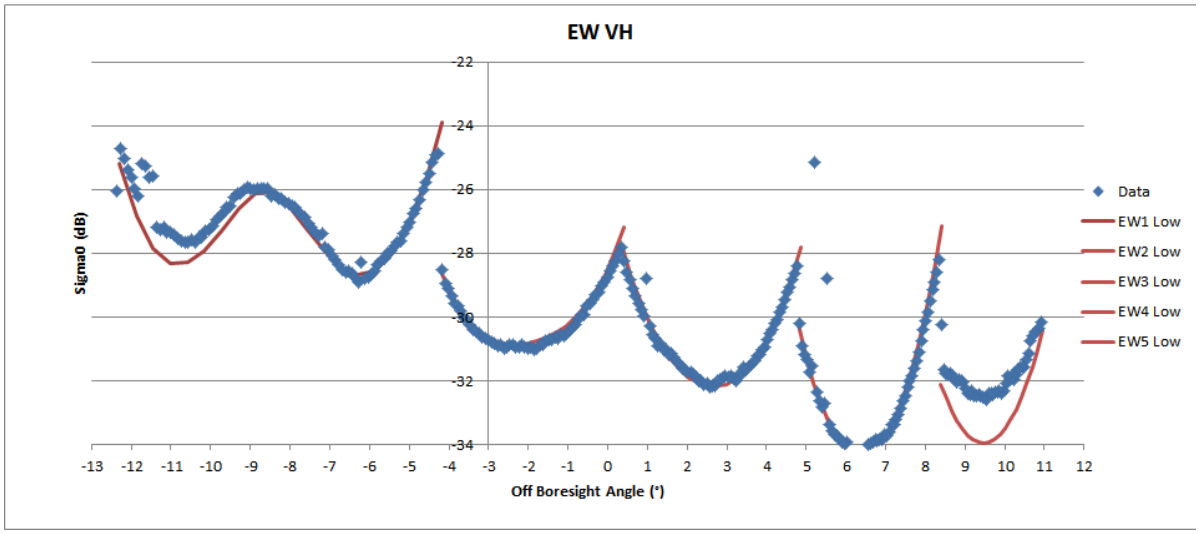

S1B_EW_GRDH_1SDV_20160721T060456_20160721T060611_001259_0014E6_9436.SAFE

Figure 83: NESZ measures for EW. Blue is the measured NESZ and the red lines are the predicted NESZ at the minimum orbital altitude.

Figure 84 shows the measured WV VV NESZ met the -22 dB requirement and they are all slightly better than the predicted NESZ. Note the NESZ is significantly higher for imagette WV2 than for WV1. For WV1 VV there is some structure in the imagette which accounts for the structure in the NESZ measurement in the far range portion of the imagette. The number after the file name refers to the imagette number within the product. Note that no HH imagettes were available during the S-1B commissioning phase.

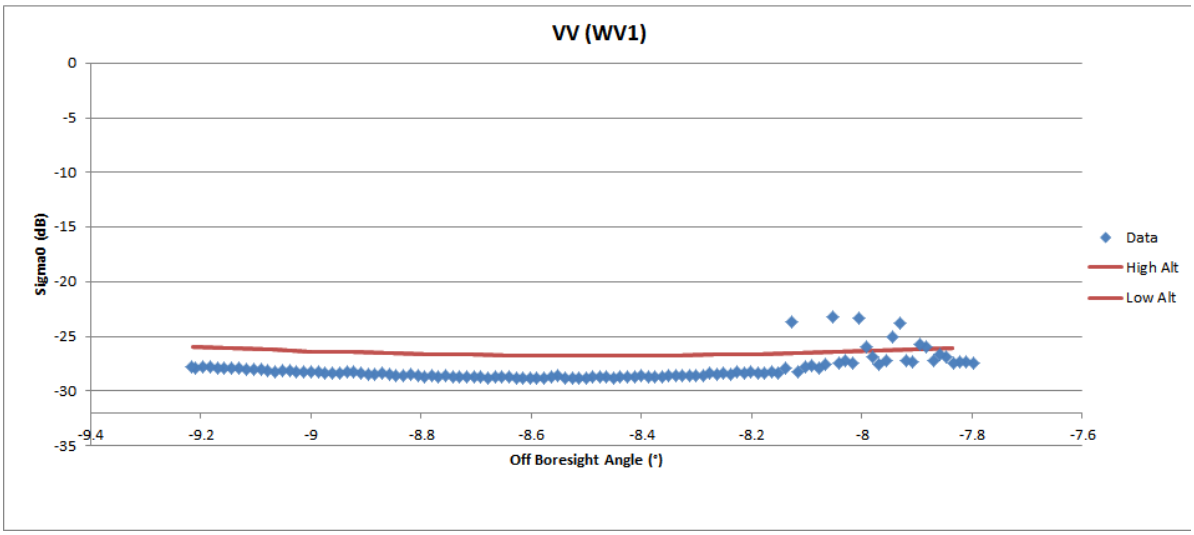

S1B_WV_SLC__1SSV_20160814T060509_20160814T061019_001609_0022B2_3B38.SAFE (17)

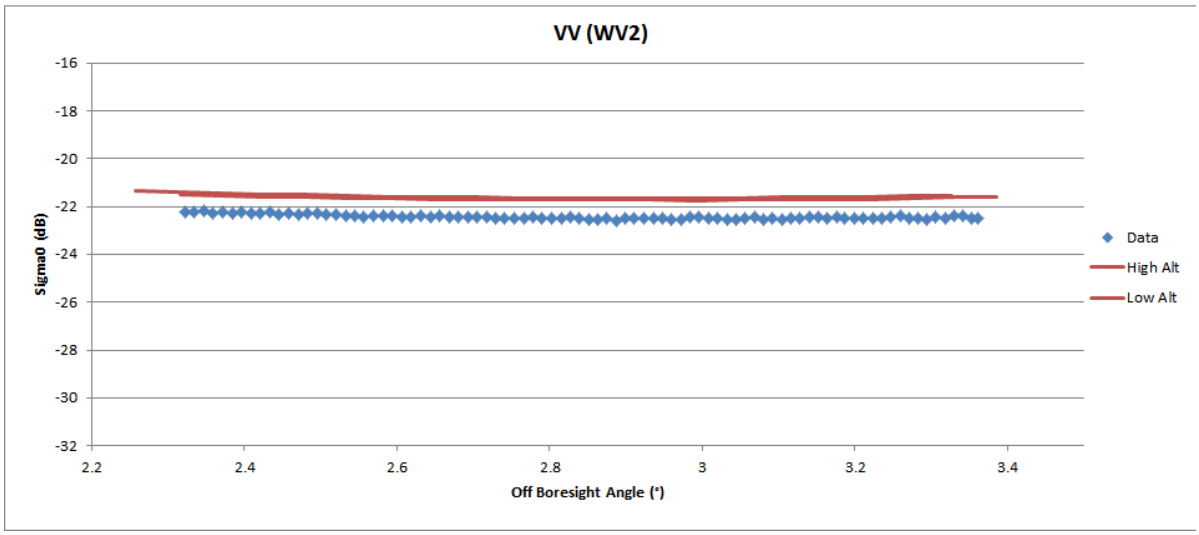

S1B_WV_SLC__1SSV_20160815T055021_20160815T062716_001623_00235E_1623.SAFE (88)

Figure 84: NESZ measures for WV . Blue is e measured NESZ and the red lines are the predicted NESZ at minimum and maximum orbital altitudes.

6.2.9. Summary of Anomalies

6.2.9.1. Radio Frequency Interference

As observed for S-1A, a small percentage of S-1B imagery is affected by the presence of Radio Frequency Interference from the ground. An example is shown below. Usually RFI only affects a few range lines of raw data.

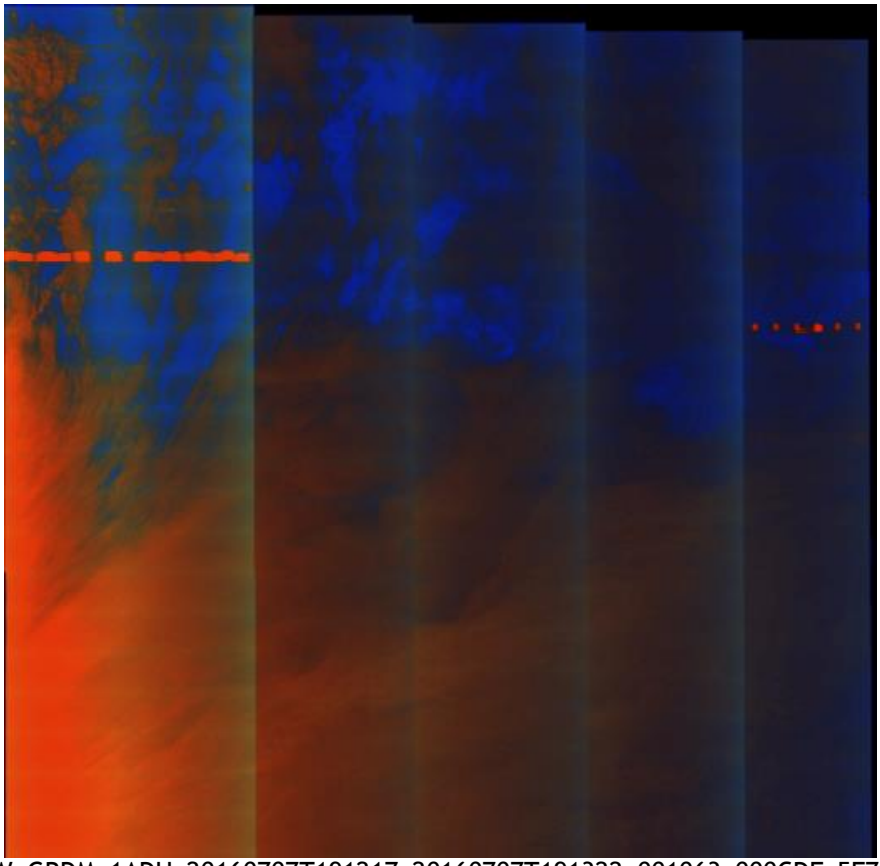

S1B_EW_GRDM_1ADH_20160707T191217_20160707T191322_001063_000CDF_5F73.SAFE

Figure 85: An example of Radio Frequency Interference

6.2.9.2. Radarsat-2/Sentinel1-A Mutual Interference

Also as observed for S-1A, a small percentage of S-1B imagery is affected by mutual interference between S-1B and Radarsat-2. An example is shown below:

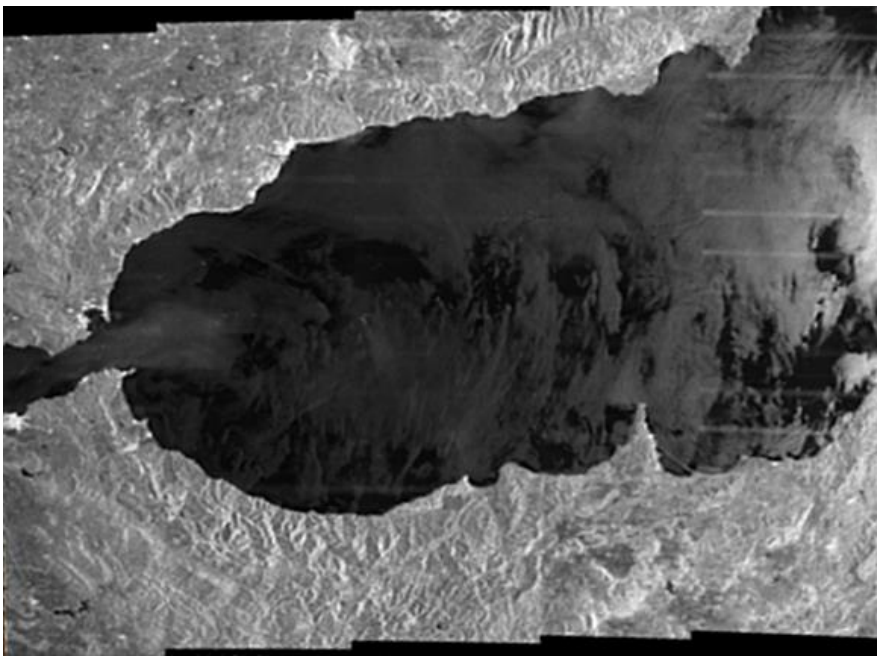

Figure 86: An example of Radarsat-2/Sentinel1-A Interference (2nd July 2016)

6.2.10. Quality Disclaimers

Quality disclaimers issued during 2016 are given in Appendix H -.

6.3. S-1B Level 2 products

6.3.1. Wind measurement

6.3.1.1. Image Mode (SM-IW-EW)

The SAR wind measurement is strongly dependant of the product calibration accuracy. Before the products delivery to the end user, the L1 processing parameters has been optimized in order to improve beam to beam of set, EAP ... It takes benefit from the efforts made on the SAR Level1 products to improve the calibration constant and align the gamma profile as the function of the elevation angle over Rain Forest.

Statement of the wind measurements accuracy:

The strategy to assess the accuracy of the wind retrieval is the same as S-1A, consisting in comparing it with an auxiliary wind source (buoys, scaterrometters, atmospherical model...) which is used as a reference.

Figure 87 presents the performances achieved on the last months of 2016 (October/November/December) for IW mode in VV polarisation of the retrieved wind compared to model references (Arome, Arpege and ECMWF). The statistics are close to the ones observed on S-1A. It can be noticed the strong correlation of the SAR-derived wind speeds with the wind references. The bias and the RMS are less important for ECMWF re-analysis since the wind inversion is based on the ECMWF forecast as an a priori wind input. A typical RMS of 1.5m/s to 2m/s is observed. The quality of the wind product derived for this mode is fairly good. Same kind of performances (bias nearly equal to zero and RMS of about 2m/s) is achieved on EW HH mode.

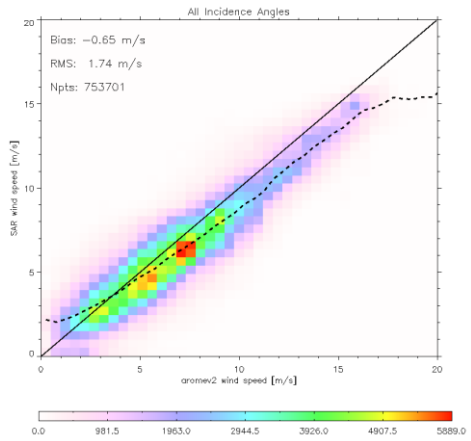

a) Arome

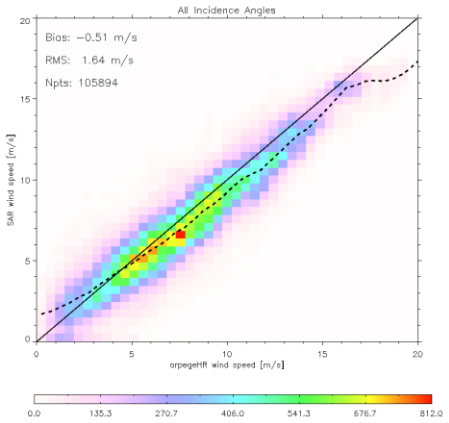

b) Arpege HR

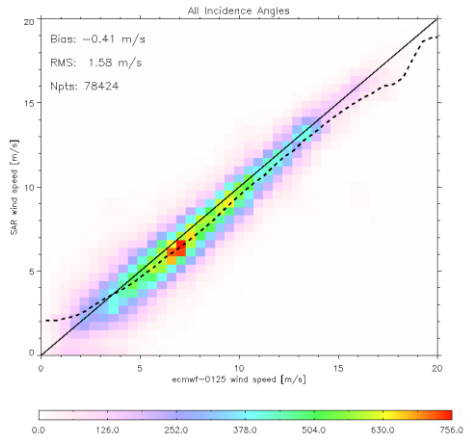

c) ECMWF

	bias	Rms
Arome	-0.65 m/s	1.74m/s
Arpege	-0.51 m/s	1.64 m/s
ECMWF	-0.41m/s	1.58 m/s

Figure 87: SAR Wind speed compared with reference wind speed for IW mode VV polarisation.

Improvement performed during 2016:

The data delivery to the end users has happened on the end of September. No change in the configuration and processing has been done since.

Coming Improvements for 2017:

No changes specific to S-1B is planned during 2017. The changes described on S-1A Wind measurement assessment paragraph are related to the processor and then will be applied on S-1B as well. Please refer to this section 4.3.1.1 for more details

6.3.1.2. Wave Mode

2016 also offers the first data set for Sentinel-1 B. However, the commissioning phase officially ended 9 months after the launch date, the 25th of November 2016. A preliminary assessment of the Level-2 products performances is thus possible relying on December.

For level-2 products as measured by Sentinel-1 B, the major changes are:

- Update of the processing gains coefficients. This mostly impacts performances on ocean surface wind speed (oswWindSpeed)

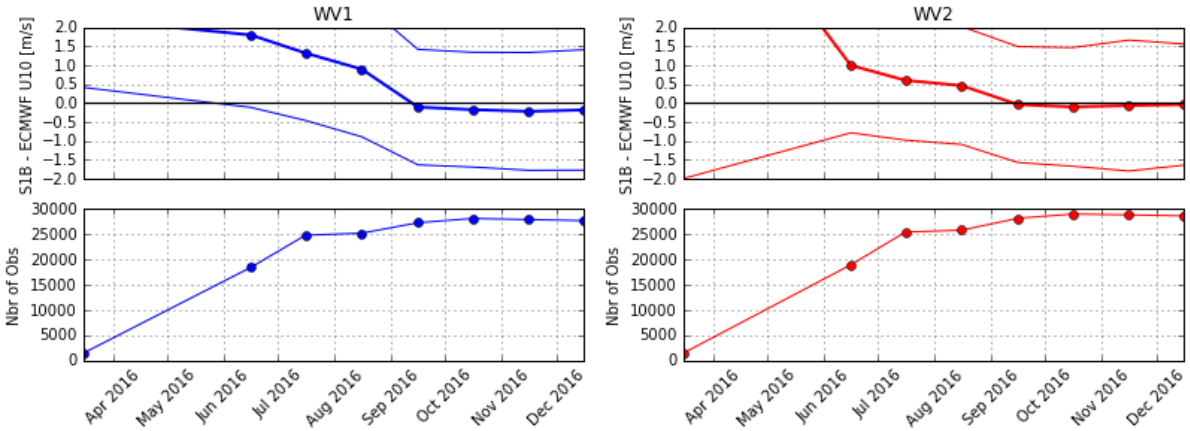

Figure 88 S-1B WV1 and WV2 wind speed performances as function of time. Ocean surface wind monthly performances for WV1 (top-left) and WV2 (top-right) and number of acquisitions co-located to reference data for validation for WV1 (bottom-left) and WV2 (bottom- right). For top panels, colored thick solid lines stand for the mean difference between Sentinel-1 and ECMWF model wind speeds. Colored thin solid lines are for standard deviation.

Figure 88 shows the monthly performances with respect to time in 2016 for WV1 and WV2. Top panel presents the bias and the standard deviation for the wind speed. Bottom panel presents the number of acquisitions and bottom panel the mean and median wind speed from ECMWF model. The bias is computed by comparing the wind speed from Sentinel-1 and the wind speed from ECMWF analysis (3 hours and 0.125 degrees). An example for December 2016 is shown on Figure 89.

As shown on Figure 88, the wave mode has been activated at global scale over the oceans since July, producing a comprehensive number (between ~20000 and 27000 for both WV1 and WV2 each month) of acquisitions every cycle.

Figure 88 shows a significant change in the wind speed bias after September 2016. This corresponds to a change in the processing gain coefficients. We observe that after September 2016 bias remain lower than -0.2 m/s and around 0. m/s, respectively for WV1 and WV2. Standard deviation values are lower than 1.7 m/s for both WV1 and WV2. These results are within the specifications and very consistent with Sentinel-1 A. In the contrary of S-1A, no trend can be derived from these analyses as the time series are too short.

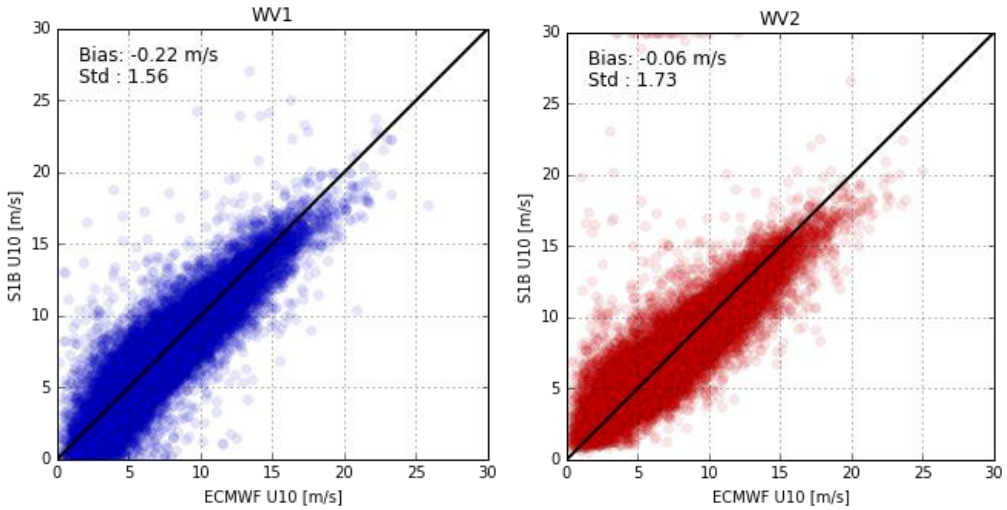

Figure 89: Scatter plot of wind speed from S-1B WV1 versus ECMWF Dec 2016. The model outputs are considered as reference here. This is only valid from a statistical point of view.

Coming improvements for 2017:

Further analysis will be conducted to monitor the quality of the wind speed (oswWindSpeed) with respect to time. A complete year will allow to exhibit possible seasonal trend or drift in the performances.

6.3.2. Swell Measurement

6.3.2.1. Wave Mode

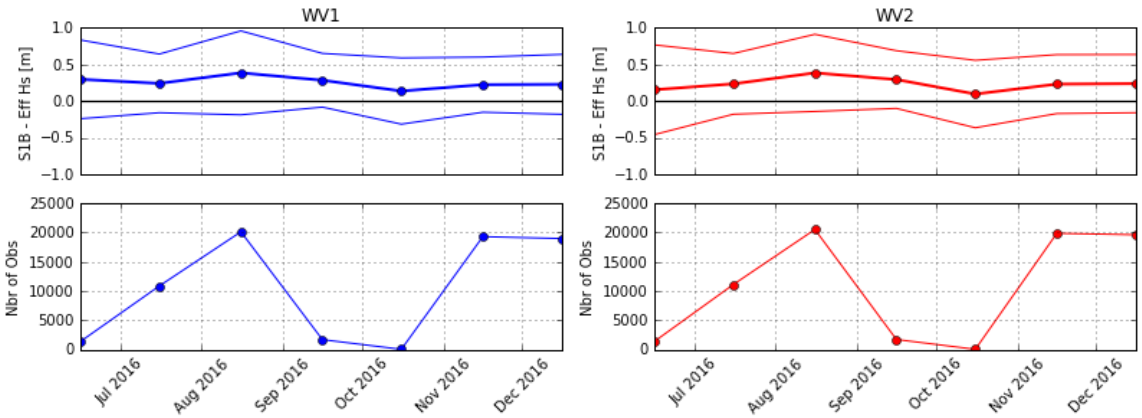

Figure 90 S-1B WV1 Ocean Swell monthly performances as function of time. For top panels, colored thick solid lines stand for the mean difference between effective significant wave height from Sentinel-1 and from WW3 model. Colored thin solid lines are for standard deviation.

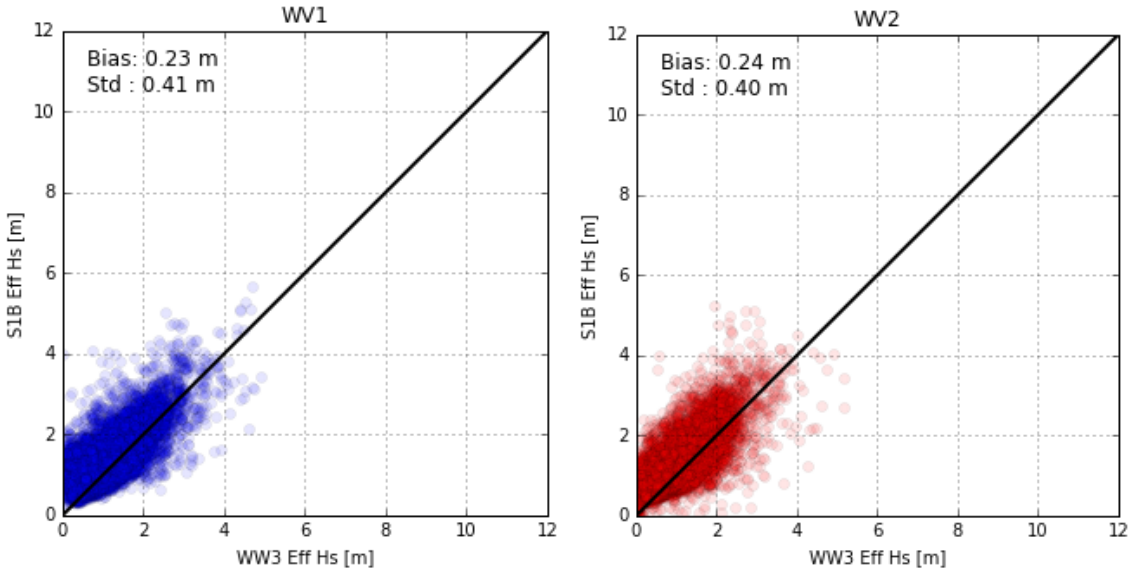

Figure 91: Significant wave height for the long waves performances for December 2016 in Wave Mode 1. The model outputs from WW3 are considered as reference here. This is only valid from a statistical point of view.

Coming improvements for 2017:

- As S-1B and S-1A have very close behaviour, same actions are foreseen.
- As for Sentinel-1 A, the observed change in September 2016 will be further investigated
- As for Sentinel-1 A, in some cases the quality of the ocean swell spectrum is degraded. In particular
    - Azimuth cut-off is a key parameter for the wave inversion. The quality of its estimate will be investigated.
    - Heterogeneity in the SAR scene may impact the swell retrieval.

  We will propose a quality flag combining both heterogeneity and azimuth cut-off parameters (other may be added) to filter out cases where ocean swell measurement is not optimal.

6.3.3. Radial Velocity Measurement

6.3.3.1. Wave Mode

Statement of the ocean surface radial velocities measurements accuracy:

As shown for Sentinel-1A, (see section 4.3.3), we observe the same issue with the geophysical Doppler shift as derived from the different Doppler components included in the Level-2 products. However, Figure 92 and Figure 93 show that the geophysical Doppler as obtained with S-1B exhibits less non-geophysical variability than what is observed with S-1A.

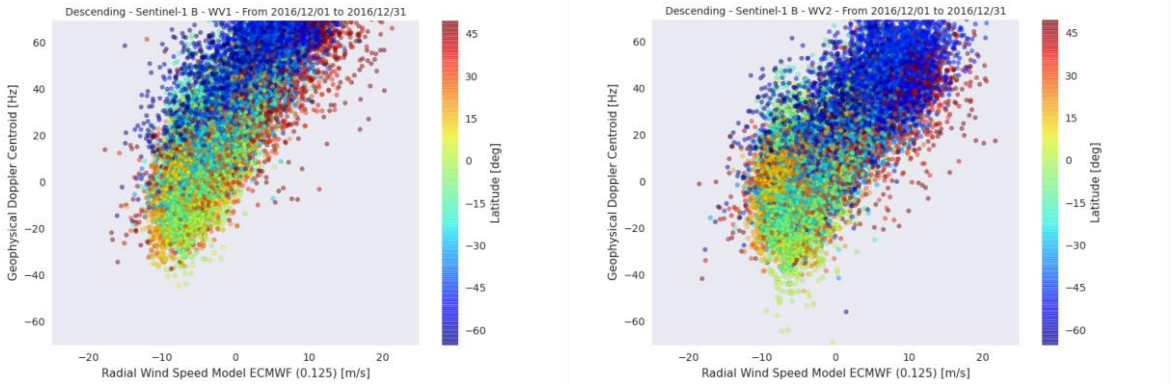

Figure 92 Geophysical Doppler as included in the Level 2 products as a function of radial wind speed (wind speed projected in the line of sight of the radar) for WV1 and WV2 December 2016. The color code indicates the latitude. Only Descending orbits are taken into account.

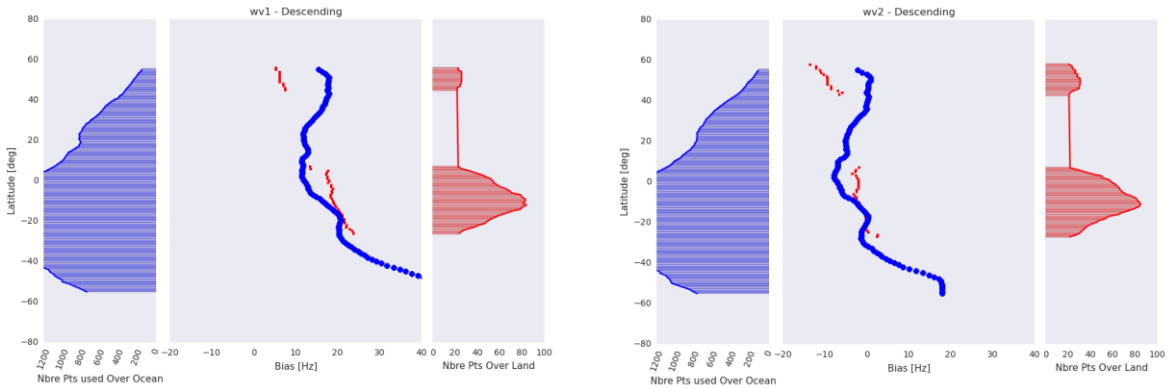

(WV1) (WV2)

Figure 93 Doppler WV1 and WV2 bias as a function of latitude estimated over ocean (blue) and land (red).

The differences (around 10Hz) observed in the land Doppler between wv1 and wv2, as shown in Figure 93, can be well predicted by the recent antenna model.

A dedicated investigation was performed to understand the attitude DC of the Sentinel 1b mission. One month (October 2016) of S-1B WV data were used. A data driven approach to simultaneously model and solve for the geophysical and geometric DC were developed, implemented and validated. The model performance shows an accuracy of predicting the attitude DC to around 3Hz when compared to land data (see next plot Figure 94).

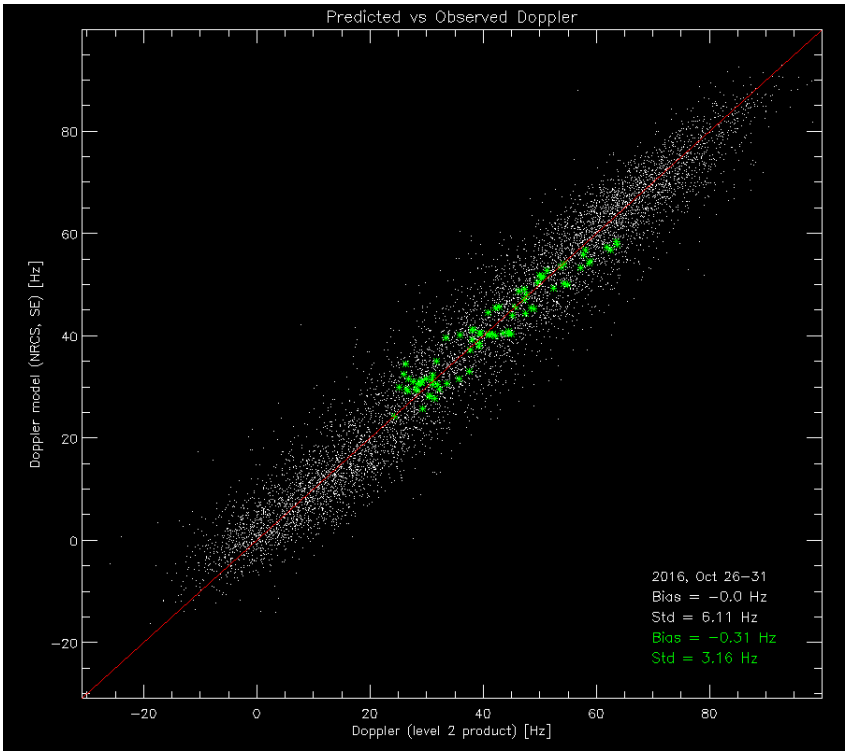

Figure 94: Scatter plot of total DC model versus measured DC from the period of 26-31 October 2016 from S-1B acquired in WV1. The green dots are data acquired over land areas.

The data driven approach revealed oscillations in the attitude DC on orbit scale with amplitude of up to 20Hz and main period of around 400 sec. The estimated geometric DC has been compared with attitude DC computed directly from restituted quaternions provide by ESA. The comparison is shown in Figure 95.

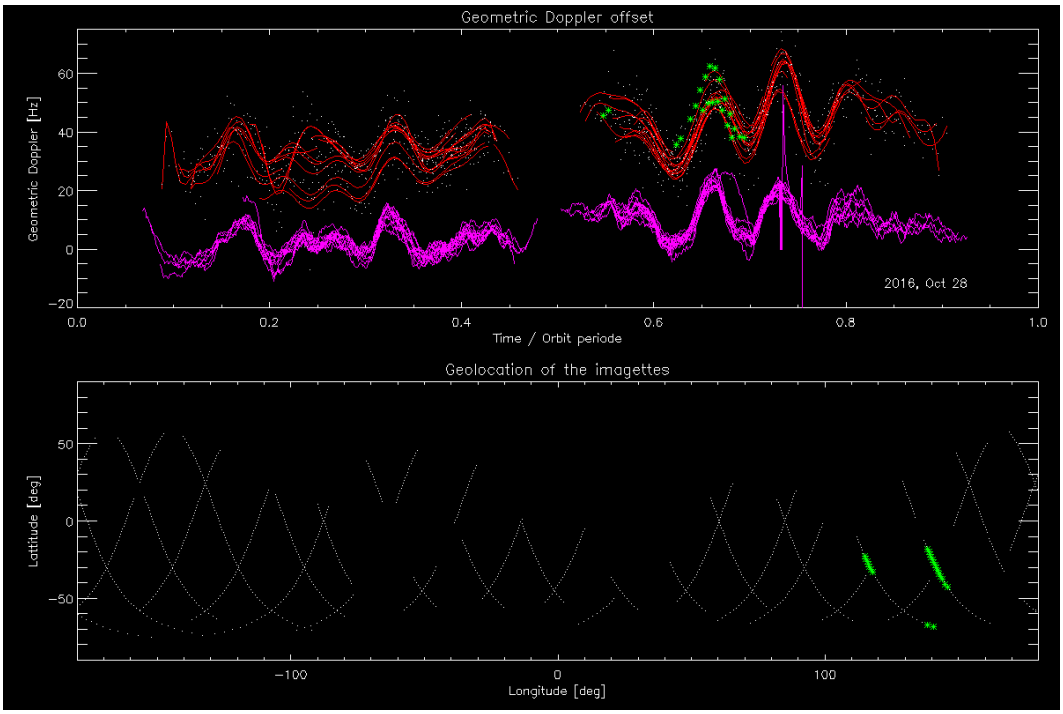

Figure 95: Upper: Geometric Doppler computed from data (red) and from restituted attitude data (pink) for 28 October 2016 for Sentinel 1b WV1. Lower: Location of tracks. The green points are data acquired over land areas.

Improvement performed during 2016: None

Coming improvement for 2017:

We have the same recommendation for both S-1A and S-1B regarding the radial velocity processing (see section 4.3.3).

The radial velocity measurement is derived from the Geophysical Doppler anomaly. In the S-1 IPF, this geophysical Doppler is estimated by:

$$F_{dc_{RVL}} = F_{dc_{SAR}} - F_{dc_{attitude}} - F_{dc_{antenna}}$$

where:

- FdcSAR is estimated from the SAR data
- FdcOcean is the component related to the ocean radial velocities.
- FdcAttitude is estimated from the geometry knowledge (quaternion based)
- Fdcantenna is the antenna contribution related to TRM drifts, failures, misalignements, etc

At global scale, the expected relationship between the geophysical Doppler and the sea state (or ocean surface wind vector) is well known since Envisat/ASAR. The performances of the geophysical Doppler are assessed by estimating the bias between the expected Doppler given the sea state conditions (provided by ECMWF) and the geophysical Doppler as included in the Level 2 products.

6.3.3.2. TOPS Mode

Statement of the ocean surface radial velocities measurements accuracy:

As for Wave Mode, the contamination of the geophysical Doppler by the geometry knowledge (quaternion based) and the antenna contribution prevents us for getting any quantitative geophysical signature such as ocean surface currents in the product. Nevertheless, in cases where land areas are present in the image an ad-hoc DC calibration has been performed. An example is shown in next figure.

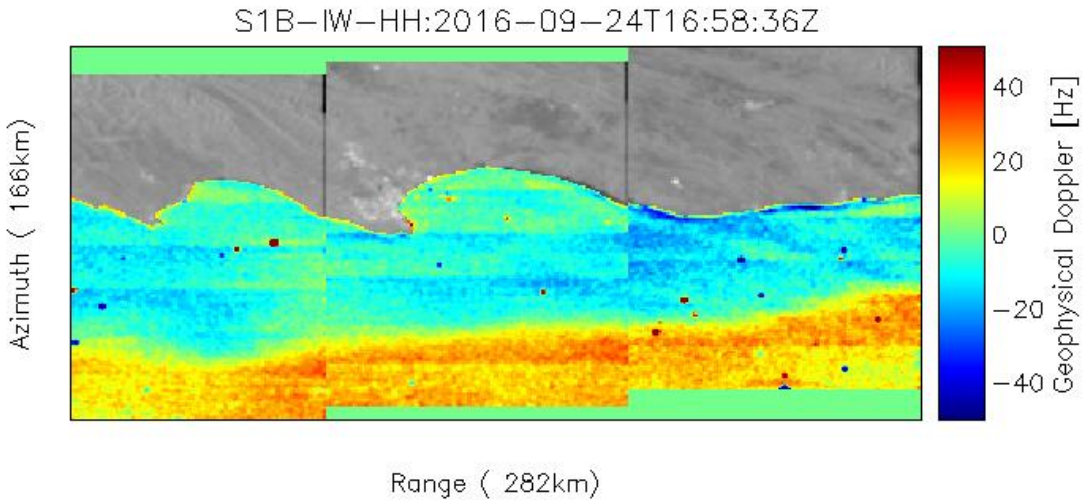

Figure 96: Doppler anomaly field from Sentinel 1B IW OCN RVL product acquired over Agulhas in ascending mode. Here land areas are used to calibrate the Doppler. A clear signature of the Agulhas current is observed.

Azimuth scalloping in the DC over the bursts are also observed in S-1B. This is similar to what is observed in S-1A IW and EW modes. The scalloping is quantified to be around ±5 Hz amplitude as shown in Figure 97.

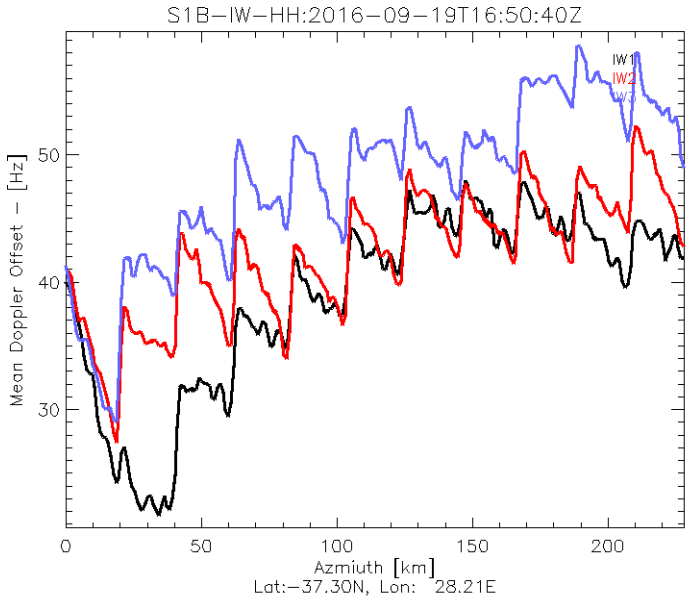

Figure 97: S-1B IW OCN RVL mean DC bias as function of azimuth pixel. Data acquired over ocean areas.

Improvement performed during 2016:

Efforts are undertaken to better predict and compensate the measured Doppler for the electromagnetic (EM) Doppler bias introduced by the skewness of the antenna elevation pattern. A new version of the antenna model parameters has been ingested into the Level 2 processor and the EM Doppler bias over IW and EW swaths are compared with the data driven Doppler estimated over rain forest areas (see next figure).

We note that the performance of the antenna model is not as good as for S-1A.

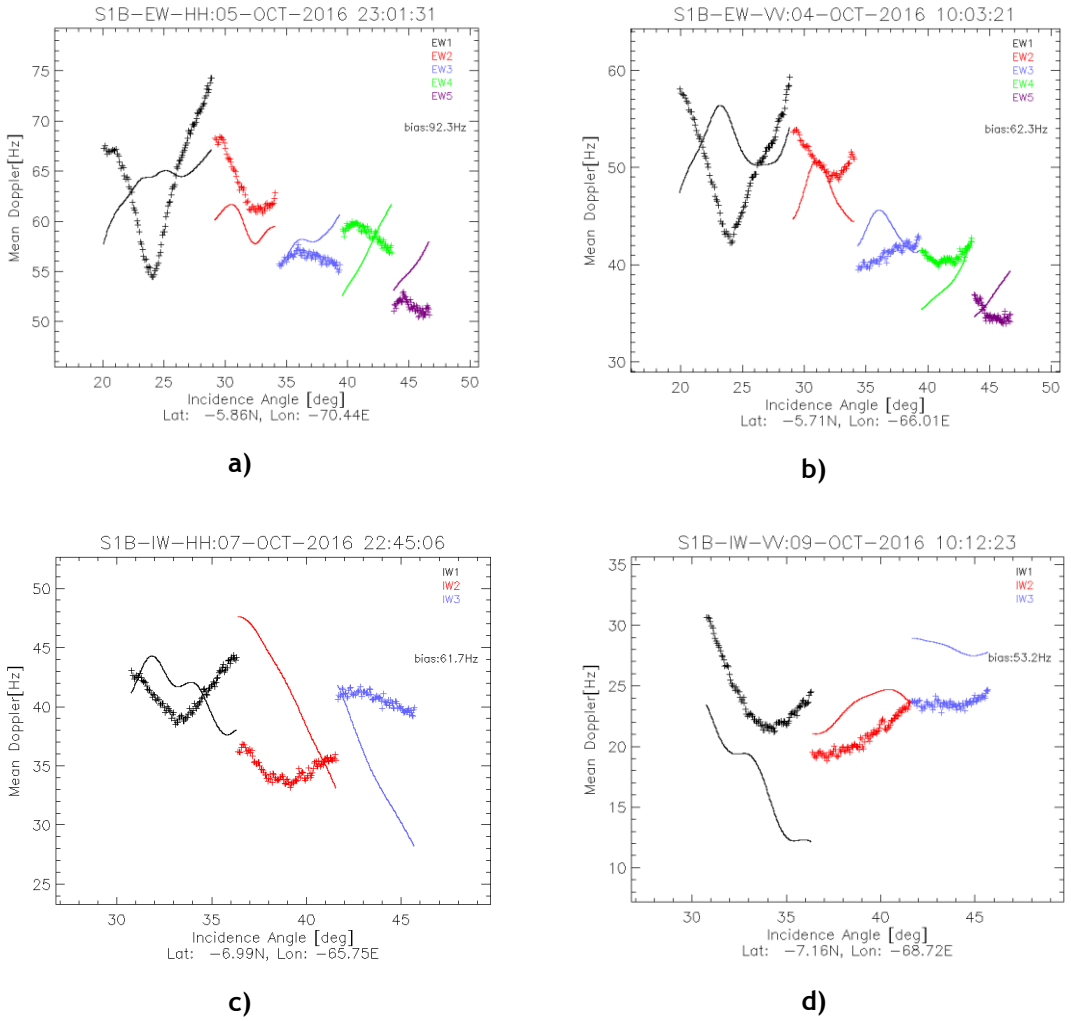

Figure 98: S-1B EM DC offset computed from antenna model (full line) with error matrix corresponding to the day of acquisition, and estimated from rain forest data using the Level 2 processor (***). A) EW mode in HH-polarisation, B) EW mode in VV-polarisation, C) IW mode in HH-polarisation, D) IW mode in VV-polarisation

Coming Improvements for 2017:

Improve the descalloping of S-1B IW and EW OCN DC data.

6.3.4. Geophysical Calibration

6.3.4.1. Wave Mode

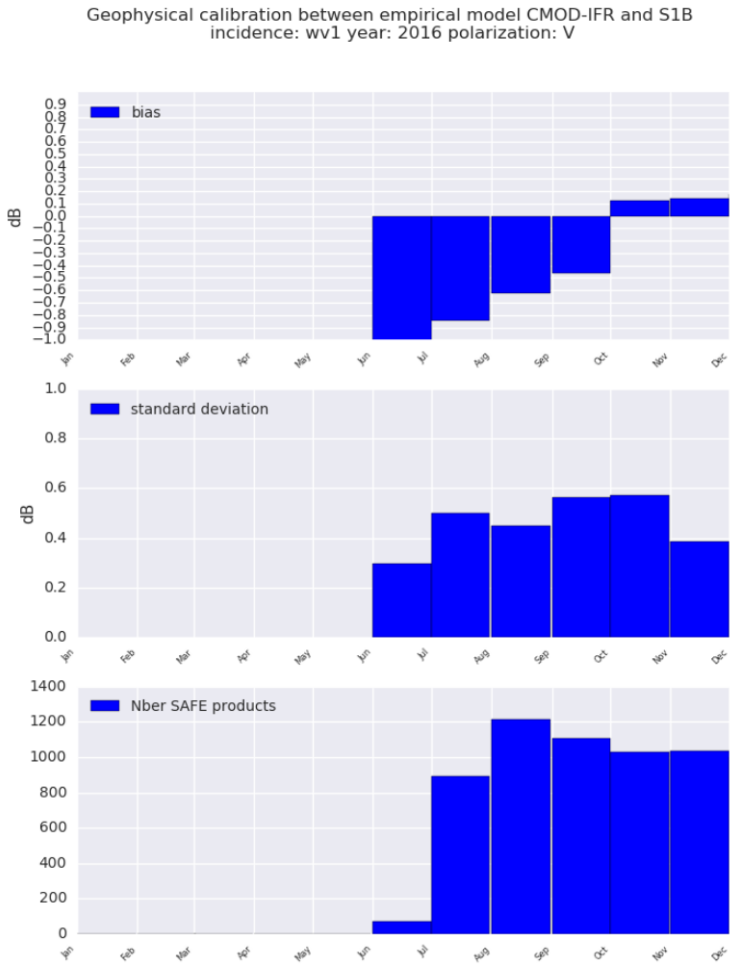

Figure 99 Sentinel-1B geophysical calibration constant given by CMOD-IFRv2 for WV1 VV polarisation between 50° and -50° latitude. Panel 1 shows the mean bias between ECMWF and Sentinel-1B. Panel 2 shows the bias standard deviation. Panel 3 shows the number of SAF SAFE used to perform the analysis.

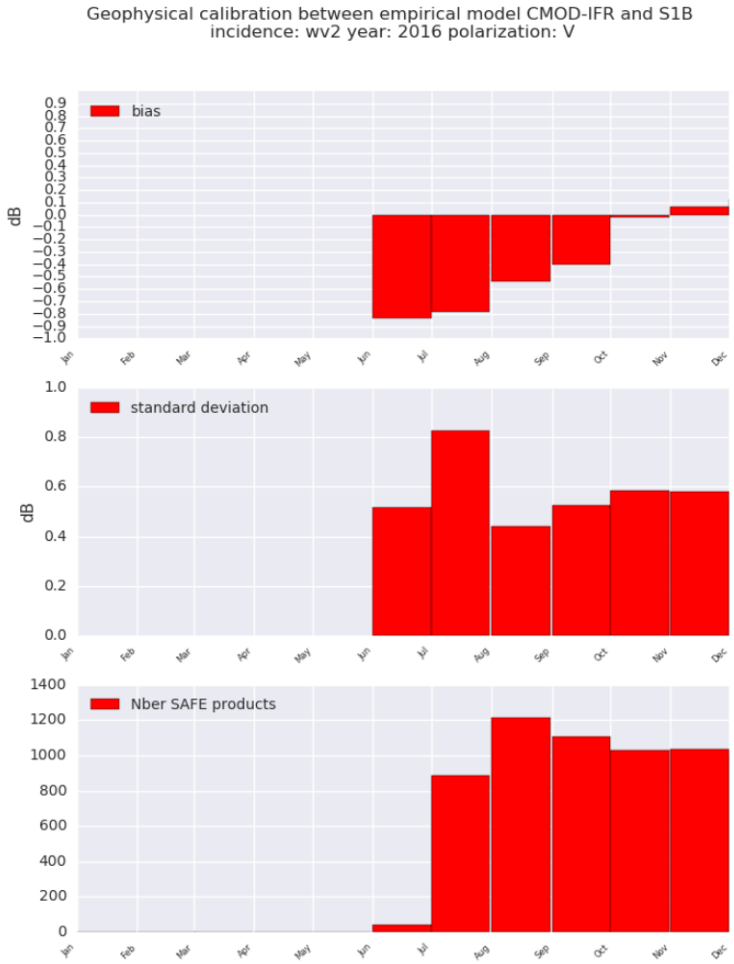

Figure 100 Sentinel-1B geophysical calibration constant given by CMOD-IFRv2 for WV2 VV polarisation between 50° and -50° latitude. Panel 1 shows the mean bias between ECMWF and Sentinel-1B. Panel 2 shows the bias standard deviation. Panel 3 shows the number of SAFE used.

As shown in Figure 99 and Figure 100, S-1B calibration has been corrected during the first 4 months (June-Sept) to reach values around 0dB in December. As for S-1A calibration, there is a standard deviation bump (~0.1dB) occurring during Oct-Nov-December. There is no particular performance difference regarding the incidence angles. It is impossible to status on a potential drift since the time series are too short.

7. S-1A and S-1B Cross-comparison

7.1. Cross-platform Permanent Scatter Calibration

The following shows a recent IW VV Permanent Scatter Calibration series over Paris. The series covers the whole 2016 and includes both S-1A and S-1B acquisitions, in order to perform a cross-calibration between the sensors. The blue dots (S-1A) show, after the tile 11 issue (June 2016), a small reduction of the calibration constant (about 0.1 dB). The red dots show that the calibration constant for S-1B is around 0.05 dB. The S-1B calibration constant is well aligned with S-1A values before tile 11 issue. After the issue a very small radiometric imbalance can be observed (around 0.15 dB).

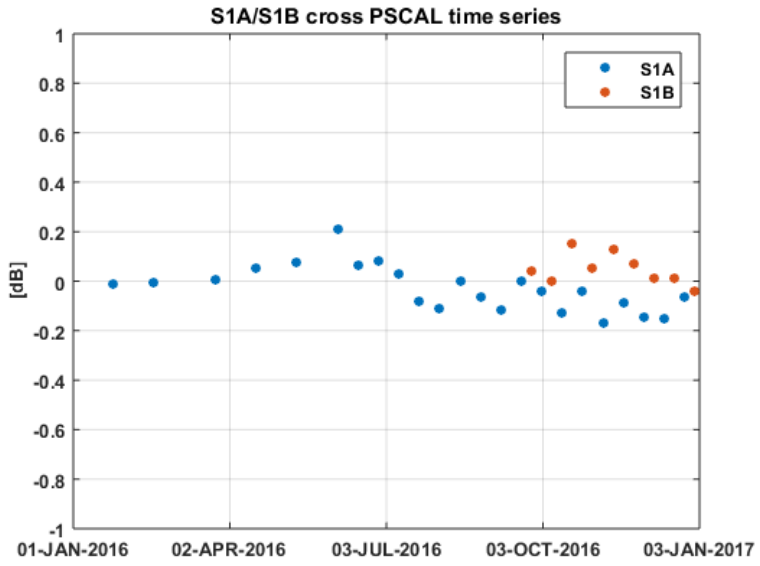

Figure 101 PSCAL time series for IW DV acquisitions over Paris. The colour represents the sensor.

7.2. Cross-interferometry burst synchronization

The burst synchronization between repeat pass interferometric acquisitions is relevant for the TOPSAR modes (IW and EW) to provide an indication of the quality of the interferometric phase that can be expected. The SAR acquisition start time is planned over a discrete set of points round orbit with precision down to milliseconds. The performance of the synchronization is monitored by the PDGS OBS tool.

The S-1A and S-1B constellation offers the possibility to perform repeat pass interferometry at 6 days temporal baseline. The following figure shows the S-1B vs. S-1A burst synchronization over time for IW and EW mode. Each dot represents a S-1B repeat pass acquisition, considering as reference cycle number the S-1A cycle number 60 (30 September - 12 October 2015). Note that overall synchronization, even though slightly worse than single sensor, is still very good.

Figure 103 shows the S-1B vs. S-1A burst synchronization distribution for IW and EW separately. It can be noticed that the synchronization is above 98% for most of the acquisitions.

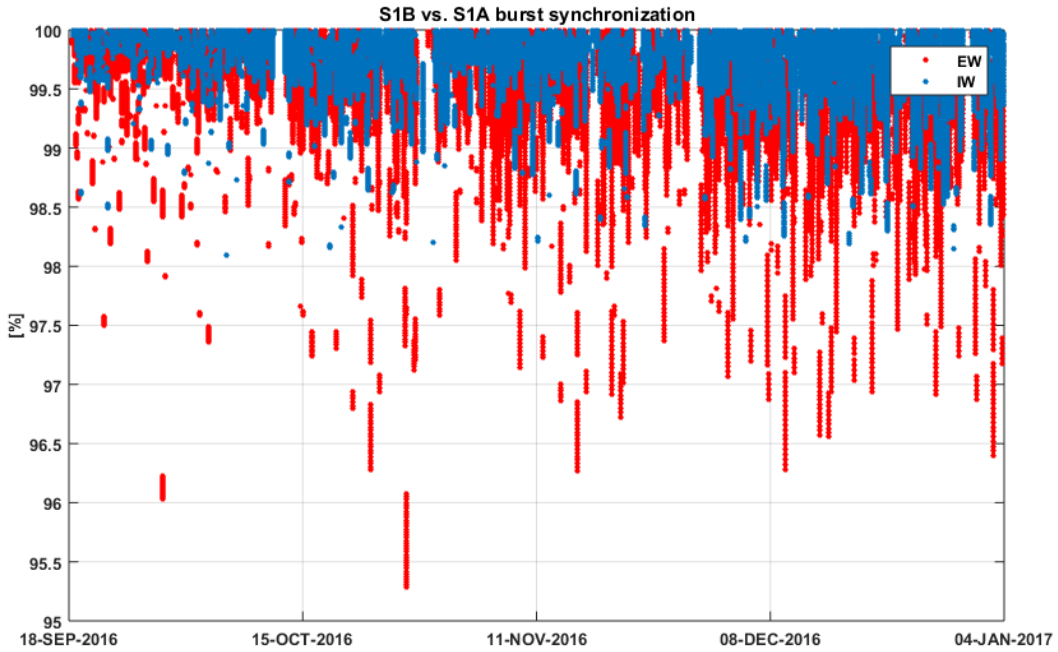

Figure 102 S-1B vs. S-1A burst synchronization since the end of the Commissioning Phase.

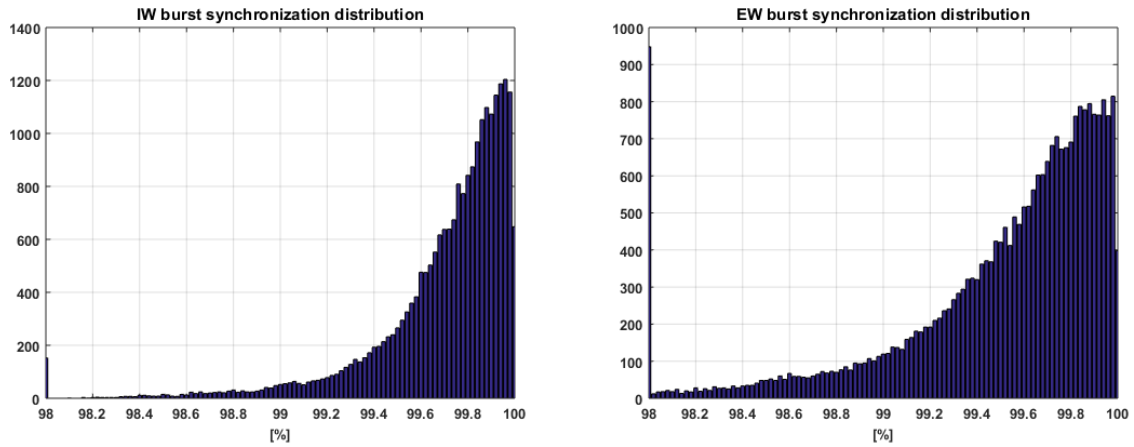

Figure 103 S-1B vs. S-1A burst synchronization statistics for IW (left) and EW (right).

7.3. Absolute Calibration

As explained in Sections 4.2.3.1and 6.2.3.1, the BAE corner reflector has been used for absolute calibration. Figure 104 shows the relative RCS of the corner reflector during 2016. Like the above permanent scatter results shown above, a reduction in the S-1A relative RCS can be seen after the S-1A tile 11 issue (June 2016).

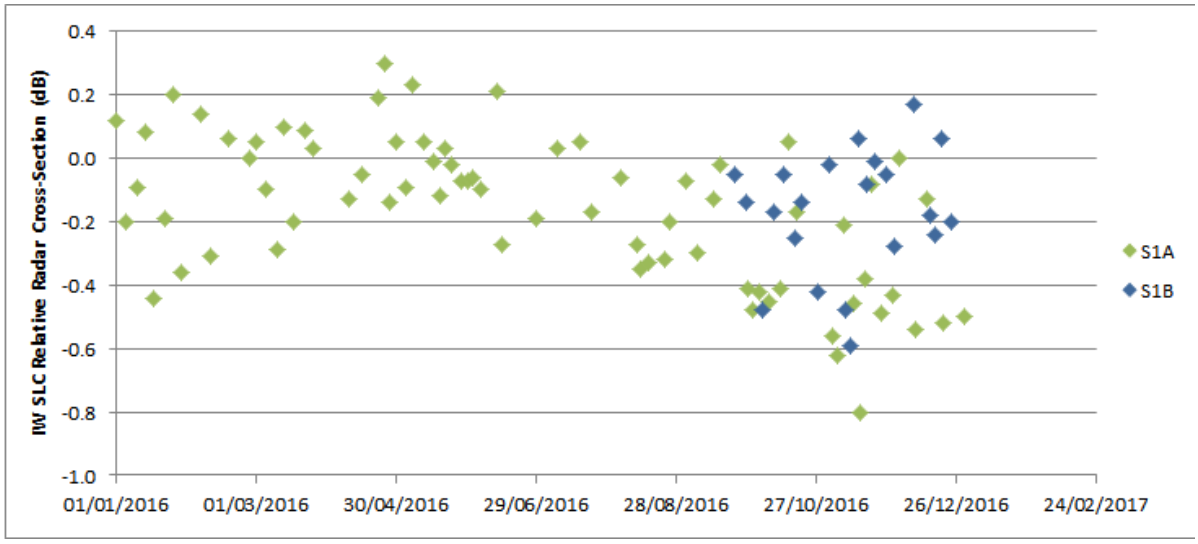

Figure 104: S-1A and S-1B IW SLC Relative Radar Cross-Section for the BAE Corner Reflector

Appendix A - **List of Acronyms**

AD	Applicable Document
ADF	Auxiliary Data File
CFI	Customer Furnished Item
DC	Doppler Centroid
ECMWF	European Centre for Medium-Range Weather Forecasts
ENL	Equivalent Number of Look
FDBAQ	Flexible Dynamic Block Adaptive Quantisation
IRF	Impulse Response Function
NESZ	Noise Equivalent Sigma Zero
PDGS	Payload Data Ground Segment
PG	Power x Gain
PSC	Permanent Scatterers Calibration
QCSS	Quality Control SubSystem
RD	Reference Document
RDB	Radar DataBase
RFC	Radio Frequency Characterization mode
RFI	Radio Frequency Interference
SAR	Synthetic Aperture Radar
STT	STar Tracker
TBC	To be confirmed
TBD	To be defined
TRM	Transmit Receive Module

Appendix B - **ESA S-1A & S-1B Technical Reports**

The following ESA S-1A & S-1B Technical Reports were issued during 2016:

- Sentinel-1A Tile #11 Failure, OI-MPC-OTH-0324, Issue 1.2, October 2016
- Sentinel-1A Debris Collision, DI-MPC-ACR-0352, Issue 1.0, October 2016

Appendix C - **S-1A Orbit Cycles**

The table below gives the cycle number with start and stop acquisition dates during 2016. The start of a cycle is at approximately 18:00 UT on the dates below.

Cycle	Start Date	End Date
69	16/01/2016	28/01/2016
70	28/01/2016	09/02/2016
71	09/02/2016	21/02/2016
72	21/02/2016	04/03/2016
73	04/03/2016	16/03/2016
74	16/03/2016	28/03/2016
75	28/03/2016	09/04/2016
76	09/04/2016	21/04/2016
77	21/04/2016	03/05/2016
78	03/05/2016	15/05/2016
79	15/05/2016	27/05/2016
80	27/05/2016	08/06/2016
81	08/06/2016	20/06/2016
82	20/06/2016	02/07/2016
83	02/07/2016	14/07/2016
84	14/07/2016	26/07/2016
85	26/07/2016	07/08/2016
86	07/08/2016	19/08/2016
87	19/08/2016	31/08/2016
88	31/08/2016	12/09/2016
89	12/09/2016	24/09/2016
90	24/09/2016	06/10/2016
91	06/10/2016	18/10/2016
92	18/10/2016	30/10/2016
93	30/10/2016	11/11/2016
94	11/11/2016	23/11/2016
95	23/11/2016	05/12/2016
96	05/12/2016	17/12/2016
97	17/12/2016	29/12/2016
98	29/12/2016	10/01/2017

Appendix D - **S-1A Transmit Receive Module Failures**

The following S-1A antenna Transmit/Receive Modules (TRMs) failed during 2016 (a full list since launch can be found in Appendix B - of any S-1A N-Cyclic Performance Report):

TRM	Description	Date of Failure
Tile 11, Rows 1 to 10	Tx H, Tx V	16 June - 27 June 2016

Appendix E - **S-1A Instrument Unavailability**

The S-1A instrument was unavailable during 2016 (a full list since launch can be found in Appendix C - of any S-1A N-Cyclic Performance Report):

Start Date/Time	End Date/Time	MPC Reference	Summary
02/01/2016 04:45	02/01/2016 15:14	SOB-255	Sentinel-1A Unavailability on 02/01/2016
16/01/2016 14:59	16/01/2016 19:57	SOB-257	Sentinel-1A Unavailability on 16/01/2016
21/02/2016 18:17	22/02/2016 10:51	SOB-310	Sentinel-1A Unavailability from 21/02/2016 to 22/02/2016
13/03/2016 08:23	13/03/2016 16:14	SOB-332	Sentinel-1A Unavailability on 13/03/2016
15/03/2016 07:46	15/03/2016 09:36	SOB-340	Sentinel-1A Planned Maintenance on 15/03/2016
06/05/2016 21:17	07/05/2016 14:27	SOB-389	Sentinel-1A Unavailability from 06/05/2016 to 07/05/2016
22/05/2016 14:51	22/05/2016 18:11	SOB-411	Sentinel-1A Unavailability on 22/05/2016
16/06/2016 05:59	16/06/2016 13:57	SOB-447	Sentinel-1A Unavailability on 16/06/2016
16/06/2016 16:45	17/06/2016 11:26	SOB-448	Sentinel-1A Unavailability between 16/06/2016 and 17/06/2016
17/06/2016 11:45	27/06/2016 16:32	SOB-467	Sentinel-1A Unavailability between 17/06/2016 and 27/06/2016
02/07/2016 04:52	02/07/2016 13:23	SOB-476	Sentinel-1A Unavailability on 02/07/2016
10/07/2016 06:39	10/07/2016 17:51	SOB-483	Sentinel-1A Unavailability on 10/07/2016
11/07/2016 21:32	12/07/2016 12:05	SOB-507	Sentinel-1A Unavailability on 11/07/2016
27/07/2016 07:49	27/07/2016 15:42	SOB-508	Sentinel-1A Unavailability on 27/07/2016
27/08/2016 23:58	28/08/2016 09:45	SOB-533	Sentinel-1A Unavailability from 27/08/2016 to 28/08/2016
24/11/2016 20:38	25/11/2016 11:34	SOB-614	Sentinel-1A Unavailability from 24/11/2016 to 25/11/2016
04/12/2016 06:52	04/12/2016 11:07	SOB-624	Sentinel-1A Unavailability on 04/12/2016

Appendix F - **S-1A Auxiliary Data Files**

The following S-1A Auxiliary Data Files (ADFs) were updated during 2016:

Instrument ADF (AUX_INS)

ADF	Update Reason
S1A_AUX_INS_V20140406T133000_G20160215T161024.SAFE	Updated PG model and default noise values related to RDB#1.
S1A_AUX_INS_V20140616T135500_G20160215T161549.SAFE	Updated PG model and default noise values related to RDB#2.
S1A_AUX_INS_V20140915T100000_G20160215T161938.SAFE	Updated PG model and default noise values related to RDB#3.
S1A_AUX_INS_V20150519T120000_G20160215T162440.SAFE	Updated PG model and default noise values related to RDB#4.
S1A_AUX_INS_V20150722T120000_G20160215T163523.SAFE	Updated PG model and default noise values related to RDB#5.

Calibration ADF (AUX_CAL)

ADF	Update Reason

L1 Processor Parameters ADF (AUX_PP1)

ADF	Update Reason
S1A_AUX_PP1_V20150722T120000_G20160413T100954.SAFE	Update of IPF internal configuration parameters (aziFilterLength and aziFftOversampFactor). Related to RDB#5.
S1A_AUX_PP1_V20150519T120000_G20160413T100930.SAFE	Update of IPF internal configuration parameters (aziFilterLength and aziFftOversampFactor). Related to RDB#4.
S1A_AUX_PP1_V20140908T000000_G20160413T100901.SAFE	Update of IPF internal configuration parameters (aziFilterLength and aziFftOversampFactor). Related to RDB#3.
S1A_AUX_PP1_V20140616T133700_G20160413T100821.SAFE	Update of IPF internal configuration parameters (aziFilterLength and aziFftOversampFactor). Related to RDB#2.
S1A_AUX_PP1_V20140402T000000_G20160413T100648.SAFE	Update of IPF internal configuration parameters (aziFilterLength and

	aziFftOversampFactor). Related to RDB#1.
S1A_AUX_PP1_V20150722T120000_G20160517T085710.SAFE	Update of the processing gains to improve WV calibration on VV polarisation. Related to RDB#5.
S1A_AUX_PP1_V20150519T120000_G20160517T085640.SAFE	Update of the processing gains to improve WV calibration on VV polarisation. Related to RDB#4.
S1A_AUX_PP1_V20140908T000000_G20160517T085612.SAFE	Update of the processing gains to improve WV calibration on VV polarisation. Related to RDB#3.
S1A_AUX_PP1_V20140616T133700_G20160517T085546.SAFE	Update of the processing gains to improve WV calibration on VV polarisation. Related to RDB#2.
S1A_AUX_PP1_V20140402T000000_G20160517T085509.SAFE	Update of the processing gains to improve WV calibration on VV polarisation. Related to RDB#1.

L2 Processor Parameters ADF (AUX_PP2)

ADF	Update Reason

Simulated Cross Spectra ADF (AUX_SCS)

ADF	Update Reason
S1__AUX_SCS_V20150722T120000_G20160413T105410.SAFE	Introduction of AUX_SCS. Related to RDB#5.
S1__AUX_SCS_V20150519T120000_G20160413T105253.SAFE	Introduction of AUX_SCS. Related to RDB#4.
S1__AUX_SCS_V20140908T000000_G20160413T105124.SAFE	Introduction of AUX_SCS. Related to RDB#3.
S1__AUX_SCS_V20140616T133700_G20160413T104849.SAFE	Introduction of AUX_SCS. Related to RDB#2.
S1__AUX_SCS_V20140402T000000_G20160413T103855.SAFE	Introduction of AUX_SCS. Related to RDB#1.

Appendix G - **S-1A Orbit Manoeuvres**

The S-1A orbit manoeuvres during 2016 were:

Start Date	Start Time	Stop Date	Stop Time
07/01/2016	00:51:08.217	07/01/2016	00:51:16.717
14/01/2016	00:56:41.960	14/01/2016	00:56:53.210
14/01/2016	01:46:19.941	14/01/2016	01:46:21.816
21/01/2016	00:28:25.060	21/01/2016	00:28:27.435
27/01/2016	22:13:23.916	27/01/2016	22:16:54.416
11/02/2016	01:42:58.359	11/02/2016	01:43:19.109
18/02/2016	01:35:20.835	18/02/2016	01:35:28.335
25/02/2016	01:26:53.953	25/02/2016	01:27:05.328
03/03/2016	01:20:45.097	03/03/2016	01:20:48.847
10/03/2016	01:09:16.354	10/03/2016	01:09:33.104
17/03/2016	01:07:37.774	17/03/2016	01:07:44.774
24/03/2016	01:02:42.393	24/03/2016	01:02:50.018
31/03/2016	00:25:29.842	31/03/2016	00:25:35.592
06/04/2016	23:19:20.214	06/04/2016	23:22:27.339
07/04/2016	00:19:36.305	07/04/2016	00:20:04.930
14/04/2016	00:09:39.933	14/04/2016	00:09:44.058
21/04/2016	00:00:36.333	21/04/2016	00:00:45.708
27/04/2016	23:55:40.933	27/04/2016	23:55:46.308
05/05/2016	00:23:56.576	05/05/2016	00:28:59.326
05/05/2016	01:32:51.673	05/05/2016	01:33:26.923
05/05/2016	02:22:47.154	05/05/2016	02:22:57.154
19/05/2016	01:04:23.544	19/05/2016	01:04:36.794
26/05/2016	00:56:29.821	26/05/2016	00:56:34.946
01/06/2016	23:52:34.737	01/06/2016	23:55:06.112
02/06/2016	00:47:22.856	02/06/2016	00:47:46.606
09/06/2016	00:36:45.440	09/06/2016	00:36:51.065
16/06/2016	00:27:57.840	16/06/2016	00:28:30.215
16/06/2016	01:17:47.832	16/06/2016	01:18:12.332
23/06/2016	00:27:34.133	23/06/2016	00:27:44.633
23/06/2016	01:17:03.220	23/06/2016	01:17:08.970

30/06/2016	00:22:42.980	30/06/2016	00:22:56.355
30/06/2016	01:12:15.631	30/06/2016	01:12:21.381
13/07/2016	23:57:48.630	13/07/2016	23:58:18.255
14/07/2016	00:47:36.207	14/07/2016	00:47:53.332
20/07/2016	22:05:41.897	20/07/2016	22:08:17.022
20/07/2016	23:45:44.102	20/07/2016	23:45:52.727
27/07/2016	21:30:43.437	27/07/2016	21:31:18.562
27/07/2016	23:08:43.437	27/07/2016	23:09:18.562
28/07/2016	00:46:43.687	28/07/2016	00:47:18.312
28/07/2016	02:24:43.687	28/07/2016	02:25:18.312
28/07/2016	04:02:52.875	28/07/2016	04:03:09.125
03/08/2016	23:27:59.990	03/08/2016	23:30:35.865
04/08/2016	02:04:33.498	04/08/2016	02:04:52.373
11/08/2016	01:03:20.231	11/08/2016	01:03:54.606
11/08/2016	01:53:12.349	11/08/2016	01:53:31.724
17/08/2016	23:11:48.245	17/08/2016	23:13:54.370
18/08/2016	02:13:52.235	18/08/2016	02:14:00.610
24/08/2016	23:27:06.087	24/08/2016	23:27:09.212
31/08/2016	22:54:55.375	31/08/2016	22:57:53.750
01/09/2016	01:45:34.633	01/09/2016	01:45:39.258
08/09/2016	00:43:08.274	08/09/2016	00:43:13.524
15/09/2016	00:23:06.417	15/09/2016	00:23:09.292
16/09/2016	15:38:14.375	16/09/2016	15:38:45.625
16/09/2016	17:12:16.437	16/09/2016	17:12:43.562
21/09/2016	22:30:08.182	21/09/2016	22:33:21.557
22/09/2016	01:45:07.324	22/09/2016	01:45:15.449
22/09/2016	02:34:33.438	22/09/2016	02:34:36.563
28/09/2016	09:40:40.250	28/09/2016	09:41:11.750
28/09/2016	11:18:42.187	28/09/2016	11:19:09.812
06/10/2016	00:43:20.400	06/10/2016	00:43:24.275
06/10/2016	01:32:47.214	06/10/2016	01:32:52.589
12/10/2016	22:54:59.983	12/10/2016	22:57:44.733
13/10/2016	00:35:06.817	13/10/2016	00:35:28.692
19/10/2016	22:08:26.254	19/10/2016	22:08:37.254

02/11/2016	21:53:21.472	02/11/2016	21:53:28.347
09/11/2016	22:22:40.452	09/11/2016	22:24:15.452
10/11/2016	00:01:25.042	10/11/2016	00:03:00.042
10/11/2016	01:31:32.185	10/11/2016	01:31:54.685
16/11/2016	23:44:47.444	16/11/2016	23:44:53.569
23/11/2016	21:54:40.778	23/11/2016	21:54:42.903
01/12/2016	00:59:32.884	01/12/2016	00:59:39.384
07/12/2016	23:28:44.104	07/12/2016	23:29:50.604
08/12/2016	00:55:21.620	08/12/2016	00:55:30.620
15/12/2016	00:44:18.469	15/12/2016	00:44:24.594
02/11/2016	21:53:21.472	02/11/2016	21:53:28.347
09/11/2016	22:22:40.452	09/11/2016	22:24:15.452
10/11/2016	00:01:25.042	10/11/2016	00:03:00.042
10/11/2016	01:31:32.185	10/11/2016	01:31:54.685
16/11/2016	23:44:47.444	16/11/2016	23:44:53.569
23/11/2016	21:54:40.778	23/11/2016	21:54:42.903
01/12/2016	00:59:32.884	01/12/2016	00:59:39.384
07/12/2016	23:28:44.104	07/12/2016	23:29:50.604
08/12/2016	00:55:21.620	08/12/2016	00:55:30.620
15/12/2016	00:44:18.469	15/12/2016	00:44:24.594
21/12/2016	22:59:46.091	21/12/2016	22:59:49.216
27/12/2016	03:09:14.438	27/12/2016	03:09:49.563
27/12/2016	04:47:59.438	27/12/2016	04:48:34.563
27/12/2016	06:26:44.813	27/12/2016	06:27:17.188
27/12/2016	08:05:29.813	27/12/2016	08:06:02.188

Appendix H - **S-1A Quality Disclaimers**

S-1A quality disclaimers were issued during 2016:

Number	Description	Start Validity Date	End Validity Date	Issue Status
17	Incorrect Cycle Number in S-1A Products acquired between 26/01/2016 and 04/02/2016.	2016-01-26 21:17:42 UT	2016-02-04 16:29:59 UT	Issued
18	Invalid annotation of NSSDC identifier of Sentinel-1A between April 2014 and July 5th 2016	2014-09-30 15:17:26 UT	2016-07-05 10:16:00 UT	Issued
21	Issue on geolocation of Sentinel-1A SM SLC products with IPF v2.71	2016-05-11 21:02:59 UT	2016-08-22 21:35:50 UT	Issued
22	Invalid annotation of SSPPDU in the manifest of S-1A products	2014-09-30 15:17:26 UT	ongoing	Issued
24	Incorrect Cycle Number in S-1A Products acquired between 12/01/2017 and 24/01/2017	2017-01-12 00:18:59	2017-01-24 00:08:00	Issued

Appendix I - **S-1A Antenna Pointing**

The following plots show trends for yaw, pitch and roll errors during 2016 against ascending node crossing time (ANX). The red horizontal lines show the nominal ±0.01° bounds for these attitude errors. The short duration changes in yaw are due to orbit manoeuvres. The increase in calculated yaw around ANX of 3000 is not an issue with Sentinel1-A itself but with how the yaw is calculated on-ground and consequently there is no impact of the quality of products.

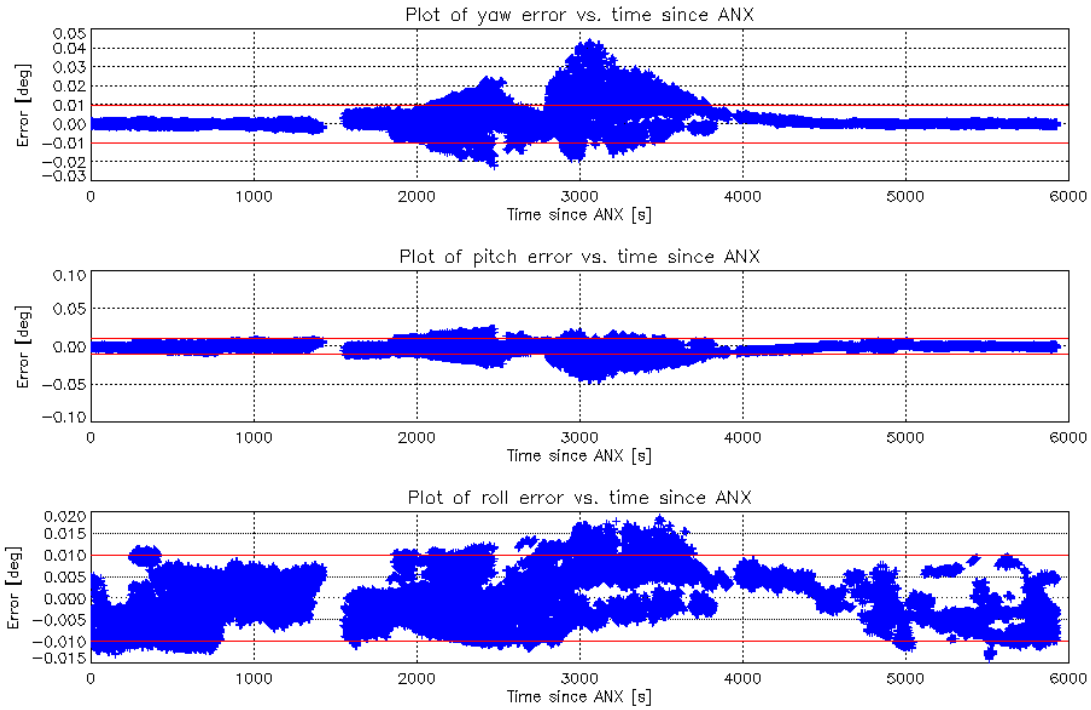

Cycles 69 & 70

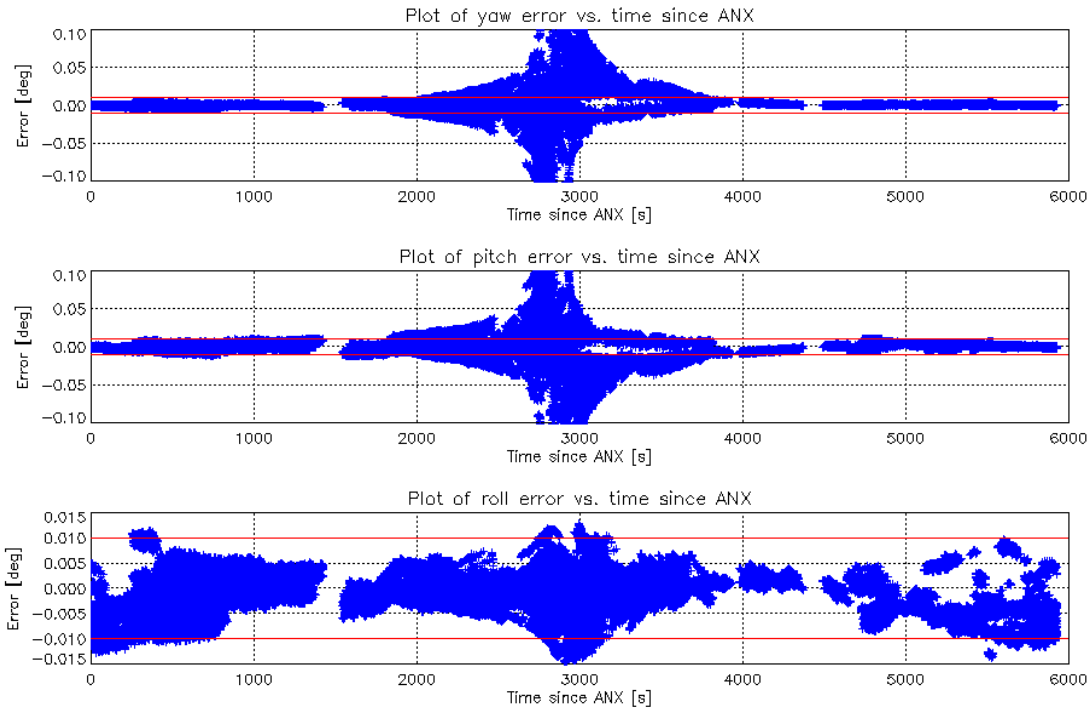

Cycles 71 & 72

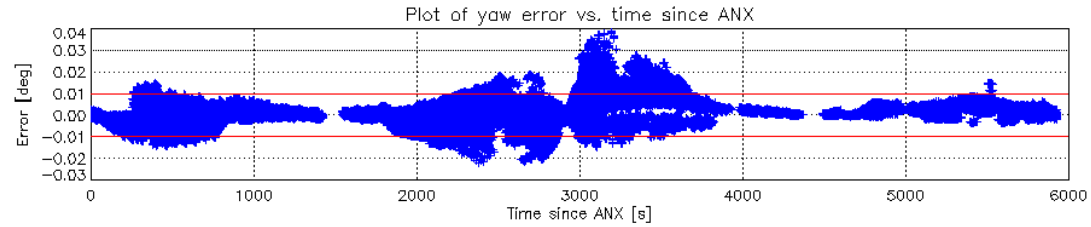

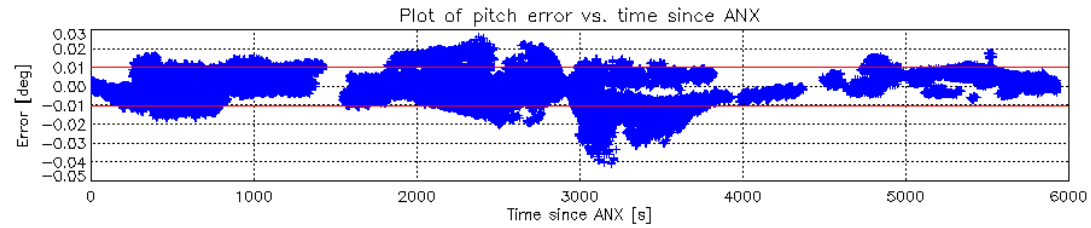

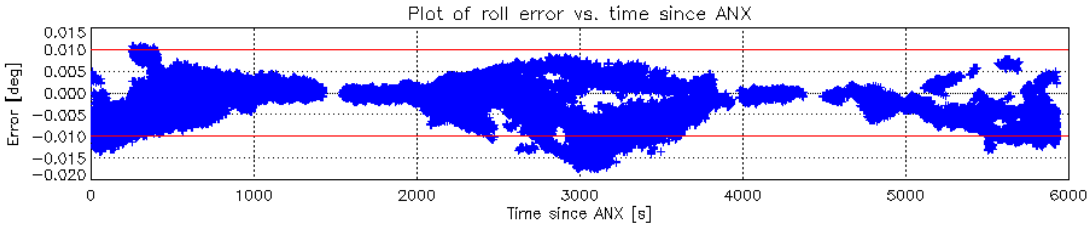

Cycles 73 & 74

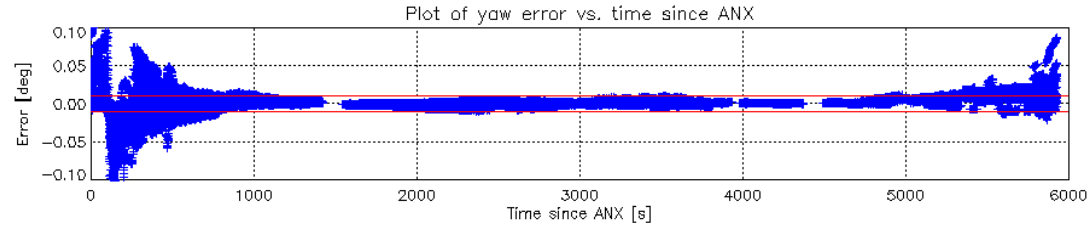

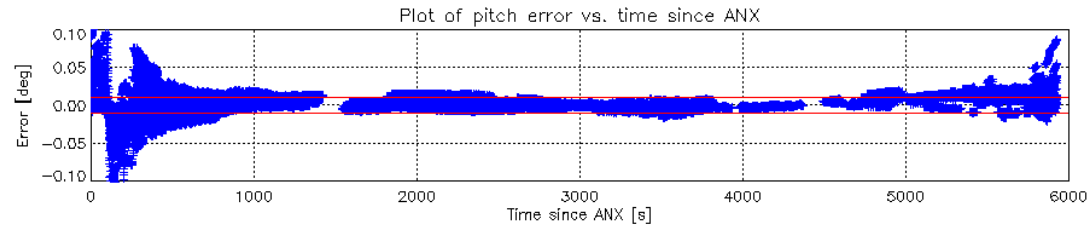

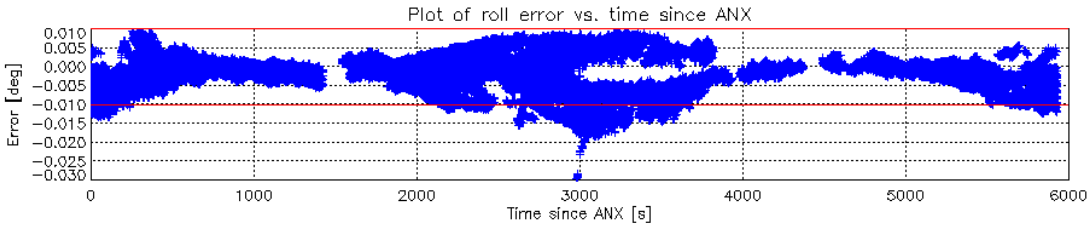

Cycles 75 & 76

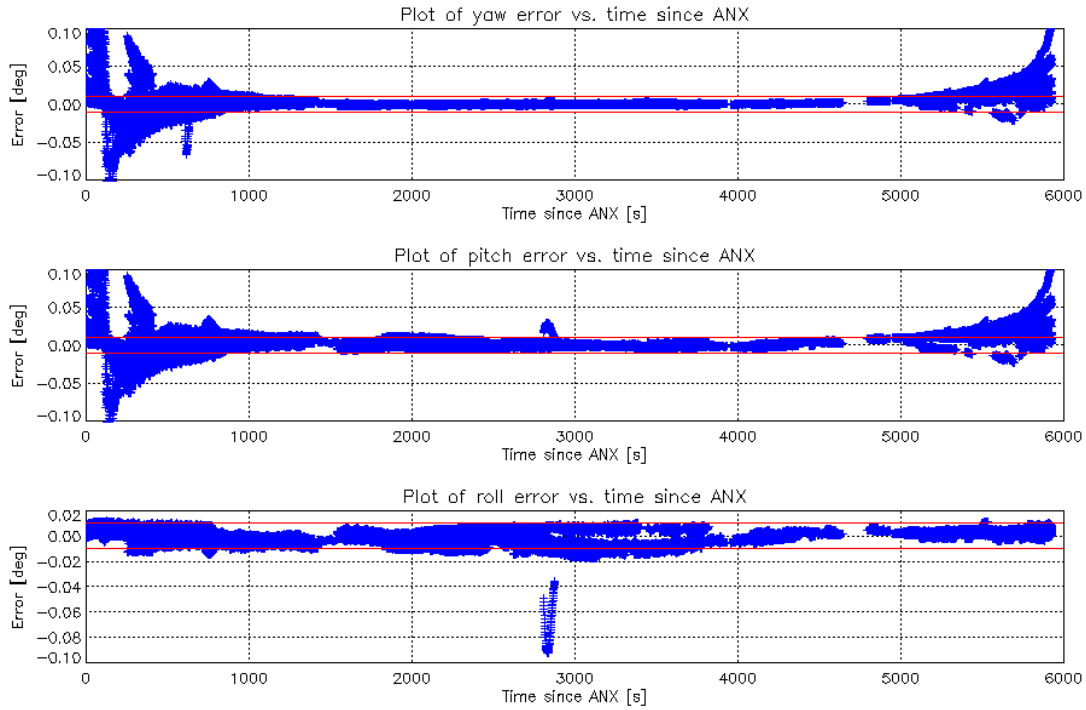

Cycles 77 & 78

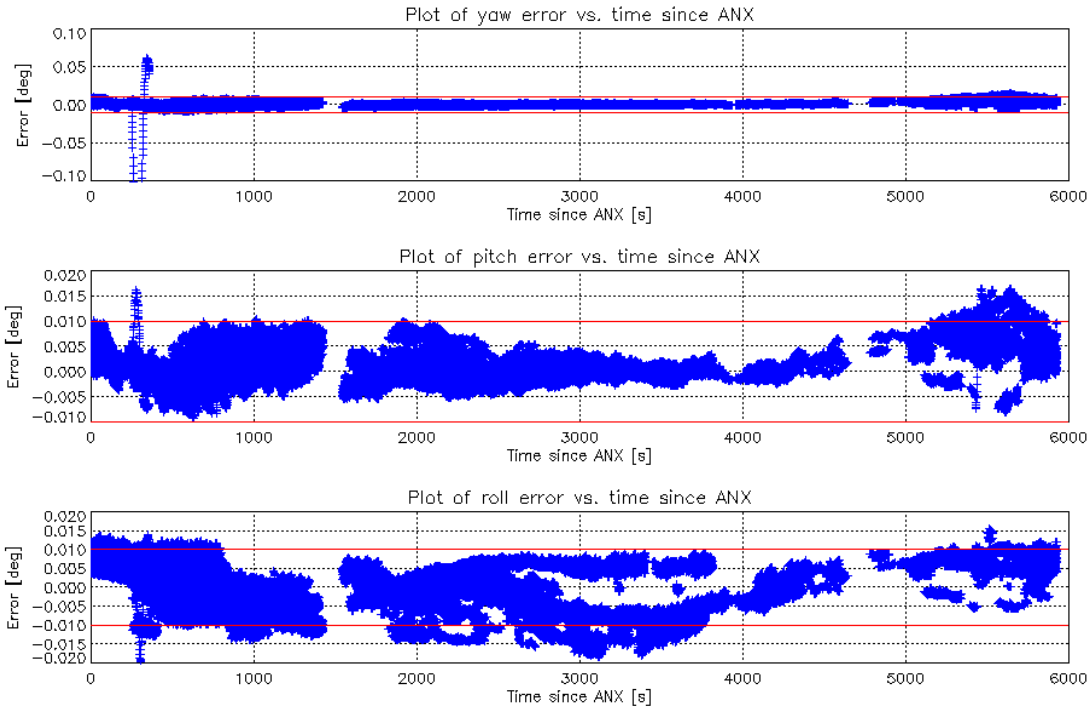

Cycles 79 & 80

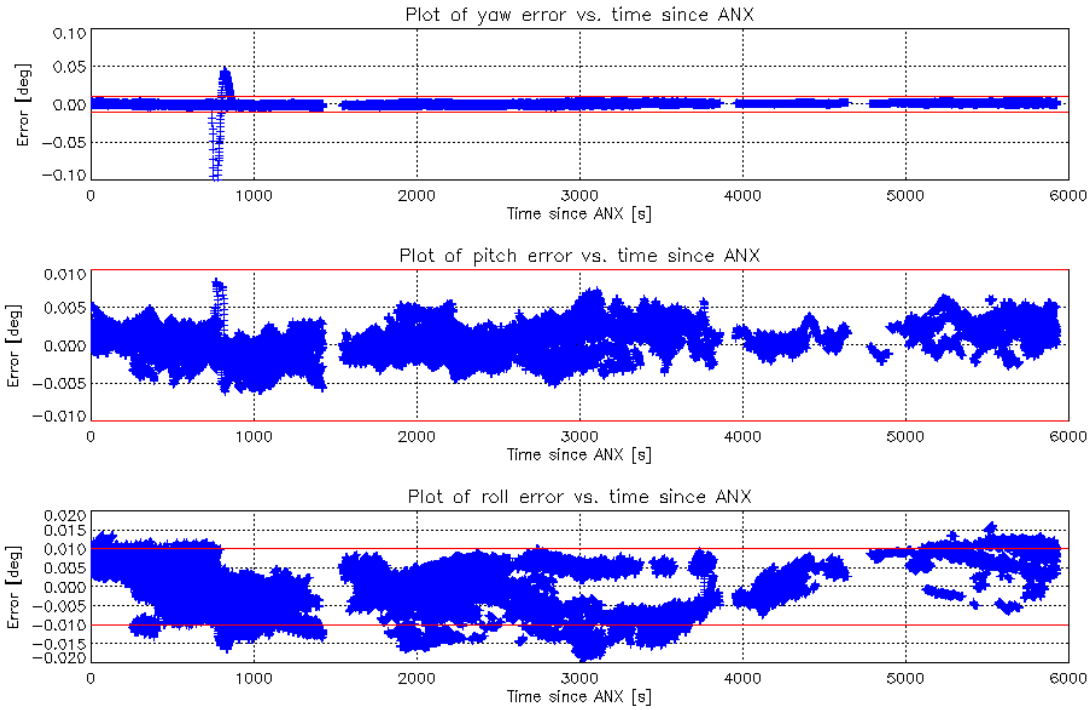

Cycles 81 & 82

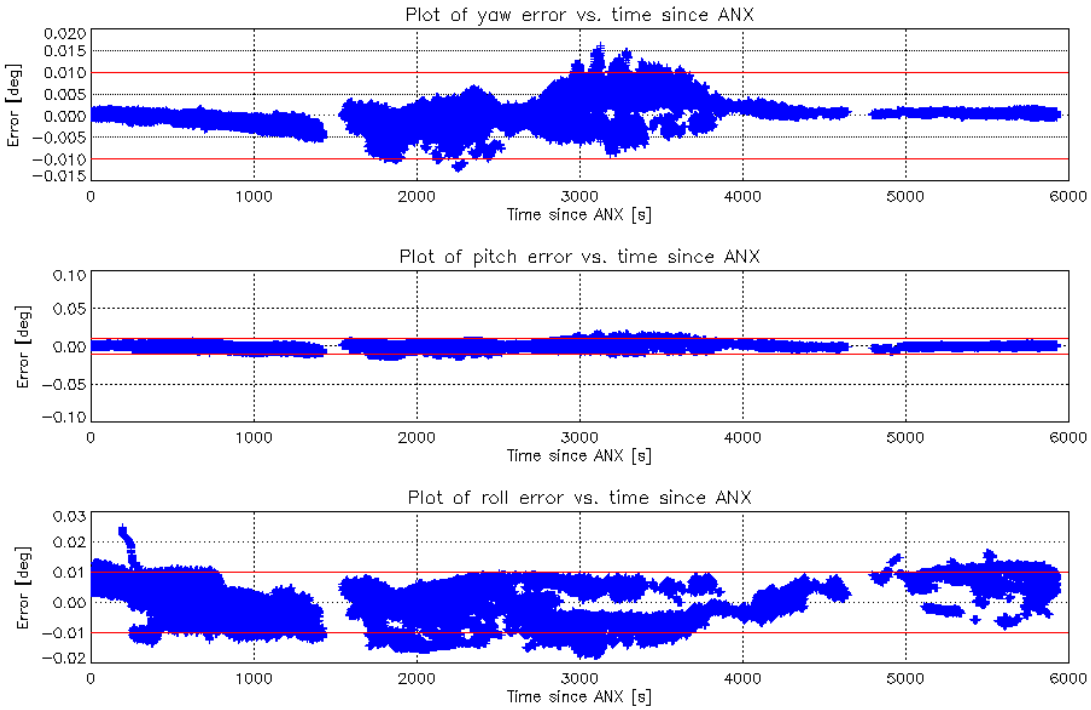

Cycles 83 & 84

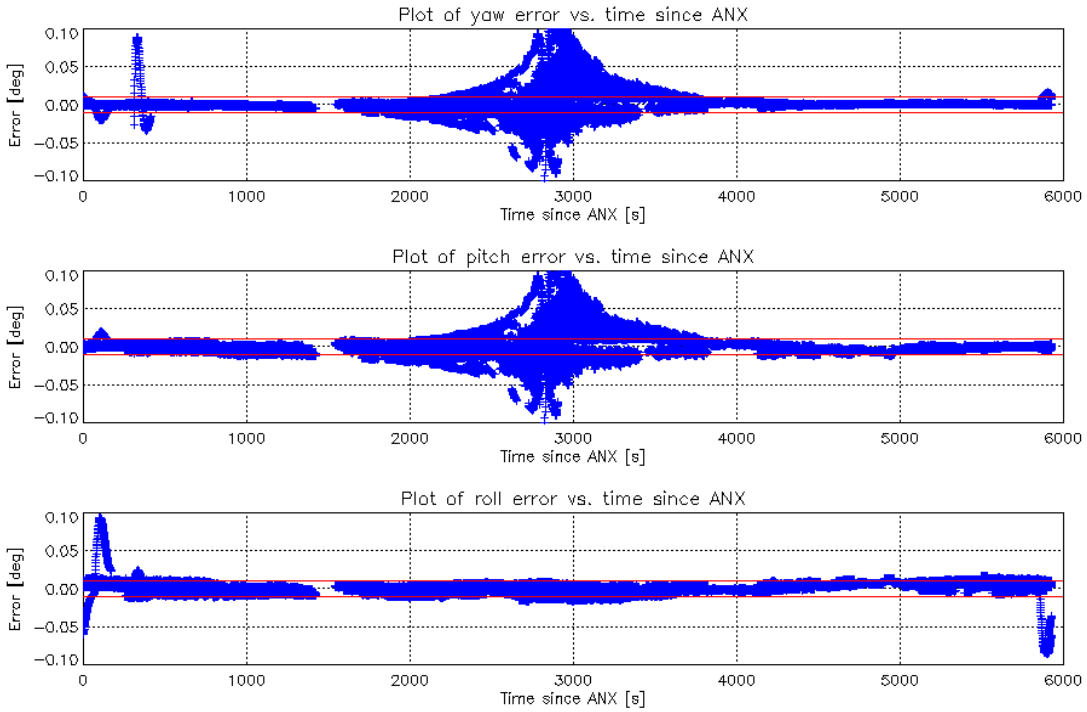

Cycles 85 & 86

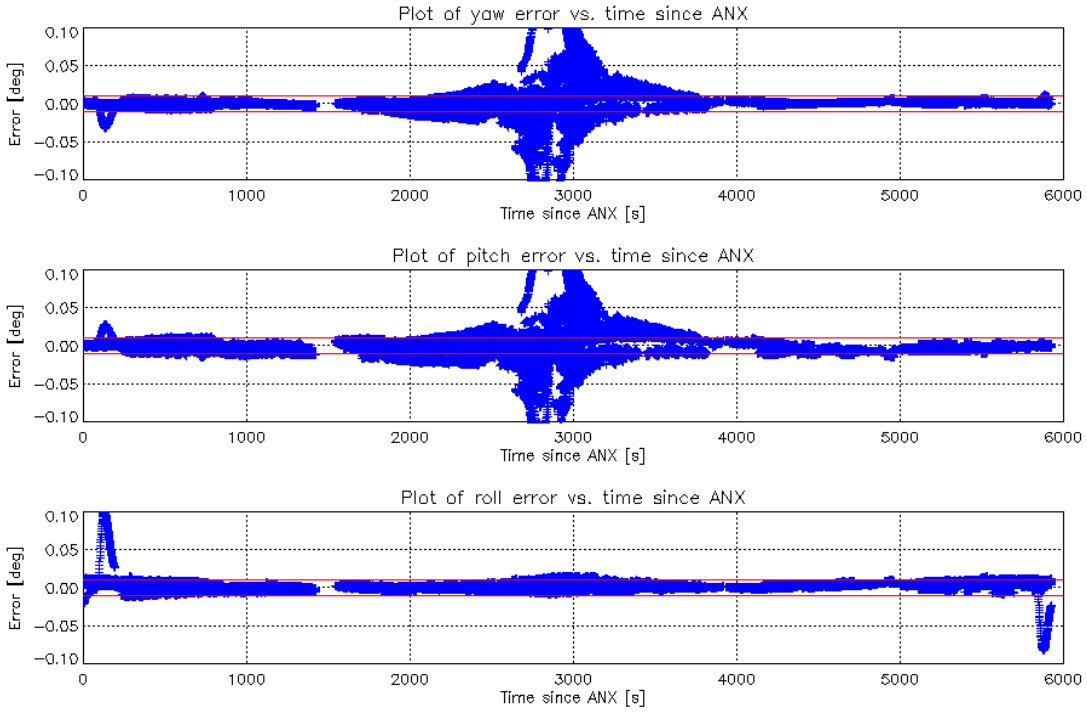

Cycles 87 & 88

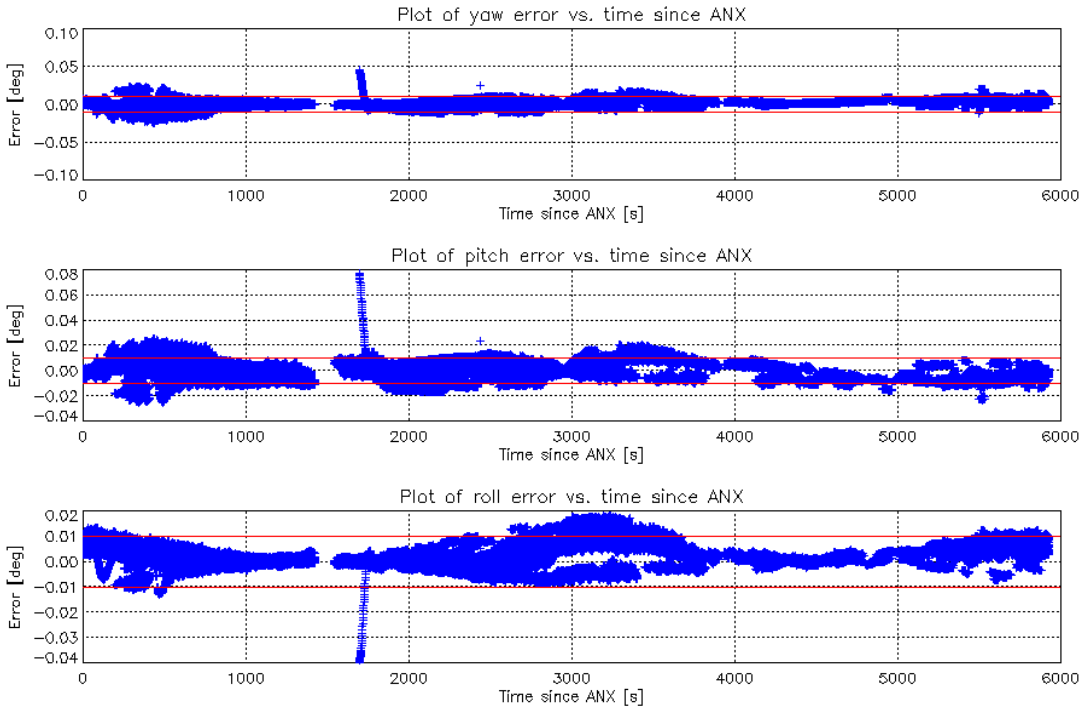

Cycles 89 & 90

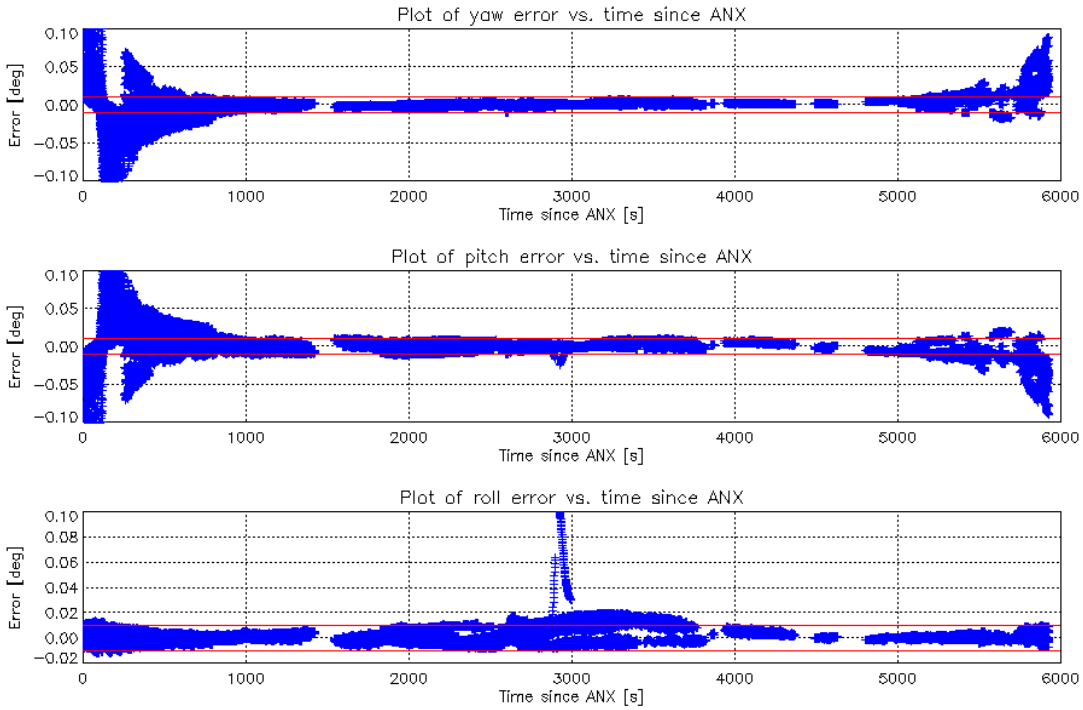

Cycles 91 & 92

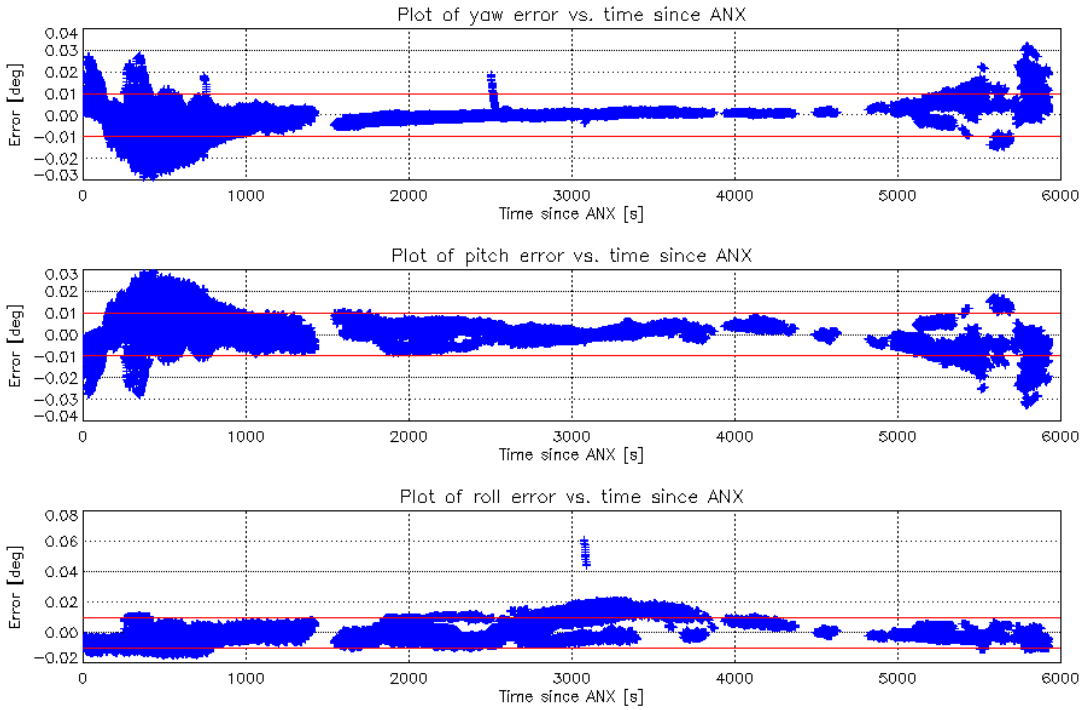

Cycles 93 & 94

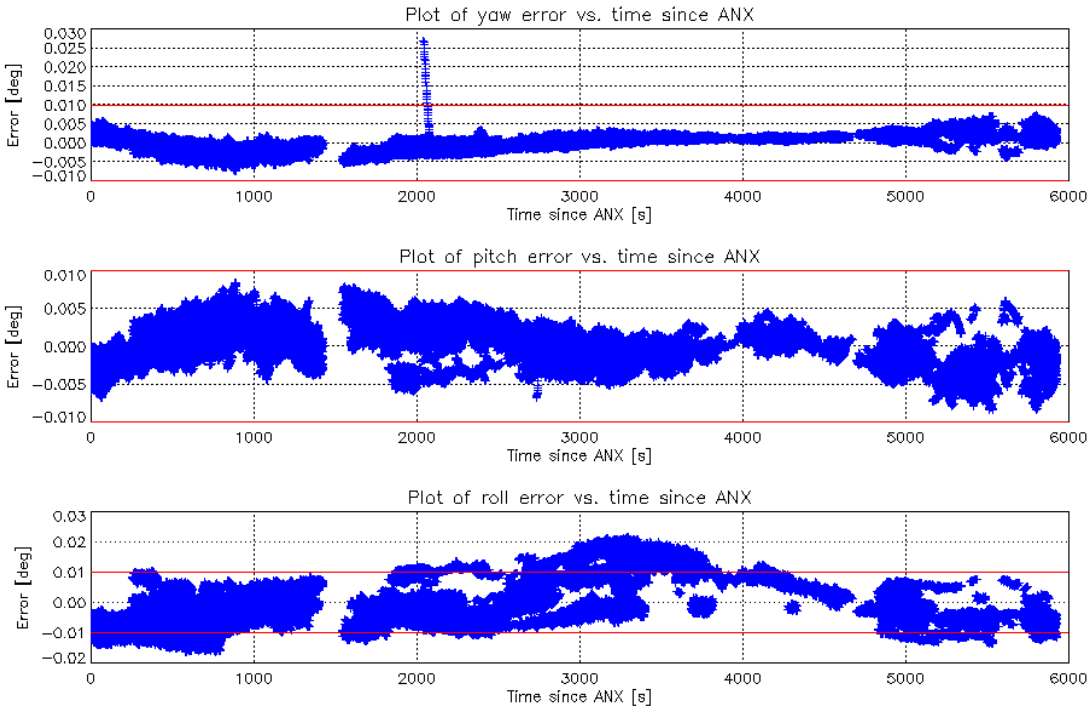

Cycles 95 & 96

Appendix J - **S-1B Orbit Cycles**

The table below gives the cycle number with start and stop acquisition dates since the start of the routine phase in September 2016. The start of a cycle is at approximately 18:00 UT on the dates below.

Cycle	Start Date	End Date
21	12/10/2016	24/10/2016
22	24/10/2016	05/11/2016
23	05/11/2016	17/11/2016
24	17/11/2016	29/11/2016
25	29/11/2016	11/12/2016
26	11/12/2016	23/12/2016

Appendix K - **S-1B Transmit Receive Module Failures**

The following S-1B antenna Transmit/Receive Module (TRM) failed since launch in April 2016:

TRM	Description	Date of Failure
Tile 5, Row 7	Tx, H & V - Rx V	22-April-2016
Tile 5, Row 8	Tx, H & V	22-April-2016
Tile 5, Row 8	Rx, V	17-June-2016

Appendix L - **S-1B Instrument Unavailability**

The S-1B instrument was unavailable since the start of the routine phase in September 2016 (a full list since launch can be found in Appendix C - of any S-1B N-Cyclic Performance Report):

Start Date/Time	End Date/Time	MPC Reference	Summary
16/06/2016 00:00	16/06/2016 08:17	SOB-446	Sentinel-1B Unavailability on 16/06/2016
28/06/2016 19:41	29/06/2016 10:32	SOB-461	Sentinel-1B Unavailability from 28/06/2016 to 29/06/2016
04/07/2016 03:28	04/07/2016 10:42	SOB-477	Sentinel-1B Unavailability on 04/07/2016
12/10/2016 07:00	13/10/2016 15:34	SOB-572	Sentinel-1B SAR issue from 12/10/2016 to 13/10/2016

Appendix M - **S-1B Auxiliary Data Files**

The following S-1B Auxiliary Data Files (ADFs) were updated since the start of the routine phase in September 2016:

Instrument ADF (AUX_INS)

ADF	Update Reason
S1B_AUX_INS_V20160422T000000_G20160922T094114.SAFE	First applicable auxiliary file for user released products. Related to RDB#1.

Calibration ADF (AUX_CAL)

ADF	Update Reason
S1B_AUX_CAL_V20160422T000000_G20160922T094442.SAFE	First applicable auxiliary file for user released products. Related to RDB#1.

L1 Processor Parameters ADF (AUX_PP1)

ADF	Update Reason
S1B_AUX_PP1_V20160422T000000_G20160922T094703.SAFE	First applicable auxiliary file for user released products. Related to RDB#1.

L2 Processor Parameters ADF (AUX_PP2)

ADF	Update Reason
S1B_AUX_PP2_V20160422T000000_G20160420T135034.SAFE	First applicable auxiliary file for user released products. Related to RDB#1.

Simulated Cross Spectra ADF (AUX_SCS)

ADF	Update Reason
S1__AUX_SCS_V20140402T000000_G20160413T103855.SAFE	First applicable auxiliary file for user released products. Related to RDB#1.

Appendix N - **S-1B Orbit Manoeuvres**

The S-1B orbit manoeuvres since the start of the routine phase in September 2016 were:

Start Date	Start Time	Stop Date	Stop Time
12/10/2016	23:43:52.648	12/10/2016	23:46:12.773
13/10/2016	01:23:47.289	13/10/2016	01:24:02.414
20/10/2016	01:15:33.498	20/10/2016	01:15:36.123
20/10/2016	02:17:52.935	20/10/2016	02:18:02.435
02/11/2016	21:03:50.078	02/11/2016	21:03:54.703
09/11/2016	23:10:41.201	09/11/2016	23:13:35.326
10/11/2016	00:41:43.324	10/11/2016	00:42:03.324
17/11/2016	00:36:26.764	17/11/2016	00:36:35.889
17/11/2016	14:16:15.000	17/11/2016	14:16:43.000
17/11/2016	15:56:15.000	17/11/2016	15:56:43.000
17/11/2016	17:36:13.750	17/11/2016	17:36:44.250
17/11/2016	19:16:13.750	17/11/2016	19:16:44.250
23/11/2016	22:18:59.084	23/11/2016	22:19:02.709
01/12/2016	00:16:51.759	01/12/2016	00:16:55.384
07/12/2016	22:38:47.193	07/12/2016	22:39:38.943
08/12/2016	00:01:31.421	08/12/2016	00:01:39.046
14/12/2016	23:55:05.992	14/12/2016	23:55:10.617
21/12/2016	22:00:50.544	21/12/2016	22:00:56.169
21/12/2016	22:50:19.220	21/12/2016	22:50:21.720
28/12/2016	23:35:11.447	28/12/2016	23:35:13.947

Appendix O - **S-1B Quality Disclaimers**

S-1B quality disclaimers were issued from the start of the routine phase in September 2016:

Number	Description	Start Validity Date	End Validity Date	Issue Status
19	S-1B Denoising vectors not qualified	2016-08-20 00:00:00	ongoing	Issued
20	S-1B Dual Polarisation Timing De-synchronisation & Single H polarisation Localisation Error	2016-10-12 08:31:00	2016-10-13 15:36:00	Issued
23	Invalid annotation of SSPPDU in the manifest of S-1B products	2016-08-20 00:00:00	ongoing	Issued
25	Incorrect Cycle Number in S1-B Products acquired between 12/01/2017 and 24/01/2017	2017-01-12 07:48:29	2017-01-24 07:14:46	Issued

Appendix P - **S-1B Antenna Pointing**

The following plots show trends for yaw, pitch and roll errors since the start of the routine phase in September 2016 against ascending node crossing time (ANX). The red horizontal lines show the nominal ±0.01° bounds for these attitude errors. The short duration changes in yaw are due to orbit manoeuvres. The increase in calculated yaw around ANX of 3000 is not an issue with Sentinel1-B itself but with how the yaw is calculated on-ground and consequently there is no impact of the quality of products.

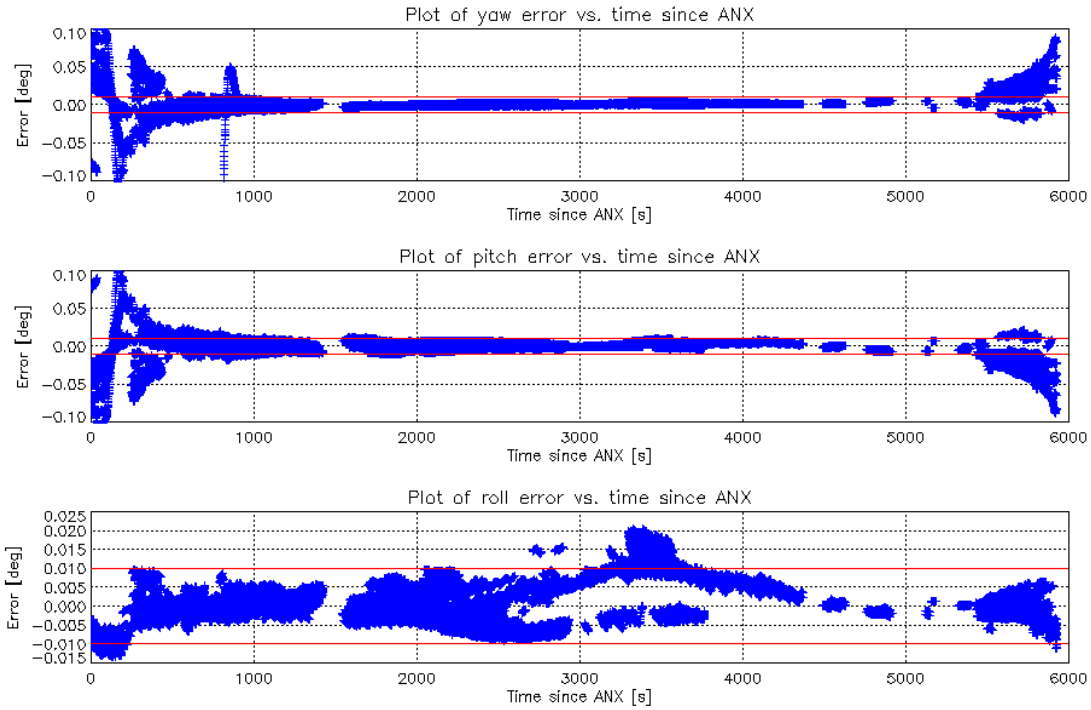

Cycles 21 & 22

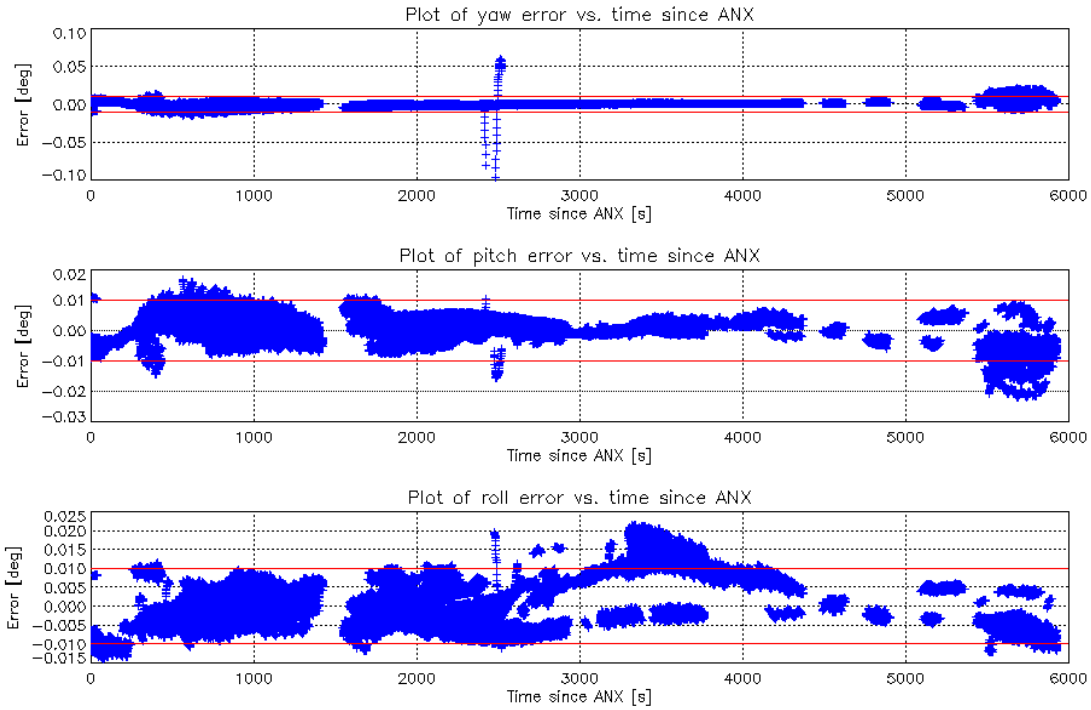

Cycles 23 & 24

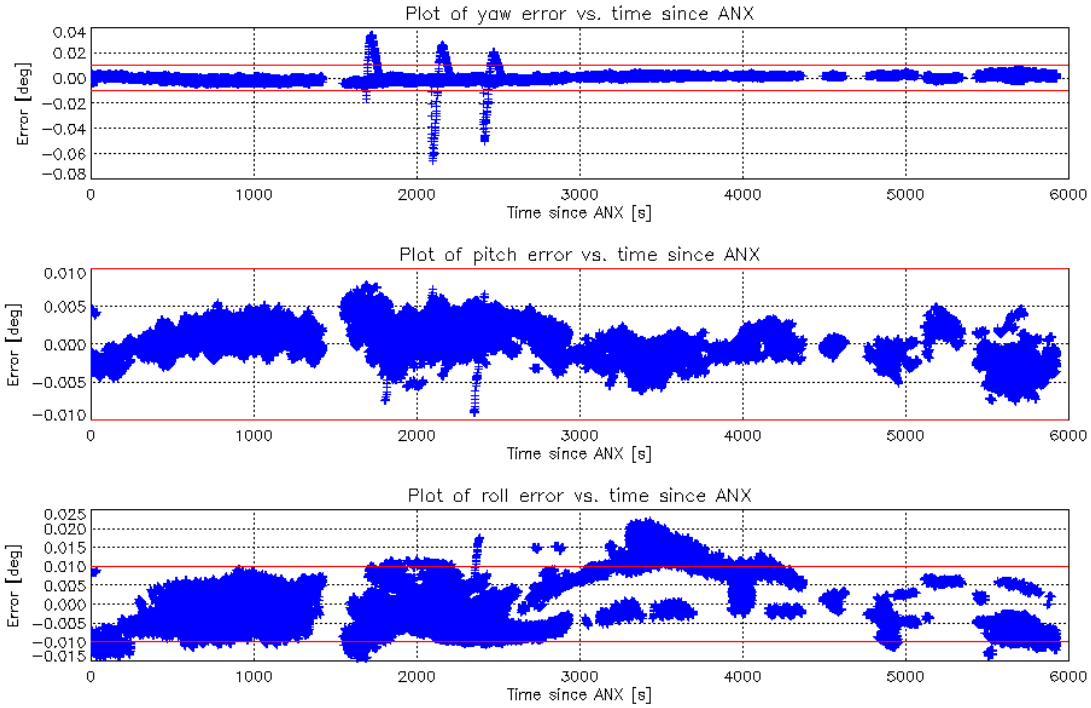

Cycles 25 & 26